Anticipating Bifurcations for Identifying Dynamic Characteristics of Complex Systems

by

Amin Ghadami

A dissertation submitted in partial fulfillment
of the requirements for the degree of
Doctor of Philosophy
(Mechanical Engineering)
in the University of Michigan
2019

Doctoral Committee:

Professor Bogdan I. Epureanu, Chair
Professor Carlos E. S. Cesnik
Professor Charles R. Doering
Assistant Research Scientist Eleni Gourgou
Professor Kon-Well Wang

Amin Ghadami
aghadami@umich.edu
ORCID iD: 0000-0001-5883-4153

© Amin Ghadami 2019

To my parents and my wife,
for their unconditional love and support.

Acknowledgements

I have been extremely fortunate to be able to study at the University of Michigan. During my Ph.D. studies, I grew considerably both on an academic and a personal level. To all the people who provided me with support, guidance, and encouragement, I would like to express my heartfelt gratitude.

First and foremost, I would like to express my sincere gratitude to my advisor Prof. Bogdan Epureanu, for giving the opportunity to study at University of Michigan, and his continuous support as I walked down the path to my Ph.D. degree. I thank you for providing me the opportunity to explore different subjects during my Ph.D., being encouraging and inspiring during our meetings, and for teaching me greatly in the process. Thank you for making me feel welcome all these years. This research would not have been possible without your continuing support and encouragement.

I would also like to thank my doctoral committee, Prof. Carlos Cesnik, Prof. Kon-Well Wang, Prof. Charles Doering, and Dr. Eleni Gourgou, for their insightful comments, mentorship and advice which made this dissertation possible, and for their continued support to my study and career. I am especially thankful to Prof. Carlos Cesnik for dedicating his precious time in supporting and revising my work related to the fluid-structural systems. Moreover, I am indebted to Dr. Eleni Gourgou for all her efforts in teaching me about experimental biology. Without her help and support, I would never have been able to conduct my research in the field of experimental biology.

I am also grateful to my colleagues and friends of Applied Nonlinear Dynamics of Multi-Scale Systems Laboratory, including Woochul Nam, Seunghoon Baek, Kiyoung Oh, Jauching Lu, Mainak Mitra, Weihan Tang, Adegbenga Odofin, Chenyu Yi, Kejie Chen, Andrea Lupini, Mert Egilmez, Mohammad Khodabakhsh, Ehsan Mirzakhalili, Mohammad Ravandi, Sean Kelly, and Cristina Riso for their insights and suggestions.

I am forever thankful to my amazing family for their unconditional love and support, and instilling in me a passion for learning and pursuing my goals. Lastly, I would like to thank my wife, Neda, for her love and encouragement. Thank you, Neda, for being always supportive with your helpful advice and positive thoughts and inputs.

Finally, I am thankful to all my friends in Ann Arbor for being supportive and encouraging during these years. Without them, I would not have been able to enjoy my life here at Ann Arbor throughout many winters and summers

Table of Contacts

List of Figures

List of Tables

Abstract

Complex systems are at risk of critical transitions when the system shifts abruptly from one state to another when a threshold is crossed. Recent studies have revealed that a variety of systems, ranging from systems examined by engineering, physics, and biology, to others related to climate sciences, medicine, social sciences, and ecology are susceptible to transitions leading to drastic re-organization or collapse. Such an unexpected transition is usually undesirable, because it is often difficult to restore a system to its pre-transition state once the transition occurs. It is exceedingly difficult to know if a system comes close to critical transitions because typically no easily noticeable changes can be observed unless the transition happens. Furthermore, accurate models are often not available, and predictions based on models of limited accuracy face difficulties. Hence, we are still ill-equipped to predict critical transitions, and there is an acute need for reliable methods to predict such catastrophic events.

In this research, a data-driven, model-free approach is introduced to forecast critical points and post-critical dynamics of complex dynamical systems using measurements of the system response collected only in the pre-transition regime. Based on observations of the system response to perturbations only in the pre-transition regime, the method forecasts the bifurcation diagram and discovers the system's stability after the transition. The forecasting approach is based on the phenomenon of critical slowing down, referring to the slowing down of a system's dynamics when approaching a tipping point. The rate of the system's recovery from perturbations decreases when the system approaches the transition. Thus, the rate of recovery from perturbations can be used as an indicator, and is correlated to the distance to the transition.

The method is employed to forecast critical transitions in several classes of complex systems including flutter instabilities in fluid-structural systems, collapse of natural populations in ecological systems, and the onset of traffic congestions in vehicular traffic flow systems. The theoretical and experimental results of this study address important challenges in forecasting safety and stability of complex systems. The capabilities of the methods proposed make them unique tools for analysis of complex systems in both computational and experimental studies.

Chapter 1

Introduction

1.1 Motivation

Bifurcations occur in the dynamics of complex systems, from natural ecosystems to engineered systems. Such phenomena lead to various types of stability issues and can cause dramatic changes in the dynamics. Therefore, forecasting such bifurcations, i.e. predicting bifurcations and the bifurcation diagram with measurements only from the pre-bifurcation regime is a significant challenge and an important need. This is especially important for complex large-dimensional systems when an accurate model of the system is not easily available or when the system properties/parameters are unknown.

Numerous studies have revealed the variety of systems that are at risk of undergoing bifurcations and critical transitions [1,2], ranging from systems examined by engineering [3,4], chemistry [5,6], physics [7,8], and biology [9–11], to others related to climate sciences [12–14], medicine and disease [15–17], social sciences [18–20], and ecology [21–23]. Spontaneous systemic failures such as epileptic seizures in medicine, market crashes in finance, abrupt climate changes in earth science, collapse of natural populations in ecology, and flutter instability in engineering are a few examples of such transitions. Such an unexpected change in the equilibrium state is usually undesirable, because it is exceedingly difficult to restore a system to its pre-transition state once the transition occurs [24,25]. Hence, it is necessary to develop methods capable of forecasting the upcoming transition, as part of a preventive plan against possible detrimental consequences.

Forecasting bifurcations can be straightforward if a mathematical model exists for the system. However, accurate predictive modeling can be challenging, especially when the system is complex (e.g., it has many agents with nonlinear interactions). For complex nonlinear dynamical systems, it is usually not possible to have a model of the system accurate enough to predict bifurcations of the system without performing measurements in the post-bifurcation regime. Moreover, even when a mathematical model is introduced, it may be incomplete or inaccurate due to assumptions and uncertainties in modeling and parameter values. Hence, predictions based on models of limited accuracy face substantial difficulties [26]. As a result, researchers have focused on developing model-free approaches to extract early warning signals from observed time series, and several indicators have been introduced for this purpose [26–33].

Recent studies demonstrate that even without knowing the system equations, tipping points in the dynamics can be forecasted using early warning indicators which can be extracted from observed time series of system behavior in the pre-bifurcation regime [32–40]. Several early warning signals based on the analysis of measured time series have been developed and can successfully provide an alarm when a system approaches a critical transition. These methods are applicable to systems with small fluctuations around the equilibrium state resulting from stochastic perturbations. The most important clues that have been suggested as indicators of whether a system is getting close to a critical threshold are related to a phenomenon known in dynamical systems theory as critical slowing down [2,12,34–36]. As the system approaches a threshold, rate of its recovery from perturbations decreases and the time required for the system to return to its equilibrium state is increased. This implies that the system becomes more correlated with its past, which leads to an increase in autocorrelation. Furthermore, the perturbations accumulate which lead to an increase in the size of the fluctuations and as a result, an increase in variance would be observed. In summary, the phenomenon of critical slowing down leads to three possible early-warning signals in the dynamics of a system approaching a bifurcation: slower recovery from perturbations, increased autocorrelation and increased variance. Such features are observed in recoveries in the vicinity of catastrophic bifurcation points, and analyses of models exposed to stochastic forcing show that if the system is gradually approaching to a catastrophic threshold, an increase in these indicators usually may be detected well before a tipping point [22–24,40]. Several other indicators have been also explored as early warning signals such as the noise-induced spectrum [37], the skewness of the probability distribution [30], and the flickering between basins of attraction before bifurcations [38] (see also ref. [2] for a review).

The advantage of applying early warning indicators to successfully rise the alarm when approaching a tipping point has been described in many recent studies [26–33,35]. However, predicting key aspects of the system's future stability and dynamics still remains a challenge. For example, although the indicators start to increase as the system approaches the tipping point, it is necessary to know how much is the quantitative distance to the upcoming transition to better evaluate and therefore manage the system. Second, it is pivotal to know the type of upcoming transition, i.e. whether the system is approaching to a catastrophic or a non-catastrophic transition. Based on nonlinear systems theory, critical slowing down and increase in most of the early warning indicators is also possible in non-catastrophic transitions, such as transcritical and supercritical pitchfork bifurcations. Finally, to plan for future management actions, it is important to predict the equilibria of the system before and after the transition, by using knowledge of the current system condition. A forecasting method capable of addressing these questions would be of great importance as it would help to assess the existence of crucial thresholds and to evaluate the future consequences of surpassing them [41].

To address these limitation, bifurcation forecasting methods were introduced by Lim and Epureanu [8]. This method uses the recovery rate of the system from perturbations in the pre-bifurcation regime to forecast the bifurcation diagram of the system. The method resolves main disadvantages of stochastic methods. However, it was developed for one dimensional manifolds and simple systems, and still has limitations which cannot be applied to a lot of cases consist of more complex and large dimensional systems.

The main goal of this research is to remove limitations of existing bifurcation forecasting methods and develop a method for large dimensional systems and for systems with more complex dynamics. We consider the main features of dynamical systems and different types of the bifurcations and develop the forecasting method to the point that it can be applied to real complex systems with good accuracy. Based on observations of the system response to perturbations only in the pre-transition regime, the method forecasts the bifurcation diagram which discovers the system's stability and equilibria in upcoming conditions. The forecasting approach is based on the phenomenon of critical slowing down, referring to the slowing down of a system's dynamics around its equilibrium when approaching a tipping point. We show that rate of recovery from perturbations at each amplitude can be used as an indicator, and is correlated to the distance to the bifurcation. This finding is used to predict the bifurcation diagram which discovers the system's stability and equilibria. In this research, we focus on developing the forecasting method for several classes of complex nonlinear systems. Theoretical and experimental results of this study address some of the most important challenges in forecasting safety and stability of complex systems.

1.2 Dissertation contributions and outline

In this dissertation, a set of unique techniques, called bifurcation forecasting methods, are proposed to predict instabilities and bifurcation diagrams of nonlinear dynamical systems without analyzing system equations. Constructing such a diagram using conventional numerical or experimental methods needs accurate models, or massive computational or experimental efforts.

Below is the summary of dissertation contributions and outline. The chapters of this dissertation are compiled from a collection of manuscripts published, accepted or submitted to scientific journals. Therefore, some of the background materials as well as mathematical developments are repeated in various chapters.

1.2.1 Forecasting flutter in fluid-structural systems

An important class of nonlinear complex engineering systems prone to critical transitions is fluid-structural systems. Subcritical and supercritical flutter can occur in fluid-structural systems and can cause dramatic changes in the dynamics resulting in damage and failure. Hence, one of the demanding topics of research in fluid-structure interactions is determining the flow speed above which the system becomes unstable, i.e. determining the flutter speed, and the dynamics beyond the flutter speed. In this study, we develop a model-free forecasting method which is able to forecast both the flutter speed and post-flutter dynamics in fluid-structural systems using a limited number of measurements in the pre-flutter regime. This approach minimizes the effort required for a comprehensive nonlinear stability analysis of the system. For example, high-fidelity finite element models of complex fluid-structural systems often have millions of degrees of freedom. Stability analysis and extracting bifurcation diagrams for such models using theoretical and classical computational methods is very difficult. Furthermore, experimental methods to analyze the stability of the system and to determine the bifurcation diagram place the system in the post-bifurcation regime. This can result in the collapse of the system, which is dangerous if the test is done in real operating conditions. The proposed forecasting method is effective in both experimental and theoretical analyses. Details of this study are included in Chapters 2 to 4 where novel techniques are introduced to forecast the flutter speed and post-flutter dynamics of complex fluid-structural systems.

1.2.2 Forecasting the onset of traffic congestions on roads

Study of traffic flow dynamics has a long tradition. However, predicting traffic jams before they occur is still a challenge. In this study, we introduce recently developed tools of tipping point forecasting in complex systems, namely early warning indicators and bifurcation forecasting methods, and investigate their application to predict traffic jams on a circular road. The main advantage of the proposed methods is that they are model-less. The methods are based on exploiting the phenomenon of critical slowing down which occurs in dynamical systems near certain types of bifurcations, such as traffic jams. One can forecast the onset of traffic jams and the dynamics of the traffic after the bifurcation by using a few traffic measurements before the tipping point occurs. The measurements required for forecasting are recorded headways between cars in traffic. Forecasting approaches are applied to several simulated traffic flow conditions and the onset of traffic jams and the traffic dynamics after this critical point are forecasted while no model of the system is required. The proposed approach represents a substantial advantage for complex systems such as traffic flow systems where an accurate mathematical model is not easily available. The introduced approaches and ideas can be used as a basis for more developments to address some of the challenges related to the complexity of traffic dynamics. Details of this study are included in Chapter 5.

1.2.3 Forecasting critical transitions in natural populations

Regime shifts in ecological systems have received a growing attention since the cumulative human impact on the environment is increasing the risk of ecological regime shifts. Possible consequences include the collapse of natural populations which inhabit the ecosystem. Hence, it is necessary to develop methods capable of forecasting upcoming transitions, as part of a preventive plan against possible detrimental consequences. For example, there is a need for methods to predict catastrophic events in populations of plants and animals because such events can lead to irreversible consequences such as extinction of species. The potential impact of such methods is high also when applied to disease eradication (populations of infectious diseases).

To address this important topic, we develop and experimentally evaluate a unique forecasting method to forecast critical transitions in ecological systems and natural populations. We evaluate the method using as a model ecological system a population of budding yeast with cooperative growth which exhibits a catastrophic transition as the environment deteriorates, resembling an ecological collapse. This system shares similar dynamics with many natural ecological systems which exhibit a catastrophic transition. The goal of this study is to forecast crucial information about the future system's safety and stability, such as the quantitative distance to upcoming transition (collapse), the type of upcoming transition (i.e., catastrophic/non-catastrophic) using some observations of system dynamics in the safe pre-transition regime. Developing such approach is exceedingly important in ecological management. Details of this experimental study are included in Chapter 6 where we explain how we developed and evaluated a method to forecast the bifurcation diagram and stability of a model ecological system in the lab.

1.2.4 Identification of the best indicator species in ecological systems

Critical slowing down indicators can alarm approaching to an impending transition in ecological systems. However, in a network of interacting components, not all the components provide the same level of information to detect a system-wide transition. Identifying the best indicator species in complex ecological systems is a challenging task without a model of the system available. Here we propose a data driven approach to rank the elements of ecological system based on their reliability in providing the best early warning indicators of critical transitions. The system response to perturbations are recorded and employed as an input to experimental modal analyses techniques which are common tools in identifying dynamical systems features. Taking advantage of the proposed approach, the dominant eigenvectors of the system are approximated and the best indicator species/regions of abrupt transitions are recognized. The approach is applied to several models of ecological systems with different number of species, different dynamics and connectivity pattern, and the system species/regions are successfully ranked based on the reliability of their provided early warning signals of catastrophic regime shifts. The challenges associated with ranking the nodes in networks of interacting components are also studied and some conditions resulting in false early warning signals are analyzed. Details of this study are included in Chapter 7.

Chapter 2

Forecasting Flutter in Fluid-Structural Systems

2.1 Introduction

Bifurcations occur in the dynamics of nonlinear systems and lead to various types of stability issues [2,42,43]. Forecasting such bifurcations with measurements only from the pre-bifurcation regime is of great interest. This is especially important for complex large-dimensional systems when accurate models are not easily available or when their parameters are unknown. A common type of bifurcations in engineering systems is Hopf bifurcations. Subcritical and supercritical Hopf bifurcations have been observed in a variety of systems such as fluid-structural systems [44–47], automotive dynamics [48], machine tools [49,50], nonlinear circuits [51], etc. Such bifurcations can cause dramatic changes in the dynamics and failure. In supercritical Hopf bifurcations above the bifurcation point, the system exhibits limit cycle oscillations that gradually increase with the parameter. For systems exhibiting subcritical bifurcations, possible jump phenomena (bi-stability) exist even below the (linear) bifurcation point.

There are many studies focused on the identification of the bifurcations and the system dynamics in the post-bifurcation regime. These studies use mathematical models of the system and methods such as harmonic balance [52,53], multiple scales [54,55], normal forms and nonlinear normal modes [56,57] to analyze their stability and determine the bifurcation diagrams.

Furthermore, there exist numerous numerical methods regarding construction of bifurcation diagrams of systems using the system equations [58,59]. Based on these techniques, several software are also developed to construct bifurcation diagrams in different types of systems (e.g. AUTO [60], MATCONT [61], DDE-BIFTOOL [62], and PDDE-CONT [63]).

These analytical and computational methods work very well in determining bifurcations and bifurcation diagrams; however, they are model-based methods and require a known and accurate model of the system to analyze the stability. This causes two main drawbacks that make the methods difficult or impossible to use in a large class of realistic applications. First, extracting a model for the desired system is sometimes not feasible especially when the system is complex (e.g., it has many components with nonlinear interactions). Second, even when a mathematical model is established, it may be incomplete or inaccurate due to assumptions and uncertainties in modeling and parameter values. Hence, predictions and real results may be different.

Experimental methods to analyze the stability of the system and to determine the bifurcation diagram place the system in the post-bifurcation regime. This is a demanding task, and can result in the collapse of the system, which is dangerous if the test is done in real operating conditions.

An important class of nonlinear complex engineering systems prone to subcritical and supercritical Hopf (flutter) bifurcations is the fluid-structural interaction [43,64–69]. These phenomena can cause dramatic changes in the system dynamics typically resulting in loss of performance is possible is total failure. Hence, one of the demanding topics of research in fluid-structure interactions is determining the speed above which the system becomes linearly unstable, i.e. determining the flutter speed. Furthermore, identifying the flutter type (supercritical and subcritical) and the limit cycle amplitude beyond the flutter speed are also important especially when operating close to the linear flutter boundary. Because of the existing challenges in analyzing the stability of nonlinear systems, new methods capable of forecasting the bifurcation point and post-bifurcation dynamics of fluid-structural systems is necessary. To address this challenge and due to the importance of the topic, we introduce a new method of forecasting bifurcations in fluid-structural systems. The approach is based on the phenomenon of critical slowing down which accompanies many bifurcation phenomena including flutter, i.e. when the systems is close to the bifurcations, perturbations lead to long transient oscillations before the system reach to its stable state. This approach is capable of forecasting not only the distance to bifurcations but also the dynamics of system in the post-bifurcation regime. The unique feature of the method is that it is model-less: no mathematical model of the system is required for forecasting. Hence, it is applicable to complex nonlinear systems where a model of the system is not available, or where analysis would require massive computations. To forecast the bifurcation diagrams using this method, one measures several system responses to perturbations in the pre-bifurcation regime. As a result, the method is computationally efficient and is safe in real applications since the system is never placed in the potentially dangerous post-bifurcation regime.

To demonstrate the proposed method and to highlight its advantages, the approach is employed to determine bifurcation diagrams of two- and three-degree-of-freedom (DOF) fluid-structural systems with cubic nonlinearity. This system is composed of a typical airfoil section in pitch and plunge, equipped with a trailing-edge control surface. Instead of experimental measurements, we use surrogate data obtained as time series from simulation of the model as input to our method. To reflect realistic situations, gust loads are applied as disturbances to the system while system recoveries are measured. These perturbations mimic better the actual behavior of the system compared to simply choosing different initial conditions in position or velocity coordinates.

Note that in general, the forecasting method works based on measurements not on model equations. In this study, these measurements are surrogate measurements generated using a theoretical model. Surrogate data are used so that we can show the applicability of the proposed method while at the same time we have knowledge of the exact behavior of the system. The exact behavior of the system is used to validate the forecasting method.

2.2 Forecasting method

Consider a system that exhibits Hopf bifurcations. The system oscillates during its recovery from perturbations in the pre-bifurcation regime. When the system is close to the bifurcation, perturbations lead to long transient oscillations before the system reaches its equilibrium position. This phenomenon is known as critical slowing down. This means that the rate of the system's recovery from perturbations decreases when the system approaches the bifurcation. Therefore, the recovery rate of the system from perturbations can be used as an indicator, and is correlated to the distance to the bifurcation.

Consider a co-dimension one nonlinear system with the parameter μ and amplitude of r. The change rate of system amplitude can be generally written as

$$\dot{r} = f(\mu, r) \tag{2.1}$$

Using a Taylor series around the bifurcation point ($\mu = \mu_c$), the recovery rate can be expressed as

$$\dot{r} = r(p(r) + \alpha_1(r)(\mu - \mu_c) + \alpha_2(r)(\mu - \mu_c)^2 + HOT), \tag{2.2}$$

where $p(r)$, $\alpha_1(r)$ and $\alpha_2(r)$ are polynomial functions independent of parameter μ. This relation means neither that the dynamics of the system have been linearized in state space nor that the dynamics have small amplitudes. The linearization is only in the parameter space about the critical value μ_c of the parameter. Thus, we are not restricted to small perturbations.

For parameter values close to the bifurcation, in this study we assume that the system has second order polynomial dependence on the parameter, and higher order terms can be neglected. However, depending on the application, one may use higher order terms in the approximation especially when the forecasting is used at parameters far from the tipping point (μ_c). Now consider that a perturbation is applied to the system. The recovery in Eq. (2.2) can be written as

$$\lambda(\mu, r) = \frac{\dot{r}}{r} = p(r) + \alpha_1(r)(\mu - \mu_c) + \alpha_2(r)(\mu - \mu_c)^2. \tag{2.3}$$

Here, $\lambda(\mu, r)$ is the rate of system recovery from perturbations expressed as

$$\lambda(\mu, r) = \frac{d(\ln r)}{dt}. \tag{2.4}$$

The polynomial used in Eq. (2.3) determines the minimum number of measurements required for forecasting the bifurcation diagram. Since in this study we use a second order polynomial, forecasting is possible using at least three measurements in the pre-bifurcation regime (i.e., recoveries at three values of the bifurcation parameter). That being said, generally the more measurements are available in the pre-bifurcation regime, the more accurate the forecasting is.

Using measurements of the amplitude of the dynamics, one can employ the following finite-difference approximation to estimate $\lambda(\mu, r)$ (see also Fig. 2.1 (a)) as

$$\lambda(\mu, r) = \frac{d\,(\ln r)}{dt} \cong \frac{\ln r_+ - \ln r_-}{2\Delta t}, \tag{2.5}$$

where Δt is the time between samples, r_+ is the value measured at time $t + \Delta t$, and r_- is the value measured at time $t - \Delta t$. The recovery rate plays the most important role in the forecasting method. The critical slowing down phenomenon at the bifurcation point influences the dynamics near that point also. Specifically, the recovery rate decreases when the system approaches that point. At a fixed system amplitude r, the farther the system is from its corresponding post-bifurcation regime, the weaker the critical slowing down and the faster the recovery rate of the system is at that amplitude. This is used for predicting the post-bifurcation regime (namely the bifurcation diagram).

Suppose that we collect time series during recoveries at several different parameter values $\mu_1, \mu_2, \dots, \mu_n$. At a given parameter value μ_k (with $k = 1, \dots, n$), we can choose a value $r = \tilde{r}$ and compute $\lambda(\mu_k, \tilde{r})$ using the measurements. Therefore, *n* equations are obtained from Eq. (2.3), one for each k, in the form

$$\lambda(\mu_k, \tilde{r}) = p(\tilde{r}) + \alpha_1(\tilde{r})(\mu_k - \mu_c) + \alpha_2(\tilde{r})(\mu_k - \mu_c)^2. \tag{2.6}$$

The values of $\lambda(\mu_k, \tilde{r})$ in Eq. (2.6) are obtained from measurements using Eq. (2.5). Fitting a 2nd order polynomial to these values in the $\mu - \lambda(\mu, \tilde{r})$ space, the unknown constants $\alpha_1(\tilde{r})$, $\alpha_2(\tilde{r})$ and μ_c can be found. Individual values of $\lambda(\mu_k, r)$ and the resulting fitted curve are conceptually shown in Fig. 2.1 (b). The intersection at $\mu = \tilde{\mu}$ of the fitted curve with the μ axis corresponds to a zero recovery rate. That is the most important point, and represents the forecasted parameter for the corresponding $\tilde{r}$ value. This means that a fixed point exists in the post-bifurcation regime at $\tilde{r}$ when the parameter value is $\tilde{\mu}$. This procedure can be repeated for different values of $\tilde{r}$ and hence the bifurcation diagram is predicted. This is conceptually shown in Fig. 2.1 (c). Note that in this procedure the measurements are collected only in the pre-bifurcation regime, and the bifurcation diagram is predicted without any measurements in the post-bifurcation domain.

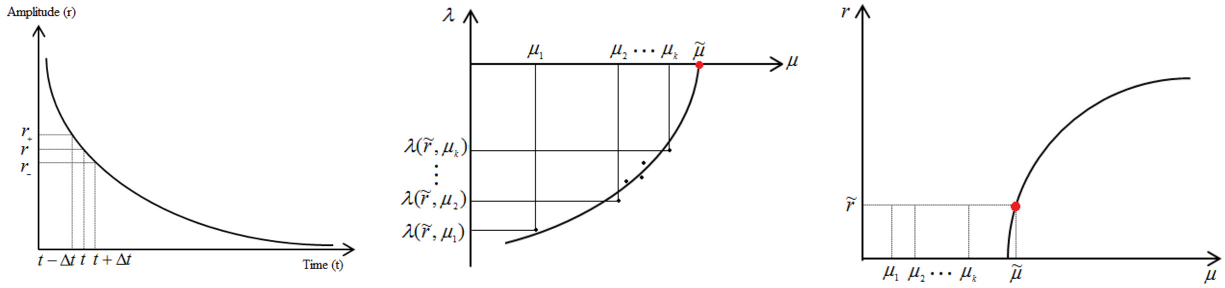

(a) (b) (c)

Figure 2.1: (a) Schematic of the response of the system during the recovery from a perturbation, (b) Recovery rate vs. bifurcation parameter and the value obtained for the forecasted $\tilde{\mu}$, (c) Forecasted bifurcation diagram

This procedure can be easily used in the cases that the system recovers from perturbation without oscillations. However, in fluid-structural systems with flutter bifurcations, the system oscillates during its recovery in response to perturbations in the pre-bifurcation regime (Fig. 2.2). In this case, Eq. (2.5) cannot be used for all of the data collected in measurements. That is because the motion is essentially two-dimensional and data points may be adjacent to each other but they do not necessarily have the same phase. The simple solution for this problem is to fix the phase by selecting the local maxima of the recovery data and using only those measured values in the same procedure (as for the non-oscillating case). This is a good approximation in the cases where the system oscillates with high frequencies. However, in the case of low frequency oscillations, there may not be enough samples available to have a good approximation.

To overcome this limitation we enhance the forecasting method to obtain recovery rates by nonlinear optimization. At each parameter value, the recovery rate is assumed to be represented by a polynomial of order p in r. One obtains

$$\lambda(\mu,r)=\lambda_0(\mu)+\lambda_1(\mu)r(\mu,t)+\cdots+\lambda_p(\mu)r^p(\mu,t), \tag{2.7}$$

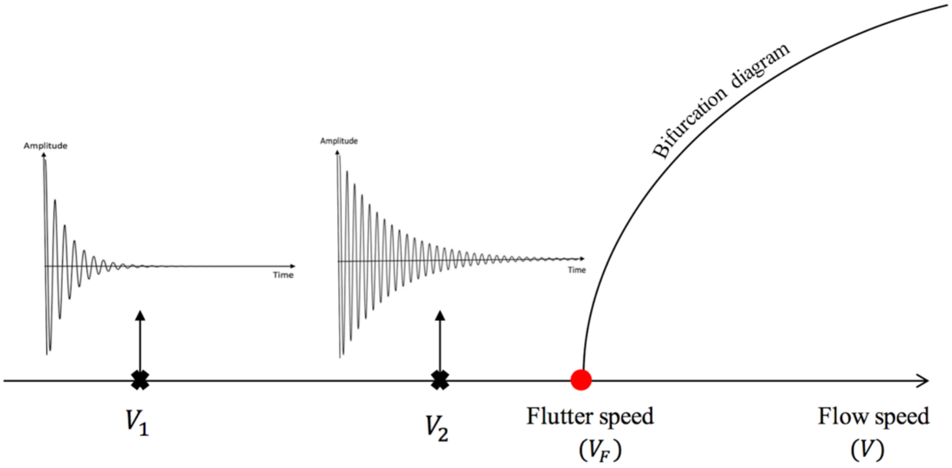

Figure 2.2. Schematic of the change in the rate of recovery from perturbations in a system approaching flutter; oscillations last longer when the system is closer to the flutter speed.

where in general the coefficients λ_i $(i = 0, \ldots, p)$ are dependent on the bifurcation parameter. At a fixed parameter value (μ), these coefficients are constant over time. Using the definition of $\lambda(\mu, r) = \dot{r}/r$ from Eq. (2.3), one may re-write Eq. (2.7) as

$$\dot{r} = r(\lambda_0 + \lambda_1 r + \cdots + \lambda_p r^p). \tag{2.8}$$

For a set of given values of the coefficients λ_i $(i = 0, \ldots, p)$, Eq. (2.8) can be integrated in time to obtain $r(t)$. When the coefficients λ_i are accurate, the values obtained for $r(t)$ from the integration match the values $r_m(t)$ obtained from measurements. In particular, this match has to hold for the local peak values in the measurements. Hence, the coefficients λ_i can be obtained at each μ value using a nonlinear least squares optimization which minimizes the difference between $r_m(t)$ and $r(t)$ for all t values which correspond to local peak responses at that μ value.

Using this method, a more precise approximation of recovery rate λ can be obtained when the time history has low oscillation frequency and only a few peaks. The order p of the polynomial has to be chosen via a convergence test. In the current work we used a value of 4 which was sufficient to capture both supercritical and subcritical bifurcations. The forecasting procedure is shown in Fig. 2.3.

There are several requirements for the forecasting method to be accurate. A first requirement is that the system is close enough to the bifurcation as to exhibit measurable slowing down in its recoveries. Moreover, measurements containing identifiable parts are on the inertial manifold to ensure that changes in the recovery rates are due to the slowing down phenomenon. The inertial manifold is an invariant set where the dynamics is slowest in time and contains main features of the system. Thus, this manifold is the slowest, and if the system starts from a state in this set, it remains in that set at all times. A second requirement is that the system dynamics and its inertial manifold vary smoothly with the bifurcation parameter, which is the flow speed in the current study. The assumptions made in the forecasting method, although restrictive, do not reduce the method applicability to just a few special cases. Many biological, ecological, engineering systems exhibit bifurcations such as Hopf, saddle node, pitchfork and transcritical bifurcations which satisfy the method assumptions. Examples are bifurcations in population dynamics, fluid-structural systems, periodically forced systems in engineering systems and disease dynamics, nonlinear circuits, to name a few. However, note also that critical slowing down does not exist in all types of bifurcations. For example, systems undergoing period doubling cannot be forecasted using the proposed approach.

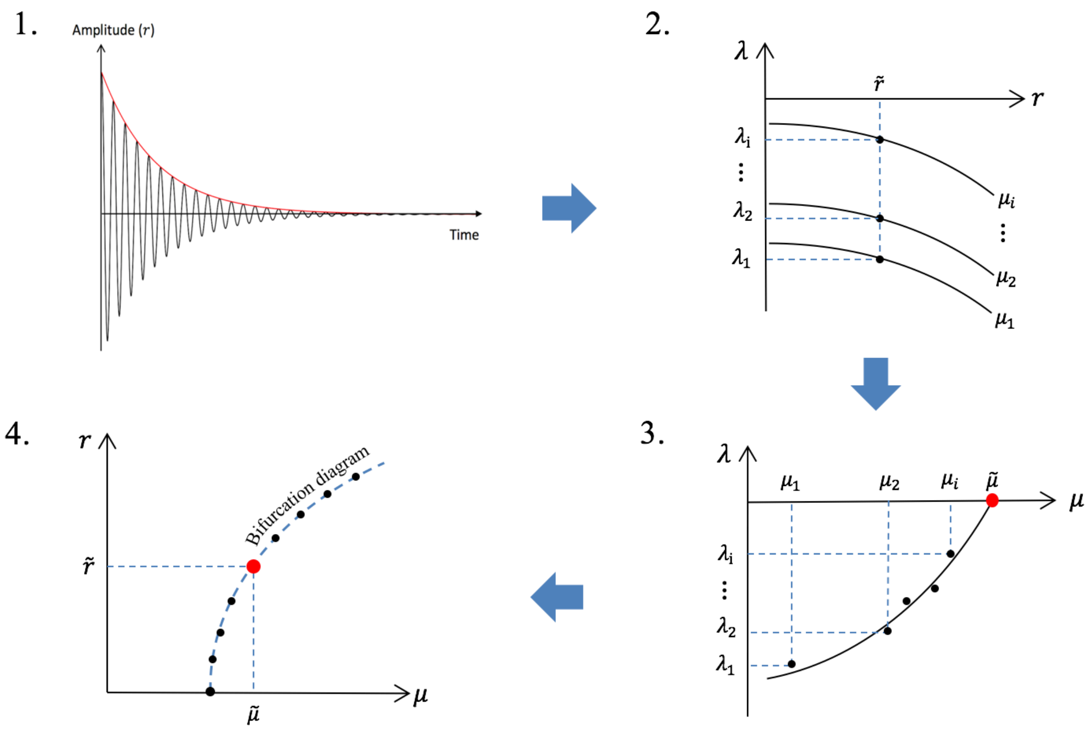

Figure 2.3. Schematic of proposed forecasting method procedure: 1) System recoveries are measured after perturbations, and the recovery rate is estimated using nonlinear optimization for the local maxima of the measurements. 2) The estimated recovery rates for a fixed amplitude at each measured parameter are analyzed. 3) The parameter $\tilde{\mu}$ where the recovery rate becomes 0 at amplitude $\tilde{r}$ is determined using a low order polynomial. 4) Steps 2 and 3 are repeated for several amplitude values $\tilde{r}$, and the bifurcation diagram is constructed using the forecasted pairs of values ($\tilde{\mu}$,$\tilde{r}$).

2.3 Forecasting Hopf bifurcations in large dimensional systems

In the previous section, the forecasting method was developed for a single degree of freedom system oscillating during its recovery from perturbations. However, in large dimensional systems there might be a large number of active spatial coherences (e.g., modes) in a measured recovery from perturbations. In the great majority of Hopf bifurcations, including flutter, only one pair of conjugate eigenvalues is involved in the bifurcation (as shown in Fig. 2.4). This means that only one of the existing modes is involved in the instability, and the effect of other modes can be expressed as a function of this key mode thus being removed from the measurements to achieve maximum accuracy in forecasting. This is exploited in the proposed forecasting method to enhance the accuracy of bifurcation prediction.

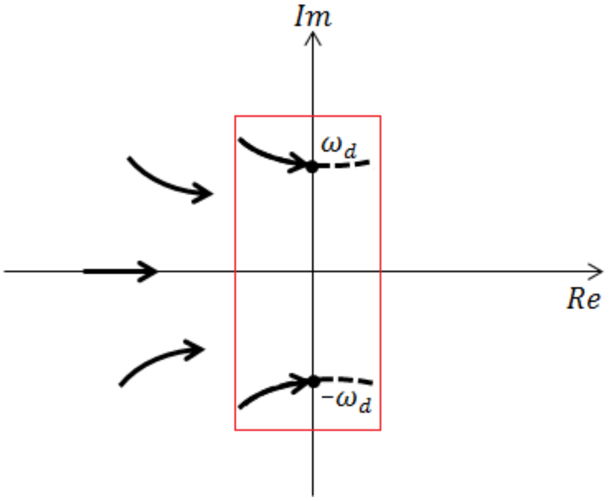

Figure 2.4. Eigenvalues of the fixed point at the origin as a function of the bifurcation parameter

In the aeroelastic systems, the inertial manifold near flutter is generally a two-dimensional nonlinear manifold. This manifold is tangent to the (two-dimensional) center space of the system (Fig. 2.5). Hence, the center space is a good approximation of the inertial manifold near the bifurcation and the coordinate of the mode involved in the bifurcation captures the entire dynamics near the bifurcation point. Thus, we project the dynamics of the system on the center space. In this two dimensional space, we can capture and study the critical slowing down behavior for forecasting when the system is close to the bifurcation. A basis in the center space is obtained as linear modes by using a measurement-based modal decomposition technique. This technique allows us to identify and separate the effects of the mode which exhibits critical slowing down from the other modes. Hence, the dynamics of the system is projected onto the space spanned by the eigenvectors of the bifurcating mode while unwanted modes are filtered out. That leads to more accurate data for the mode which does have critical slowing down, and that enhances the precision of forecasting the post-bifurcation regime.

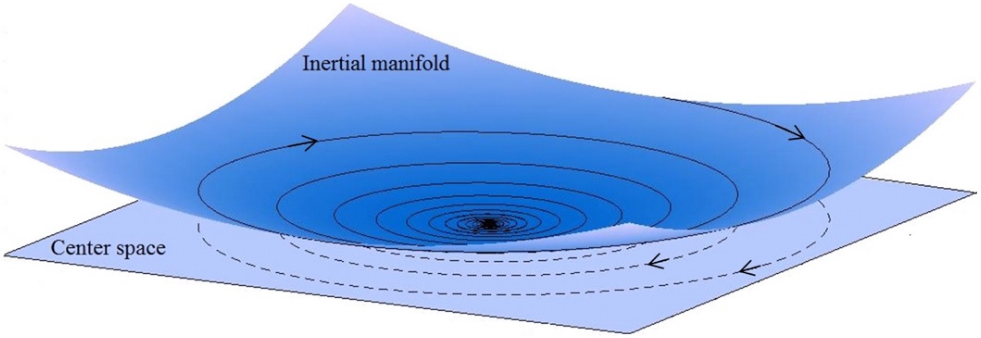

Figure 2.5. Schematic of the system dynamics on the inertial manifold and its projection on the center space.

There are several modal identification approaches which can be used to extract mode shapes of a system from measured responses of the system to perturbations [70,71]. Since we apply the forecasting method close to the bifurcation, the mode corresponding to the pair of eigenvalues with the smallest real part is the one which experiences critical slowing down and is most closely involved in the bifurcation. Here, we use an eigensystem realization algorithm (ERA) [72–75]. This ERA is designed for linear modal analysis and provides an approximation for the spatial correlations in the dynamics close to the bifurcation point. This approximation has acceptable accuracy for the aeroelastic system we consider and for the range of perturbations which occur in this system.

ERA is a time domain MIMO algorithm to identify modal parameters of the system based on the Hankel matrix and its singular value decomposition. The fundamentals of this method can be found in the literature [72–75]. Here, only the major steps of the algorithm are presented as related to the aeroelastic system of interest. Specifically, ERA starts with the state-space representation of the system as

$$\begin{aligned}\dot{\mathrm{x}}(t) &= \mathrm{Ax}(t) + \mathrm{Bu}(t)\\ \mathrm{y}(t) &= \mathrm{Cx}(t) + \mathrm{Du}(t)\text{,}\end{aligned} \tag{2.9}$$

where x is an N-dimensional vector of state variables, y is an n-dimensional vector of measured state variables, u is an m-dimensional excitation vector, and A, B, C, and D are state space matrices (constant over time).

Consider that the system is exposed to an initial gust which provides a perturbation/excitation of the type usually occurring during the system operation. The solution of Eq. (2.9) for the system recovering from this perturbation with $\mathrm{u}(t) = 0$ from the initial conditions x_0 can be expressed as

$$\mathrm{y}(\mathrm{t}) = \mathrm{C}\Phi(t)\mathrm{x}_0 \text{ ,} \tag{2.10}$$

where $\Phi(t)$ is the state transition matrix from state x_0 at time $t = 0$ to state $\mathrm{x}(t) = \Phi(t)\mathrm{x}_0$ at time t. Further consider that the response of the system measured in time and is sampled with a Δt time increment. Equation (2.10) at time $t = k\,\Delta t$ (for $k = 0,1,2,\ldots$) can be written as

$$\mathrm{y}_k(t) = \mathrm{C}\Phi^k(\Delta t)\mathrm{x}_0 \text{ .} \tag{2.11}$$

Repeating the measurements for a sequence of l distinct non-zero initial conditions $\mathrm{X}_0 = [\mathrm{x}_{0,1}, \mathrm{x}_{0,2}, \ldots, \mathrm{x}_{0,l}]$ and letting $S = \Phi(\Delta t)$, Eq. (2.11) can be rewritten as

$$\mathrm{Y}_k(t) = \mathrm{CS}^{\mathrm{k}}\mathrm{X}_0 \text{ ,} \tag{2.12}$$

where Y_k is a matrix with dimension $n \times l$.

The objective of the ERA is to find S, X_0, and C such that Eq. (2.9) is satisfied as closely as possible by using a sequence of experimentally measured Y_k (for $k = 0,1,2,\ldots$). The measurements are organized in generalized Hankel matrices for each k as follows

$$\mathrm{H}(k) = \begin{bmatrix} \mathrm{Y}(k) & \mathrm{Y}(k+1) & \dots & \mathrm{Y}(k+v-1) \\ \mathrm{Y}(k+1) & \mathrm{Y}(k+2) & \cdots & \mathrm{Y}(k+v) \\ \vdots & \vdots & \ddots & \vdots \\ \mathrm{Y}(k+r-1) & \mathrm{Y}(k+r) & \cdots & \mathrm{Y}(k+r+v-2) \end{bmatrix}_{nr\times lv}, \tag{2.13}$$

where r and v are chosen depending on the particular application.

The singular value decomposition of $\mathrm{H}(0)$ can be written as $\mathrm{H}(0) = \underline{\mathrm{P}}\,\underline{\mathrm{Z}}\,\underline{\mathrm{J}}^{\mathrm{T}}$, with the singular values in $\underline{\mathrm{Z}}$ ordered in decreasing order. Only the first N of them are nonzero. These singular values are grouped in a truncated version of $\underline{\mathrm{Z}}$ denoted by Z. Matrices $\underline{\mathrm{J}}$ and $\underline{\mathrm{P}}$ are truncated accordingly to obtain J and P by keeping only their first N columns. It can be shown that one solution for the matrices S, X_0, and C can be expressed as

$$\begin{aligned} &\mathrm{S} = \mathrm{Z}^{-1/2}\,\mathrm{P}^{\mathrm{T}}\,\mathrm{H}(1)\,\mathrm{J}\,\mathrm{Z}^{-1/2}, \\ &X_0 = \mathrm{Z}^{1/2}\mathrm{J}^T\mathrm{E}_l\,, \\ &\mathrm{C} = \mathrm{E}_n^T\mathrm{P}\mathrm{Z}^{1/2}\,, \end{aligned} \tag{2.14}$$

where $\mathrm{E}_n^T = [\mathrm{I}_\mathrm{n} \quad 0_n \quad 0_n \quad \dots \quad 0_n]$ and $\mathrm{E}_l^T = [\mathrm{I}_\mathrm{l} \quad 0_l \quad 0_l \quad \dots \quad 0_l]$, while I_i and 0_i are identity and zero matrices of order i, respectively.

Equation (2.14) is not a unique solution. For example, for any nonsingular matrix T, $\tilde{\mathrm{S}} = \mathrm{T}^{-1}\mathrm{ST}$, $\tilde{\mathrm{X}}_0 = \mathrm{T}^{-1}\mathrm{X}_0$, and $\tilde{\mathrm{C}} = \mathrm{CT}$ are also a solution. Letting T be the eigenvector matrix of S, and transforming the computed matrices to modal coordinates, it can be shown that $\tilde{\mathrm{C}}$ contains the mode shapes of the system [75]. Furthermore, natural frequencies and damping ratios of continuous system can be obtained as follows

$$\eta_\mathrm{i} = \sigma_i \pm i\omega_d = \frac{1}{\Delta t}\ln\,(\tilde{s}_i), \tag{2.15}$$

where $\tilde{s}_i$ is the i^{th} diagonal element of matrix $\tilde{\mathrm{S}}$ (which is a diagonal matrix).

2.4 Two-degree-of-freedom aeroelastic model

The proposed forecasting method is applied to an aeroelastic system. The system is modeled as a 2D airfoil oscillating in pitch and plunge as shown in Fig. 2.6. The free stream velocity is the bifurcation parameter in this demonstration of the forecasting approach. The system is considered to be exposed to gusts which create perturbations. The recovery of the system from these perturbations is measured and used for forecasting.

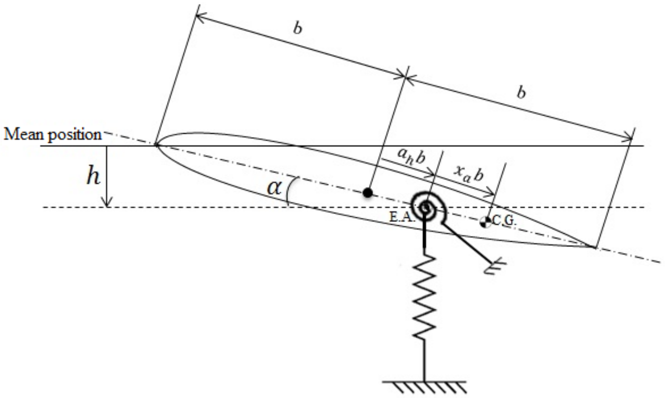

Figure 2.6. Two-degree-of freedom aeroelastic model showing an airfoil of chord $2b$, its aeroelastic axis (EA), its center of mass (CG) (at a distance $x_\alpha b$ from the EA), and the pitch and plunge coordinates α and h

An actual model of this system is not needed for forecasting. However, a model can provide simulated or surrogate measurement data. Closely following [65], the equations of motion for this system can be written as

$$\begin{aligned} &\ddot{\xi} + x_\alpha \ddot{\alpha} + \frac{2\zeta_\xi \bar{\omega}}{U^*}\dot{\xi} + \left(\frac{\bar{\omega}}{U^*}\right)^2 G(\xi) = -\frac{C_L(\tau)}{\pi\mu} - P_g(\tau), \\ &\frac{x_\alpha}{r_\alpha^2}\ddot{\xi} + \ddot{\alpha} + \frac{2\zeta_\alpha}{U^*}\dot{\alpha} + \frac{1}{U^{*2}}M(\alpha) = \frac{2C_M(\tau)}{\pi\mu r_\alpha^2} + Q_g(\tau)\,, \end{aligned} \tag{2.16}$$

where α is the pitch angle, h is the plunge displacement, $\xi = \frac{h}{b}$ is the non-dimensional plunge displacement, $\tau = \frac{Ut}{b}$ is the non-dimensional time, and the overdot indicates differentiation with respect to τ. U is the free stream velocity, and $U^* = U/(b\omega_\alpha)$ is the non-dimensional free stream velocity. $\bar{\omega} = \omega_{\xi}/\omega_{\alpha}$ is the ratio of the natural frequencies of uncoupled plunge and pitch modes, namely ω_{ξ} and ω_{α}. The damping ratios for the pitch and plunge are ζ_{α} and ζ_{ξ}, and r_{α} is the radius of gyration about the elastic axis. $M(\alpha)$ and $G(\xi)$ are the structural elastic torque and elastic force created by the pitch and plunge motions. They are considered decoupled and nonlinear to account for structural nonlinearities as follows

$$\begin{aligned} M(\alpha) &= m_1\alpha + m_3\alpha^3 + m_5\alpha^5 , \\ G(\xi) &= g_1\xi + g_3\xi^3 + g_5\xi^5 , \end{aligned} \tag{2.17}$$

where m_i and g_i $(i = 1,3,5)$ are coefficients characterizing the airfoil elasticity in pitch and plunge, respectively.

The effects of the aerodynamics are modeled by $C_L(\tau)$ and $C_M(\tau)$ which are the coefficients of lift and moment. These coefficients are given for incompressible flow by Fung [76]. The effects of the gust are modeled by $P_g(\tau)$ and $Q_g(\tau)$ which are the lift force and pitch moment due to a gust profile, and are given by the following expressions [77]

$$\begin{aligned} P_g(\tau) &= \frac{2}{\mu}\int_0^{\tau} \dot{\psi}(\tau-\sigma) w_G(\sigma) d\sigma, \\ Q_g(\tau) &= \frac{2}{\mu r_{\alpha}^2}\left(\frac{1}{2}+a_h\right)\int_0^{\tau} \dot{\psi}(\tau-\sigma) w_G(\sigma) d\sigma, \end{aligned} \tag{2.18}$$

where $w_G(\tau)$ is the vertical gust velocity distribution, and ψ is the Kussner function [77].

The aerodynamic states are contributing many degrees of freedom to the system, and that is reflected in the existence of the integral terms in the model for the aerodynamic forces (such as the terms in Eq. (2.18) involving the Kussner function). For enhanced computational efficiency, new variables (augmented states) and some simplifications can be introduced [65]. These transform Eq. (2.15) into a set of 8 first order ordinary differential equations as follows

$$\dot{\mathbf{x}} = \boldsymbol{f}(\mathbf{x}, U^*, \tau) \tag{2.19}$$

where $\mathbf{x} = [x_1, x_2, \ldots, x_8]^T$ is the vector of state space variables, namely $x_1 = \alpha$, $x_2 = \dot{\alpha}$, $x_3 = \xi$, $x_4 = \dot{\xi}$, $x_5 = w_1$, $x_6 = w_2$, $x_7 = w_3$, $x_8 = w_4$. The augmented variables w_i are defined as [65]

$$\begin{gathered} w_1 = \int_0^\tau e^{-\epsilon_1(\tau-\sigma)}\alpha(\sigma)d\sigma \quad , w_2 = \int_0^\tau e^{-\epsilon_2(\tau-\sigma)}\alpha(\sigma)d\sigma \\ w_3 = \int_0^\tau e^{-\epsilon_1(\tau-\sigma)}\xi(\sigma)d\sigma \quad , w_4 = \int_0^\tau e^{-\epsilon_2(\tau-\sigma)}\xi(\sigma)d\sigma \end{gathered} \tag{2.20}$$

where $\epsilon_1 = 0.0455$ and $\epsilon_2 = 0.3$ are parameters obtained to approximate the properties of the integral terms in the aerodynamics (such as the ones involving the Kussner function).

Equation (2.19) is used to simulate the dynamic of the system and obtain recovery data from perturbations (gusts) in the pre-bifurcation regime. These data are used as surrogate measurements to demonstrate the forecasting method. Note that the actual model in Eq. (2.19) is not needed for the forecasting, but only for generating surrogate measurement data.

2.4.1 Results and discussion

In this section, the forecasting method is demonstrated in a numerical example. The parameters used for the aeroelastic system are $r_\alpha = 0.7$, $\bar{\omega} = 0.2$, $a_h = -0.5$, $x_\alpha = 0.25$, $\mu = 100$, $\zeta_\xi = \zeta_\alpha = 0$. A wind gust of (1-cos) type is used as perturbation to the system [77]. The vertical gust velocity distribution is zero except for $0 \le \tau \le 2\tau_G$ where it is given by

$$w_G(\tau) = \frac{w_0}{2}\left(1 - \cos\frac{\pi\tau}{\tau_G}\right), \tag{2.21}$$

where w_0 is the gust intensity, and τ_G is the gust gradient expressed in half-chord unit length.

After the airfoil passes the gust, i.e. after $\tau = 2\tau_G$, the system starts to recover from the perturbation caused by the gust. This response of the system can be obtained by solving Eq. (2.19) in time, and the results can be used as surrogate data to demonstrate the forecasting method. Also, depending on the structural nonlinearities, the system may face supercritical or subcritical Hopf bifurcations. The forecasting method is applied for each case in the next two sections.

2.4.1.1 Supercritical bifurcations

For supercritical bifurcations, the coefficients of the elasticity of the airfoil in Eq. (2.17) are selected as $m_1 = 1$, $m_3 = 1.5$, $m_5 = 0$, $g_1 = 2$, $g_3 = 0$ and $g_5 = 0$. Based on Eq. (2.3), we discuss results obtained using the lowest number of measurements (i.e., three measurements). Three parameter values ($U^* = 7.55, 7.50$, and 7.45) are chosen in pre-bifurcation regime, and time histories of the dynamics of the aeroelastic system in response to gust perturbations are obtained by solving the equations of motion numerically (Fig. 2.7). We confirm that the forecasted bifurcation diagrams have good accuracy. Note that increasing the number of measurements does not change these results.

The applied gust parameters are chosen as $w_0 = 0.1$ and $\tau_G = 5$ for all three flow speeds. Note that in the proposed method, the perturbations do not have to be all the same and they do not have to be dependent on the bifurcation parameter. For the aeroelastic system that means that the intensity of the gusts which provide the perturbation does not have to be the same and the gusts do not have to be related to the far field flow speed. In addition, perturbations do not have to have the same source (e.g., gust). They could be caused by any perturbation (e.g., maneuvering). However, each perturbation creates an amplitude for the resulting (perturbed) dynamics. The largest forecasted amplitude in the forecasted bifurcation diagram cannot be larger than the amplitude created by these perturbations. For the aeroelastic system, we used only gust perturbations. Also, since the gust intensity can be any value, we used the same value.

To extract the modal parameters of the system, the ERA method is used. We assume that the measured states in the aeroelastic system are pitch, plunge and their velocities (i.e., α, $\dot{\alpha}$, ξ, and $\dot{\xi}$). Therefore, the vector y in Eq. (9) is $y(\tau) = \left[\alpha(\tau), \dot{\alpha}(\tau), \xi(\tau), \dot{\xi}(\tau)\right]^T$. The parameters r and ν are chosen to have a value of 500 in this study, and $\varDelta\tau = 0.5$.

The modal parameters are only computed at the largest flow speed value and used for all measurements (at all flow speeds). That is consistent with the assumption made in the forecasting method that the inertial manifold varies slowly with the bifurcation parameter. Therefore, we only need to find the center space at the nearest parameter value to the bifurcation point and use that for the entire forecasting procedure.

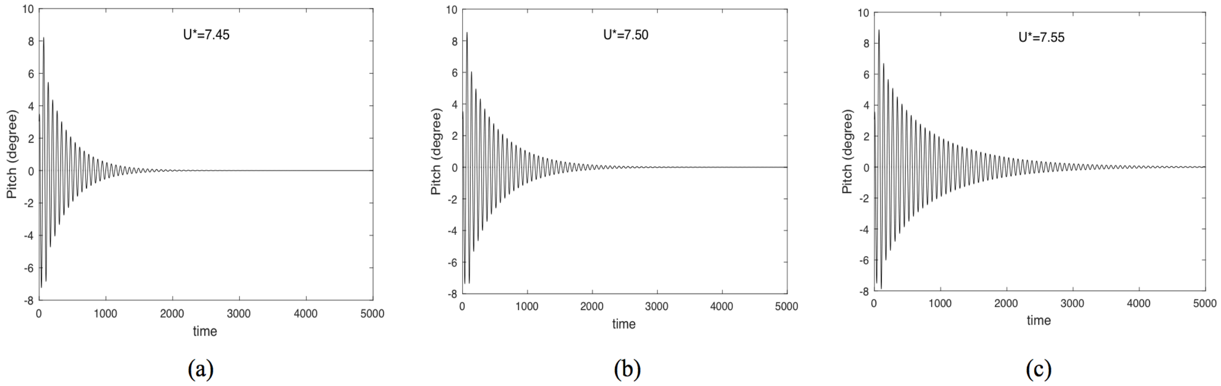

(a) (b) (c)

Figure 2.7. Measured system responses to perturbations in pitch displacement at 3 non-dimensional flow speeds $U^* = 7.45$, 7.50, and 7.55 in supercritical case.

The forecasting method is applied to obtained time series data of pitch and plunge displacements. Figure 2.8 shows the recovery rate λ versus pitch amplitude obtained for a fixed flow speed value. Figure 2.9 shows the plot of $U^* - \lambda$ for the pitch displacement. In this figure, the intersection between each curve and the horizontal axis is the forecasted flow speed U^* value in the post-bifurcation regime for its corresponding amplitude.

Figure 2.10 shows the actual and the predicted bifurcation diagrams of pitch and plunge displacements, demonstrating that the method predicts the post-bifurcation regime accurately.

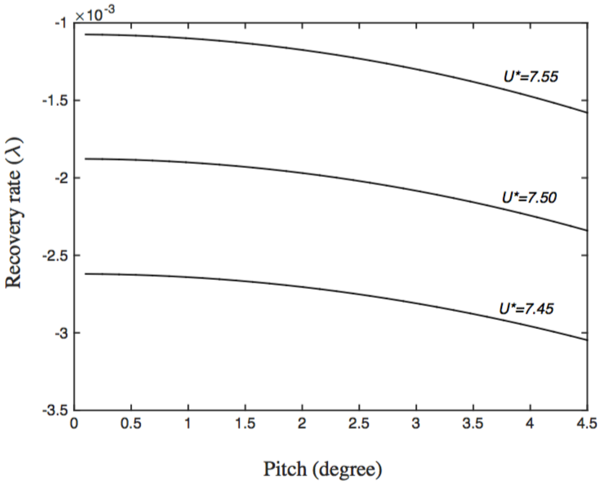

Figure 2.8. λ versus LCO amplitude for different flow speed values.

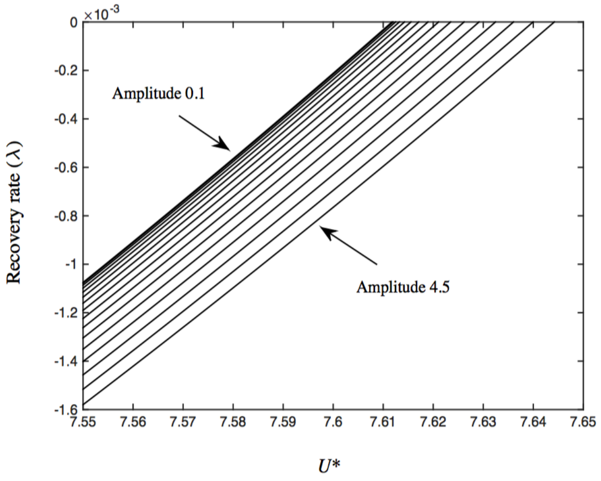

Figure 2.9. λ versus flow speed U^* for prediction of post-bifurcation regime for several pitch amplitudes.

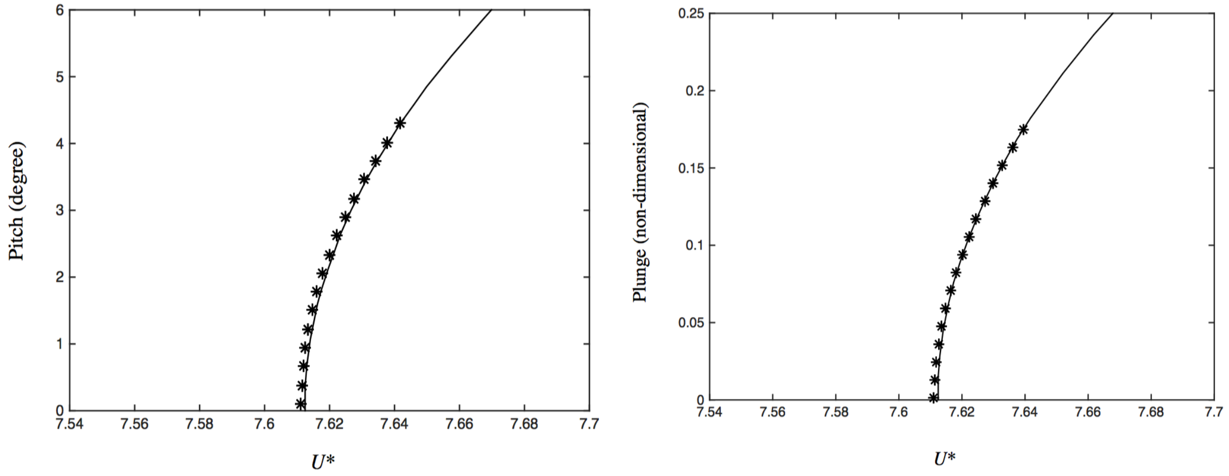

(a) (b)

Figure 2.10. Forecasted bifurcation diagrams ($*$) for (a) pitch and (b) plunge displacements in a supercritical case.

To understand the importance of applying the modal decomposition and projection to the center space, the forecasted bifurcation diagram of the pitch displacement when these are not applied is shown in Fig. 2.11. The prediction is not accurate especially at large amplitudes which are affected more by the modes that are not involved in the bifurcation. The smaller amplitudes have better accuracy since they correspond to later times in the recovery, when the components of the response which do not have critical slowing down are lower (they had time to decay). This effect can be observed in Fig. 2.12, where the system response of pitch and plunge displacements are compared before and after modal decomposition. The difference between the signals used for forecasting at small amplitudes is negligible. However, at large amplitudes the difference is larger and affects the forecasting accuracy. Note in Fig. 2.12(b) that the plunge amplitudes greater than 0.1 cannot be predicted using original data because these values are highly affected by the modes without critical slowing down. These results show the importance of separating modes for Hopf bifurcation predictions.

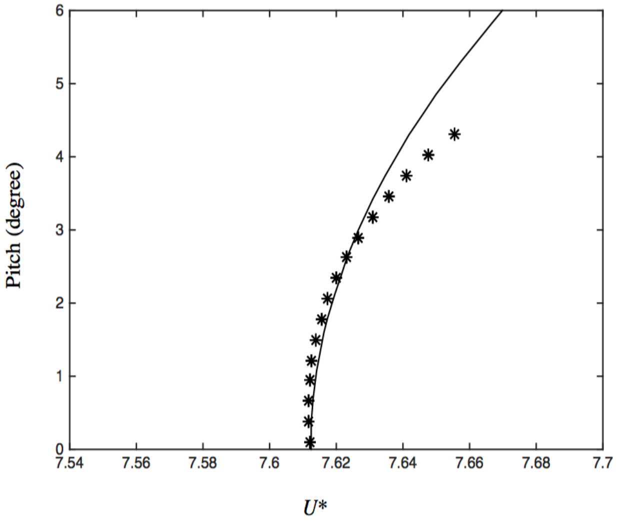

Figure 2.11. Forecasted(*) and exact (-) pitch bifurcation diagram without applying modal decomposition

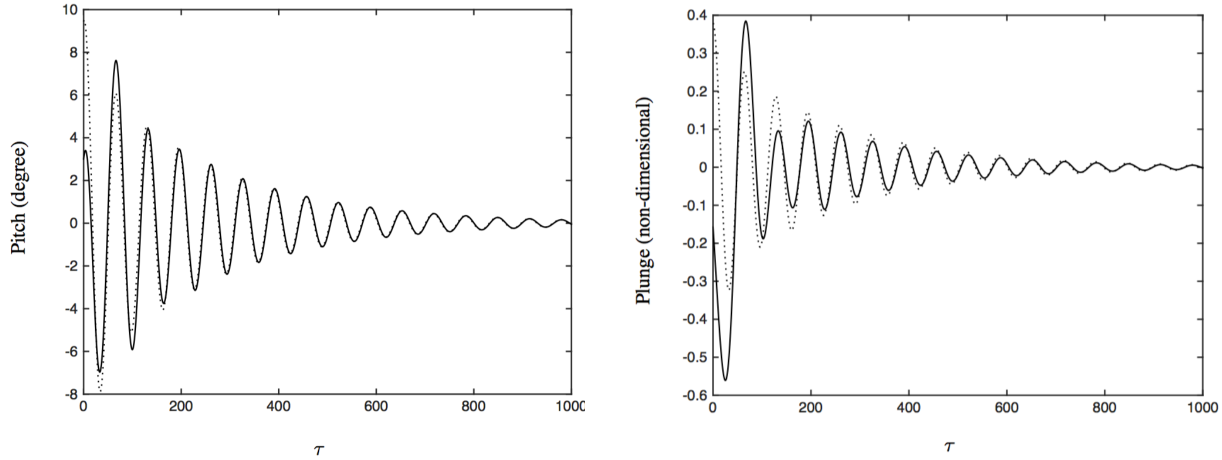

(a) (b)

Figure 2.12. Comparison between system gust response for (a) pitch and (b) plunge displacements before (solid line) and after (dashed line) modal decomposition

2.4.1.2 Subcritical bifurcations

Prediction of subcritical bifurcations has an even greater importance than supercritical ones because it can cause sudden and dramatic change in the LCO amplitude. To demonstrate the forecasting method in such a case, the coefficients of Eq. (2.17) are chosen as $m_1 = 1, m_3 = -1.5$, $m_5 = 50$, $g_1 = 2$, $g_3 = 0$ and $g_5 = 0$. Then, gust perturbations are applied to the system and data is collected in recovery periods at flow speeds $U^* = 7.55, 7.50$, and 7.45 in the pre-bifurcation regime. These surrogate measurement data is used to forecast the bifurcation diagram for pitch and plunge displacements as shown in Fig. 2.13. In this figure, the very largest amplitudes in the bifurcation diagram could not be predicted accurately because these very large values of amplitudes are not present in the recovery time series. In fact, gust perturbations of low intensity are not strong enough to perturb the system into such large amplitudes. Nonetheless, the important fact is that the forecasting method can predict the bifurcation diagram sufficiently to indicate that the system is approaching a subcritical bifurcation.

As the gust intensity is increased, larger perturbations are created and the forecasting method predicts larger ranges of the bifurcation diagram (Fig. 2.14). As an example, the forecasted post-bifurcation regime for pitch and plunge displacements are shown in Fig. 2.15.

In summary, the results show that the proposed method is able to forecast both supercritical and subcritical bifurcation diagrams for both pitch and plunge displacements with a good accuracy. When large amplitude perturbations are not available, the method predicts accurately the linear bifurcation point as well as the type of bifurcation (supercritical or subcritical). This is an important advantage of the proposed method compared to other techniques such as the ones based on variance [30,37,38].

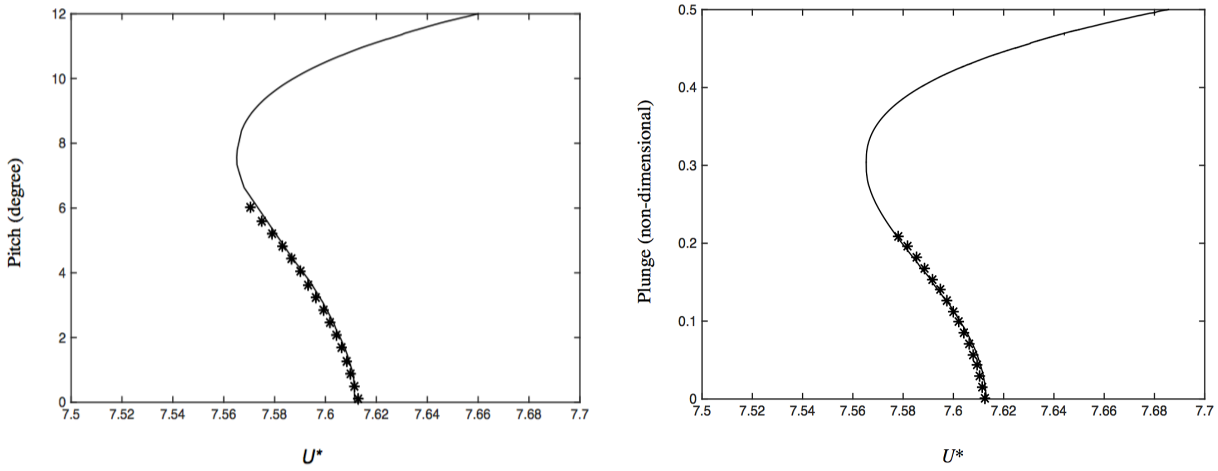

(a) (b)

Figure 2.13. Forecasted (*) and exact (-) bifurcation diagram for (a) pitch and (b) plunge displacements in subcritical case

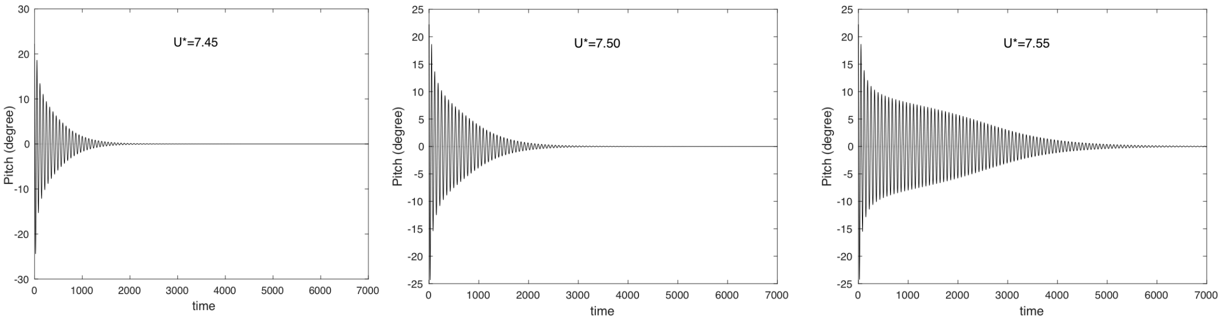

(a) (b) (c)

Figure 2.14. Measured system responses to large perturbations in pitch displacement at 3 non-dimensional flow speeds $U^* = 7.45$, 7.50, and 7.55 in subcritical case.

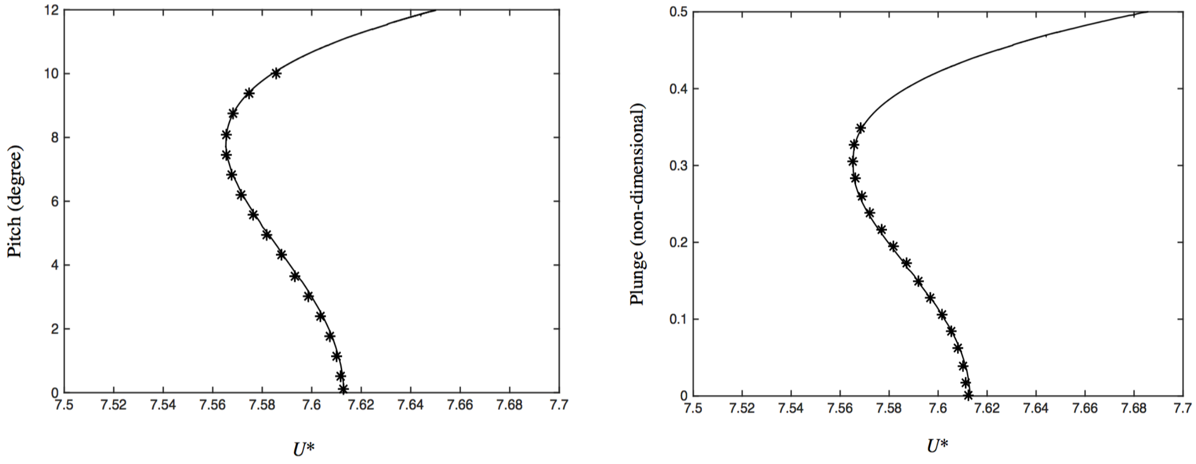

(a) (b)

Figure 2.15. Forecasted ($*$) and exact (-) bifurcation diagram for (a) pitch and (b) plunge displacements in subcritical case for larger perturbations.

2.5 Forecasting three-dimensional bifurcation diagrams

In a large class of oscillatory systems, the inertial manifold of the system close to Hopf bifurcations is a two-dimensional manifold containing states at different phases. In the previous section, the maximum limit cycle amplitudes of pitch and plunge displacements in the post-bifurcation regime were forecasted. Each of these forecasted bifurcation diagrams corresponds to a fixed phase on the inertial manifold which is the phase at which the post-bifurcation limit cycles exhibit their maximum amplitudes for the corresponding state variable.

The proposed forecasting method successfully forecasts the maximum limit cycle amplitudes, but not the entire limit cycles (i.e., the response at all phases in the inertial manifold). In this section, we include the phase difference between system states in an improved forecasting procedure to forecast three-dimensional bifurcation diagrams where the dimensions are: parameter, position state, and velocity state. Therefore, the new approach allows us to forecast more comprehensively the post-bifurcation dynamics, i.e. the limit cycle amplitudes of system states at all phases. This is a significant advantage since constructing these bifurcation diagrams using conventional numerical or experimental methods needs accurate models, or massive computational effort, especially for complex large dimensional systems.

The forecasting idea proposed in Sec. 2.2 can be generalized to forecast three-dimensional bifurcation diagrams of nonlinear oscillatory systems for a large category of systems which exhibit a Hopf bifurcation with a two-dimensional inertial manifold. Therefore, the dynamics of the system can be studied using any two coordinates on the inertial manifold. Moreover, choosing any phase in the two dimensional manifold reduces the system to a one-dimensional nonlinear map and the described forecasting method can be used. Thus, we can choose any arbitrary phase in the center space, i.e., the $x_1 - x_2$ plane in Fig. 2.16, where x_1 and x_2 are any two arbitrary system state variables (coordinates), and separately forecast the bifurcation diagrams of x_1 and x_2 at this phase using the described forecasting method. Alternatively, one may forecast one of the states and relate that to the other state using the selected phase. This pair of forecasted diagrams is a curve in the $\mu - x_1 - x_2$ space, which is the forecasted bifurcation diagram at the selected phase. Repeating this procedure for different phases, the complete three-dimensional bifurcation diagram in the $\mu - x_1 - x_2$ space is forecasted. This procedure can be interpreted as choosing different phase lines on the inertial manifold, and forecasting the bifurcation diagram for the selected phase (Fig. 2.16). The same procedure can be followed for any combination of state variables to forecast three-dimensional bifurcation diagrams for other coordinates.

Note that forecasting three-dimensional diagrams does not require an increased number of recoveries. However, more measurements are needed so that all desired phases are measured and the bifurcation diagrams are forecasted for different phases of the measured recoveries.

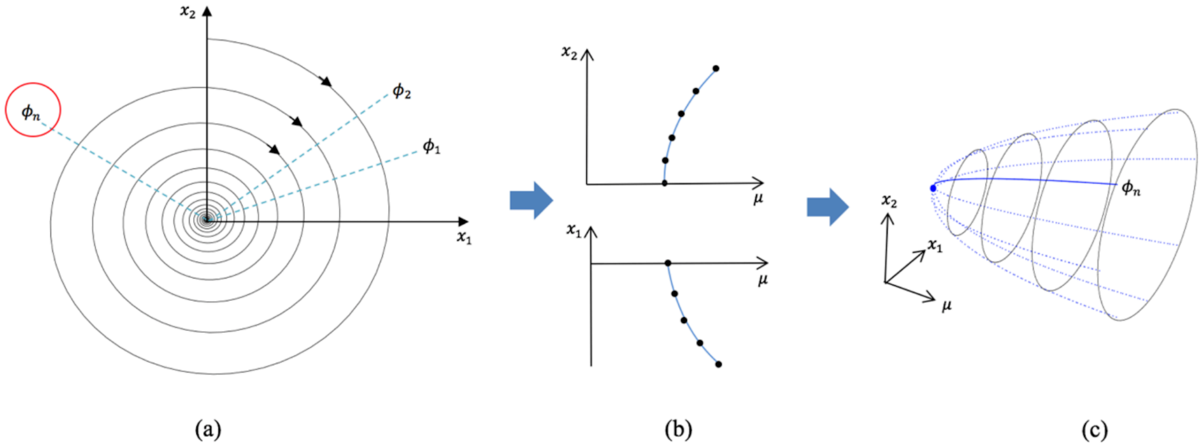

Figure 2.16. Procedure of forecasting three-dimensional bifurcation diagrams: a) select a phase in x_1-x_2 plane at measured recoveries. b) forecast bifurcation diagrams of x_1 and x_2 at the selected phase using forecasting procedure (Fig. 2.3), c) combine the pair of forecasted diagrams to construct a curve in three-dimensional space. The procedure is repeated for different phases to construct complete three-dimensional bifurcation diagram in μ –x_1-x_2 space

Following the described forecasting procedure, three-dimensional bifurcation diagrams of the two-degree-of-freedom airfoil of Sec. 2.4 are forecasted. For the considered system in Sec. 2.4.1.1, bifurcation diagram for supercritical bifurcation in *flow speed-pitch-pitch velocity* space is computed and the results are shown in Fig. 2.17(a). Figure 2.17(b) shows the forecasted limit cycle amplitudes at $U^* = 7.65$ for the bifurcation diagrams of Fig. 2.17(a). It can be observed that the forecasting method accurately predicts the limit cycle amplitudes at different phases. Three-dimensional bifurcation diagrams for any other combination of state variables can be obtained similarly.

Similarly, three-dimensional bifurcation diagrams can be forecasted for systems exhibiting subcritical bifurcations. The bifurcation diagrams in *flow speed-pitch-pitch velocity* space for the two-degree-of-freedom airfoil considered in Sec. 2.4.1.2 is forecasted and the results are shown in Fig. 2.18. Results show that the dynamics of the system is comprehensively forecasted in the post-bifurcation regime. Constructing these bifurcation diagrams using the forecasting method is a substantial advantage compared to conventional numerical or experimental methods that need massive experimental campaigns or computational efforts.

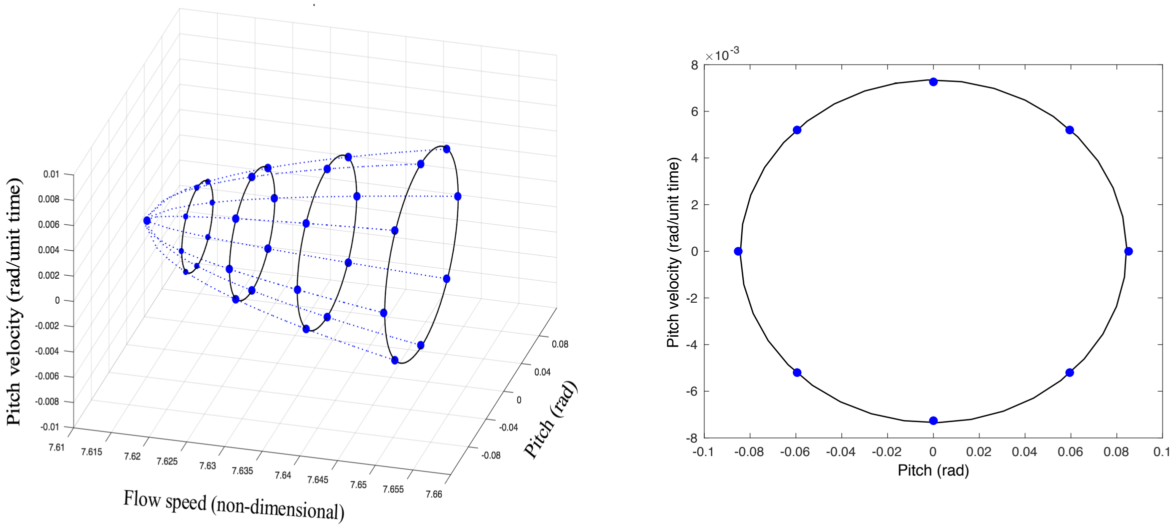

(a) (b)

Figure 2.17. (a) Forecasted three-dimensional bifurcation diagrams in flow speed-pitch-pitch velocity space for a system that exhibits a supercritical bifurcation. Dashed lines are forecasted bifurcation diagrams at different phases, solid circles are the forecasted value at a few selected flow speeds, and solid lines are the exact limit cycles of the system computed at the selected flow speeds. (b)Forecasted limit cycles at $U^* = 7.65$ in pitch-pitch velocity plane for a system that exhibits a supercritical bifurcation. Solid line is exact limit cycle and circles are forecasted values.

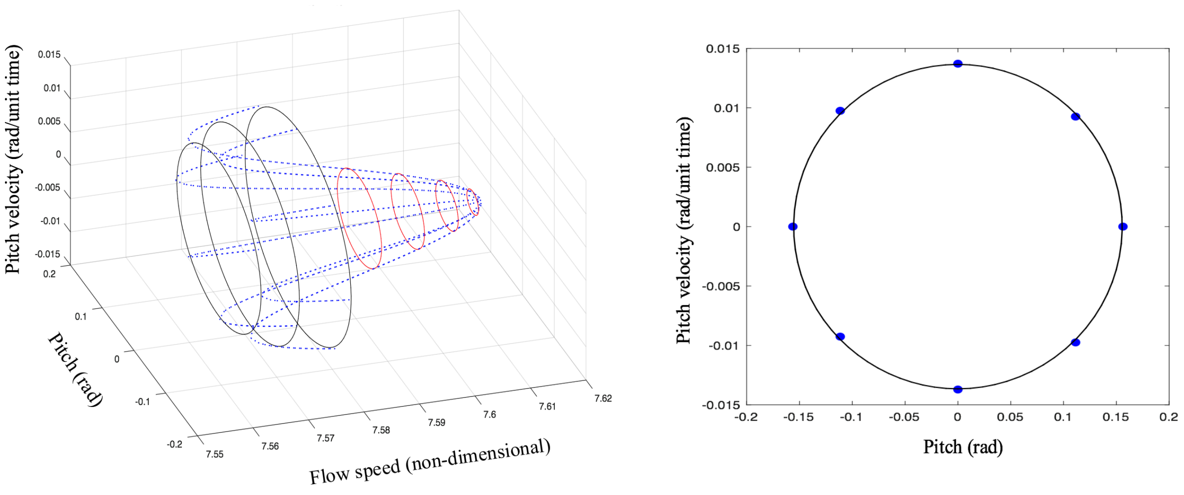

(a) (b)

Figure 2.18. (a) Forecasted three-dimensional bifurcation diagrams in flow speed-pitch-pitch velocity space for a system that exhibits a subcritical bifurcation. Dashed lines are forecasted bifurcation diagrams at different phases, and solid lines are the exact limit cycles of the system computed at the selected flow speeds. (b)Forecasted limit cycles at $U^* = 7.57$ in pitch-pitch velocity plane for a system that exhibits a supercritical bifurcation. Solid line is exact limit cycle and circles are forecasted values.

2.6 Three-degree-of-freedom aeroelastic model

The proposed method is employed to forecast the bifurcation diagrams of a nonlinear fluid-structural system composed of a 3-DOF typical aeroelastic section with a trailing-edge control surface schematically shown in Fig. 2.19. This system may experience both supercritical and subcritical Hopf (flutter) bifurcations depending on the system parameters. The equations of motion of this system can be written as follows [78]

$$\begin{gathered}
\ddot{\xi} + x_\alpha \ddot{\alpha} + x_\beta \ddot{\beta} + \frac{2\zeta_\xi \bar{\omega}_1}{U^*}\dot{\xi} + \left(\frac{\bar{\omega}_1}{U^*}\right)^2 G_\xi(\xi) = -\frac{C_L(\tau)}{\mu}, \\
\frac{x_\alpha}{r_\alpha^2}\ddot{\xi} + \ddot{\alpha} + \frac{2\zeta_\alpha}{U^*}\dot{\alpha} + \frac{r_\beta^2+(c_h-a_h)x_\beta}{r_\alpha^2}\ddot{\beta} + \frac{1}{U^{*2}}G_\alpha(\alpha) = \frac{C_{M_\alpha}(\tau)}{\mu r_\alpha^2}, \\
\frac{x_\beta}{r_\beta^2}\ddot{\xi} + \ddot{\beta} + \frac{2\zeta_\beta \bar{\omega}_2}{U^*}\dot{\beta} + \frac{r_\beta^2+(c_h-a_h)x_\beta}{r_\beta^2}\ddot{\alpha} + \left(\frac{\bar{\omega}_2}{U^*}\right)^2 G_\beta(\beta) = \frac{C_{M_\beta}(\tau)}{\mu r_\beta^2},
\end{gathered} \tag{2.22}$$

where α is the pitch angle, $\xi = h/b$ is the non-dimensional plunge displacement, β is the flap angle, $\tau = Ut/b$ is the non-dimensional time, and the overdot indicates differentiation with respect to τ. U is the free stream velocity, and $U^* = U/(b\omega_\alpha)$ is the non-dimensional free stream velocity, which is used as bifurcation parameter in this study. $\bar{\omega}_1 = \omega_\xi/\omega_\alpha$ is the ratio of the natural frequencies of uncoupled plunge and pitch modes, and $\bar{\omega}_2 = \omega_\beta/\omega_\alpha$ is the ratio of the natural frequencies of uncoupled flap and pitch modes. The damping ratios for the pitch, plunge and flap are ζ_α , ζ_ξ and ζ_β. r_α and r_β are the radius of gyration about the elastic axis and flap hinge. $G_\alpha(\alpha)$, $G_\beta(\beta)$ and $G_\xi(\xi)$ are the structural elastic torques and elastic force created by the pitch, flap and plunge motions. C_L is the aerodynamic lift coefficient, and $\mathrm{C}_{\mathrm{M}_\alpha}$ and $\mathrm{C}_{\mathrm{M}_\beta}$ are pitching moment coefficients about elastic axis and flap hinge, respectively, and are given in reference[79] for incompressible flow. $\mu = m/\rho\pi b^2$ is the mass ratio, where m is the total mass of the airfoil and ρ is the air density.

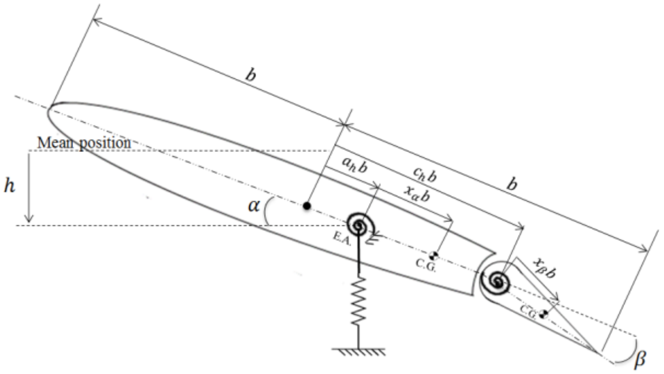

Figure 2.19. Schematic of a 3-DOF airfoil with a control surface

The equations of motion for this system, including a reduced order model of the aerodynamics, can be written as a set of 12 first-order ordinary differential equations [78]

$$\dot{\mathbf{x}} = \boldsymbol{f}(\mathbf{x}, U^*, \tau), \tag{2.23}$$

where $\mathbf{x} = [x_1, x_2, \dots, x_{12}]^T$ is the vector of state space variables defined as $x_1 = \alpha$, $x_2 = \dot{\alpha}$, $x_3 = \xi$, $x_4 = \dot{\xi}$, $x_5 = \beta$, $x_6 = \dot{\beta}$, $x_7 = w_1$, $x_8 = w_2$, $x_9 = w_3$, $x_{10} = w_4$, $x_{11} = w_5$, $x_{12} = w_6$, with

w_1 to w_6 being augmented states resulting from model for the aerodynamics. These six augmented variables are defined as

$$\begin{aligned} w_1 &= \int_0^\tau e^{-\epsilon_1(\tau-\sigma)}\alpha(\sigma)d\sigma, w_2 = \int_0^\tau e^{-\epsilon_2(\tau-\sigma)}\alpha(\sigma)d\sigma, \\ w_3 &= \int_0^\tau e^{-\epsilon_1(\tau-\sigma)}\xi(\sigma)d\sigma, w_4 = \int_0^\tau e^{-\epsilon_2(\tau-\sigma)}\xi(\sigma)d\sigma, \\ w_5 &= \int_0^\tau e^{-\epsilon_1(\tau-\sigma)}\beta(\sigma)d\sigma, w_6 = \int_0^\tau e^{-\epsilon_2(\tau-\sigma)}\beta(\sigma)d\sigma. \end{aligned} \tag{2.24}$$

where $\epsilon_1 = 0.0455$ and $\epsilon_2 = 0.3$ [76]. The function $\boldsymbol{f}(\mathbf{x}, U^*, \tau)$ in Eq. (2.23) is a complex nonlinear vector function of the 12 state variables that contains the effects of the structure and the aerodynamics. Details about this formulation can be found in refs. [52,78].

To demonstrate the forecasting method for this system, Eq. (2.23) is solved numerically to produce surrogate recovery data from perturbations in the pre-bifurcation regime. To reflect realistic situations, and instead of randomly perturbing the initial conditions (such as position or velocity) of the system, a *"1-cos"* type gust load is applied as disturbance to the system. The system response to this gust is used for forecasting. It is worth mentioning that the actual model in Eqs. (2.22) - (2.24) is only used for generating surrogate measurement data, and is not required for the proposed forecasting approach.

Equations (2.22) and (2.23) govern the dynamics of an aeroeleastic system which can exhibit Hopf bifurcations (flutter). When we choose a specific phase of the oscillations, for example in the pitch-plunge plane, we in fact reduce the system to a one dimensional system similar to Eq. (2.1), which represents conceptually the one-dimensional nonlinear system exhibiting pitchfork bifurcations. The forecasting procedure is applied to forecast the bifurcation diagram at that specific phase.

In this example, the parameters considered for the aeroelastic system are $\bar{\omega}_1 = 0.5$, $\bar{\omega}_2 = 3.5$, $\mu = 100$, $c_h = 0.6$, $a_h = -0.5$, $x_\alpha = 0.25$, $x_\beta = 0.0125$, $r_\alpha = 0.5$, $r_\beta = 0.05$, $\zeta_\xi = \zeta_\alpha = \zeta_\beta = 0$, and the structural elastic functions considered are $G_\xi(\xi) = \xi$ and $G_\beta(\beta) = \beta$.

The system is perturbed using gust loads at three flow speeds in the pre-bifurcation regime, i.e. $U^* = 4.40$, 4.50, and 4.60. The equations of motion are solved numerically to generate surrogate measurement data in the form of system responses to perturbations at these flow speeds. The time series are recorded and used as inputs to the proposed forecasting method. In following sections, "measurements" refers to "surrogate data" instead of experiments.

2.6.1 Forecasting two-dimensional bifurcation diagrams

In this section, we consider first the forecasting of two-dimensional bifurcation diagrams separately for supercritical and subcritical bifurcations. Thus, first we consider a system which has $G_\alpha(\alpha) = \alpha + 10\alpha^3$, which means that the airfoil has cubic nonlinearity in the pitch displacement. In this case, the system faces supercritical Hopf (flutter) bifurcations. Figure 2.20 shows that the plunge displacement in response to perturbations at the three flow speeds considered. As it can be observed, the slowing down phenomenon is present in the recorded measurements, as revealed by the increasingly long recovery times as the flow approaches the flutter speed.

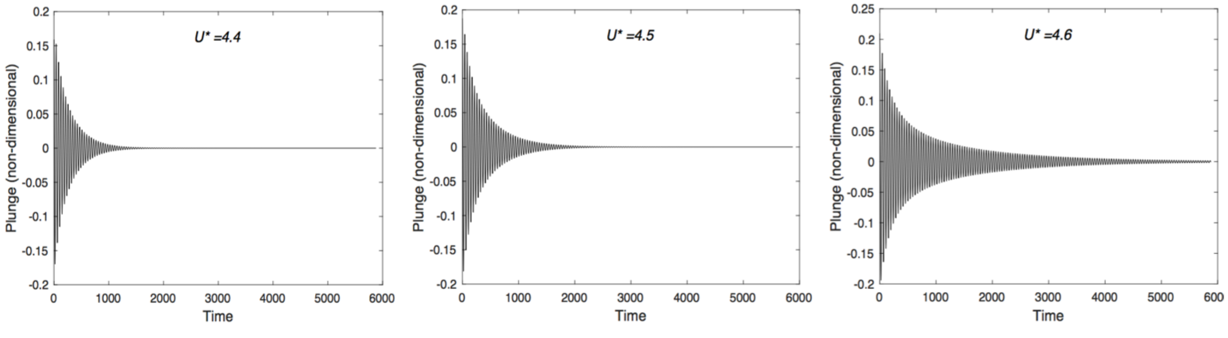

(a) (b) (c)

Figure 2.20. System responses to perturbations in plunge displacement at 3 non-dimensional flow speeds $U^* = 4.40$, 4.50, and 4.60.

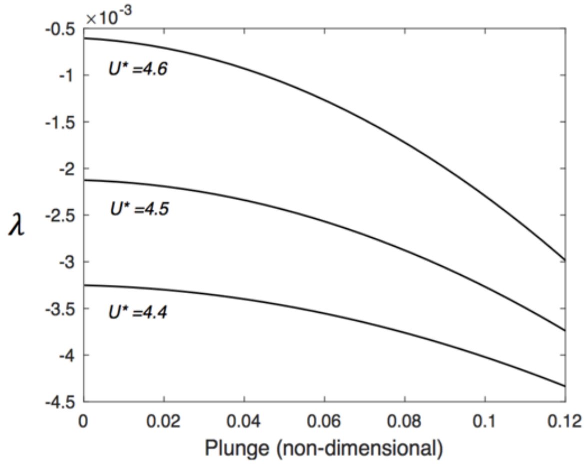

Figure 2.21. Recovery rate vs. plunge amplitude for a case of supercritical bifurcations. Non-dimensional values of the flow speeds are shown.

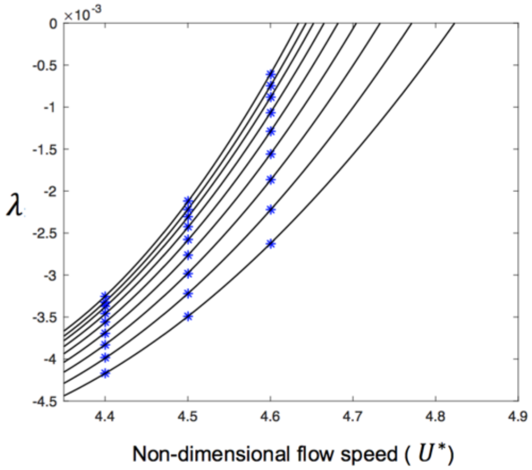

Figure 2.22. Second order approximation in the $\lambda - U^*$ plane for several plunge amplitudes. Each curve corresponds to a different plunge amplitude. Symbols (*) show recovery rates obtained using the data in Fig. 2.21.

Here, we first forecast two-dimensional bifurcation diagrams corresponding to maximum amplitudes of the post-bifurcation limit cycles for each degree of freedom. For this purpose, we select local maxima of the measured recoveries, and forecasting approach is used as described in Sec. 2.2. This means we have chosen a specific value of the phase in the plane $x - \dot{x}$, where x is the considered state variable (pitch, plunge or flap angle). We consider this as reference for the phase, i.e. phase is zero. Following the forecasting procedure, curves of $\lambda - r$ are obtained for the plunge displacement as shown in Fig. 2.21. Using these curves and Eq. (2.6) for each amplitude, $\lambda - U^*$ curves are obtained (as shown in Fig. 2.22), and the bifurcation diagram of the system for plunge displacement is forecasted. Similarly, the bifurcation diagrams for other DOFs, i.e. pitch and flap-angle, are forecasted as shown in Fig. 2.23.

These results show that the method forecasts bifurcation point and bifurcation type (supercritical) accurately. Moreover, the bifurcation diagrams at lower amplitudes are forecasted accurately, while the accuracy decreases for larger amplitudes in the diagram, as expected. From these results, one can identify the maximum limit cycle amplitudes that each of the plunge, pitch and flap degrees of freedom exhibit in post-bifurcation flow speeds. For example, it is forecasted that plunge displacement reaches to the maximum amplitude of 0.0726 (non-dimensional) during its oscillations at $U^* = 4.7$.

The decreased forecasting accuracy at higher amplitudes in the bifurcation diagrams in Fig. 2.23 is expected and can be explained by examining the forecasting approach. Generally, the parts of the bifurcation diagram that are farther from the pre-bifurcation regime are forecasted with less accuracy because the accuracy of the Taylor series in Eq. (2.2) is lower. This issue can be alleviated by using parameter values closer to the bifurcation. For example, Fig. 2.24 shows the forecasting results using measurements collected at flow speeds of $U^* = 4.52$, 4.56, and 4.60, which are closer to bifurcation compared to the data used to obtain the results in Fig. 2.23. As it can be observed comparing Figs. 2.23 and 2.24, bifurcation diagrams are forecasted more accurately.

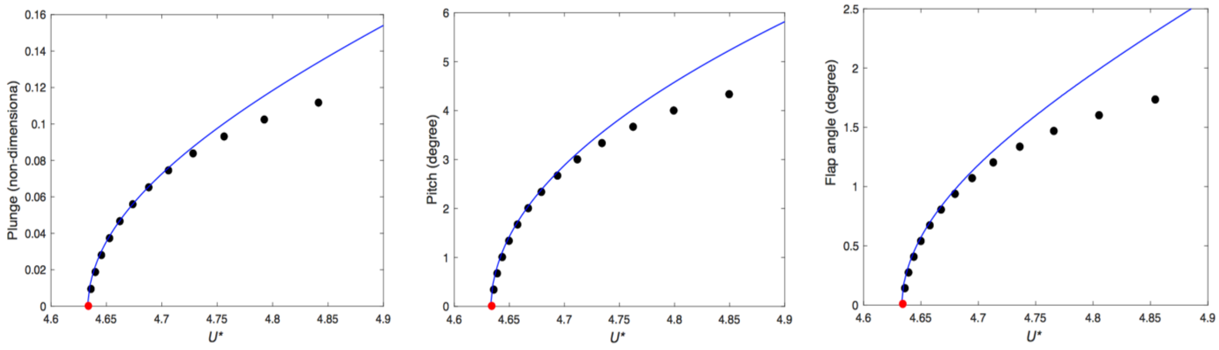

(a) (b) (c)

Figure 2.23. Exact (solid line) and forecasted (solid circles) bifurcation diagrams of maximum limit cycle amplitudes for (a) plunge displacement, (b) pitch angle, and (c) flap angle displacements in a system which exhibits a supercritical bifurcation using measurements at $U^* = 4.40$, 4.50, and 4.60.

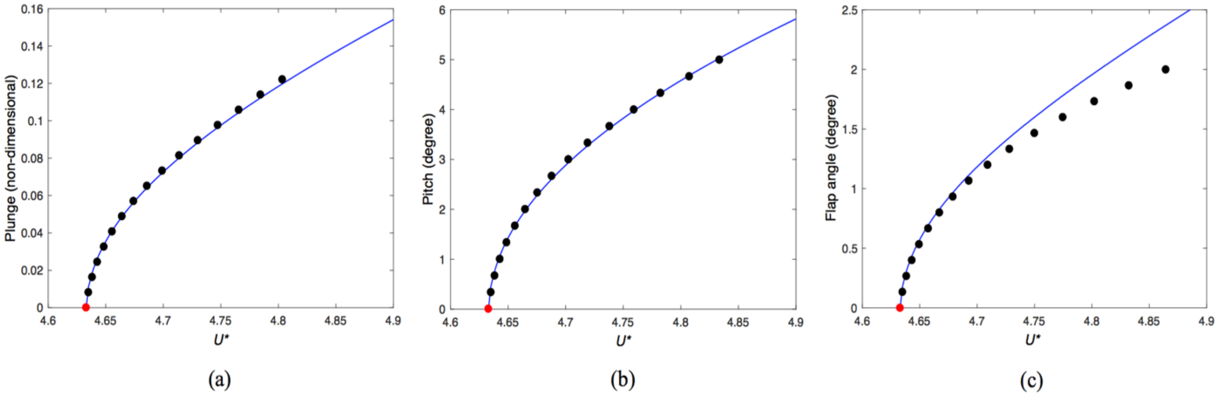

(a) (b) (c)

Figure 2.24. Exact (solid line) and forecasted (solid circles) bifurcation diagrams of maximum limit cycle amplitudes for (a) plunge displacement, (b) pitch angle, and (c) flap angle displacements in a system which exhibits a supercritical bifurcation using measurements at $U^* = 4.52$, 4.56, and 4.60.

In this example, parameters which are used for forecasting are equal or greater than 95% of the critical speed (i.e. $U_{cr}^* = 4.634$), and the bifurcation diagrams are forecasted up to 5% after the critical parameter. However, there is no general conclusion about these boundaries. Forecasting accuracy and the forecasted region of the bifurcation diagrams depend on several factors and could vary from system to system depending on their dynamics. First, the accuracy depends on how close the parameters used for forecasting are to the bifurcation. Closer parameters to the bifurcation result in more accurate forecasting. Forecasting accuracy also depends on the characteristics of the dynamics around the bifurcation. Specifically, if the inertial manifold of the system remains (almost) unchanged in a larger parameter region prior and after the bifurcation, then parameters father from the bifurcation can be used for forecasting, and a larger parameter region of the bifurcation diagrams can be forecasted accurately. Forecasting results depend also on the intensity/magnitude of the perturbations. For example, if the parameters used for forecasting are close to the bifurcation but the perturbations are very small, then only small amplitudes of the bifurcation diagram can be forecasted. This is because the largest forecasted amplitude in the forecasted bifurcation diagram cannot be larger than the amplitude created by perturbations.

Next, we consider a system, with a different nonlinear structural elastic behavior in pitch displacement. Specifically, we consider a system where $G_\alpha(\alpha) = \alpha - 2.5\alpha^3 + 75\alpha^5$. Note that this system has the same linear behavior as the previous system studied. The only difference is in the nonlinear terms. This system exhibits subcritical bifurcations. Similar to the previous case, the system is perturbed using a *"1-cos"* type gust at three flow speeds $U^* = 4.46$, 4.50, and 4.54. Surrogate system responses are obtained by solving Eq. (2.23). The forecasting procedure is the same as in the previous example for forecasting the maximum post-bifurcation limit cycle amplitudes. However, the $\lambda - r$ curves obtained are considerably different, as expected.

Consider, for example, the plunge displacement. The slowest recovery rate corresponds to a non-zero amplitude, as shown in Fig. 2.25. This amplitude corresponds to the saddle node bifurcation of cycles (the turning point in the bifurcation diagram). Identifying the flow speed for this bifurcation is usually very difficult and is essential for ensuring safety and guaranteeing stability. This speed is the beginning of the bi-stable region, where a large perturbation may cause dramatic changes in the dynamics of the system even though the flow speed is below the linear flutter speed. The forecasted bifurcation diagrams for the pitch, plunge and flap angle are shown in Fig. 2.26. These results show that the method forecasts the bifurcation point (flutter speed) and the post-bifurcation regime accurately. More importantly, the type of bifurcation is (correctly) forecasted to be subcritical. Therefore, one should expect that the system dynamics has a dramatic change beyond the linear flutter speed or even below the flutter speed, in the bi-stable region, which can result in catastrophic consequences for the structure. According to the results, the method forecasts all points on the bifurcation diagram regardless of their stability. Both the stable and unstable parts of the bifurcation diagrams are forecasted using the same procedure. However, the method does not identify which point is stable and which point is not, although that can be easily determined when interpreting the results simply by noting that solutions between outer branches are unstable.

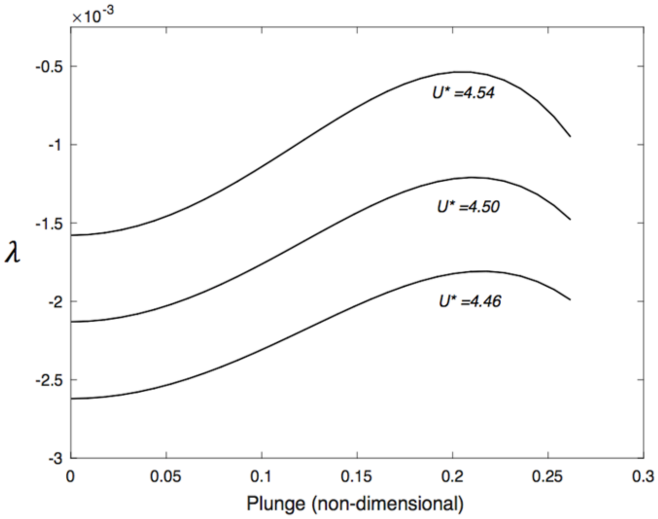

Figure 2.25. Recovery rate vs. plunge amplitude for the system with a subcritical bifurcation

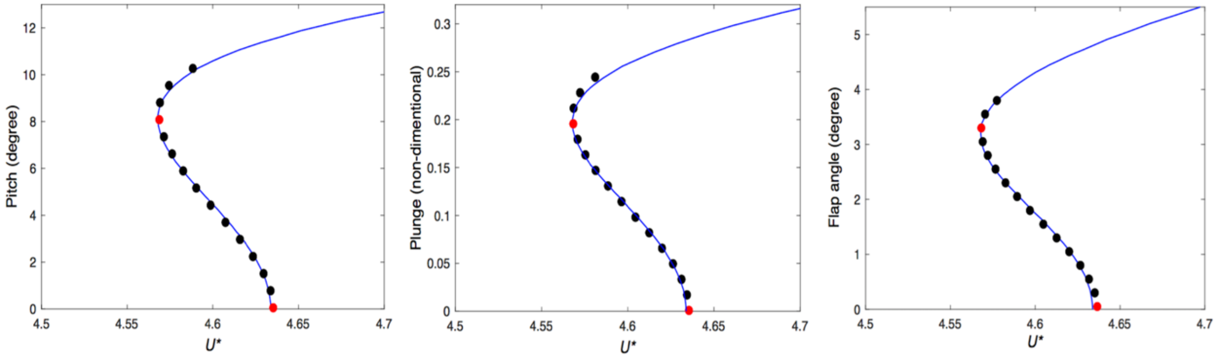

(a) (b) (c)

Figure 2.26. Exact (solid line) and forecasted (solid circles) bifurcation diagrams for (a) plunge displacement, (b) pitch angle, and (c) flap angle displacement in a system which exhibit a subcritical bifurcation.

2.6.2 Forecasting three-dimensional bifurcation diagrams

In the previous section, the maximum limit cycle amplitudes of pitch, plunge and flap displacements in the post-bifurcation regime were forecasted. Each of these forecasted bifurcation diagrams corresponds to a fixed phase on the inertial manifold which is the phase at which the post-bifurcation limit cycles exhibit their maximum amplitudes for the corresponding state variable. This phase is the reference *zero* phase in the $x - \dot{x}$ space, where x is one of the considered state variables (pitch, plunge or flap) because x is maximum when $\dot{x}$ is zero.

In this section, we extend the approach to a much comprehensive bifurcation diagram, not only for the maximum amplitudes. Specifically, we focus on forecasting three-dimensional bifurcation diagrams, defined as diagrams in the $U^* - x - \dot{x}$ space, where x can be the pitch, plunge, or flap angle.

To construct such bifurcation diagrams, we follow the procedure described in Fig. 2.16. For the considered system, bifurcation diagrams for supercritical bifurcations in *flow speed-pitch-pitch velocity, flow speed-plunge-plunge velocity,* and *flow speed-pitch-plunge* spaces are computed and the results are shown in Fig. 2.27. Figure 2.28 shows the forecasted limit cycle amplitudes at $U^* = 4.65$ for the bifurcation diagrams of Fig. 2.27. It can be observed that the forecasting method accurately predicts the limit cycle amplitudes at different phases. Three-dimensional bifurcation diagrams for any other combination of state variables can be obtained similarly.

Similarly, three-dimensional bifurcation diagrams can be forecasted for systems exhibiting subcritical bifurcations. The bifurcation diagrams in *flow speed-pitch-plunge, flow speed-pitch-pitch velocity and flow speed-plunge-plunge velocity* spaces are forecasted and the results are shown in Figs. 2.29 and 2.30. As it can be observed from the results, the dynamics of the system is comprehensively forecasted in the post-bifurcation regime. Constructing these bifurcation diagrams using the forecasting method is a substantial advantage compared to conventional numerical or experimental methods that need massive experimental campaigns or computational efforts.

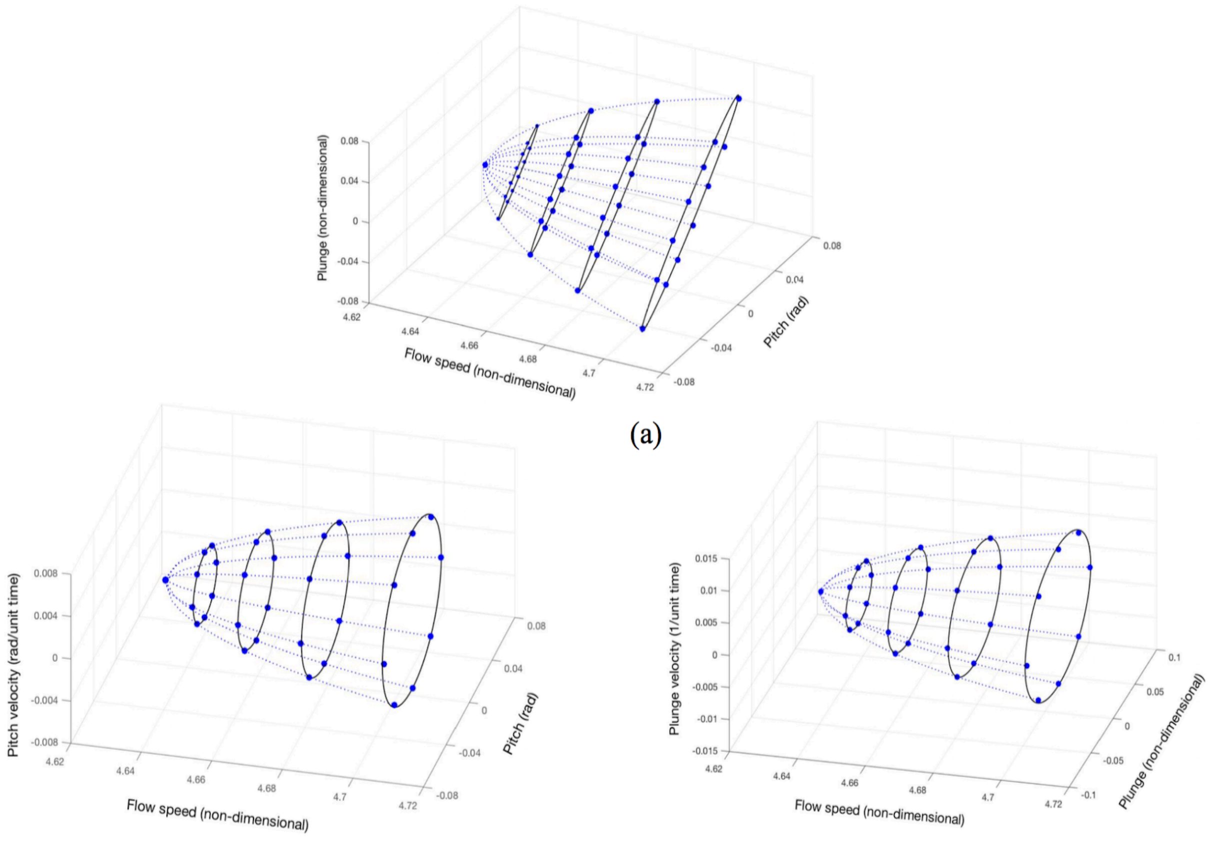

(a)

(b)

(c)

Figure 2.27. Forecasted three-dimensional bifurcation diagrams in (a) flow speed-pitch-plunge, (b) flow speed-pitch-pitch velocity, and (c) flow speed-plunge-plunge velocity space for a system that exhibits a supercritical bifurcation. Dashed lines are forecasted bifurcation diagrams at different phases, solid circles are the forecasted value at a few selected flow speeds, and solid lines are the exact limit cycles of the system computed at the selected flow speeds.

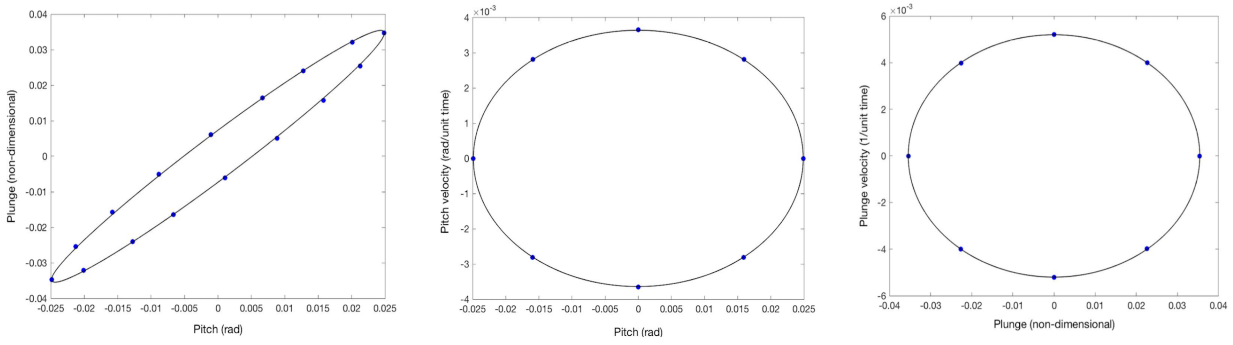

(a) (b) (c)

Figure 2.28. Forecasted limit cycles at $U^* = 4.65$ in (a) pitch-plunge, (b) pitch-pitch velocity, and (c) plunge-plunge velocity planes for a system that exhibits a supercritical bifurcation. Solid lines are exact limit cycles and circles are forecasted values.

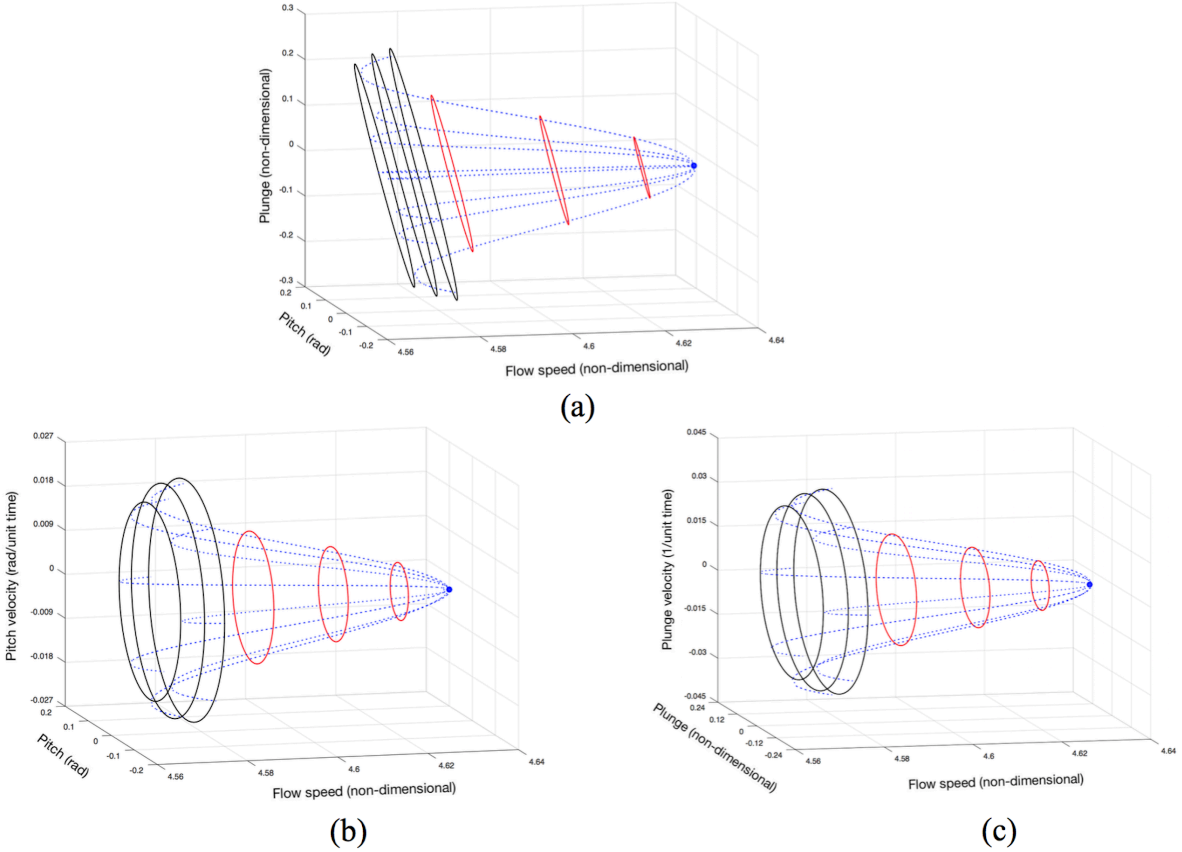

Figure 2.29. Forecasted three-dimensional bifurcation diagrams in (a) flow speed-pitch-plunge, (b) flow speed-pitch-pitch velocity, and (c) flow speed-plunge-plunge velocity space for a system that exhibits a subcritical bifurcation. Dashed lines are forecasted bifurcation diagrams at different phases, and solid lines are the exact limit cycles of the system computed at the selected flow speeds.

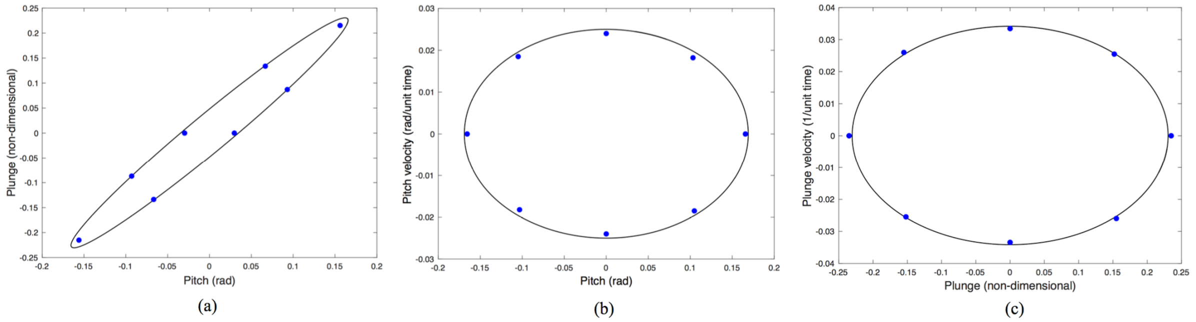

Figure 2.30. Forecasted limit cycles at $U^* = 4.58$ in (a) pitch-plunge, (b) pitch-pitch velocity, and (c) plunge-plunge velocity planes for a system that exhibits a subcritical bifurcation. Solid lines are exact limit cycles and circles are forecasted values.

2.6.3 Effects of measurement noise

Noise can contaminate measurements, thus influencing the forecasting accuracy. Accuracy is expected to decrease as noise increases. One possible solution to this issue is to increase the number of measurements. The number of measurements needed depends on the level of noise and on the level of the desired accuracy. These measurements should be collected at multiple parameter values (more than just the three used in the deterministic case). Also, several recoveries should be measured at each parameter value.

To investigate the effects of noise on the forecasting results in the case of supercritical bifurcations, 10% noise is added to the measurements, and the forecasting procedure is applied without any noise filtering. At each flow speed, the system response to ten separate perturbations is measured. The recovery rates corresponding to each separate measurement are computed (as described in Sec. 2.2). The recovery rates are then averaged to obtain the average measured recovery rate at each amplitude. This procedure is repeated at several flow speeds. Finally, the average recovery rates for each flow speed are used in the forecasting procedure. As an example, Fig. 2.31 shows the computed recovery rates and forecasted bifurcation diagram using the averaged recovery rates for the maximum plunge amplitudes, i.e. zero phase in *plunge-plunge velocity* plane. By using the same set of measurements, this procedure is repeated for different phases to forecast three dimensional bifurcation diagrams. The bifurcation diagram in *flow speed-plunge-plunge velocity* space is forecasted using noisy measurements at $U^* = 4.60$, 4.56 and 4.52, and the results are shown in Fig. 2.32. The bifurcation diagrams for all other combinations of state variables can be obtained similarly.

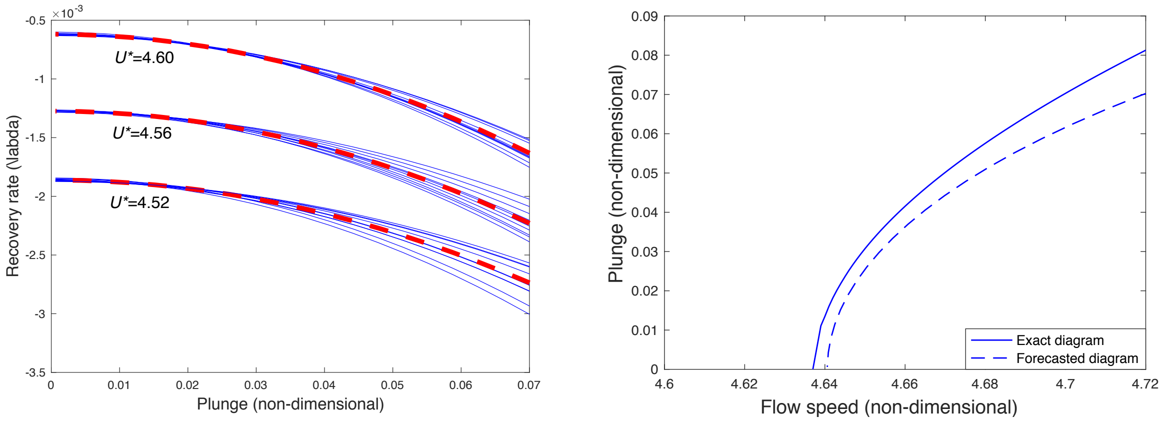

(a) (b)

Figure 2.31. (a) Approximated recovery rates of maximum plunge amplitudes at three flow speeds $U^* = 4.60$, 4.56 and 4.52. Each line represents the approximated recovery rate using a separate set of noisy measurements. Dashed lines are average recovery rates at each flow speed, which are employed for forecasting. (b) Forecasted bifurcation diagram using the average recovery rates.

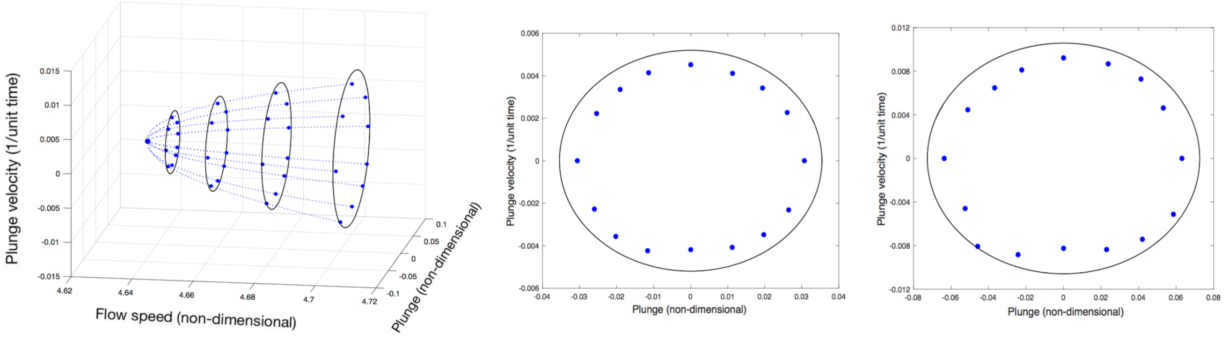

(a) (b) (c)

Figure 2.32. (a) Forecasted three-dimensional bifurcation diagrams in *flow speed-plunge-plunge velocity* space for a system that exhibits a supercritical bifurcation and in presence of 10% measurement noise. Dashed lines are forecasted bifurcation diagrams at different phases, solid circles are forecasted value at a few selected flow speeds, and solid lines are exact limit cycles of the system computed at the selected flow speeds. (b) and (c) demonstrate exact and forecasted limit cycles at $U^* = 4.65$ and $U^* = 4.70$, respectively. Solid lines are exact limit cycles, and circles are forecasted values.

2.7 Conclusions

In this chapter, a unique approach of forecasting supercritical and subcritical flutter (Hopf bifurcations) was presented. The proposed method was developed based on the critical slowing down phenomenon present in oscillating systems near certain types of bifurcations. The recovery rate of the system was extracted using an optimization approach which improves the forecasting accuracy especially when the system has transient recoveries with low frequency oscillations. Moreover, it was shown that applying modal decomposition to the collected transient recovery and keeping only the effects of the mode involved in the bifurcation can increase the forecasting accuracy. The forecasting method relies on local maxima in the measurements, and the accuracy of these measurements is enhanced by the ERA.

To demonstrate the proposed method and to highlight its advantages, the approach was applied to determine bifurcation diagrams of two fluid-structural systems with cubic nonlinearity. The systems were composed of a typical airfoil section in pitch and plunge, equipped with a trailing-edge control surface. Instead of experimental measurements, we used surrogate data obtained as time series from simulation of the model as input to our method. To reflect realistic situations, gust loads were applied as disturbances to the system while system recoveries are measured.

Results show that the proposed method accurately predicts the bifurcation point (i.e., the flutter speed) and the post-bifurcation regime (i.e., the bifurcation type and the limit cycles) of the considered fluid-structural systems despite the fact that it does not use a model of the system. Two and three dimensional bifurcation diagrams were accurately forecasted in both supercritical and subcritical cases. Since bifurcations can cause dramatic changes in system dynamics, this type of forecasting which does not require exploring the post-bifurcation regime provides great advantages to a variety of applications especially when safety and maximum system performance is needed.

Chapter 3

Forecasting the Post-Bifurcation Dynamics of Large-Dimensional Slow-Oscillatory Systems Using Critical Slowing Down and Center Space Reduction

3.1 Introduction

Hopf bifurcations are common and important types of bifurcations which have been observed in a variety of systems such as aeroelastic systems [43], machine tools [49], automotive dynamics [48], predator–prey systems [80], nonlinear circuits [51], neuron systems [81], to name a few. Such phenomena lead to various types of stability issues and may cause catastrophic system dynamics. Therefore, forecasting such bifurcations, i.e. predicting bifurcations with measurements only from the pre-bifurcation regime, is an important challenge to overcome. The importance of forecasting methods is even higher when dealing with complex and large-dimensional systems since accurate models of such systems is not easily available. In particular, forecasting methods for Hopf bifurcations have not been studied much [2] although such bifurcations have been observed and studied in various systems. Thus, developing a forecasting method for this class of bifurcations is necessary for this important type of bifurcations.

Several indicators have been explored as early warning signals such as the noise-induced spectrum [37], the skewness of the probability distribution [30], and the flickering between basins of attraction before bifurcations [38] (see also [2] for a review). Based on these indicators, several forecasting methods using observation of system recovery from perturbations have been proposed

[8,32,34,82–87] (see [2] for a review). In particular, critical slowing down (CSD) is one of the most important indicators used for bifurcation forecasting. These forecasting methods can be classified into two groups: (a) stochastic methods, and (b) bifurcation forecasting methods. Stochastic methods use features of the dynamics such as an increased variance, increased autocorrelation and flickering. Such features can be observed in recoveries in the vicinity of catastrophic bifurcation points. These methods can forecast tipping points; however, they cannot identify the distance to the bifurcations or the type of bifurcations. To address that limitation, bifurcation forecasting methods have been developed [8,84,88]. These methods use the recovery rate of the system from perturbations in the pre-bifurcation regime and the CSD phenomenon to forecast the post-bifurcation dynamics. Although these methods resolve some of the main disadvantages of stochastic methods, they still have to be developed for forecasting bifurcations in more complex and large-dimensional systems.

There are several challenges in forecasting Hopf bifurcations which make forecasting more complicated. First, systems can recover to equilibrium with oscillations in the pre-bifurcation regime. Since the phases of measurements of the dynamics during one or multiple recoveries are not the same, one cannot directly use all of the time data measurements in the forecasting algorithms. The common way of solving this problem is to use local maxima of the system recovery from perturbations and to approximate the recovery rate using these peaks [84]. However, this approach does not have enough accuracy especially for low-frequency oscillations when only a few peaks are available before reaching the noise floor in recoveries. Furthermore, Hopf bifurcations often occur in large-dimensional systems, where several modes are involved in the dynamics. The large-dimensionality makes forecasting substantially more complicated and increases the forecasting error. Moreover, methods able to forecast large ranges of the bifurcation diagram with a good accuracy are desirable. This is especially important for subcritical bifurcations since the stable region of post-bifurcation regime has large amplitudes.

In this study, we present a unique approach to forecast Hopf bifurcations in large-dimensional systems to resolve the above-mentioned challenges. The proposed method builds on the work of Lim and Epureanu [8] in that the approach is based on the phenomenon of CSD which accompanies such bifurcations, i.e. when the systems is close to the bifurcation point, perturbations lead to long transient oscillations before the system reach to its stable state. Similar to previous work [8], the bifurcation diagram is forecasted based on observations of the system only in the pre-bifurcation regime. Moreover, the method is model-less and does not require a mathematical model of system for forecasting the bifurcation diagram. The method is not limited to small perturbations and is not based on linearization. Hence, it can use recoveries from large perturbations for bifurcation forecasting. However, distinct from previous work [8], the proposed method is able to provide accurate forecasts even in the case of systems with low-frequency oscillations and large dimension. To deal with large-dimensional systems, the proposed technique uses a data-based modal decomposition approach to extract the mode involved in the bifurcation. Therefore, the accuracy of the forecasts increases especially at larger amplitudes in the bifurcation diagram. Even more importantly, a modal coordinate method is introduced to enable the use of all measurements in the oscillating recovery data (and not just the peaks) for forecasting. This is a great advantage which considerably increases the forecasting accuracy especially for noisy measurements and for system recoveries with low frequency oscillations (in contrast to using only local maxima of the system recovery [8,89]).

To demonstrate the method and to highlight its advantages, we use surrogate measurements, namely time-series obtained from simulations of a complex nonlinear aeroelastic system that can experience different operating conditions and bifurcations. While the system has only two mechanical degrees of freedom, the aerodynamic part of the model leads to a more complex 8-dimensional nonlinear aeroelastic system. Instead of using random perturbations, gust loads are applied as disturbances to the system. System recoveries from gust perturbations are measured and used as surrogate data. These perturbations are similar to the actual behavior of many aeroelastic systems. The proposed method is applied to forecasting both supercritical and subcritical bifurcations. It is shown that the method can predict the type of bifurcation as well as the bifurcation diagrams using transient data collected only in the pre-bifurcation regime.

3.2 Forecasting method

In this section, the key aspects of the proposed forecasting method are presented. First, the general method which is applicable to non-oscillating systems is introduced. Next, this method is extended to forecasting bifurcations in large-dimensional oscillatory systems.

3.2.1 Forecasting bifurcations in non-oscillatory or fast-oscillatory systems

In this section we briefly review the approach used for forecasting bifurcations in non-oscillatory or fast-oscillatory systems [8,84]. Consider a nonlinear system with a parameter μ and an amplitude r which represents the distance from the current state to the equilibrium state. The time rate of change the of the amplitude can be written as

$$\dot{r} = f(\mu, r). \tag{3.1}$$

Using a Taylor series with respect to the parameter around the bifurcation point ($\mu = \mu_c$), the system can be expressed as

$$\dot{r} = r(p(r) + \alpha_1(r)(\mu - \mu_c) + \alpha_2(r)(\mu - \mu_c)^2 + HOT), \tag{3.2}$$

where $p(r)$, $\alpha_1(r)$ and $\alpha_2(r)$ are polynomial functions considered to be independent of the parameter μ, and *HOT* represents higher order terms in $\mu - \mu_c$. Note that this relation means neither that the dynamics of the system have been linearized in state space nor that the dynamics have small amplitudes. Only the parameter is assumed to have small variations. Therefore, we are not restricted to use small perturbations, but the analysis is applied near the critical value μ_c of the bifurcation parameter μ. Also, neglecting terms of order higher than 2 when the system is close to the bifurcation means that a second order polynomial dependence on the parameter value is used. Mathematically, using more terms in the Taylor series approximation in Eq. (3.2) results in a more accurate approximation. However, using higher order terms does not have a considerable effect on the forecasting results according to our recent studies. For flutter, the optimum order of the approximation appears to be the second order, as used in the study. There are many possible reasons for this. First, it may so be that the first two terms dominate the dynamics. Second is that there are other effects affecting the dynamics as data is collected farther from the bifurcation point, which have more dominant effects on the forecasting procedure than the order of the approximation in Eq. (3.2).

The rate $\lambda(\mu, r)$ at which the system recovers to its equilibrium after a perturbation depends on the amplitude and the parameter value, and is defined as

$$\lambda(\mu, r) = \frac{\dot{r}}{r} = \frac{d\,(\ln r)}{dt}. \tag{3.3}$$

Therefore, the dynamics of system can be re-written using Eqs. (3.2) and (3.3) as

$$\lambda(\mu,r) = p(r) + \alpha_1(r)(\mu - \mu_c) + \alpha_2(r)(\mu - \mu_c)^2. \tag{3.4}$$

Using time-series of measured system recoveries from perturbations, one can employ the following approximation to approximate $\lambda(\mu,r)$ as

$$\lambda(\mu,r) = \frac{d\,(\ln r)}{dt} \cong \frac{\ln r_+ - \ln r_-}{2\Delta t} \tag{3.5}$$

where Δt is the time between samples, r_+ is the value of the amplitude measured at time $t + \Delta t$, and r_- is the value of the amplitude measured at time $t - \Delta t$. The recovery rate plays the most important role in the forecasting method. When the system is close to a bifurcation, the recovery rate is decreased. At a fixed system amplitude r, the farther the system is from its corresponding post-bifurcation steady state behavior, the less is the recovery rate of the system. This fact is used for predicting the post-bifurcation dynamics.

Note that the fundamental limitation of this method is that measurements area available in large numbers and for small values of Δt. That holds for systems which recover without oscillations and where the amplitude is an actual value of a measured state variable of the system. This also holds for systems that recover with fast oscillations, where the time interval between consecutive peaks in the system dynamics is in fact Δt and small. Such systems were discussed in [8,84].

Consider that system recoveries from perturbations are measured at several different parameter values $\mu_1, \mu_2, \dots, \mu_n$. For each fixed parameter value (μ_k), one can choose a value of the amplitude $r = \tilde{r}$ and estimate $\lambda(\mu_k, r)$ using the time-series measurements (Fig. 3.1). Using the expression in Eq. (3.4), one can fit a second order polynomial to the estimated values of λ in the

$\mu - \lambda(\mu, \tilde{r})$ plane. The most important point in Fig. 3.2 is the intersection of the fitted curve with the μ axis. That intersection represents the forecasted parameter value $\tilde{\mu}$ for the corresponding post-bifurcation dynamics of amplitude $\tilde{r}$ (Fig. 3.3). This procedure can be repeated for different values of $\tilde{r}$, and the overall bifurcation diagram can be predicted.

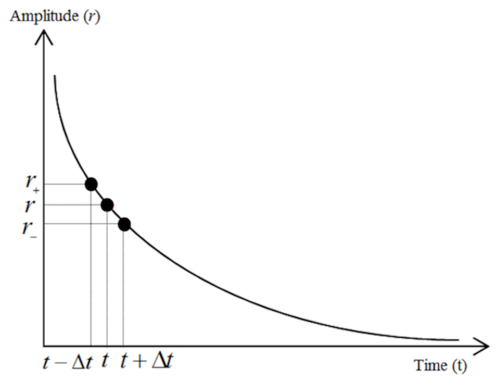

Figure 3.1. Conceptual example of a system recovery without oscillations over time from an initial perturbation.

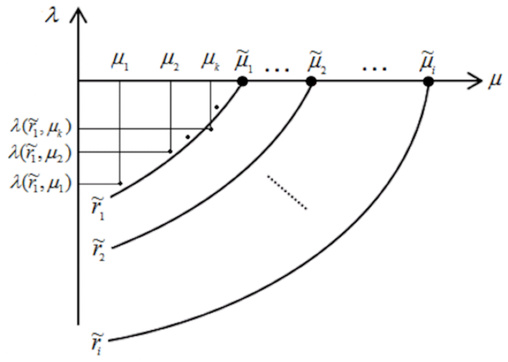

Figure 3.2. recovery rate vs. parameter and forecasting $\tilde{\mu}$.

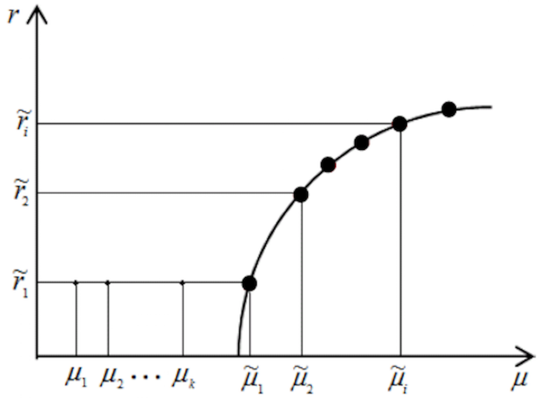

Figure 3.3. Forecasted bifurcation diagram

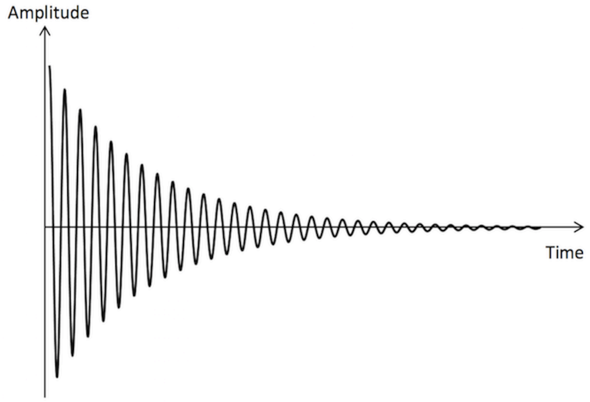

Figure 3.4. Conceptual example of a system recovery with oscillations over time from an initial perturbation.

3.2.2 Bifurcation forecasting in slow-oscillatory systems

Distinct from previous work, in this study, we are considering Hopf-bifurcations where the system oscillates (potentially with low frequency) during its recovery from perturbations in the pre-bifurcation regime (Fig. 3.4). Hence, we cannot use Eq. (3.5) for all of the points in the measured system recovery since data points adjacent to each other are in different phases. The common solution of this problem is to choose local maxima of the recovery data and use the same procedure as for the non-oscillatory case. This is an acceptable approximation when the system oscillates with high frequencies. However, for low frequency oscillations, there are not enough samples to have a good approximation and forecasting. Hence, Eq. (3.5) does not hold. Therefore, existing forecasting methods [8,84] fail to predict the post-bifurcation regime.

To address this issue, a novel method is proposed in this section. This method approximates the instantaneous recovery rate using all of the points in the measurements not only the local maxima. Hence, unlike previous approaches, forecasting is possible for system recoveries with low-frequency oscillations. Furthermore, the proposed method is generalized for forecasting bifurcations in large-dimensional systems that resolves another limitation of previous methods. For this purpose, the proposed approach uses a data-based modal decompositions technique.

In general, in a large-dimensional nonlinear system there can be several active modes in the measured system recovery from perturbations. However, in the great majority of Hopf bifurcations, only one pair of conjugate eigenvalues is involved in the bifurcation. That means only one of the system modes causes the bifurcation (Fig. 3.5). This holds for a large category of systems experiencing co-dimension one bifurcations. Hence, one mode experiences CSD whereas the other modes do not. Thus, the effects of these other modes are detrimental for forecasting.

Their presence distorts the analysis of the part of the dynamics that critically slows down. Hence, these models should be filtered out and neglected in forecasting. Filtering is done to enhance the accuracy of forecasting especially for large-dimensional systems.

For most co-dimension one Hopf bifurcations observed in practice, the center space is two-dimensional, namely only one complex conjugate pair of eigenvalues of the Jacobian of the dynamics crosses the imaginary axis (Fig. 3.5). The two-dimensional center space leads to a two-dimensional inertial manifold (a two-dimensional nonlinear manifold). This manifold is tangent to the (two-dimensional) center space of the system. The center space is a good approximation of the inertial manifold near the bifurcation. Thus, one can project the dynamics of the system on the center space, and capture and study the CSD behavior in this space for forecasting when the system is close to the bifurcation (Fig. 3.6).

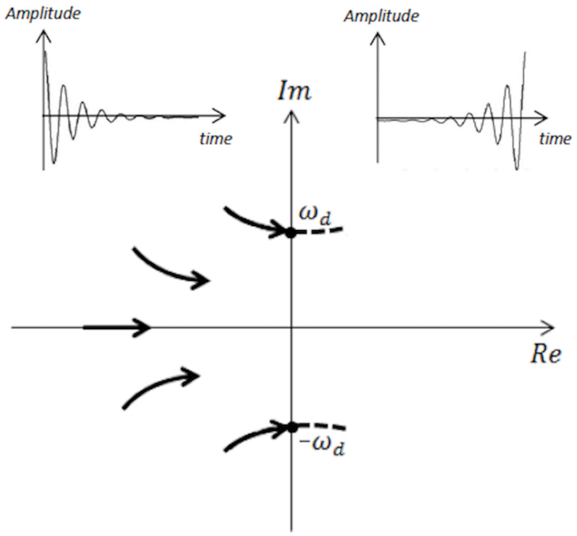

Figure 3.5. Real and imaginary parts of the eigenvalues of the system dynamics near a fixed point that is involved in a Hopf bifurcation; the change in the imaginary part is small when the eigenvalues traverse the zero real part axis

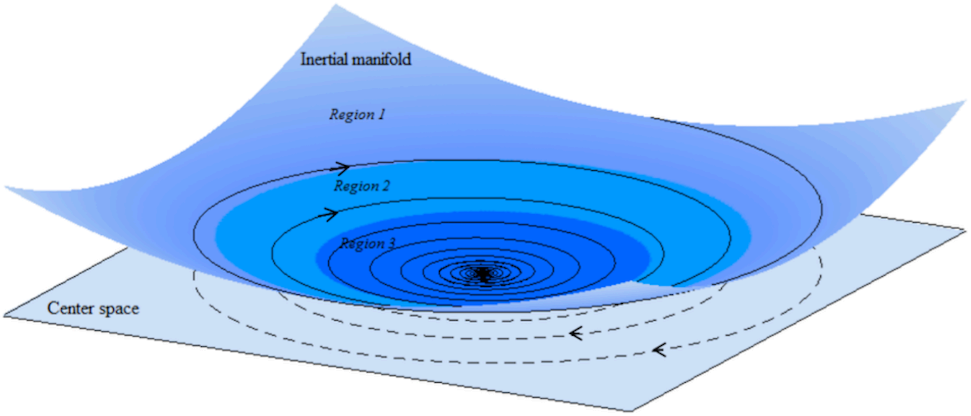

Figure 3.6. Schematic of the system dynamics on the inertial manifold and its projection on the center space; several regions are labeled and for forecasting using the piecewise modal decomposition approach

A basis in the center space can be obtained by using the linear modes of the system close to the bifurcation. Note that the forecasting method is model-less. That means that a mathematical model of the system is not needed (or not available) for forecasting. Hence a data-based / measurement-based modal decomposition technique is employed to obtain a basis for the center space. Once the basis is found, the bifurcating mode can be analyzed separately from the other modes. The bifurcating mode is a complex eigenvector computed at the bifurcation parameter that is closest to the bifurcation point. This mode is used for the other parameter values. The implication is that the center space and the inertial manifold are assumed to vary only weakly with the parameter. Hence, the dynamics of the system is projected onto the space spanned by the real and the imaginary components of the complex eigenenvector so that the unwanted modes (not involved directly in the bifurcation) are filtered out.

There are several measurement-based approaches that can be used to extract modal parameters and mode shapes. In this study, we use the eigensystem-realization algorithm (ERA).

ERA is a time domain multiple-input multiple-output algorithm based on the Hankel matrix of the dynamics and its singular value decomposition. The fundamentals of this method can be found in the literature [71,74,75]. Since we apply the forecasting method close to a bifurcation, the mode corresponding to the pair of eigenvalues with the largest real part represents the mode that causes the bifurcation.

Now, consider a nonlinear dynamical system. Let Φ be the matrix of eigenvectors of the system extracted from a measurement-based modal decomposition as

$$\Phi = \left[\phi_{1,R}\ \ \phi_{1,I}\ \ \phi_{2,R}\ \ \phi_{2,I}\ \ \dots\ \phi_1\ \ \phi_2\ \dots\right], \tag{3.6}$$

where $\phi_{i,R}$ and $\phi_{i,I}$ are real and imaginary parts of the eigenvector corresponding to the *ith* oscillating mode, and ϕ_n is the eigenvector corresponding to the *nth* non-oscillating mode of the system. Using Eq. (6) one can define the transformation

$$\mathrm{x} = \Phi \mathrm{q}\,, \tag{3.7}$$

where x is a vector of measured states of system, and q is a vector of modal coordinates expressed as

$$\mathrm{q} = \left[q_{1,R}(t)\ \ q_{1,I}(t)\ \ q_{2,R}(t)\ \ q_{2,I}(t) \dots\ \ q_1(t)\ \ \ q_2(t)\ \ \dots\right]^{\mathrm{T}}. \tag{3.8}$$

In Eq. (3.8), $q_{i,R}(t)$ and $q_{i,I}(t)$ are real and imaginary parts of the modal coordinate corresponding to the *i*th oscillating mode, and q_n is the modal coordinate corresponding to *n*th non-oscillating mode. For example, in the next section we consider a nonlinear aeroelastic system where x contains the pitch and plunge displacements and their velocities as measured states.

Suppose that the i^{th} oscillating mode is the mode involved in a Hopf bifurcation. To separate the effect of this mode from the other modes in the state variables one can define a vector of decomposed state variables as

$$\mathrm{x_i}(t) = \phi_{i,R} q_{i,R}(t) + \phi_{i,I} q_{i,I}(t), \tag{3.9}$$

$q_{i,R}(t)$ and $q_{i,I}(t)$ contain an exponential decay and oscillations at ω_i which is the identified frequency of bifurcating mode. In mechanical systems, $q_{i,R}(t)$ and $q_{i,I}(t)$ form a spiral in the $q_{i,R} - q_{i,I}$ plane, and they have the same decay rate. Here, one may define a function $h(t)$ as

$$h(t) = \sqrt{q_{i,R}^2(t) + q_{i,I}^2(t)}\,. \tag{3.10}$$

The function $h(t)$ can be interpreted as a modal amplitude in the $q_{i,R} - q_{i,I}$ plane. Moreover, $h(t)$ decays at the same rate as $q_{i,R}$ and $q_{i,I}$. The corresponding vectors $\phi_{i,R}$ and $\phi_{i,I}$ may be chosen in such a way that $q_{n,R}(t)$ and $q_{n,I}(t)$ are in quadrature by simply selecting them as the real and imaginary parts of the complex eigenvector. Then, $h(t)$ is a non-oscillatory function which has the approximate form of $h(t) = h_0 e^{\lambda(h)t}$, where $\lambda(h)$ is the recovery rate. This rate is very important since it contains the CSD information. For a mechanical system (governed by a system of second order differential equations for the generalized coordinates), $q_{i,R}$ and $q_{i,I}$ are in quadrature when the bases of the center space are chosen to be position and velocity. Thus, the modal coordinates involved in the bifurcation may be approximated in the following form (see Appendix A for more details)

$$
\begin{aligned}
q_{i,R}(t) &\approx a(t)\cos\big(\omega_i t - \beta(t)\big), \\
q_{i,I}(t) &\approx a(t)\sin\big(\omega_i t - \beta(t)\big).
\end{aligned}
\tag{3.11}
$$

Note that $h(t)$ computed from Eq. (10) may have small oscillations due to nonlinearities and the presence of multiple harmonics in the modal coordinates. These oscillations, although small, may cause difficulties and errors in the forecasting procedure. To resolve this issue and ensure that the function $h(t)$ is free of oscillations, a frequency filter (using Fourier transforms) is used to separate the components of frequency of ω_i from $q_{i,R}(t)$ and $q_{i,I}(t)$, and to filter out the effects of the higher frequencies.

Using Eqs. (3.9), (3.10) and (3.11), an amplitude $r_j(t)$ can be defined such that it passes through the local maxima of the *jth* degree of freedom (i.e., position and velocity) of the decomposed (filtered) state vector $\mathrm{x_i}(t)$ as

$$
r_j(t) = h(t)\sqrt{{\phi_{i,R}^{j}}^{2} + {\phi_{i,I}^{j}}^{2}} \;, \tag{3.12}
$$

where $h(t)$ is expressed as in Eq. (3.10), while $\phi_{i,R}^{j}$ and $\phi_{i,I}^{j}$ is the *jth* element of the vectors $\phi_{i,R}$ and $\phi_{i,I}$ which correspond to the *jth* degree of freedom . All values on the right hand side of Eq. (3.12) are extracted from measurements (after modal decomposition). Therefore, $r_j(t)$ can be identified using measured data. The factor $\sqrt{{\phi_{i,R}^{j}}^{2} + {\phi_{i,I}^{j}}^{2}}$ in Eq. (3.12) is a constant, and $h(t)$ contains the recovery rate and the CSD information of the system. In addition, $r_j(t)$ is a non-oscillating decaying function containing the CSD information that passes through the local maxima of the *jth* degree of freedom with a good accuracy.

Next, the forecasting method described for non-oscillating recoveries is applied to $r_j(t)$ functions obtained from system recoveries at different parameter values μ to forecast the post-bifurcation dynamics of the j^{th} degree of freedom. The important feature of this method is that $r_j(t)$ is approximated using all of the measurements, not only the local maxima. This approach has the significant advantage of being applicable in cases of low-frequency oscillations where using local maxima does not provide enough data for estimating the recovery rate. The proposed approach separates the effects of the bifurcating mode from the measurements by using the shapes of the modes. That holds even if modes very close in frequency to the bifurcating mode. Nonetheless, one may also use other experimental techniques to approximate $r_j(t)$ depending on the application, such as a method presented in ref. [90], when the active modes in measurements are separated enough in frequency.

For a mechanical system, the decaying amplitude $r_j(t)$ and the corresponding recovery is estimated for each degree of freedom. Choosing this amplitude implies use of local maxima (peaks) which is equivalent to choosing a fixed phase of the spiral trajectory of the system in the center space during a recovery. Since the inertial manifold is assumed to change very little with the parameter in the forecasting region, it is expected that the maximum amplitudes of the post-bifurcation limit cycles occur at the same chosen phase. Figure 3.7 shows schematically a bifurcation diagram in three dimensions for a two-degree of freedom system, where x_1 and x_2 are the degrees of freedom, and μ is the bifurcation parameter. The red lines are the usual (two dimensional) bifurcation diagrams for x_1 and x_2 which correspond to the local maxima (peaks) in the time series for x_1 and x_2. The proposed approach forecasts separately these two red lines by using time series for x_1 and x_2, respectively.

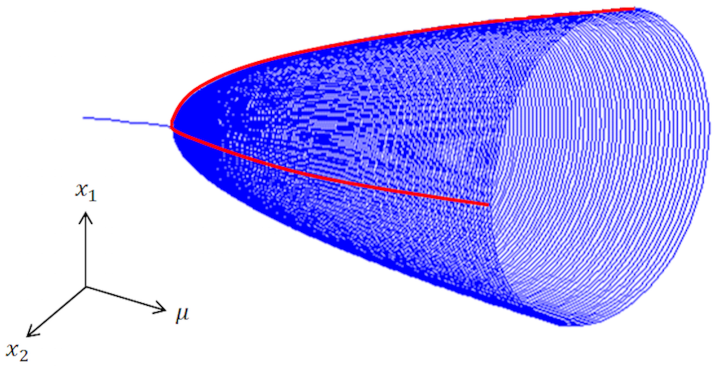

Figure 3.7. Schematic of the three dimensional bifurcation diagram showing the limit cycle oscillations in post bifurcation regime at each bifurcation parameter μ; blue lines show the entire diagram, whereas the red lines show the separately forecasted diagrams for x_1 and x_2 states.

For very large perturbations, forecasting the bifurcation diagram based on the projected dynamics on the center space may have errors for large state amplitudes. This is because the motion at larger amplitudes corresponds to regions of the inertial manifold that are farther from the fixed point (contact point between the center space and the inertial manifold) as shown in Fig. 3.6. As a result, the difference between the inertial manifold and the center space may not be negligible at large amplitudes. Note that this does not mean that the center space does not capture the system dynamics and the CSD for large amplitudes. Using projection on the center space still results in an accurately forecasted bifurcation type, post bifurcation dynamics for smaller amplitudes, and all of the critical speeds. However, forecasted larger amplitudes in the bifurcation diagram may have errors compared to the actual behavior of the system in the post-bifurcation regime.

To address this, one may use a piecewise modal decomposition approach. In this approach, the inertial manifold is divided into several regions (3 are shown as an example in Fig. 3.6) based on the maximum amplitudes of the dynamics. For each region, one may apply a separate modal decomposition using ERA and obtain a basis for the tangent space of that region. Then, the dynamics is projected to the tangent space spanned by this basis in each region. This approach gives a better approximation for the larger state amplitudes since the difference between each region and the approximated tangent space is less than using the center space for all regions. Note that the tangent space for the last region (region 3 in Fig. 3.6 containing smaller amplitudes) is the same as previously defined center space.

3.3 Aeroelastic model

The proposed method is applied to forecast supercritical and subcritical flutter in a nonlinear aeroelastic system. The parameters and notation used in the analysis are shown in Fig. 3.8. The system oscillates in pitch and plunge. In Fig. 3.8, α is the pitch angle and h is the plunge displacement. The free-stream velocity is the bifurcation parameter. The system is exposed to gusts that create perturbations the equilibrium of the airfoil. The recovery of the system from these perturbations is measured and used for forecasting. The equations can be written as [65]

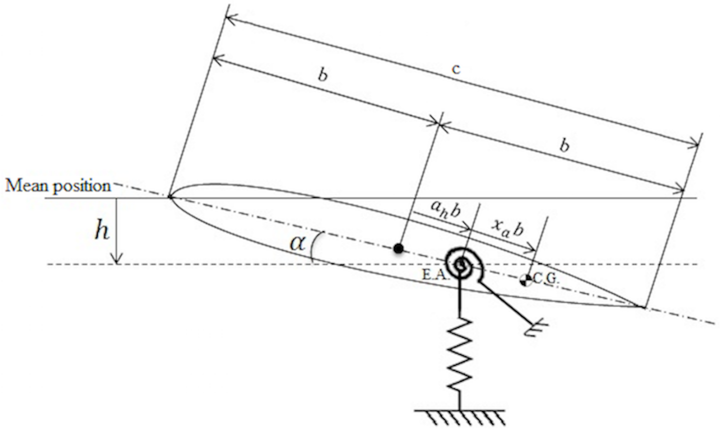

Figure 3.8. Two-degree-of freedom nonlinear aeroelastic model showing an airfoil of chord c. EA is aeroelastic axis (at a distance $a_h b$ from the mid-chord), CG is center or mass (at a distance $x_a b$ from the EA), and α and h are the pitch and plunge coordinates.

$$\begin{aligned}&\ddot{\xi} + x_\alpha \ddot{\alpha} + \frac{2\zeta_\xi \bar{\omega}}{U^*}\dot{\xi} + \left(\frac{\bar{\omega}}{U^*}\right)^2 G(\xi) = -\frac{C_L(\tau)}{\pi\mu} - P_g(\tau),\\ &\frac{x_\alpha}{r_\alpha^2}\ddot{\xi} + \ddot{\alpha} + \frac{2\zeta_\alpha}{U^*}\dot{\alpha} + \frac{1}{U^{*2}}M(\alpha) = \frac{2C_M(\tau)}{\pi\mu r_\alpha^2} + Q_g(\tau)\,,\end{aligned} \tag{3.13}$$

where α is the pitch angle, $\xi = \frac{h}{b}$ is the non-dimensional plunge displacement, $\tau = \frac{Ut}{b}$ is the normalized time, and the overdot indicates differentiation with respect to τ. U is the free-stream velocity, and $U^* = U/(b\omega_\alpha)$ is the non-dimensional free-stream velocity, which is used as bifurcation parameter. $\bar{\omega} = \omega_\xi/\omega_\alpha$ is the ratio of the natural frequencies ω_ξ and ω_α of the uncoupled plunge and pitch motions. ζ_α and ζ_ξ are the damping ratios in the structure. r_α is the radius of gyration about the elastic axis. $G(\xi)$ and $M(\alpha)$ are the structural elastic torque and elastic force created by pitch and plunge ; they contain structural nonlinearities of the system as

$$\begin{aligned}&M(\alpha) = \alpha + m_3\alpha^3 + m_5\alpha^5\,,\\ &G(\xi) = \xi + g_3\xi^3 + g_5\xi^5\,.\end{aligned} \tag{3.14}$$

Functions $C_L(\tau)$ and $C_M(\tau)$ are the lift and pitching moment coefficients. These coefficients are given by Fung et al. [76] for incompressible flow as

$$\begin{aligned}C_L(\tau) = {}& \pi(\xi - a_h\alpha + \alpha) + 2\pi\left(\alpha(0) + \xi(0) + \left(\frac{1}{2} - a_h\right)\alpha(0)\right)\phi(\tau)\\ &+ 2\pi\int_0^\tau \phi(\tau - \sigma)\left(\alpha(\sigma) + \xi(\sigma) + \left(\frac{1}{2} - a_h\right)\alpha(\sigma)\right)d\sigma,\end{aligned}$$

$$\begin{aligned}C_M(\tau) = {}& \pi\left(\frac{1}{2} + a_h\right)\left(\alpha(0) + \xi(0) + \left(\frac{1}{2} - a_h\right)\alpha(0)\right)\phi(\tau)\\ &+ \pi\left(\frac{1}{2} + a_h\right)\int_0^\tau \phi(\tau - \sigma)\left(\alpha(\sigma) + \xi(\sigma) + \left(\frac{1}{2} - a_h\right)\alpha(\sigma)\right)d\sigma\\ &+ \frac{\pi}{2}a_h(\xi - a_h\alpha) - \left(\frac{1}{2} - a_h\right)\frac{\pi}{2}\alpha - \frac{\pi}{16}\alpha\,,\end{aligned} \tag{3.15}$$

where $\phi(\tau)$ is the Wagner's function. A well-known approximation for $\phi(\tau)$ is given by [76]

$$\phi(\tau) = 1 - A_1 e^{-\epsilon_1 \tau} - A_2 e^{-\epsilon_2 \tau}, \tag{3.16}$$

with $A_1 = 0.165$, $A_2 = 0.335$, $\epsilon_1 = 0.0455$ and $\epsilon_2 = 0.3$.

$P_g(\tau)$ and $Q_g(\tau)$ in Eq. (13) are the lift force and pitch moment due the gust profile, and are given by the following expressions [77]

$$\begin{aligned} P_g(\tau) &= \frac{2}{\mu}\int_0^\tau \psi(\tau-\sigma) w_G(\sigma) d\sigma, \\ Q_g(\tau) &= \frac{2}{\mu r_\alpha^2}\left(\frac{1}{2}+a_h\right)\int_0^\tau \psi(\tau-\sigma) w_G(\sigma) d\sigma, \end{aligned} \tag{3.17}$$

where w_G is vertical gust velocity distribution, and ψ is the Kussner function [77].

Because of the existence of the integral terms in these governing equations, it is difficult to study the dynamic behavior of the system analytically. Instead, a system augmentation is used by introducing four new augmented variables as follows [65]

$$\begin{aligned} w_1 &= \int_0^\tau e^{-\epsilon_1(\tau-\sigma)}\alpha(\sigma)d\sigma \ , w_2 = \int_0^\tau e^{-\epsilon_2(\tau-\sigma)}\alpha(\sigma)d\sigma\,, \\ w_3 &= \int_0^\tau e^{-\epsilon_1(\tau-\sigma)}\xi(\sigma)d\sigma \ , w_4 = \int_0^\tau e^{-\epsilon_2(\tau-\sigma)}\xi(\sigma)d\sigma. \end{aligned} \tag{3.18}$$

Now, one may introduce a state variable vector $\mathbf{x} = [x_1, x_2, \dots, x_8]^T$, with namely $x_1 = \alpha$, $x_2 = \dot{\alpha}$, $x_3 = \xi$, $x_4 = \dot{\xi}$, $x_5 = w_1$, $x_6 = w_2$, $x_7 = w_3$, $x_8 = w_4$. With this notation, Eq. (3.13) can be written as a set of 8 first order ordinary differential equations as follows

$$\dot{\mathbf{x}} = \boldsymbol{f}(\mathbf{x}, U^*, \tau), \tag{3.19}$$

The components of this set of augmented governing equations can be written as follows

$$\dot{x}_1 = x_2,\ \dot{x}_3 = x_4,$$

$$\begin{aligned} x_2 &= a_{21}x_1 + (a_{22} - 2jc_0\zeta_\alpha \frac{1}{U^*})x_2 + a_{23}x_3 + (a_{24} + 2jd_0\zeta_\xi \frac{\bar{\omega}}{U^*})x_4 + a_{25}x_5 + a_{26}x_6 + a_{27}x_7 + a_{28}x_8 \\ &+ j\left(d_0(\frac{\bar{\omega}}{U^*})^2 G(x_3) - c_0(\frac{1}{U^*})^2 M(x_1) \right) + j\left(c_0 g(\tau) - d_0 f(\tau)\right), \end{aligned}$$

$$\begin{aligned} x_4 &= a_{41}x_1 + (a_{42} + 2jc_1\zeta_\alpha \frac{1}{U^*})x_2 + a_{43}x_3 + (a_{44} - 2jd_1\zeta_\xi \frac{\bar{\omega}}{U^*})x_4 + a_{45}x_5 + a_{46}x_6 + a_{47}x_7 + a_{48}x_8 \\ &+ j\left(c_1(\frac{1}{U^*})^2 M(x_1) - d_1(\frac{\bar{\omega}}{U^*})^2 G(x_3) \right) + j\left(d_1 f(\tau) - c_1 g(\tau)\right), \end{aligned} \tag{3.20}$$

$$\dot{x}_5 = x_1 - \varepsilon_1 x_5,\ \dot{x}_6 = x_1 - \varepsilon_2 x_6,\ \dot{x}_7 = x_3 - \varepsilon_1 x_7,\ \dot{x}_8 = x_3 - \varepsilon_2 x_8,$$

and where coefficient a_{ij} can be found in [65], and the functions $f(\tau)$ and $g(\tau)$ are given by

$$\begin{aligned} f(\tau) &= \frac{2}{\mu}((\frac{1}{2} - a_h)\alpha(0) + \xi(0))(A_1\varepsilon_1 e^{-\varepsilon_1\tau} + A_2\varepsilon_2 e^{-\varepsilon_2\tau}) - P_g(\tau) = f'(\tau) - P_g(\tau), \\ g(\tau) &= -\frac{(1+2a_h)}{2r_\alpha^2} f'(\tau) + Q_g(\tau). \end{aligned} \tag{3.21}$$

The aerodynamic part of the model raises the dimensionality of the system from a two-degree-of-freedom system to to a more complex 8-dimensional nonlinear one. In the following, Eq. (3.20) is used to obtain surrogate measurements of time-series of recoveries from the perturbations induced by gusts in the pre-bifurcation regime. The effects of the gust (i.e., $P_g(\tau)$ and $Q_g(\tau)$) are applied and the system response to gust is collected after the gusts subside.

It is worth recalling that the actual model in Eq. (3.20) is not needed for forecasting the bifurcation diagram. The only input to the algorithm is the transient time data measured from sensors (or surrogate data from numerical simulations). Hence, the actual model in Eq. (3.20) is used only for generating surrogate measurement data to demonstrate the forecasting method.

3.4 Results and discussion

In this section, the forecasting method is demonstrated for the nonlinear aeroelastic system presented in the previous section. Depending on the values of the structural nonlinearities, the system may face supercritical or subcritical flutters. Each are considered next.

To perturb system in the pre-bifurcation regime, wind gusts of a "*1-cos*" type are used as perturbations [91]. The vertical gust velocity distribution is zero except for a time interval $0 \le \tau \le 2\tau_G$ where it is given by

$$w_G(\tau) = \frac{w_0}{2}\left(1 - \cos\frac{\pi\tau}{\tau_G}\right), \tag{3.22}$$

where $w_G(\tau)$ is the vertical gust velocity at ¼ chord, w_0 is the gust intensity, and τ_G is the gust gradient. Then, the governing equations in Eq. (3.20) are solved by time marching.

After the airfoil passes the gust, i.e. at times after $\tau = 2\tau_G$, the system response to the gust perturbation is recorded. This transient response can be used as surrogate data to demonstrate the forecasting method.

For modal decomposition, we measure the pitch and plunge and their velocities (i.e., α, $\dot{\alpha}$, ξ, and $\dot{\xi}$). These values are input to the ERA method to extract the modal parameters of the system. Hence, the vector x in Eq.(3.7) is $\mathrm{x} = \left[\alpha(\tau), \dot{\alpha}(\tau), \xi(\tau), \dot{\xi}(\tau)\right]^T$.

3.4.1 Supercritical bifurcations

In this case, the parameters used for the aeroelastic system are $r_\alpha = 0.7$, $\bar{\omega}^2 = 0.08$, $a_h = -0.5$, $x_\alpha = 0.25$, $\mu = 100$, $\zeta_\xi = \zeta_\alpha = 0$. The nonlinearity is described by parameters

$m_3 = 2$, $m_5 = 0$, $g_3 = 0$ and $g_5 = 0$ in Eq. (3.14). This set of parameters create supercritical bifurcations in the system. Three free-stream velocities are considered in pre-bifurcation regime, namely $U^* = 7.55, 7.50$ and 7.45. The applied gust parameters are chosen to be $w_0 = 0.2$ and $\tau_G = 10$.

For modal decomposition, the ERA approach is used at $U^* = 7.55$ as that is the available free-stream velocity closest to the bifurcation point. The modal properties (e.g., frequencies, mode shapes) obtained from the ERA approach are used for other flow speeds as well. Next, the forecasting steps presented in Section 2 are applied to collected measurements of pitch and plunge. Figure 3.9 shows the decomposed pitch displacement and the corresponding pitch amplitude $r(t)$ at $U^* = 7.45$. The amplitude $r(t)$ follows the local maxima of the time data with good accuracy. This function is obtained for all of the parameter values that are used for forecasting, as described in Section 3.2. Figure 3.10 shows the plot of $U^* - \lambda$ obtained from Eq. (3.6) for pitch. In this figure, the intersection of each curve and the horizontal axis is the forecasted U^* in the post-bifurcation regime for its corresponding pitch amplitude.

Figure 3.11 shows the actual and the predicted bifurcation diagrams for pitch and plunge displacements. As the results show, the proposed method predicts the post-bifurcation dynamics accurately. Figure 3.12 shows the exact three-dimensional bifurcation diagram of this system in the pitch-plunge-flow-speed space. The forecasted diagrams shown in Fig. 3.11 correspond to the maximum pitch and plunge amplitudes of limit cycle oscillations (similar to the bifurcations shown in Fig. 3.12 for a generic two-degree of freedom system with displacements x_1 and x_2).

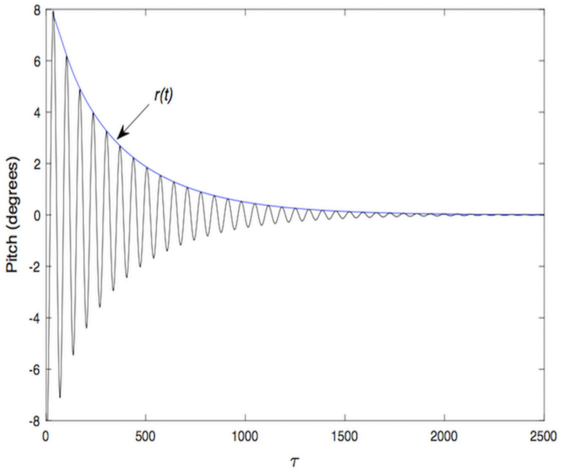

Figure 3.9. Approximated amplitude $r(t)$ for pitch at $U^* = 7.45$

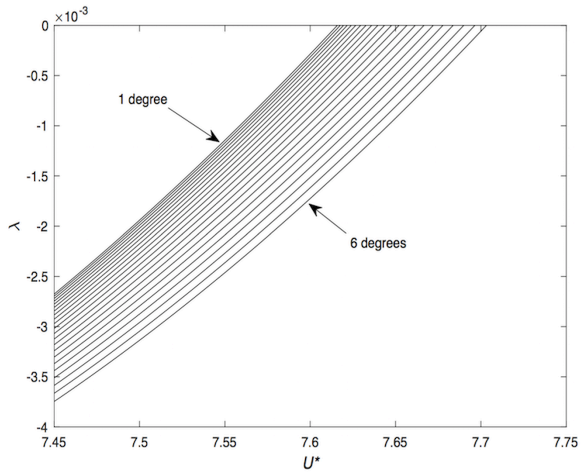

Figure 3.10. Recovery rate λ versus free-stream flow speed $U*$ for prediction of the post-bifurcation dynamics at several pitch amplitudes

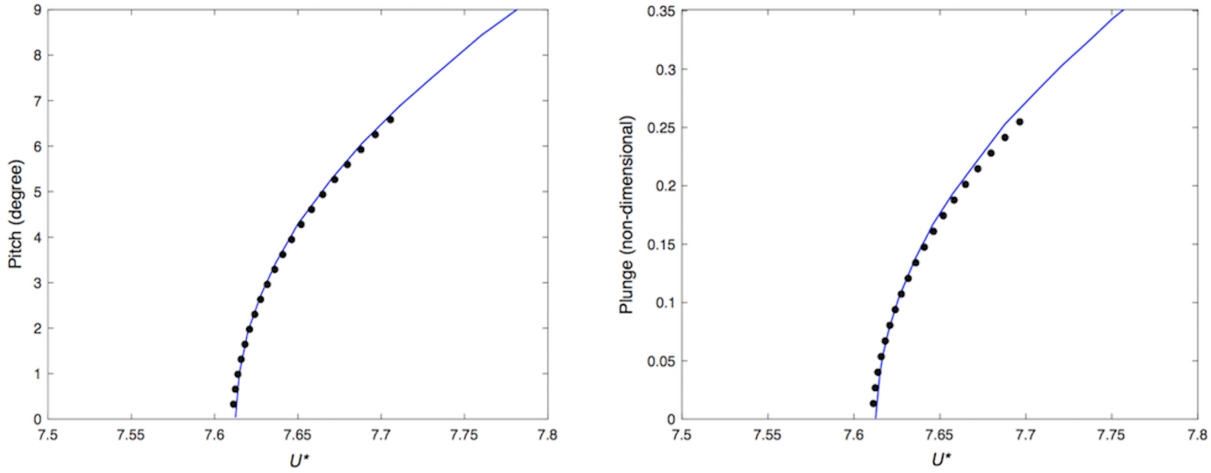

Figure 3.11. Exact (-) and forecasted (•) bifurcation diagrams for pitch (left) and plunge (right) in a supercritical case

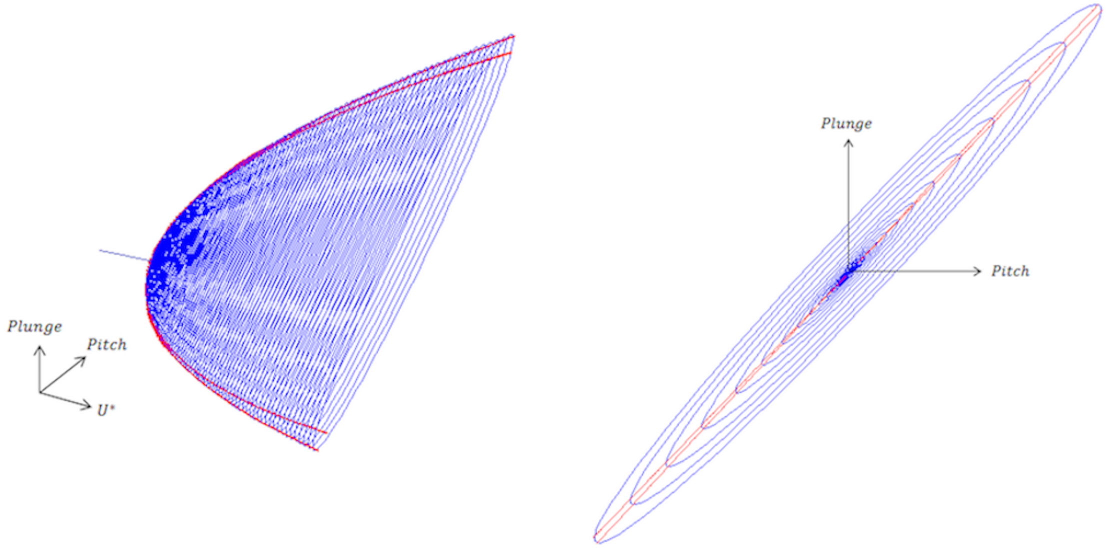

Figure 3.12. Three dimensional bifurcation diagram showing the limit cycle oscillations in the post bifurcation regime at each free-stream flow velocity (left); and a view of the pitch-plunge plane of the diagram (right); blue lines show limit cycles at each free-stream flow velocity; red lines show separately forecasted pitch and plunge diagrams

As another example, we consider next an aeroelastic system that oscillates with low frequency while recovering from perturbations in the pre-bifurcation regime. The system parameters used for this system are $r_\alpha = 0.4$, $\bar{\omega}^2 = 0.01$, $a_h = -0.5$, $x_\alpha = 0.25$, $\mu = 300$, $\zeta_\xi = \zeta_\alpha = 0$ and the coefficients of the nonlinearities are parameters $m_3 = 2$, $m_5 = 0$, $g_3 = 0$, $g_5 = 0$.

Similar to the previous example, the system is perturbed using a gust load at three bifurcation parameter values $U^* = 9.32, 9.30$ and 9.28. The system recovery from perturbations at $U^* = 9.28$ is shown in Fig. 3.13. It can be seen that the system oscillates with a lower frequency during its recovery compared to the previous case. Hence, methods based only on the local maxima fail to predict the actual recovery rate of the system. However, the proposed method works and is applied to forecast the post-bifurcation regime. The forecasting results are shown in Fig. 3.14.

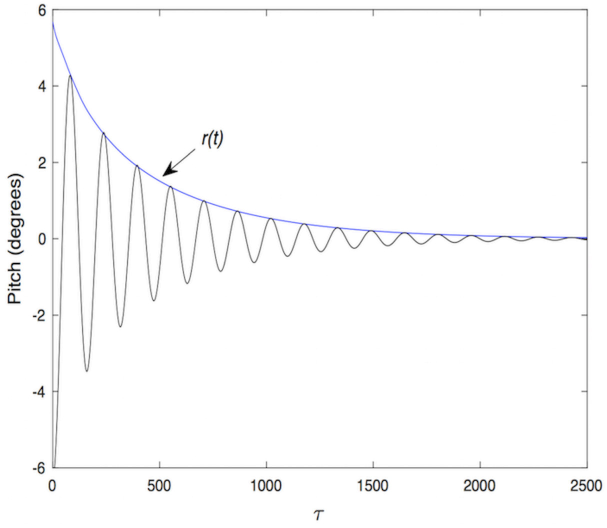

Figure 3.13. Approximated amplitude $r(t)$ for pitch at $U^* = 9.28$ for a slow-oscillating system in a supercritical case

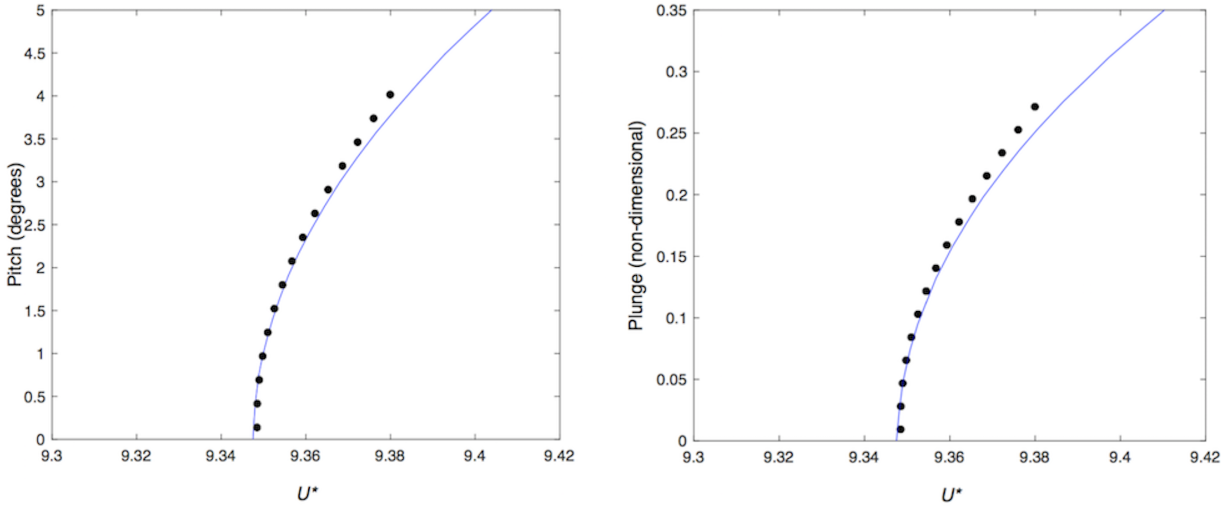

Figure 3.14. Exact (-) and forecasted (•) bifurcation diagram for pitch (left) and plunge (right) displacements for a slow-oscillating system in a supercritical case

3.4.2 Subcritical bifurcations

Forecasting subcritical bifurcations such as subcritical flutter has a great importance since this type of bifurcations causes sudden changes in the dynamics of the system. To demonstrate the effectiveness of the proposed forecasting approach for subcritical flutter, the values of the coefficients in Eq. (3.14) are chosen as $m_3 = -1.5, m_5 = 50, g_3 = 0, g_5 = 0$, and the system parameters are chosen as $r_\alpha = 0.7$, $\bar{\omega}^2 = 0.08$, $a_h = -0.5$, $x_\alpha = 0.25$, $\mu = 100$, $\zeta_\xi = \zeta_\alpha = 0$. Perturbations are applied to the system at U^* =7.55, 7.50 and 7.45 in the pre-bifurcation regime. In this case, the system is perturbed with a large intensity, which induces larger perturbations enabling the proposed method to forecast a larger range of the bifurcation diagram.

To forecast a bifurcation diagram, the dynamics in the pre-bifurcation regime are projected on the center space, and the forecasting method is employed. Results obtained for pitch and plunge displacements are shown in Fig. 3.15. The exact bifurcation diagrams contain unstable limit cycles. These limit cycles were obtained using a shooting method [92,93]. It can be observed that the bifurcation diagram for pitch is forecasted accurately. However, the bifurcation diagram forecasted for plunge has some error at large amplitudes.

The error at large amplitudes is not large and can be further reduced by partitioning the inertial manifold in several regions and using separate projections based on modes determined by ERA in separate amplitude ranges. When the applied perturbations are large, the response of the system to the perturbations is large as well. Therefore, the forecasted large amplitudes of the bifurcation diagrams for some of the degrees of freedom may have errors, and a local modal decomposition can be used to improve forecasting accuracy. Here, three regions are considered (as shown in Fig. 3.6) based on the measured amplitudes of pitch and plunge. Using the forecasting method, the forecasted bifurcation diagram for plunge displacement is shown in Fig. 3.16. As the results show, the post-bifurcation dynamics for plunge is forecasted accurately in this case. It can be observed also that the type of bifurcation is clearly predicted to be subcritical. This is an important advantage of the forecasting method because in the case of subcritical bifurcations the system stability will change dramatically, and that may result in system damage. Forecasting the critical points and the type of upcoming bifurcations is a significant result.

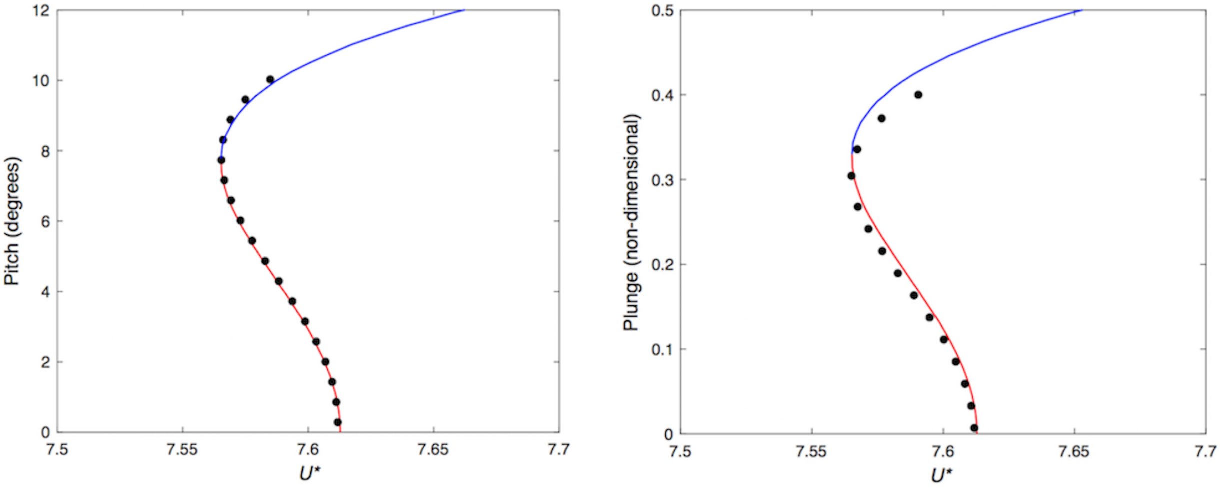

Figure 3.15. Exact (-) and forecasted (•) bifurcation diagrams for pitch (left) and plunge (right) displacements in a subcritical case without partitioning the inertial manifold; blue and red lines show stable and unstable parts of the bifurcation diagrams, respectively

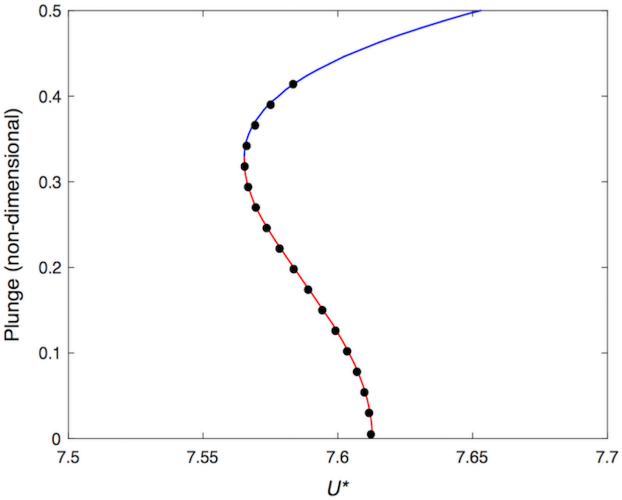

Figure 3.16. Exact (-) and forecasted (•) bifurcation diagrams for plunge displacements in a subcritical case with partitioning the inertial manifold; blue and red lines show stable and unstable parts of the bifurcation diagram, respectively

3.4.3 Effects of measurement noise

Measurement noise are an inseparable part of experiments. In this section, the accuracy of the forecasting method is examined in presence of measurement noise. In the case of supercritical bifurcations (e.g., the case where $m_3 = 2$, $m_5 = 0$, $g_3 = 0$ and $g_5 = 0$), 5% and 10% noise is added to the measurements, and the forecasting procedure is followed without noise filtering. Figure 3.17 shows the decaying function $r(t)$ computed for the pitch amplitude in the presence of 10% measurement noise at $U^* = 7.55$. To approximate the smooth decaying function from this noisy data, an approximation is used [3], where it is assumed that the recovery rate depends on the amplitude at a fixed bifurcation parameter as:

$$\lambda = \frac{\dot{r}}{r} = \lambda_0 + \lambda_1 r + \lambda_2 r^2, \tag{3.23}$$

where coefficients λ_i are constants chosen using optimization algorithm such that calculated $r - t$ solution of Eq. (3.23) best fits the data points available in the measured time history. Using this approach, a more precise approximation of recovery rate λ can be obtained, and a smooth decaying function is obtained as shown in Fig. 3.18. The approximation can be compared to the actual values (where there is no noise in the system), as shown in Fig. 3.18. As it can be observed, the results are very close to each other. Moreover, the decaying function obtained by simply connecting the local maxima of the noisy measurement is also shown in Fig. 3.18 to reveal that using only the local maxima for forecasting does not lead to accurate results in noisy measurements (in addition to the issues introduced by the low frequency oscillations discussed before).

The forecasted bifurcation diagrams of the pitch displacement are shown in Fig. 3.19. The same procedure is followed for subcritical bifurcations, and results are presented in Fig. 3.20. All results are presented as mean values with standard deviation error bars obtained from 20 separate forecasts. It is observed that the results match very well the exact bifurcation diagrams.

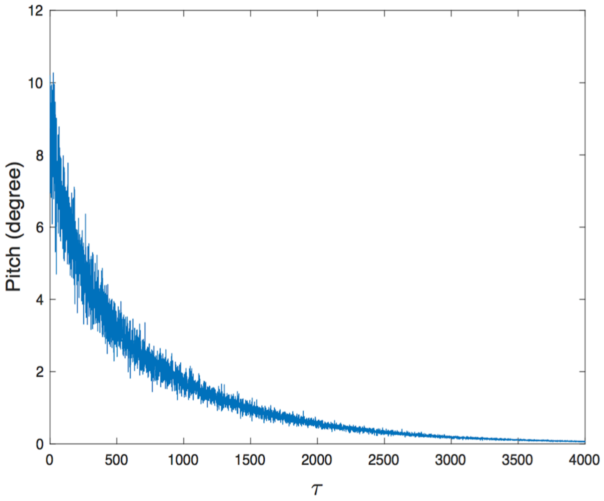

Figure 3.17. Noisy decaying function of the pitch displacement in the presence of 10% measurement noise measured at $U^* = 7.55$.

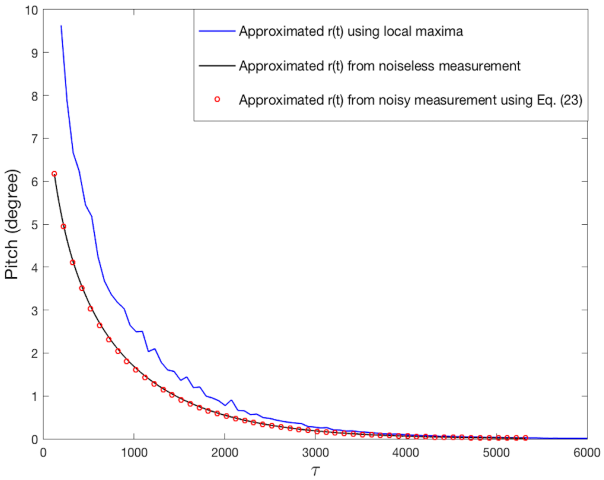

Figure 3.18. Comparison of the approximated decaying functions from noisy measurements and the approximated function from noiseless measurements as reference.

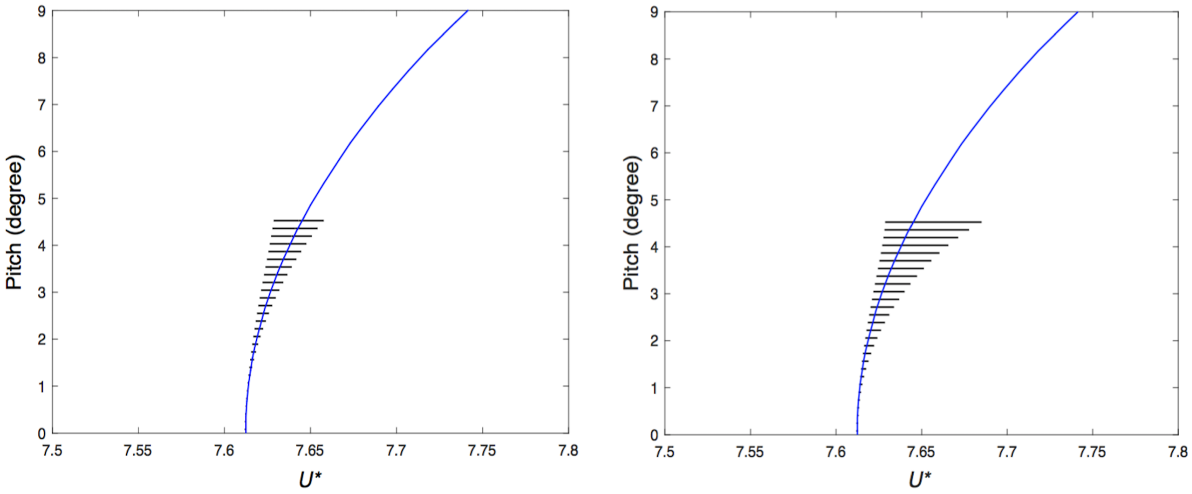

Figure 3.19. Exact and forecasted bifurcation diagrams for the pitch displacement in supercritical case and in presence of 5% (left) and 10% (right) measurement noise. Forecasted results are shown as mean values with standard deviation error bars obtained from 20 separate forecasts.

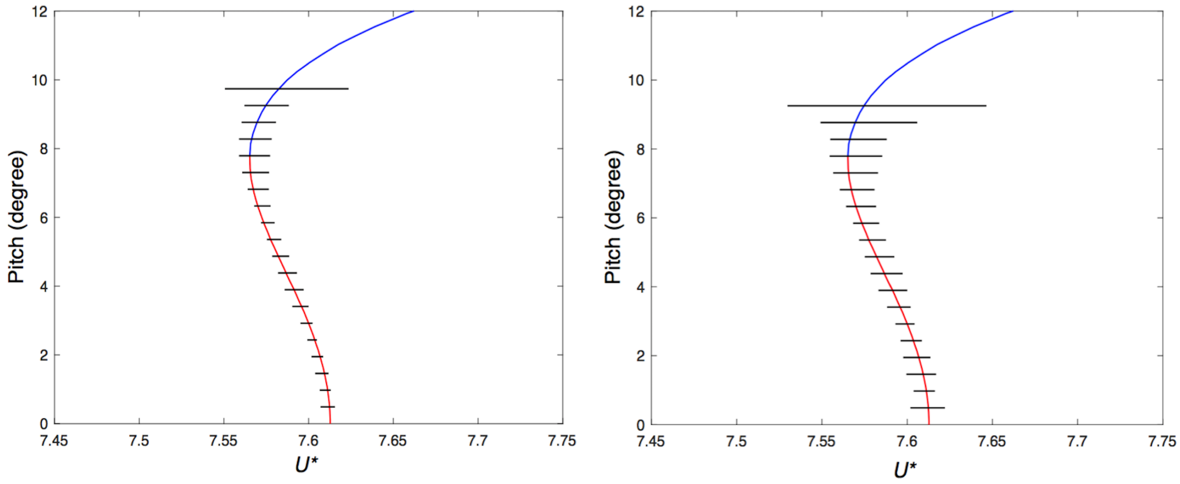

Figure 3.20. Exact and forecasted bifurcation diagrams for the pitch displacement in subcritical case and in presence of 5% (left) and 10%(right) measurement noise. Forecasted results are shown as mean values with standard deviation error bars obtained from 20 separate forecasts.

3.5 Conclusions

A novel forecasting method was presented to forecast Hopf bifurcations using measured system recoveries from perturbations only in the pre-bifurcation regime. The method is based on the critical slowing down phenomenon for oscillatory systems. A modal coordinate approach was introduced to extract smooth non-oscillating recovery of the system and the forecasting method was applied to this approximated recovery. The proposed technique can be used for forecasting bifurcations in large-dimensional systems and has high accuracy for forecasting bifurcations from large perturbations. Unlike previous approaches, the proposed method uses all measurements in oscillating recoveries (and not just local maxima) to find the recovery rate and forecast the bifurcation diagram. This ability results in higher accuracy in forecasting bifurcations when the system recovers to its stable state with low-frequency oscillations where the number of local maxima is not enough to have a good approximation for the recovery rate. Furthermore, this approach is more robust to measurement noise that affects especially the local maxima (peaks).

The method was applied to a nonlinear aeroelastic model in response to gust perturbations. Numerical simulations show that the method accurately predicts the bifurcation point and the post-bifurcation dynamics in both supercritical and subcritical cases despite the fact that it uses only pre-bifurcation regime data and it does not use a model of the system. Since dramatic changes can occur in the system dynamics at bifurcations, predicting the bifurcation type (i.e., its supercritical or subcritical characteristics) without placing the system in the post-bifurcation regime is a notable advantage. This forecasting opens the door to a variety of applications where knowledge of nearby bifurcations is important for safety and maximum system performance.

Chapter 4

Forecasting Critical Speed and Post-Critical Dynamics in Large Dimensional Fluid-Structural Systems

4.1 Introduction

A pervasive need for engineered systems when creating new designs is to improve the efficiency of existing systems while ensuring safety and reliability. Such new designs may be complex both in shape and dynamics, and often exhibit nonlinear behavior.

Studying the dynamics of nonlinear structures is an important engineering topic because such systems can exhibit a wide variety of possible behaviors. Hence, the dynamic response of such systems needs to be accurately evaluated under different operational conditions. More specifically, it is important to study the dynamic stability of systems when some of their parameters are varied, and that includes the study of their bifurcations. Bifurcations occur in the dynamics of complex nonlinear systems and lead to different types of instability problems.

There are many studies focused on analysis and identification of bifurcation diagrams in nonlinear systems. These methods apply to systems with a known model and vary from common time-marching [94,95], to normal forms and nonlinear normal modes [56,96], to multiple scales [54,97], and to harmonic balance [52,53], to name a few. Although these methods are well capable of identifying bifurcations and build their diagrams, they have drawbacks that make them difficult or impossible to use for a variety of large dimensional systems frequently encountered in real applications. First, these methods are model-based and creating an accurate model for the desired system can be infeasible or impractical especially when the system is exceedingly complex.

Second, even if a mathematical model is established, due to complex dynamics and nonlinearity, massive theoretical and numerical computations are required to analyze its dynamics. Furthermore, models may be incomplete or inaccurate due to assumptions and uncertainties as well as due to parameter variations over time, making the accurate representation of the system a challenge in itself.

Similar to theoretical and computational methods, experimental methods to determine bifurcations and bifurcation diagrams of complex systems have their own challenges. For example, some methods are only capable of predicting the bifurcation point [98]. Other methods include nonlinear analysis and system identification [99,100], but they need large sets of data and have difficulties in identifying complex nonlinear system parameters. Other approaches include set-and-observe methods [100], i.e. place the system in different operational conditions including the post-bifurcation regime to construct the bifurcation diagram. However, this is not an easy task and may also result in the collapse of the system.

Therefore, nonlinear analysis of large dimensional complex systems is still a unique challenge. To address this challenge and due to the importance of the topic, a new method of forecasting bifurcations has been introduced [8], and further developed [3] for large dimensional oscillatory systems. The approach is based on the phenomenon of critical slowing down which accompanies many bifurcation phenomena including flutter, i.e. when the systems is close to the bifurcations, perturbations lead to long transient oscillations before the system reach to its stable state. This approach is capable of forecasting not only the distance to bifurcations but also the dynamics of system in the post-bifurcation regime. The unique feature of the method is that it is model-less: no mathematical model of the system is required for forecasting. Hence, it is applicable to complex nonlinear systems where a model of the system is not available, or where analysis would require massive computations. To forecast the bifurcation diagrams using this method, one measures several system responses to perturbations in the pre-bifurcation regime. As a result, the method is computationally efficient and is safe in real applications since the system is never placed in the potentially dangerous post-bifurcation regime. In those previous studies, the bifurcation forecasting method was applied to forecast bifurcation diagrams in a feedback controlled beam [8] and ecological systems [88]. These have a different physical behavior than oscillatory, aeroelastic systems. The forecasting method was developed further to be applied to systems exhibiting Hopf bifurcations [101,102]. Challenges related to oscillatory systems were addressed. For example, the co-existence of several active modes the measurements was addressed in [89,101], and the need for a precise approximation of the recovery rate of slow oscillatory systems where the number of local peaks is very small and not enough for an accurate forecasting was accounted for in [102].

An important class of nonlinear complex engineering systems prone to subcritical and supercritical Hopf (flutter) bifurcations is the fluid-structural interaction [43,64–67]. These phenomena can cause dramatic changes in the system dynamics typically resulting in loss of performance is possible is total failure. Hence, one of the demanding topics of research in fluid-structure interactions is determining the speed above which the system becomes linearly unstable, i.e. determining the flutter speed. Furthermore, identifying the flutter type (supercritical and subcritical) and the limit cycle amplitude beyond the flutter speed are also important especially when operating close to the linear flutter boundary.

This research focuses on the forecast study to the problem of Hopf bifurcations in fluid-structural systems. The bifurcation forecasting method is employed to forecast bifurcation diagrams of a complex large dimensional fluid-structural model. The method is applied to forecast the flutter speed and bifurcation diagrams of a cantilever flexible high aspect ratio wing as an example of nonlinear large dimensional fluid-structural systems with complex fluid-structural interaction. The large dimensionality of the system causes modal interactions and allows for much more complex physical behaviors that those explored in [3,103]. Schematic of the forecasting approach is demonstrated in Fig. 4.1. The goal is to forecast the flutter speed and post-flutter dynamics of this large dimensional system using a few responses of the system to gust perturbations only in the pre-flutter regime.

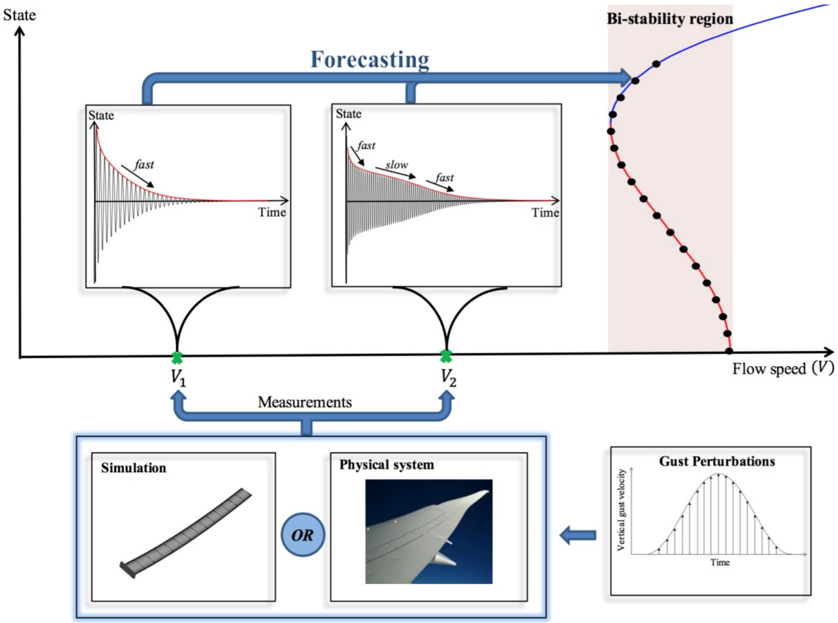

Figure 4.1. Schematic of the forecasting method for aeroelastic systems. Bifurcation diagrams are forecasted (black dots) by measuring a limited number of system responses to gust perturbations before the instability boundary.

4.2 Forecasting methodology

In this section, a bifurcation forecasting approach is introduced and adjusted to enable forecasting flutter bifurcations based on observations of the transient response of large-dimensional fluid-structural systems in the pre-bifurcation regime. Here, only the main changes made to previous approaches, and the main concepts and steps of the new forecasting method are described.

In fluid-structural systems with Hopf (flutter) bifurcations, the system oscillates during its recovery in response to perturbations in the pre-bifurcation regime. Its recovery rate from perturbations depends on the distance to the bifurcation, i.e. the difference between the current flow speed and the flutter speed. When system approaches the bifurcation, transient oscillations last longer before the system reaches equilibrium, which means that the rate of recovery decreases. This phenomenon is known as critical slowing down (Fig. 4.2). The proposed method uses this phenomenon to identify the distance to the bifurcation.

There are several requirements for the forecasting method to be accurate. A first requirement is that the system is close enough to the bifurcation as to exhibit measurable slowing down in its recoveries. Moreover, measurements containing identifiable parts are on the inertial manifold to ensure that changes in the recovery rates are due to the slowing down phenomenon. The inertial manifold is an invariant set where the dynamics is slowest in time and contains main features of the system. Thus, this manifold is the slowest, and if the system starts from a state in this set, it remains in that set at all times. A second requirement is that the system dynamics and its inertial manifold vary smoothly with the bifurcation parameter, which is the flow speed in the current study.

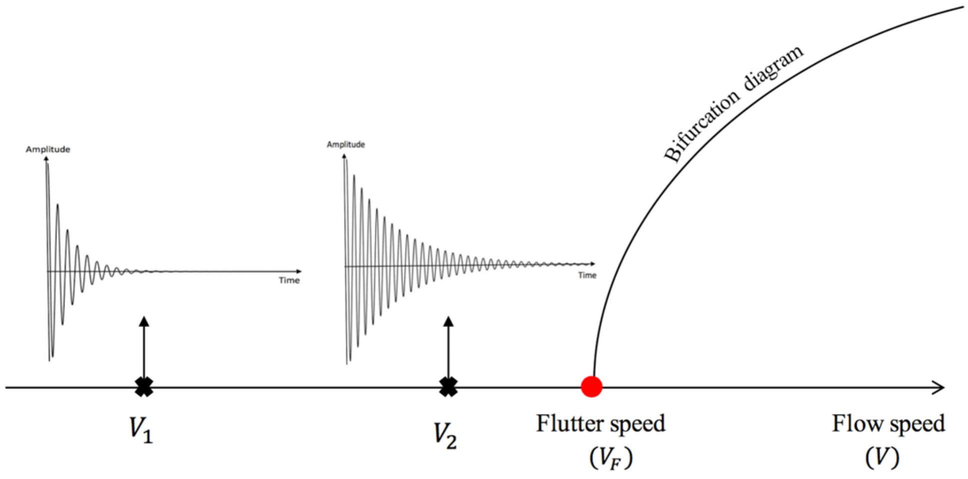

Figure 4.2. Schematic of the change in the rate of recovery from perturbations in a system approaching bifurcation; oscillations last longer when the system is closer to the flutter speed.

For large dimensional nonlinear systems, there might be a large number of active spatial coherences (e.g., modes) in a measured recovery from perturbations. When flutter occurs, one pair of complex conjugate eigenvalues of the Jacobian of the dynamics (computed at the equilibrium state) moves to the right of the imaginary axis. This means that only one of the existing modes is involved in the instability, and the effect of other modes can be expressed as a function of this key mode thus being removed from the measurements to achieve maximum accuracy in forecasting. This is equivalent to requiring that the center space of the equilibrium at the bifurcation state is two-dimensional, and the coordinate of the mode involved in the bifurcation captures the entire dynamics near the bifurcation point.

To filter out the effects of the modes not involved in the critical slowing down, two methods can be employed. The first method is to separate the bifurcating mode using frequency-filtering. In a measured recovery, one can consider the frequency of oscillations at the end of the signal as the frequency of the bifurcating mode. This idea comes from the fact that the system is close to the bifurcation and, hence, all modes but one are damped out at the end of the measurement. A band pass filter can be used to separate the desired frequency range from the measurements.

The second method is to project the dynamics of the system onto the center space of its dynamics [103]. In Hopf bifurcations, the inertial manifold near flutter is a two-dimensional nonlinear manifold, and the corresponding center space is tangent to it. One can experimentally determine the center space basis from measurements and study the slowing down behavior for forecasting on this space when the system is close enough to the bifurcation.

Although the frequency-filtering method is simpler, the center space projection method is more accurate when there are several modes with frequencies close to the frequency of the bifurcating mode. Details and a discussion of benefits and drawbacks of bifurcation forecasting using center space projection can be found in refs. [3,102].

When a system oscillates during its recovery from perturbations, measurements are collected at different phases of the oscillation. As a result, the recovery rates (computed at each instant when measurements are collected) have different phases. They cannot be compared to each other unless the phase is known, which is difficult or impossible, depending on the available measurements. An alternative solution is to use a specific phase on the inertial manifold and forecast the bifurcation diagram for that phase. Since the inertial manifold is two-dimensional, choosing a specific phase on the inertial manifold means to construct a Poincaré section and reduce the system to a one-dimensional nonlinear map at each phase. To forecast the maximum amplitude of the limit cycles in the post-bifurcation regime, one has to choose local maxima of the measured system recoveries for forecasting.

Consider a one-dimensional nonlinear system corresponding to a chosen fixed phase on the inertial manifold of a fluid-structural system prone to flutter. The flow speed V is the bifurcation parameter, and r is the amplitude of the dynamics. This amplitude can be that of any state variable of the system. The rate of change of the amplitude can be written as

$$\dot{r} = f(V, r). \tag{4.1}$$

In general, f in Eq. (1) can be a complex function of the bifurcation parameter V. For simplicity, it is considered that the amplitude is measured with respect to equilibrium. Hence, $r = 0$ is a stable state before the flutter point located at $V = V_F$. Using a Taylor series with respect to the parameter (not with respect to the state) around the bifurcation point ($V = V_F$), and retaining the first three terms, the governing equation can be expressed as

$$\dot{r} = r\ (p(r) + \alpha_1(r)\ (V - V_F) + \alpha_2(r)\ (V - V_F)^2) + H.O.T., \tag{4.2}$$

where $p(r)$, $\alpha_1(r)$ and $\alpha_2(r)$ are polynomial functions which are independent of the flow speed V. Equation (4.2) considers the first three terms in the Taylor series. For the flow speeds close to the flutter speed in this study, a second-order polynomial dependence on the parameter as shown in Eq. (4.2) provides good accuracy, and higher order terms can be neglected. Nonetheless, one can use higher order terms (especially when the forecasting is used at flow speeds far from the flutter point).

To characterize the recovery, we define the recovery rate as

$$\lambda(V, r) = \frac{d \ln (r)}{dt} = \frac{\dot{r}}{r}\,. \tag{4.3}$$

Therefore, Eq. (2) can be re-written as

$$\lambda(\mu, r) = p(r) + \alpha_1(r)(V - V_F) + \alpha_2(r)(V - V_F)^2. \tag{4.4}$$

The recovery rate is computed at each amplitude r using measured system recoveries. Forecasting is based on this computed recovery rate. At a fixed amplitude $\tilde{r}$, the recovery rate decreases when the system approaches bifurcations. Similarly, at a fixed flow speed V, the smallest recovery rate corresponds to the amplitude which is closer to the actual bifurcation diagram.

To forecast the bifurcation diagram, system recoveries from perturbations at several different flow speeds V_1, V_2, …, V_n are measured. Note that the order of the polynomial in Eq. (4.4) used for approximating the recovery rate determines the minimum number of measurements required for forecasting the bifurcation diagram. In this study, a minimum of three measurements are needed, all in the pre-flutter regime.

For a fixed amplitude $r = \tilde{r}$, one can compute $\lambda(V_k, \tilde{r})$, $k = 1,2,\dots,n$ and use a second-order approximation for the data collected in the $V - \lambda(\mu, \tilde{r})$ plane according to Eq. (4.4). The intersection of the fitted curve with the V axis ($V = \tilde{V}$) corresponds to a zero recovery rate which is the forecasted flow speed for the chosen amplitude $\tilde{r}$ in the post-flutter regime. This process is repeated for several values of $\tilde{r}$ to forecast the bifurcation diagram at the chosen phase. The forecasting procedure is conceptually shown in Fig. 4.3.

To increase the forecasting accuracy especially for low frequency oscillations, one can use methods such as nonlinear optimization [3] and center space reduction [102] to approximate the recovery rate more accurately. In this study, the nonlinear optimization approach is employed. In this method, the recovery rate is approximated in the following form

$$\lambda = \frac{\dot{r}}{r} = \lambda_0 + \lambda_1 r + \cdots + \lambda_p r^p, \tag{4.5}$$

where coefficients λ_i are constant coefficients. These coefficients are chosen using optimization such that the calculated $r(t)$ solution of Eq. (4.5) best fits the local maxima available from the measured time history. The idea behind this method is that a p^{th}-order polynomial in the $\lambda - r$ plane is sufficient to approximate recovery rate of systems with either supercritical or subcritical bifurcations. This approach gives a more accurate and smooth approximation of recovery rates than simply using discrete derivatives of local maxima. In this study, good accuracy is obtained when $p = 4$ is selected. It is worth mentioning that in the presented forecasting method, there is no assumption about the type of bifurcations *a priori*. The forecasting method can uncover bifurcation diagrams of both supercritical and subcritical bifurcations following exactly the same procedure.

The method is applied to forecast the flutter speed and bifurcation diagram of an elastic high aspect ratio wing that has a complex dynamics caused by fluid-structure interactions and large elastic deformations. Instead of experimental measurements, surrogate time-series are used as input to the forecasting method. The surrogate data is obtained from simulation of the highly flexible wing formulation described below.

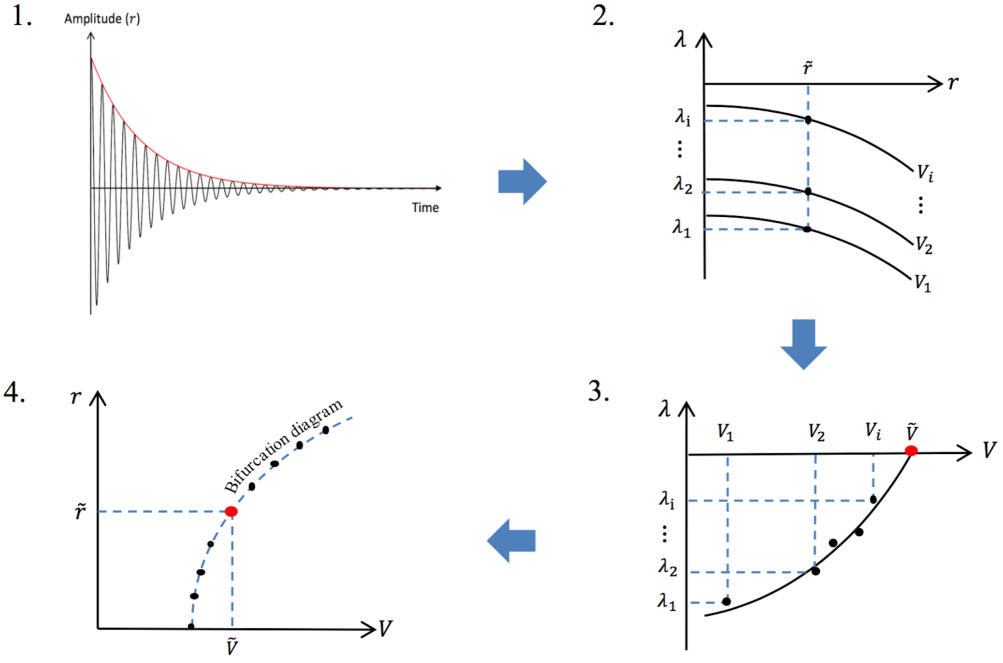

Figure 4.3. Schematic of proposed forecasting method procedure: 1) System recoveries are measured after perturbations, and the recovery rate is estimated using nonlinear optimization for the local maxima of the measurements. 2) The estimated recovery rates for a fixed amplitude at each measured flow speed are analyzed. 3) The flow speed $\tilde{V}$ where the recovery rate becomes 0 at amplitude $\tilde{r}$ is determined using a low order polynomial. 4) Steps 2 and 3 are repeated for several amplitude values $\tilde{r}$, and the bifurcation diagram is constructed using the forecasted pairs of values ($\tilde{V}$,$\tilde{r}$).

4.3 Model formulations

Modeling the interaction between structures undergoing large deflections and the flow requires a geometrically nonlinear formulation rather than a traditional linear one. Cesnik and co-workers [104,105] have developed a nonlinear aeroelastic formulation coupled with the flight mechanics to perform simulations of very flexible aircraft in free flight. In this framework, the structure is based on a strain-based geometrically nonlinear beam finite element[106], allowed for fully coupled three-dimensional bending, twisting, and extensional deformations. A finite-state unsteady potential flow airloads model [107] with stall, compressibility, and tip effect corrections is integrated into the system equations. This whole formulation is implemented in Matlab and makes the so-called University of Michigan's Nonlinear Aeroelastic Simulation Toolbox (UM/NAST)[69,104]. An overview of the formulation implemented in UM/NAST is described below.

Consider the body frame defined as wing right (+x), towards wing leading edge (+y) and normal to beam surface (+z) as shown in Fig. 4.4.

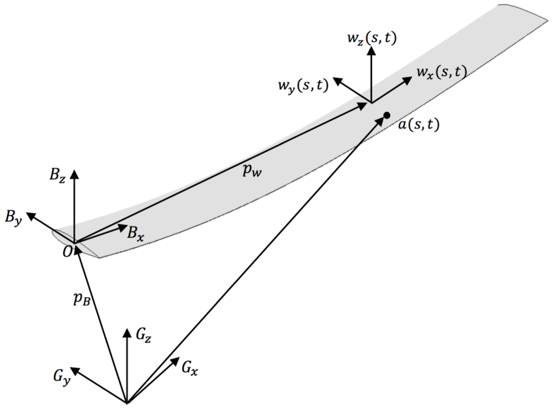

Figure 4.4. Schematic of flexible wing, frames and coordinates used in the structural model include an inertial frame G, a body fixed frame B, and a local frame w.

Each beam element has three nodes with four degrees of freedom: extensional, twist and two orthogonal bending strains about the beam reference line. The strain vector within each beam element is assumed constant and is denoted by

$$\varepsilon_e = \begin{bmatrix} \varepsilon_x & \kappa_x & \kappa_y & \kappa_z \end{bmatrix}^T. \tag{4.6}$$

As shown in Fig. 4.4, the position and orientation of each point can be described by a position vector, namely p_w, and three directrix vectors, namely w_x, w_y, w_z, resulting in 12 components. For a point at location s from the origin along the beam, one has:

$$h(s) = \begin{bmatrix} p_w(s) & w_x(s) & w_y(s) & w_z(s) \end{bmatrix}^T. \tag{4.7}$$

The rigid body motion of the body frame origin is described by the three linear and three angular velocities, denoted by

$$\beta = [\nu_B \quad \omega_B]^T. \tag{4.8}$$

Given nodal direction vectors (w_x, w_y, w_z), the direction cosine matrix C^{Bw} from the local beam frame w to the body frame B can be expressed as:

$$C^{Bw} = [w_x \quad w_y \quad w_z\,], \tag{4.9}$$

which implies that an arbitrary column vector $\{u\}_w$ expressed in the beam reference frame can be transformed to the body frame by:

$$\{u\}_B = C^{Bw}\{u\}_w\,. \tag{4.10}$$

The position and orientation $h(s)$ can be recovered from the strain ε_e and boundary condition h_0 using the kinematic relationship

$$h(s) = e^{K(s-s_0)}h_0 = e^{G(s)}h_0\,, \tag{4.11}$$

where

$$K = \begin{bmatrix} 0 & 1+\varepsilon_x & 0 & 0 \\ 0 & 0 & \kappa_z & -\kappa_y \\ 0 & -\kappa_z & 0 & \kappa_x \\ 0 & \kappa_y & -\kappa_x & 0 \end{bmatrix}_{12\times 12} . \tag{4.12}$$

Nodal displacement can then be computed by marching Eq. (4.11) from root to tip between connecting beam elements.

To model unsteady aerodynamic loads, a 2-D finite state aerodynamic theory is used [107]. The theory is developed for calculating aerodynamic loads on a two-dimensional thin airfoil with large motions in inviscid and incompressible flow. The aerodynamic lift, moment and drag of a thin airfoil about its aerodynamics center can be written as

$$\begin{gathered} L_{ac} = \pi\rho b_c^2(-\ddot{z} + \dot{y}\dot{\alpha} - d\ddot{\alpha}) + c_{l\alpha}\rho b_c \dot{y}^2\left[-\frac{\dot{z}}{\dot{y}} + (0.5b_c - d)\frac{\dot{\alpha}}{\dot{y}} - \frac{\lambda_0}{\dot{y}}\right], \\ M_{ac} = \pi\rho b_c^3\left[-\frac{1}{2}\ddot{z} - \dot{y}\dot{\alpha} - \left(\frac{b_c}{8} - \frac{d}{2}\right)\ddot{\alpha}\right] + 2\rho c_{m0} b_c^2 \dot{y}^2, \\ d_{ac} = -\rho c_{d0} b_c \dot{y}^2, \end{gathered} \tag{4.13}$$

where b_c is semi-chord, d is the distance between the mid-chord and the reference axis, c_{m0} and c_{d0} are moment and drag coefficient of zero angle of attack, respectively, and $c_{l\alpha}$ is the lift curve slope. Moreover, $\dot{y}$ and $\dot{z}$ are the velocity components along and perpendicular to the chord, respectively, and α is the angle of attack.

The inflow velocity parameter is given by

$$\lambda_0 = \frac{1}{2}\sum_{n=1}^{N} b_n \lambda_n, \tag{4.14}$$

where the b_n coefficients are given in ref. [107], and inflow states λ_n can be obtained using the following final form of the differential equation:

$$\dot{\lambda} = F_1\begin{Bmatrix} \ddot{\varepsilon} \\ \dot{\beta} \end{Bmatrix} + F_2\begin{Bmatrix} \dot{\varepsilon} \\ \beta \end{Bmatrix} + F_3\lambda, \tag{4.15}$$

Where the F_is are influence matrices [104].

Finally, to obtain the elastic equations of motion, the principle of virtual work is used. The virtual work of the system consists of the effect of inertial forces, internal strains and strain rates, and external loads. The structure is divided into several elements with length ds, and the virtual work is computed for each element. Summing up the internal and external work of all elements results in the following elastic equations of motion [104]

$$\begin{bmatrix} M_{FF}(\varepsilon) & M_{FB}(\varepsilon) \\ M_{BF}(\varepsilon) & M_{BB}(\varepsilon) \end{bmatrix} \begin{Bmatrix} \ddot{\varepsilon} \\ \dot{\beta} \end{Bmatrix} + \begin{bmatrix} C_{FF}(\varepsilon,\dot{\varepsilon},\beta) & C_{FB}(\varepsilon,\dot{\varepsilon},\beta) \\ C_{BF}(\varepsilon,\dot{\varepsilon},\beta) & C_{BB}(\varepsilon,\dot{\varepsilon},\beta) \end{bmatrix} \begin{Bmatrix} \dot{\varepsilon} \\ \beta \end{Bmatrix} + \begin{bmatrix} K_{FF} & 0 \\ 0 & 0 \end{bmatrix} \begin{Bmatrix} \varepsilon \\ b \end{Bmatrix} = \begin{Bmatrix} R_F(\varepsilon,\dot{\varepsilon},\ddot{\varepsilon},\beta,\dot{\beta},\lambda,\zeta,u) \\ R_B(\varepsilon,\dot{\varepsilon},\ddot{\varepsilon},\beta,\dot{\beta},\lambda,\zeta,u) \end{Bmatrix}, \tag{4.16}$$

where the attitude is defined by a set of quaternions, $\zeta = [\zeta_0, \zeta_1, \zeta_2, \zeta_3]^T$, which relates rotation from the inertial frame to the body frame. The quaternion ζ is governed by [104] :

$$\dot{\zeta} = -\frac{1}{2}\Omega_{\zeta}(\beta)\zeta, \tag{4.17}$$

and the propagation of the body reference system by:

$$\dot{P}_B = [C^{GB}(\zeta) \;\; 0]\,\beta. \tag{4.18}$$

The matrices $\Omega_{\zeta}(\beta)$ and $C^{GB}(\zeta)$ in Eqs. (4.17) and (4.18) are body rotations about the reference frame and reference coordinate transformation matrix, respectively, which are defined in ref. [104].

The set of equations are integrated numerically to obtain the vehicle response. The UM/NAST framework is used as the source for surrogate measurements required for the proposed forecasting method. It is worth recalling that the mathematical model is not needed for the forecasting method. The only input to the algorithm is the transient time data measured from sensors (or surrogate data from numerical simulations). Hence, the actual model introduced in this section is used only for generating surrogate measurement data to demonstrate the forecasting method.

4.4 Forecasting bifurcation diagrams of a flexible high-aspect-ratio cantilever wing

In this section, the proposed approach is used to forecast the flutter speed and the bifurcation diagrams of a very flexible high-aspect-ratio cantilever wing modeled using the formulation in Sec. 4.3. The geometric and structural properties of the wing are provided in Table 4.1.

Table 4.1: Geometric and structural properties of the high-aspect-ratio wing

Semi-Span	16 m
Chord (c)	1 m
Root Angle of Attack	2 deg
Airfoil	Thin plate
Number of Inflow States per Strip	6
Beam Reference Axis	0.5 c
Center of Gravity	0.5 c
Mass / Span	0.75kg/m
Cross-Section Mass Moment of Inertia about y-axis (I_{yy})	0.05 kg m
Cross-Section Mass Moment of Inertia about z-axis (I_{zz})	0.05 kg m
Torsional Stiffness (GJ)	$3\ 10^5$ Nm^2
Bending Stiffness about y-axis (EI_y)	$6\ 10^5$ Nm^2
Bending Stiffness about z-axis (EI_z)	$1.5\ 10^8$ Nm^2
Stiffness Proportional Damping Factor	$2.21\ 10^{-6}$

The material of the structure is linear, but its elastic deformation is large because of the high aspect ratio. Hence, the study of this nonlinear large-dimensional system using traditional methods offers unique challenges. In contrast, using the bifurcation forecasting approach for this system can dramatically reduce the efforts required for its comprehensive nonlinear stability analysis

To forecast flutter, system responses to perturbations are measured at several flow speeds in the pre-flutter regime. Surrogate measurements are generated using the proposed formulations in the previous section as input to the forecasting method. Specifically, three flow speeds of 123 m/s, 125 m/s and 127 m/s were chosen. This is the minimum number of required measurements for forecasting. At each flow speed, the static aeroelastic equilibrium for the wing at 2-deg root angle of attack resulting from the applied aerodynamic forces is obtained (which in this example was computed using a quasi-static solution process [104]). Figure 4.5 schematically shows the static equilibrium position of the wing obtained from quasi-static solution at 125 m/s flow speed.

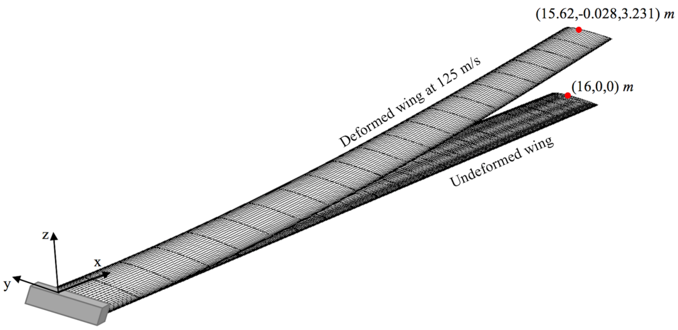

Figure 4.5. Schematic of the equilibrium position of the wing at 125m/s flow speed and 2-deg root angle of attack. The position of a point on the beam reference axis at the wing tip is shown before and after the deformation of the wing due to aerodynamic forces.

Next, perturbations are applied to the system to measure recoveries required for forecasting. In general, perturbations can be of any type. In this study, we use *"1-cos"* type gusts. The applied gust has a maximum vertical amplitude of 40 m/s and a period of 0.06 s (as shown in Fig. 4.6), and acts on the entire wingspan. After the gust passes, the wing starts to recover from the disturbance caused by the gust. At each flow speed, the response of the system after the gust encounters is recorded along the three directions at several points along the span. As an example, the recorded gust response of the wing tip in the horizontal (y) and vertical (z) directions at the flow speed of 125 m/s are shown in Fig. 4.7. These data and similar measurements recorded at several flow speeds in the pre-flutter regime are used as inputs to forecast the flutter speed and the bifurcation diagram. It is worth recalling that the proposed forecasting approach is model-less, and hence the system model is used only for generating surrogate measurements.

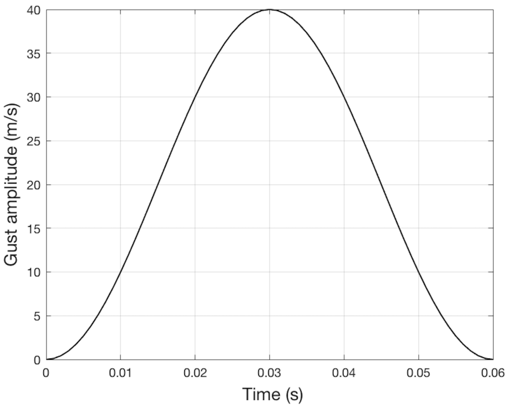

Figure 4.6. Variation of gust speed with time

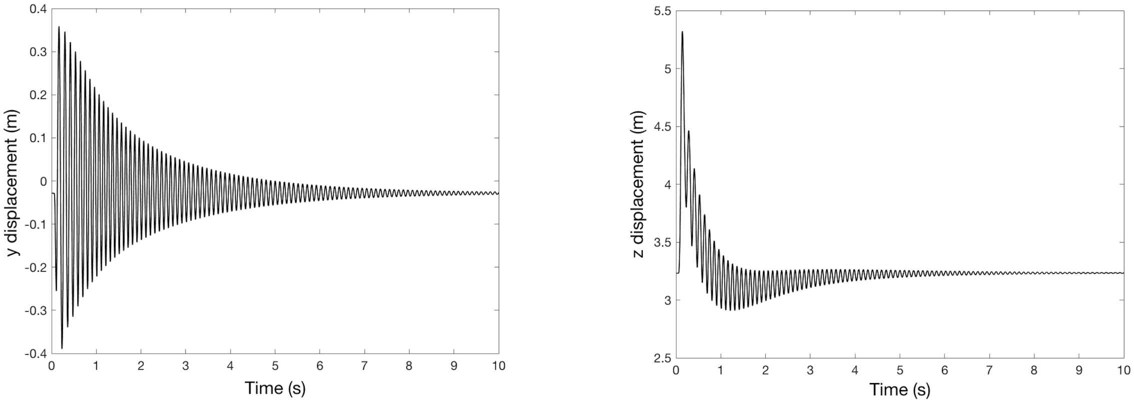

(a)

(b)

Figure 4.7. System recoveries from perturbations at 125 m/s in (a) y direction and (b) z direction, recorded for a point at the wing tip.

Since the system has many degrees of freedom, there exist many possible active modes in the recoveries, while only one of them is involved in the flutter phenomenon. The filtered measurements containing the separated bifurcating mode are shown in Fig. 4.8.

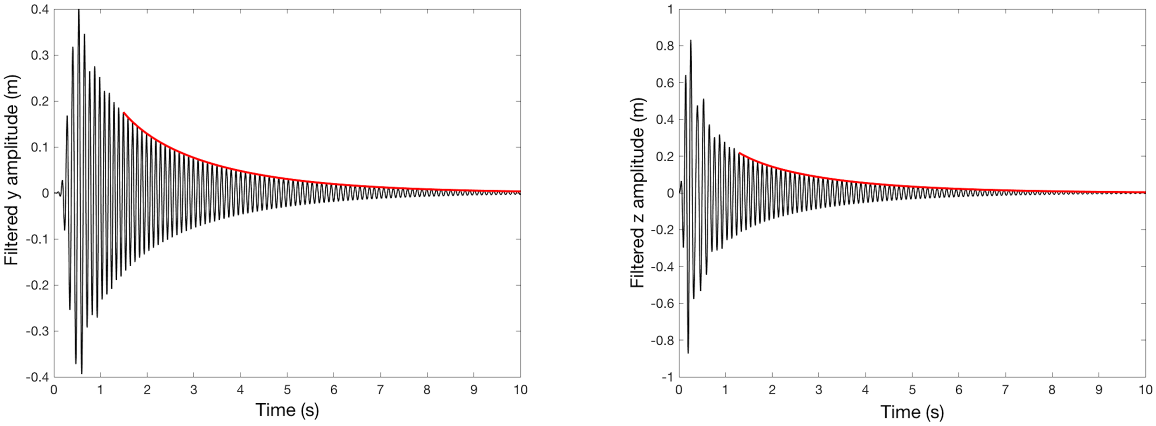

(a) (b)

Figure 4.8. System recoveries filtered to separate the effects of the bifurcating mode from measurements. Same recoveries are used as those shown in Fig. 4.7. Envelope lines approximate the decay function of local maxima.

To build the bifurcation diagram of limit cycle amplitudes, local maxima of the filtered signals are used. To ensure that the data used for forecasting are on the inertial manifold, the first second of measurements is not used. Bifurcation diagrams of the wing in each direction and for each point along the span can be forecasted separately. Following the forecasting procedure, curves of recovery rate of local maxima of y displacement for the wing tip are computed and shown in Fig. 4.9. Using these curves together with Eq. (4.4), $\lambda - V$ curves are obtained for each amplitude as shown in Fig. 4.10. The intersection of each curve with the V-axis corresponds to a zero recovery rate, which is the forecasted flow speed in the post-flutter regime for the chosen amplitude. A similar procedure can be followed for negative peaks of measured recovery to forecast the lower branch of the bifurcation diagram when signals are asymmetric. Following this approach for several amplitudes, the bifurcation diagram is constructed as shown in Fig. 4.11(a). Bifurcation diagrams show maximum amplitudes of limit cycle oscillations measured from mean position of the oscillations as function of flow speeds. Similarly, the bifurcation diagram for the wing tip deflection in the z direction is forecasted and shown in Fig. 4.11(b).

Fully-nonlinear aeroelastic simulations were conducted at given post-flutter speeds to obtain the reference limit cycle amplitudes. They are shown in Figs. 4.11(a) and 4.11(b) using solid circles and they are compared with the forecasted curves. To find the reference limit cycle amplitudes, time-marching is used to solve the equations of motion detailed in Sec. 4.3. To that aim, the system is perturbed at the corresponding post-flutter speed, and the model equations time marched until the oscillations converge to the stable limit cycle.

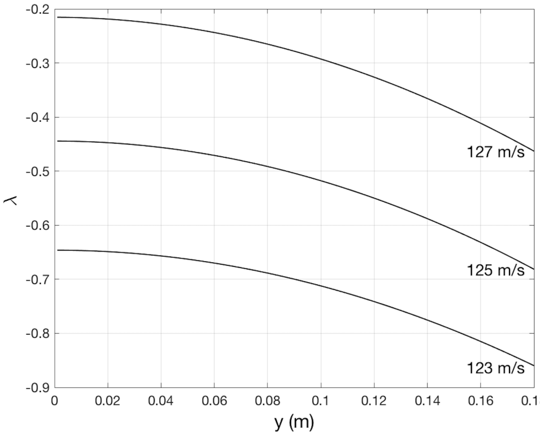

Figure 4.9. Recovery rate variation with amplitude for the horizontal (y) displacement of the wing tip at different air speeds.

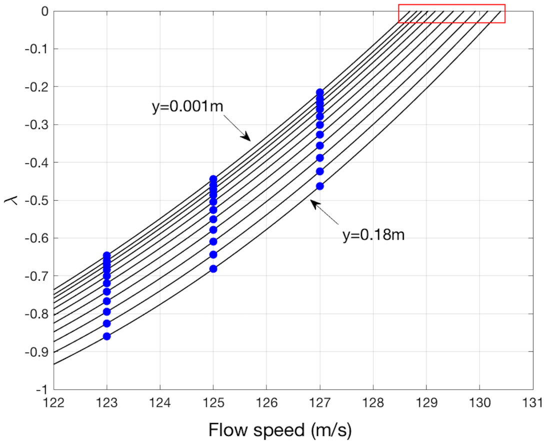

Figure 4.10. Second-order approximation in the $\lambda - V$ plane for several horizontal (y) displacement amplitudes of the wing tip. Each curve corresponds to a different amplitude. Symbols (•) show recovery rates shown in Fig. 22.

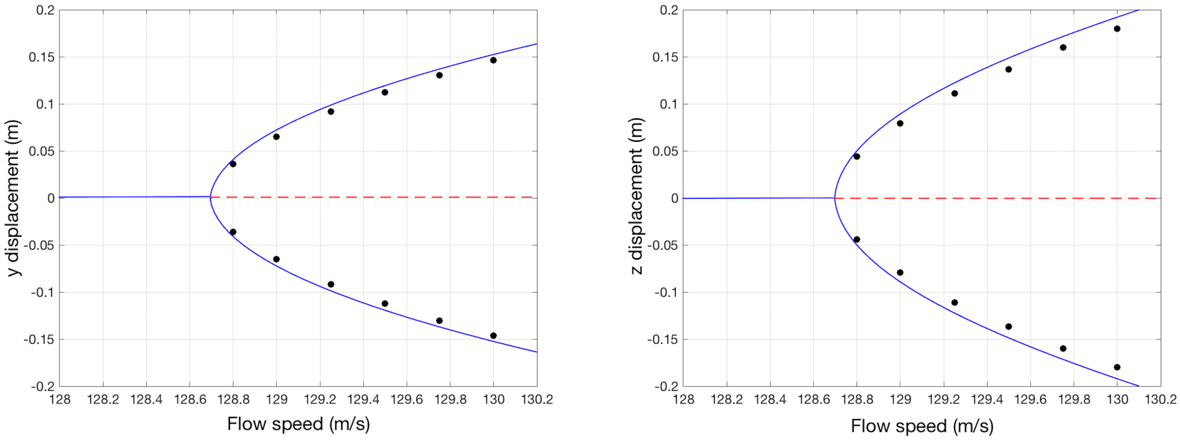

(a) (b)

Figure 4.11. Bifurcation diagrams for (a) the horizontal (y) displacement and (b) the vertical (z) displacement of the wing tip. Solid lines are forecasted results corresponding to the limit cycle amplitudes in the post-flutter regime, while dashed lines are unstable fixed points in the post-flutter regime. Symbols (•) are reference limit cycle amplitudes computed by direct nonlinear time-marching solutions.

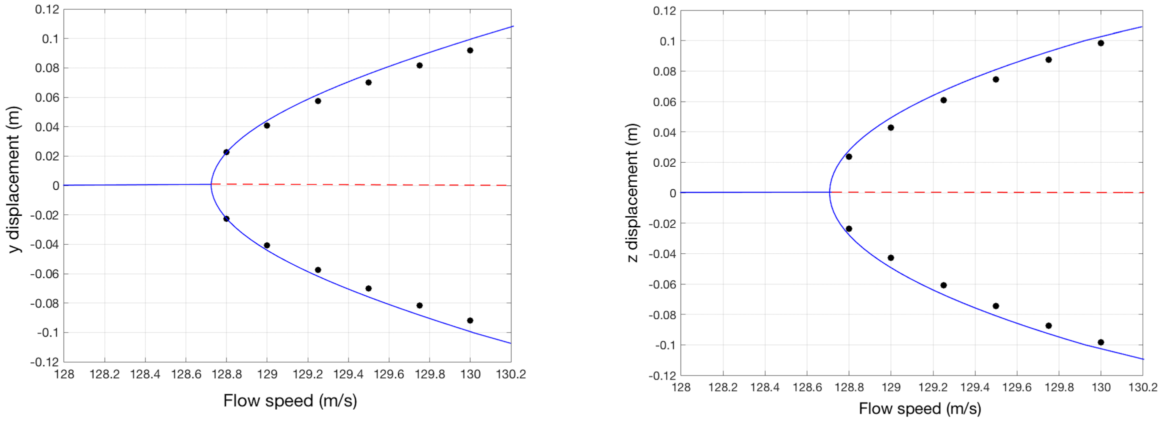

(a) (b)

Figure 4.12. Bifurcation diagrams for (a) the horizontal (y) displacement and (b) the vertical (z) displacement of a point at a distance of 4 m from the tip. Solid lines are forecasted bifurcation results corresponding to the limit cycle amplitudes in the post-flutter regime, while dashed lines are unstable fixed points in the post-flutter regime. Symbols (•) are reference limit cycle amplitudes computed by direct nonlinear time-marching solutions.

Using the same forecasting procedure, bifurcation values for other points along the span can be obtained. As another example, bifurcation diagrams of a point on the wing reference axis at a distance of 4 m from the tip are shown in Fig. 4.12. According to the forecasted bifurcation diagrams (Figs. 4.11 and 4.12), flutter is expected to occur at the speed of 128.7 m/s. Furthermore, flutter is forecasted to be supercritical. Results show that the method can effectively forecast the bifurcation diagrams of the system.

Note that since local maxima of measurements are used for forecasting, the forecasted bifurcation diagrams correspond to local maxima of limit cycle oscillations (limit cycle amplitudes) in the post-flutter regime. These bifurcation diagrams correspond to a fixed phase of the spiral trajectory on the two-dimensional inertial manifold (that is the phase where the post-flutter limit cycles exhibit their local maxima) in the y or z directions. This phase corresponds to states where velocities $\dot{y}$ and $\dot{z}$ are zero. Since the inertial manifold changes little with the flow speed near the bifurcation, it is expected that the amplitudes of the post-flutter limit cycles occur at approximately the same phase.

Bifurcation diagrams can be forecasted for any other system states using the same approach. For example, identifying maximum velocities of points along the wingspan in the post-flutter regime is also of importance. Following the same forecasting procedure, the velocity of the tip in the y and z directions at flow speeds of 123 m/s, 125 m/s and 127 m/s are recorded. The bifurcation diagrams of maximum velocities are forecasted using the forecasting method and shown in Fig. 4.13.

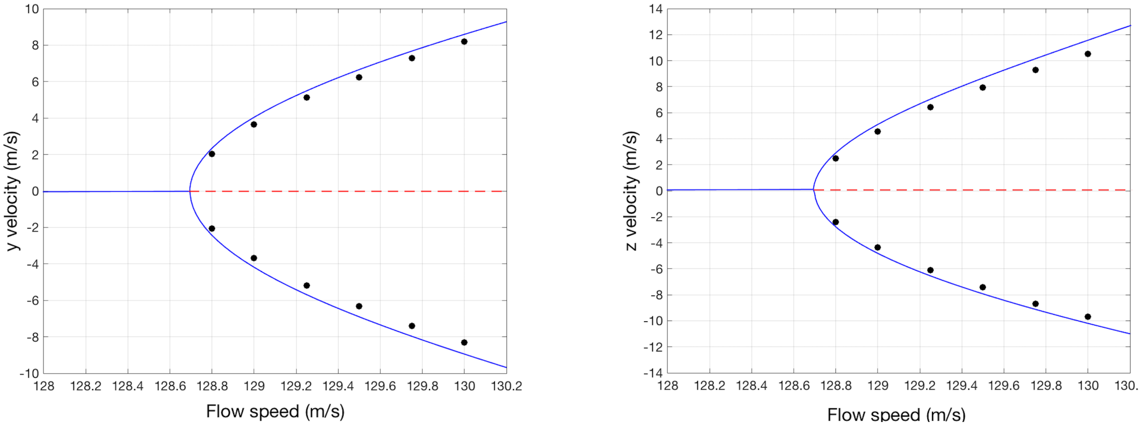

(a) (b)

Figure 4.13. Bifurcation diagrams for (a) the horizontal velocity ($\dot{y}$) and (b) the vertical velocity ($\dot{z}$) of the wing tip. Solid lines are forecasted results corresponding to the limit cycle amplitudes in the post-flutter regime, while dashed lines are unstable fixed points in the post-flutter regime. Symbols (●) are reference limit cycle amplitudes computed by direct nonlinear time-marching solutions.

To gain better insight into the usefulness of the proposed approach, forecasted bifurcation diagrams are shown in the form of three-dimensional plots in the $V - y - \dot{y}$ space and separately the $V - z - \dot{z}$ space in Fig. 4.14. Since for flutter the inertial manifold is generally two-dimensional, choosing any two independent coordinates on this manifold would determine the dynamics of the system and the bifurcation diagram can be constructed. As it can be observed in Fig. 4.14, forecasted diagrams are the maximum displacement and velocity amplitudes of limit cycles corresponding to the local maxima (peaks) in the time series.

Note that to forecast other bifurcation diagrams for any point on the wing, and for any desired state such as displacement or velocity, it is not required to perturb the system separately. It is sufficient to perturb the system at few flow speeds, and record the displacements and velocities of all desired degrees of freedom in response to a disturbance. Hence, a comprehensive nonlinear analysis for the entire system is possible measuring only three system recoveries from perturbations.

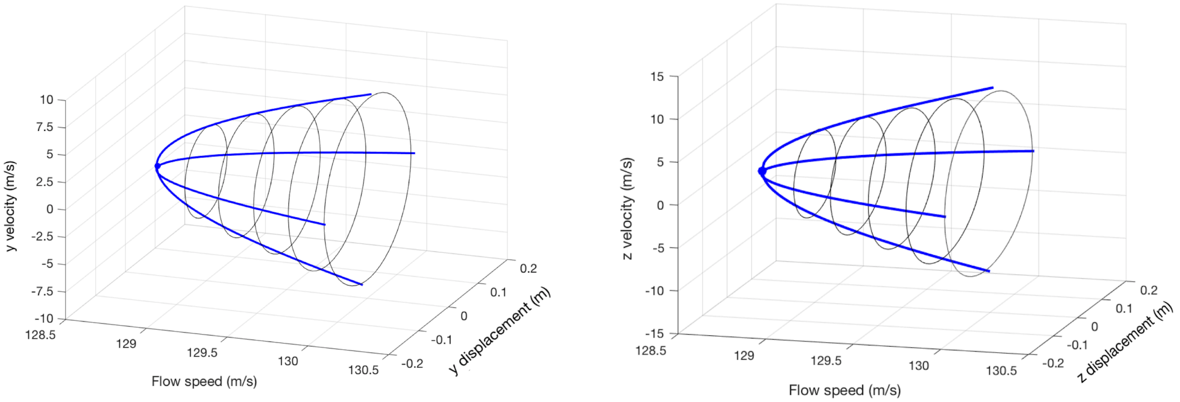

(a) (b)

Figure 4.14. Three-dimensional view of bifurcation diagrams of a point on the wing tip (a) in the $V - y - \dot{y}$ space, and (b) in the $V - z - \dot{z}$ space. Thick lines are forecasted bifurcation diagrams, and thin lines made of small circles are reference limit cycle results obtained from the nonlinear time-marching solution.

When measurements are contaminated by noise, the forecasting accuracy is expected to decrease. Noise with higher intensity makes it difficult to estimate the recovery rates and as a result, the forecasting accuracy is decreased. In such cases, the number of measurements may be increased to enhance accuracy. To investigate the effect of noise on the forecasting results, 2% and 5% white noise is added to the measurements, and the forecasting procedure is followed without any noise filtering. Figures 4.15 and 4.16 show the forecasting results for the wingtip in horizontal (y) and vertical (z) directions. All results are presented as mean values and standard deviation error bars obtained from 20 separate forecasts. Results show that increasing the noise intensity leads to larger variations in the forecasting results. Thus, forecasting using only one set of measurements is not accurate especially when the noise intensity is high. Therefore, more measurements are required to increase the forecasting accuracy.

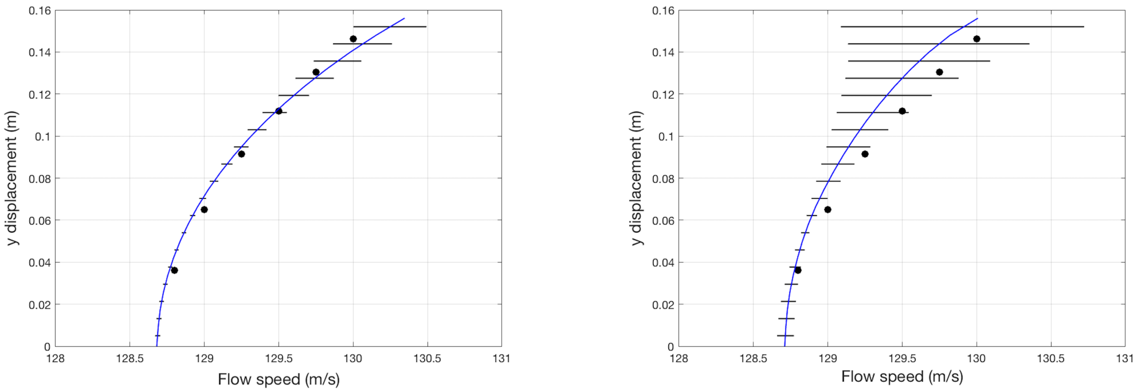

Figure 4.15. Bifurcation diagrams for the horizontal (y) displacement of the wing tip in presence of 2% (left) and 5% (right) measurement noise. Forecasted results are shown as mean values with standard deviation error bars obtained from 20 separate forecasts. The mean values are connected by solid (blue) lines. Symbols (•) show the exact maximum limit cycle amplitudes computed by nonlinear time-marching solutions.

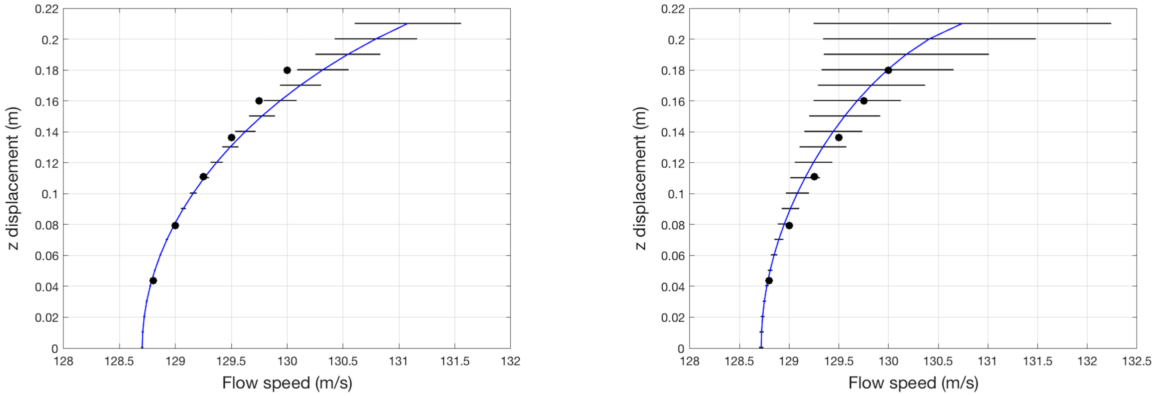

Figure 4.16. Bifurcation diagrams for the vertical (z) displacement of the wing tip in presence of 2% (left) and 5% (right) measurement noise. Forecasted results are shown as mean values with standard deviation error bars obtained from 20 separate forecasts. The mean values are connected by solid (blue) lines. Symbols (•) show the exact maximum limit cycle amplitudes computed by nonlinear time-marching solutions.

4.5 Discussions and conclusions

A novel bifurcation forecasting approach was employed to obtain the flutter speed and post-bifurcation limit cycle behavior of fluid-structural systems, exemplified by a flexible high-aspect-ratio wing. The forecasting method uses the fact that in Hopf bifurcations, the rate of the system’s recovery from perturbations decreases as the system approaches the bifurcations, known as the critical slowing down phenomenon. To forecast the bifurcation diagrams, the only required measurements are the system response to perturbations in the pre-bifurcation regime. More importantly, the method is model-less and is applicable for complex large dimensional systems where extracting a model for the system is difficult or impossible.

Using the forecasting method, bifurcation diagrams for displacements and velocities of points along the wingspan were obtained. Surrogate data was used instead of experimental data, obtained from numerical simulation using an efficient geometrically nonlinear aeroelastic solver (UM/NAST). Gust disturbances were applied to the wing to create perturbations to the system to reflect practical excitation situations. Results show that the method successfully forecasts the flutter speed and the post-flutter dynamics of the considered large dimensional fluid-structural system despite the fact that it uses only pre-bifurcation regime data and it does not use a model of the system.

Valuable information can be extracted from the forecasted bifurcation diagrams that can be of importance for design and safety purposes. First, the flutter speed, which defines the stability boundary, is forecasted. Furthermore, the flutter type can also be forecasted. The effect of noise on the forecasting results was also investigated. It was observed that when measurements are contaminated by noise, the forecasting accuracy is decreased. The forecasting accuracy can be enhanced by increasing the number of measurements depending on the level of noise and the level of desired accuracy.

The forecasted bifurcation diagrams predict the amplitudes of limit cycle oscillations in the post-flutter regime. Maximum displacements around the mean position as well as maximum velocity of points along the wingspan are forecasted in different directions and at different flow speeds of the post-flutter regime. It is worth noting that all bifurcation diagrams were forecasted using only three measurements of the system response to perturbations. This type of forecasting opens the door to linear and nonlinear dynamical analysis of complex systems, in both theoretical and experimental problems, and is important in safety analysis of complex systems.

It is worth mentioning that despite the advantages of the proposed method, there are situations when the forecasting method does not have enough accuracy. The main assumption in the proposed forecasting method is that the system exhibits a slowing down and is close enough to the bifurcation for the slowing down to be observable its recoveries. However, critical slowing down does not exist in all types of bifurcations. For example, systems undergoing period doubling cannot be forecasted using the proposed approach. Moreover, for systems which do exhibit slowing down, the region where the system exhibits a slowing down varies from system to system and is not generally known *a priori*. There are examples of systems which do not exhibit a measurable slowing down until parameters are significantly close to the instability boundary. In aeroelastic systems, for example, there are cases where the linear eigenvalues of the system do not show any decreasing trend (slowing down) unless the air speed is significantly close to the flutter speed when a sharp decrease is observed in one of the eigenvalues. Hence, in order for the forecasting method to work, measurements need to be available in a narrow parameter regime where slowing down is observed, which is a challenging task especially in experimental systems due to presence of noise and uncertainties.

Chapter 5

Forecasting the onset of traffic congestions on circular roads

5.1 Introduction

Ground car traffic jams are a serious issue which can cause significant economic and environmental problems. Hence, the study of complex nonlinear dynamics in traffic have attracted a wide interest for decades [108–113]. The ultimate goal of these studies is to alleviate and prevent traffic jams. Interactions among cars lead to the formation of a nonlinear system which experiences complex dynamics. Mathematical modeling of the complex traffic flow dynamics has a long tradition. Various approaches have been presented to model the complex dynamics of vehicular dynamics and traffic phenomenon [114–116]. Taking advantage of developed models, numerous efforts have been devoted to stability analysis of the equations governing the flow to identify the onset and type of traffic jams on a road [117–119]. Previous studies have shown that traffic jams is the result of a bifurcation where the traffic dynamics loses stability once passing a tipping point [117,120]. The stability of traffic models and the bifurcation diagram revealing the system dynamics after passing the tipping point can be investigated using linear and nonlinear stability analysis techniques, provided that accurate models of the system are available [120–124]. However, traffic jams are fundamentally affected by a variety of factors, from driver behavior to weather, which are hard to model [120]. As a result, accurate models are very difficult to obtain.

Recently, novel techniques have been developed in complex systems theory to enable forecasting the emergent behavior in nonlinear systems. In this work we discuss how to use such techniques to forecast the onset of traffic jams in vehicular traffic flow systems. A great advantage of these methods is their model-less feature. One only needs to monitor system behavior in pre-transition (stable) regime to identify how close the system is to an instability (i.e., close to a traffic jam). These methods can be classified into two groups: (a) stochastic methods, also referred to as early warning indicators/signals, and (b) bifurcation forecasting methods. All these methods rely on critical slowing down, i.e., the fact that, as the system approaches a bifurcation, perturbations to the dynamics lead to ever longer transient recoveries to the equilibrium position. The consequence of the critical slowing down in stochastic systems is an increased in variance and autocorrelation, and the appearance of flickering [2,11,28,35]. Such features observed in recoveries in the vicinity of several types of bifurcations are used in early warning indicators/signals. Using these methods, one can forecast that the system is approaching a tipping point; however, the distance to the instability is not identifiable. Bifurcation forecasting methods, however, are able to forecast both the distance to the bifurcation and a portion of the bifurcation diagram, provided that large enough perturbations are applied to the system [3,8,84,88,125–127]. These methods use measured recovery rates of system from perturbations in the pre-bifurcation regime for forecasting.

In this research, we examine the application of early waning indicators/signals and bifurcation forecasting methods to predict traffic jams on a circular road. To generate surrogate measurements of the system, microscopic modeling of traffic flow is employed. The required measurements for forecasting is the relative distance (headway) between two or more cars on the road. Results show that traffic jams are forecasted successfully. Therefore, model-less forecasting approaches are highly advantageous because traffic flows are complex and mathematical models capable of capturing their complete dynamics are not available generally.

5.2 Forecasting Methods

In the following, two main approaches of forecasting tipping points in complex systems are introduced; however, the main focus of this study is on bifurcation forecasting methods. These methods are employed to forecast traffic jams in car-following model in section 4.

5.2.1 Early warning indictors/signals

Early warning indicators are statistical indicators which reveal proximity to a tipping point. These methods are applicable to systems with small fluctuations around their equilibrium state resulting from stochastic perturbations. As a system approaches a bifurcation which exhibits critical slowing down, the rate of recovery of the system from perturbations decreases and the time required for the system to return to its equilibrium state increases. Thus, the system becomes more correlated with its past, which leads to an increase in autocorrelation. Furthermore, perturbations can accumulate, which leads to an increase in the size of the fluctuations and as a result, an increase in variance [11]. The increase in the value of early warning indicators may be detected sometimes well before a tipping point. In particular, an increase in variance and autocorrelation of fluctuations of the system has been well studied and observed in numerous theoretical and experimental complex systems [11],[16,36,128,129]. Figure 5.1 schematically shows the variation in an early warning indicator as a system approaches a saddle-node or Hopf bifurcation. Several other indicators have been explored as early warning signals such as the noise-induced spectrum [37], the skewness of the probability distribution [30], and the flickering between basins of attraction before bifurcations [38] (see also [2] for a review). In this work we focus only on the variance and autocorrelation as these are the most widely used indicators in the literature.

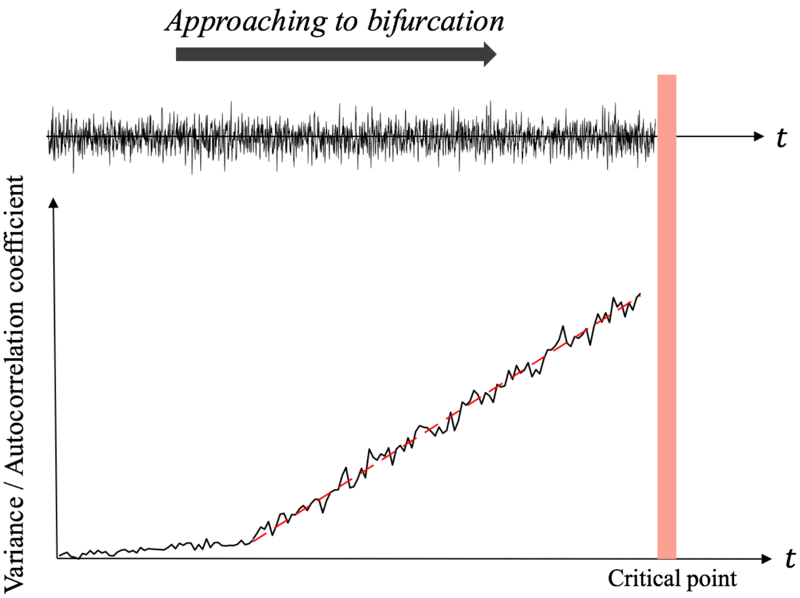

Figure 5.1. Schematic of the variation of early warning signals as the system approaches a saddle-node or a Hopf bifurcation.

5.2.2 Bifurcation forecasting methods

Distinct from stochastic methods, bifurcation forecasting methods can forecast both the critical point (i.e., the distance to the tipping point in the parameter space) and the post-critical dynamics in nonlinear systems [8,84], i.e. the bifurcation diagram. Unlike early warning indicators, this group of methods use recoveries from large perturbations at several parameter values for forecasting (Fig. 5.2).

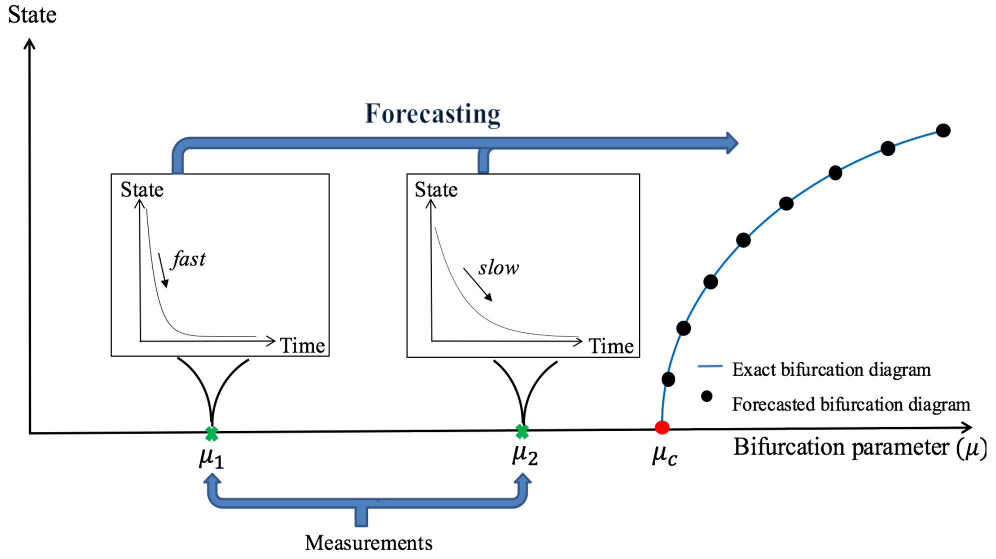

Figure 5.2. Schematic of the bifurcation forecasting method. System measurements before the critical point are employed to forecast the bifurcation diagram.

For clarity, consider the simplest case of a co-dimension-one bifurcation of a one-dimensional nonlinear system given by

$$\dot{r} = f(\mu, r), \tag{5.1}$$

where μ is the parameter, and r is the amplitude. Assume that the system has an tipping point at a parameter value $\mu = \mu_c$. If the system is operating close to this tipping point, Eq. (5.1) can be expanded using a Taylor series approximation with respect to the parameter around $\mu = \mu_c$

$$\dot{r} = r[p(r) + \alpha_1(r)(\mu - \mu_c) + \alpha_2(r)(\mu - \mu_c)^2 + H.O.T.], \tag{5.2}$$

where $p(r)$, $\alpha_1(r)$ and $\alpha_2(r)$ are polynomial functions independent of the parameter μ. The order of the polynomial in Eq. (5.2) depends on the number of parameter values at which measurements are available. In many cases, using a first or second order approximation leads to acceptable results. From Eq. (5.2), we define recovery rate at each amplitude as

$$\lambda(\mu, r) = \frac{\dot{r}}{r} = \frac{\ln(r_{t+\Delta t}) - \ln(r_{t-\Delta t})}{2\Delta t}, \tag{5.3}$$

which can be approximated using measurements of the system recovery from perturbations. The rate of recovery can be used as an indicator, and is correlated to the distance to the bifurcation. At a fixed amplitude $\tilde{r}$, the recovery rate decreases when the system approaches the bifurcation, and is zero when the system is at the equilibrium state . This fact is used to forecast bifurcation diagram of the system (Fig. 5.3).

In this forecasting approach, system recoveries from perturbations at several different parameter values $\mu_1, \mu_2, \ldots, \mu_n$ are measured. The recovery rate is computed at a fixed amplitude $\tilde{r}$ and using different set of measurements, i.e. $\lambda(\mu_k, \tilde{r})$, $k = 1,2, \ldots, n$. Data in the $\mu - \lambda(\mu, \tilde{r})$ plane are approximated using a low order polynomial to identify the parameter $\mu = \tilde{\mu}$ at which the recovery rate is zero. $\tilde{\mu}$ is the forecasted parameter on the bifurcation diagram for the chosen amplitude $\tilde{r}$. This process is repeated for all amplitudes measured in the recovery rate to forecast the complete bifurcation diagram of system (Fig. 5.3).

In a car-following model, the traffic flow system undergoes a Hopf bifurcation from microscopic point of view meaning that cars experience stop-and-go traffic once the car density reaches a critical value μ_c. If one measures the headway between two consecutive cars after a perturbation, one obtains a recovery which decays with oscillations to an equilibrium state (Fig. 5.3(a)). Therefore, the slow manifold of the dynamics is two-dimensional while the described forecasting method considers a system with a one-dimensional manifold. Thus, we choose local maxima/minima of the measured system recovery for forecasting. This reduces the system to one-dimension, and the forecasting method can be employed to forecast the maximum/minimum amplitudes of limit cycle oscillations after the critical point [3,102,130]. Hence, the bifurcation diagram of the system can be forecasted.

The main advantage of the bifurcation forecasting methods is their ability to forecast the distance to the tipping point and also the bifurcation diagram. However, these methods are not applicable to cases where perturbations are very small and stochastic. Instead, early warning indicators are best suited when the system is highly stochastic with small fluctuations around its equilibrium.

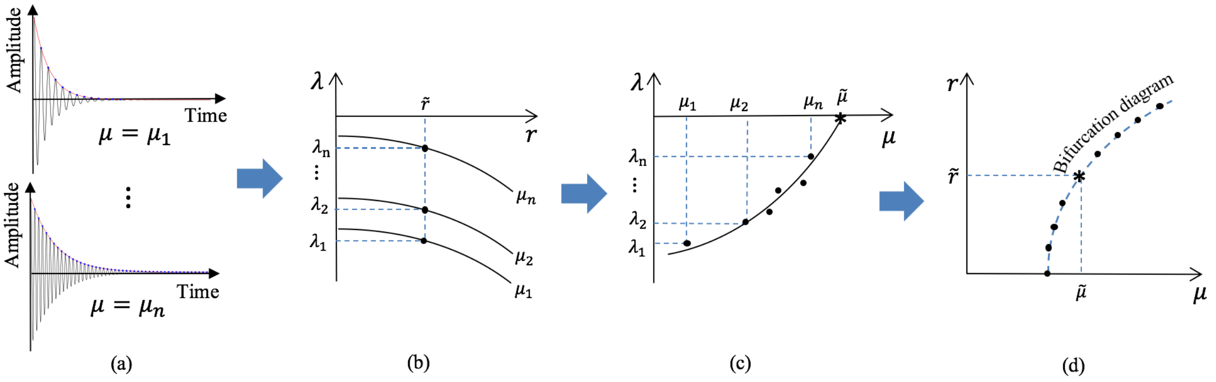

Figure 5.3. Procedure to forecast the bifurcation diagram of limit cycle amplitudes: (a) measure the system response to perturbations at several parameter values, (b) approximate the recovery rate of local maxima (minima) from time series measurements, (c) identify the parameter value $\tilde{\mu}$ at which the recovery rate for a specific amplitude $\tilde{r}$ is zero, (d) repeat steps (b) and (c) for several amplitude values $\tilde{r}$, and construct the bifurcation diagram using the pairs of values ($\tilde{\mu}$,$\tilde{r}$).

5.3 Model formulations

The focus in this section is on the general formulation of a microscopic car-following-model. The simulation results of this model are used as surrogate measurements in the forecasting algorithms.

Consider a system of N cars moving on a circular road of length $\tilde{L}$ as shown in Fig. 5.4. Cars are labeled by $i = 1, \dots, N$. Specifying an arbitrary origin on the ring, the equation of motion of each car can be written as

$$\ddot{\tilde{x}}_i = \frac{1}{\tilde{\tau}_i}\left(\tilde{V}_i\left(\tilde{h}_i\right) - \dot{\tilde{x}}_i\right), i = 1,2, \dots, N \qquad (5.4)$$

where x_i denotes the position of the i^{th} car, and an overdot represents the time derivative. $\tilde{h}_i$ is the headway defined as the bumper-to-bumper distance between the i^{th} and the $i + 1^{\text{st}}$ cars, i.e. $\tilde{h}_i = \tilde{x}_{i+1} - \tilde{x}_i$. Constant $\tilde{\tau}_i$ represents the reaction time of the i^{th} driver. Function V is the so-called optimal velocity function (OVF) which depends on the headway and satisfies some special properties [35]. In this study, all drivers are assumed identical, and therefore $\tilde{\tau}_i = \tilde{\tau}$ and $\tilde{V}_i = \tilde{V}$ for $i = 1,2,\ldots,N$. Equation (4) is a set of coupled ordinary differential equations, but despite its simplicity, it can reproduce the dynamics involved in traffic jams [111,117].

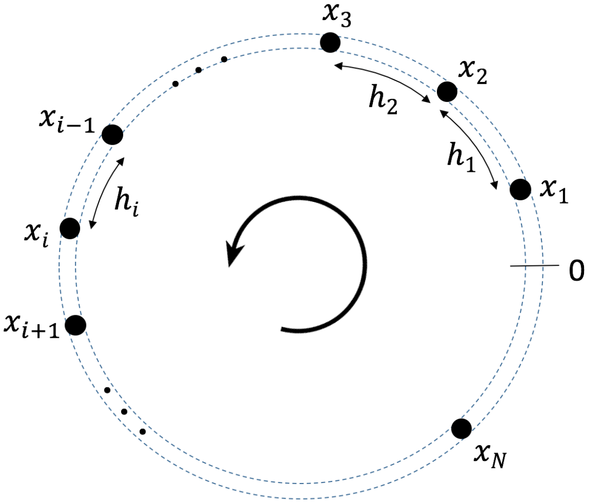

Figure 5.4. Schematic of cars flowing on a circular road.

Equation (5.4) can be non-dimensionalized defining the following variables [117]

$$x_i = \frac{\tilde{x}_i}{a}, \tau_i = \frac{\tilde{\tau}_i}{\tilde{\tau}}, t = \frac{\tilde{t}}{\tilde{\tau}}, L = \frac{\tilde{L}}{a}, V_i(x) = \frac{\tilde{\tau}}{a}\tilde{V}_i(a\tilde{x}) \tag{5.5}$$

where a is an arbitrary length value, e.g. length of a car. With these new variable, Eq. (5.4) can be written in state space form as

$$\begin{cases} \dot{x}_i = y_i \\ \dot{y}_i = \frac{1}{\tau}[V(h_i) - y_i] \end{cases}, i = 1,2,\ldots,N, \tag{5.6}$$

where $h_N = x_1 - x_N + L$.

The OVF is the source of nonlinearity and there have been various forms proposed for this function [117,131–134]. In this study, we choose the following function [117]:

$$V(h) = v_{max}\frac{h^2}{1+h^2}\,. \tag{5.7}$$

Equation (5.7) possesses a solution $x_i^*(t)$ where all cars have the same velocity v^*, constant over time. This uniform flow equilibrium, called quasi-stationary equilibrium, is expressed as

$$h_i = h^* = L/N,\;\; v_i(t) = v^* = V(h^*)\,. \tag{5.8}$$

Performing a linear stability analysis of the system around this quasi-stationary equilibrium, one obtains the following characteristics equation [117]

$$(\lambda^2 + \lambda + \beta)^N - \beta^N = 0, \tag{5.9}$$

where $\beta = V'(h^*)$, $V' = \frac{dV}{dh}$, and λ is the eigenvalue of the linearized system. Considering the critical eigenvalues $\lambda(h_{cr}^*) = \pm i\omega$, we can obtain the stability curves

$$V_k'(h_{cr}^*) = \frac{1}{1+\cos\left(\frac{2\pi k}{N}\right)}\;, k = 1, 2, \ldots, \frac{N-1}{2} \tag{5.10}$$

The couple of complex conjugate eigenvalues that first cross the stability boundary correspond to $k = 1$. This corresponds to the emergence of a stop-and-go traffic jam which we wish to predict. Figure 5.5 schematically shows V' versus $y = L/N$. Based on common assumptions made for OVFs, V' is generally a bell-shaped function. If $V_{max}' < \frac{1}{1+\cos\left(\frac{2\pi}{N}\right)}$, there is no solution for Eq. (5.10), and the system is always stable (i.e., no traffic jam occurs). However, if $V_{max}' > \frac{1}{1+\cos\left(\frac{2\pi}{N}\right)}$, there exist two critical values y_1 and y_2. The system is stable when $y < y_1$ or $y > y_2$, and is unstable otherwise. These critical values correspond to critical car densities on the road $\rho_1 = 1/y_1$ and $\rho_2 = 1/y_2$. Traffic jam emerge when the density of cars on the road hits one of the boundaries ρ_1 or ρ_2. One can assume a road on which the number of cars (and therefore the density) is gradually increasing, and at some point, a traffic jam emerges on the road.

The stability of the system can be explored in the $N-L$ plane as shown in Fig. 5.6 for the OVF given by Eq. (5.7) with $v_{max} = 0.9$. This diagram shows where the system loses its linear stability and traffic jams occur. In addition, a nonlinear analysis can show that the system undergoes supercritical/subcritical Hopf bifurcations depending on the system parameters.

The bifurcation parameter can be chosen to be $d = L/N$ or $\rho = N/L$. Alternately and without loss of generality, N can be fixed (for convenience in simulations), and L can be selected as the bifurcation parameter. Thus the goal in this study is to forecast the critical value L_c at which a traffic jam occurs. This is analogous to forecasting the critical car density on the road. Note that in the following sections, the mathematical model is used only to generate surrogate measurements. The forecasting approaches are data-driven methods, and do not require a model.

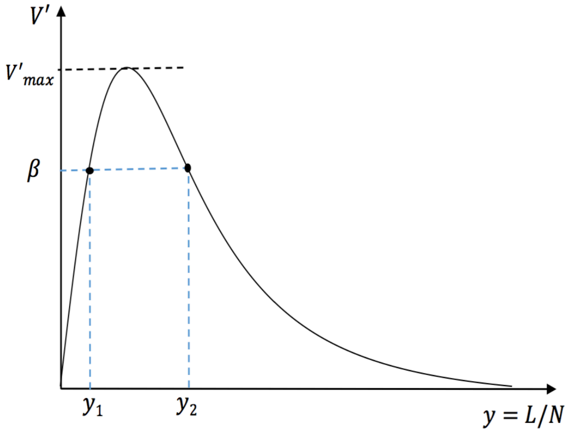

Figure 5.5. Graph of V' versus L/N and stability boundaries for $V' = \beta$.

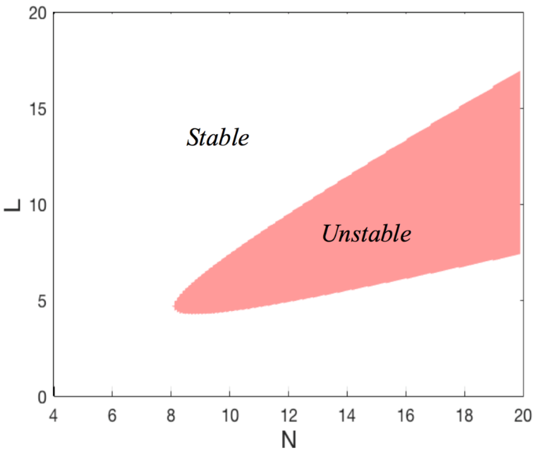

Figure 5.6. Stable and unstable regions of system with an OVF given by Eq. (7) and $v_{max} = 0.9$.

5.4 Results and discussion

5.4.1 Forecasting the onset of traffic jam using early warning indicators

In this section, we implement the early warning signals to forecast the onset of traffic jams using measurements of the system dynamics in the stable traffic flow regime. We use the model described in Section 3 to generate surrogate measurements for the data-driven forecasting. L is the bifurcation parameter.

Consider first a system where $N = 12$, and $v_{max} = 0.9$. According to theoretical results (Fig. 5.6), the critical parameters for this system are $L_c = 4.82$ and $L_c = 9.58$. Here, we focus on forecasting $L_c = 9.58$ using parameters $L > L_c$, which corresponds to forecasting the critical density of cars on a road with data from smaller densities.

When the system is at equilibrium, the headway between any two consecutive cars is L/N. We assume that small stochastic accelerations occur for each car, which creates small fluctuations in the headway around the equilibrium value. The bifurcation parameter L is gradually varied from $L = 18$ to $L = 9.7$. The resulting variance and lag 1-time unit autocorrelation of recorded headway data between two arbitrary selected consecutive cars on road is collected over time. A sample recording of the headway is shown in Fig. 5.7. The computed variance and autocorrelation of this signal are shown in Fig. 5.8. It is observed that both the variance and the autocorrelation increase as the density of cars on the road ($\rho = N/L$) increases and the system approaches an instability, i.e. a traffic jam. The indicator predicts that a traffic jam is approaching, as shown by the change in the value of the indicator in the vicinity of the linear stability boundary. As discussed earlier, this method does not provide information about the critical parameter value L_c where a traffic jam occurs and does not predict the dynamics of the system after the onset of the instability. However, this method provides valuable information about an impending instability, and it is useful especially when all that can be measured is the stochastic oscillation in one of the system states around its equilibrium.

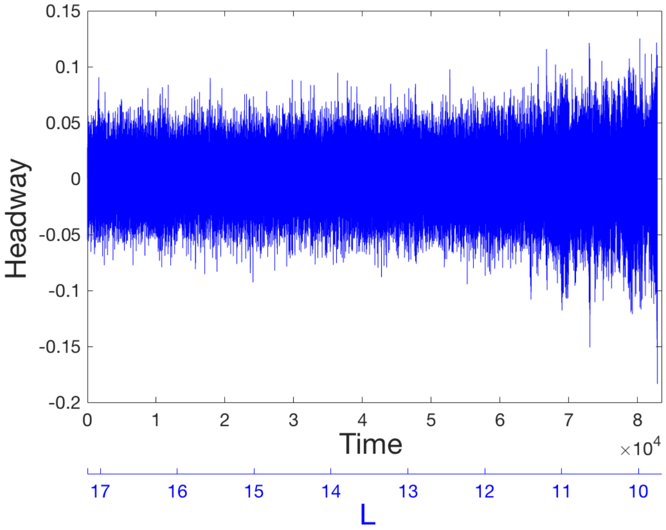

Figure 5.7. Recorded stochastic headway values between two consecutive cars used for computing early warning signals. The car density on the road is gradually decreased over time, and it approaches its critical value.

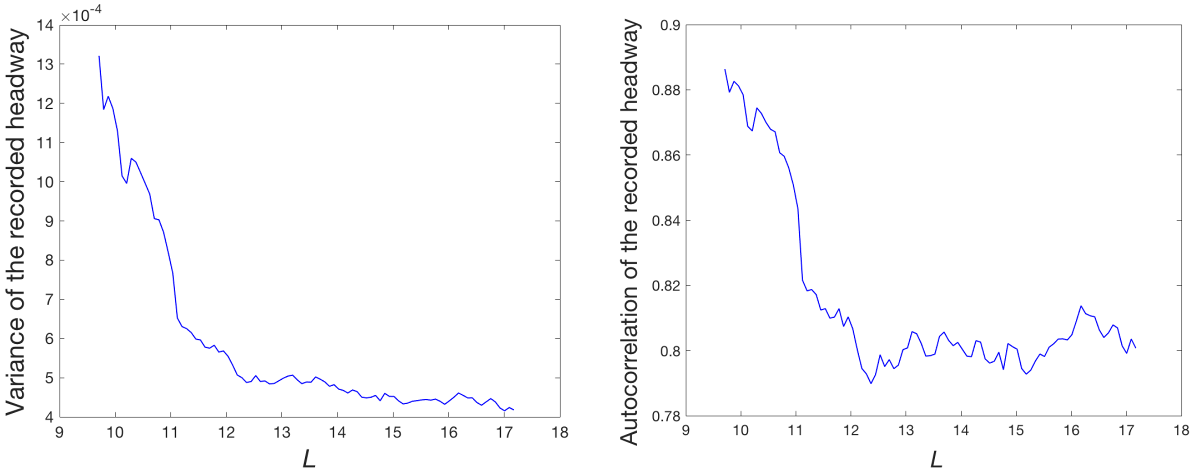

Figure 5.8. Variation of early warning signals with the bifurcation parameter. As the bifurcation parameter decreases, the system approaches a bifurcation. The coefficient of variance (left) and the autocorrelation (right) of the recorded signal increase as the system approaches the bifurcation, i.e. the traffic jam.

5.4.2 Forecasting the onset of traffic jams and post-traffic dynamics using bifurcation forecasting method

Next, we focus on bifurcation forecasting methods for predicting both the tipping point and the bifurcation diagram of the system. To use bifurcation forecasting methods efficiently, perturbations are required to be larger than the noise (stochasticity) in the system and the measurements. Large perturbations are not unexpected in traffic flow systems, and can be observed during normal operational conditions. For example, when one of the drivers suddenly reduces the car speed by a moderate or large value, a perturbation is created in the system dynamics and can be used for forecasting.

To demonstrate the method, we first consider the same system parameters as in the previous example, i.e.: $N = 12$, $v_{max} = 0.9$. This system has a critical parameter value of $L_c = 9.58$, and exhibits a supercritical Hopf bifurcation (Fig. 5.10). To collect surrogate measurement data, simulated cars start moving from a random initial condition. We focus on the headway between two arbitrary selected consecutive cars on the road. The headway is recorded at three parameter values prior to the transition, i.e. $L = 11$, $L = 10.5$ and $L = 10$, as shown in Fig. 5.9. The local maxima (minima) of the collected measurements are used to forecast the maximum (minimum) amplitudes in the bifurcation diagram using the bifurcation forecasting approach. Following the forecasting method described in Section 5.2.2, recovery rates of local maxima (minima) of the collected measurements are estimated. Figure 5.10(a) shows the variation of recovery rate versus amplitude for the local maxima. A similar plot can be obtained for the local minima of the oscillations. The recovery rates at each amplitude are then extrapolated to find the parameter at which the recovery rate is zero, as shown in Fig. 5.10(b). Figure 5.10(c) shows the forecasted bifurcation diagram. The results show that the forecasted value of L where the system loses its stability is $L_c = 9.58$, where a traffic jam occurs. This result is in great agreement with the theoretical computed critical parameter value. Furthermore, the bifurcation diagram of the system is forecasted, which is of importance also. The approach forecasts that the system faces a supercritical bifurcation, and the amplitudes of the limit cycle oscillations in the headway are forecasted. The method successfully forecasts both the critical parameter at which the traffic jam occurs and the post-bifurcation dynamics of the system despite the fact that only three measurements of the headway between two cars in the pre-bifurcation regime were used in the forecasting procedure.

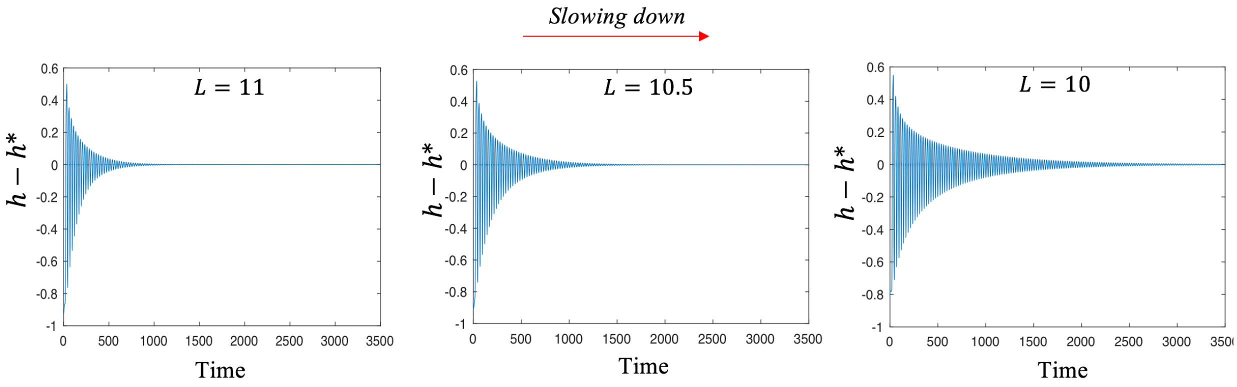

Figure 5.9. Recorded headways between two consecutive cars arbitrary selected after a perturbation from the equilibrium state at three parameter values in the pre-bifurcation regime. Dynamics of the system slows down as the system approaches the bifurcation.

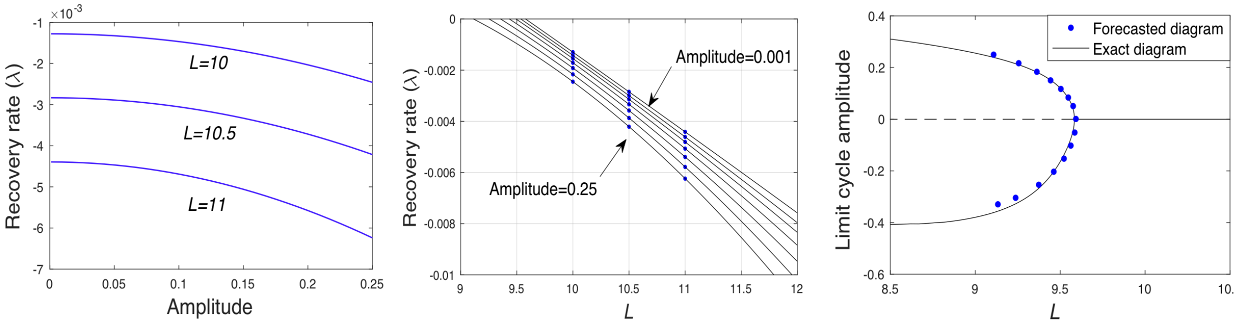

(a) (b) (c)

Figure 5.10. Forecasting using measurements depicted in Fig. 9. (a) recovery rate versus amplitude for local maxima of the data at each parameter (L) is computed to forecast the upper branch of bifurcation diagram. (b) Extrapolated recovery rates at selected amplitudes to forecast the corresponding parameter at which the recovery rate is zero. (c) Exact and forecasted bifurcation diagrams of the system.

Considering only one of the headways for forecasting is an advantage. For example, a driver can forecast that a traffic jam is approaching by monitoring its distance to the car in the front. This type of forecasting, however, is not as accurate if there is uncertainty in the system. For example, the driver in the front might not perfectly follow the OVF or may have a stochastic behavior. In such cases, a single headway may contain a large amount of noise, and cannot be used for accurate forecasting. To address this issue, a macroscopic variable capturing the system dynamics using information obtained from multiple cars can be used. The macroscopic variable which is used here is the standard deviation of all headways with respect to the quasi-stationary equilibrium, which can be written as follows [135]

$$\sigma(t) = \sqrt{\frac{1}{N-1}\sum_{i=1}^{N}\left(h_i(t) - h_{avg}\right)^2}, \tag{5.11}$$

where h_{avg} is the quasi-stationary equilibrium given by $h_{avg} = L/N$, N is the number of cars on the road, and $h_i(t)$ is the i^{th} headway (Fig. 5.4).

This macroscopic variable takes all headways into account. It can be shown that $\sigma(t)$ exhibits a pitchfork bifurcation corresponding to the Hopf bifurcation in the microscopic variables [135]. The pitchfork bifurcation occurs at a value L_c of the bifurcation parameter that corresponds to the onset of the traffic jam. Before the parameter reaches its critical value L_c, the equilibrium point of the system is at σ^*=0 meaning that variation of headways from quasi-stationary equilibrium is zero. However, this value is not zero when the system passes the stability boundary.

The variation of $\sigma(t)$ versus time for $L = 11$, $L = 10.5$ and $L = 10$ is computed and results are shown in Fig. 5.11(a). The slowing down behavior is observed in $\sigma(t)$ as the system approaches the critical parameter value. Note that it takes longer for the system to reach to its equilibrium state after a perturbation is applied. Using measurements of system recovery from initial perturbations (Fig. 5.11(a)) and following the bifurcation forecasting method in Section 5.2.2., the onset of a traffic jam and the bifurcation diagram are forecasted as shown in Fig. 5.11(b) which provides information about the macroscopic dynamics of the system near and after the onset of the instability.

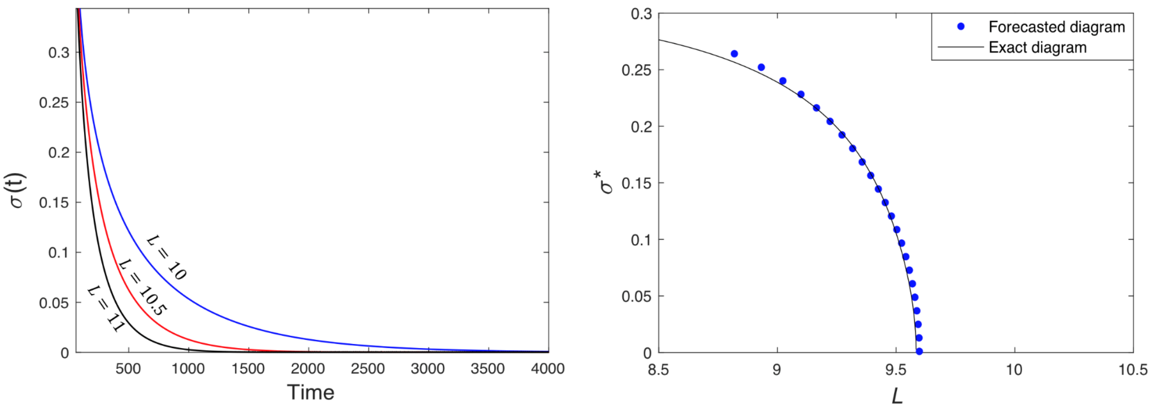

(a) (b)

Figure 5.11. (a) Measured variation of standard deviation σ of the headways versus time around the quasi-stationary equilibrium after a perturbation. Measurements are collected at parameter values before the onset of the traffic jam. (b) Exact and forecasted bifurcation diagrams for the macroscopic variable σ using measurements shown at Fig. 5.11(a) and the bifurcation forecasting method.

Note that the largest forecasted amplitude in the forecasted bifurcation diagram cannot be larger than the amplitude created by the perturbations. If the only purpose of the analysis is to forecast the critical parameter value L_c and not the bifurcation diagram, then large perturbations are not required. Furthermore, the forecasting accuracy of the bifurcation forecasting method is increased as the parameter values used for forecasting are closer to the critical value, especially when the purpose is to forecast the complete bifurcation diagram and not only the critical point. The variation of forecasting accuracy versus distance from the critical point can be examined in Fig. 5.12. Measurements at three different sets of parameter values L are used for forecasting. These sets are {12.5, 12, 11.5}, {12, 11.5, 11}, and {11, 10.5, 10}. The results show that the forecasting accuracy decreases when the parameter values used for forecasting are farther from the bifurcation point. This is expected because the forecasting is based on extrapolating the recovery rates and the accuracy of the extrapolation decreases with the distance to the bifurcation. The challenge is that the distance at which the forecasting method provides accurate results is not known in priori, and depends on the system dynamics. More importantly, there is no prior knowledge about the value of critical point when the forecasting method is applied. Hence, the current state of the system might be far from the bifurcation point which may result errors in the forecasting results. However, the forecasting result is still valuable because it provides a preliminary approximation of the critical parameter value, and the results can be updated with increased accuracy as the system approaches to bifurcation. Recall that the closer the system is to the bifurcation, the more accurate the forecasting is.

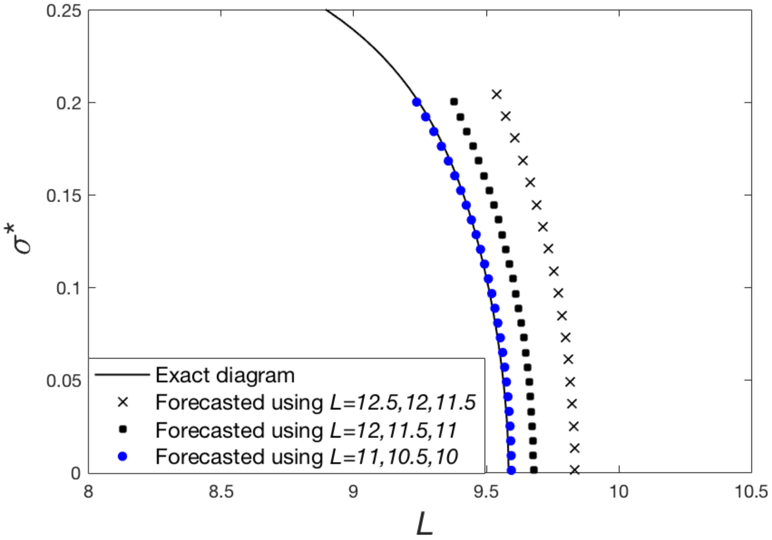

Figure 5.12. Forecasted bifurcation diagram using bifurcation forecasting method and data recorded at three different set of parameters. The forecasting accuracy increases using measurements at parameter values which are closer to the bifurcation.

In the next example, the maximum velocity of cars in the OVF is increased to $v_{max} = 1.05$. In this case, the system exhibits a subcritical bifurcation meaning that the system might jump to another stable attractor while the parameter has not yet passed the linear stability boundary. In the car following model, this means that a large perturbation, e.g. when one of the drivers suddenly reduces the speed for a short period of time, might result in a persistent traffic phenomenon even before the road reaches to its critical car density limit computed from a linear analysis.

The goal is to forecast the bifurcation diagram and predict that the system is approaching a sharp transition (i.e., heavy stop-and-go traffic). Figure 5.13(a) shows the recovery rates computed using measured recoveries from perturbations at parameters $L = 12.6$, $L = 12.3$ and $L = 12.0$. The forecasted bifurcation diagram is shown in Fig. 5.13(b), where the results match the exact ones computed directly using system equations. These results show that the forecast successfully predicts that the system experiences a subcritical bifurcation with a bi-stable region, where jumps in the dynamics are possible even before the linear critical density.

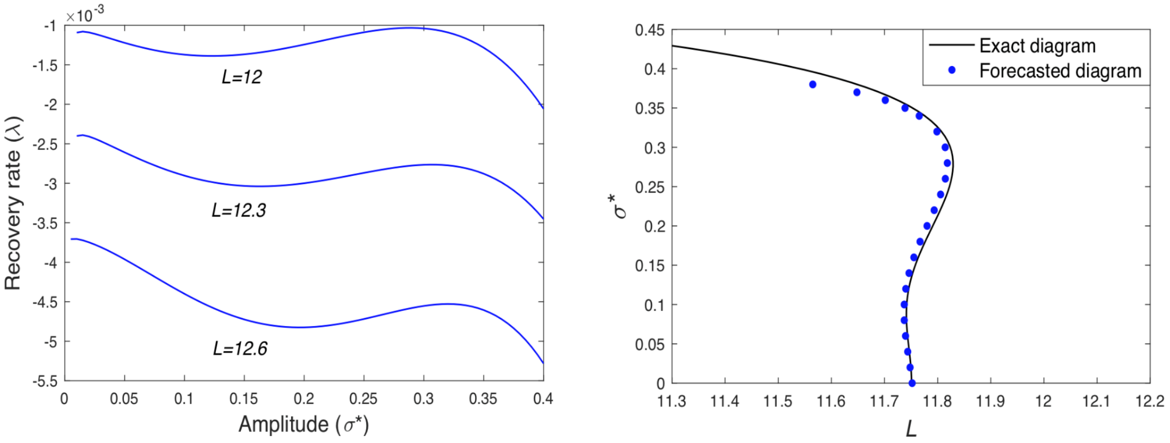

(a) (b)

Figure 5.13. Exact and forecasted bifurcation diagram of the system that exhibits a subcritical bifurcation. (a) Recovery rate versus amplitude for the measured macroscopic variable measured after perturbations applied to the system at three parameter values in the pre-bifurcation regime. (b) Exact and forecasted bifurcation diagrams of the system.

5.5 Conclusions

The onset of traffic jams on a circular road was forecasted using early warning indicators/signals and bifurcation forecasting methods. Forecasting approaches were applied to a microscopic model of cars on a circular road. Results show that forecasting approaches can successfully predict the critical parameter value at which traffic jams occur. Furthermore, the bifurcation forecasting method can be used for forecasting both the critical point (i.e., the onset of traffic jams) and the post-critical dynamics of the system (i.e. the bifurcation diagram). These results are particularly valuable when the state of the system after the bifurcation is of interest.

The forecasting approaches are model-free. That represents a substantial advantages for complex systems such as traffic flow systems where an accurate mathematical model is not easily available. All that is needed for forecasting is to collect measurements of the system dynamics in the pre-bifurcation regime (before traffic jams occur). Moreover, forecasting can be highly advantageous also for theoretical or computational analyses of traffic flow models where employing traditional methods for computation of bifurcation diagrams are computationally intense. Recall that only a few time series are needed to forecast a large portion of the bifurcation diagram, which contrasts the amount of calculations needed to simulate the system dynamics at each parameter value in the post-bifurcation regime (i.e., the many time series) needed to construct the bifurcation diagram by traditional methods.

The methodologies presented can be extended to analyze the stability of more complex traffic models. Although the model used to generate surrogate data in this study is a simple traffic model compared to real systems, and although some of the data used for forecasting cannot be easily recorded in real situations, the approaches and ideas presented can be used as a basis for more developments to address some of the challenges related to the complexity of traffic dynamics.

Chapter 6

Forecasting Critical Transitions and Future Stability of Natural Populations

6.1 Introduction

Numerous studies have revealed a variety of systems that are at risk of undergoing critical transitions [1,2], ranging from systems commonly examined in engineering [4,101], chemistry [5,6], physics [7,8], and biology [9–11], to others related to climate sciences [12–14], medicine and disease [15–17], social sciences [18–20], and ecology [21–23]. Specifically, regime shifts in ecological systems have received growing attention as the cumulative human impact on the environment has increased the risk of ecological regime shifts [21–23,36,136–139] (Fig. 6.1). Consequences include the collapse of natural populations which inhabit the ecosystem at risk [11], and these consequences are important because typically it is exceedingly difficult to reverse the system to its pre-transition condition [24,25] after a critical transition occurs. Hence, it is necessary to develop methods capable of forecasting the upcoming transition, as part of a preventive plan against possible detrimental consequences.

The need to forecast critical transitions has triggered much research in the recent years and has resulted in developing early warning signals to mark such undesirable transitions [35]. Anticipating critical transitions can be straightforward if a mathematical model exists for the system. However, accurate predictive modelling can be challenging, especially when the system is complex (e.g., it has many agents with nonlinear interactions). Moreover, even when a mathematical model is introduced, it may be incomplete or inaccurate due to assumptions and uncertainties in modeling and parameter values. Hence, predictions based on models of limited accuracy face substantial difficulties [26]. As a result, researchers have focused on developing model-less approaches to extract early warning signals from observed time series, and several indicators have been introduced for this purpose [26–33]. The most widely used early warning signals such as increasing variance [29,32] and autocorrelation [12,29], are built on the basis of critical slowing down. This phenomenon refers to the slowing down of a system's dynamics around its equilibrium when approaching a tipping point [34]. Recent observations have indicated the existence of critical slowing down before a tipping point in natural ecosystems [129,140], a finding which highlights the importance of methods developed based on this feature.

The advantage of applying early warning indicators to successfully raise the alarm when approaching a tipping point has been described in several recent studies [26–33,35]. However, many open questions remain. For example, although the indicators start to increase as the system approaches the tipping point, it is necessary to know quantitatively the distance (in the parameter space) to the upcoming transition to allow a better management of the system. Second, it is pivotal to know the type of the upcoming transition, i.e. whether the system is approaching a catastrophic or a non-catastrophic transition. However, based on nonlinear systems theory, critical slowing down [2,12,34–36] and an increase in most available early warning indicators do not predict the type of transition because they occur in both catastrophic and non-catastrophic transitions, such as transcritical and supercritical pitchfork bifurcations. In addition, management actions often require estimates for the future equilibrium points of the system before and after the transition. Such estimates have to be obtained using knowledge of the pre-transition system behavior. A forecasting method capable of addressing these questions would be of great importance for the management of ecosystems, as it would help to assess the existence of crucial thresholds and to evaluate the future consequences of surpassing them [41].

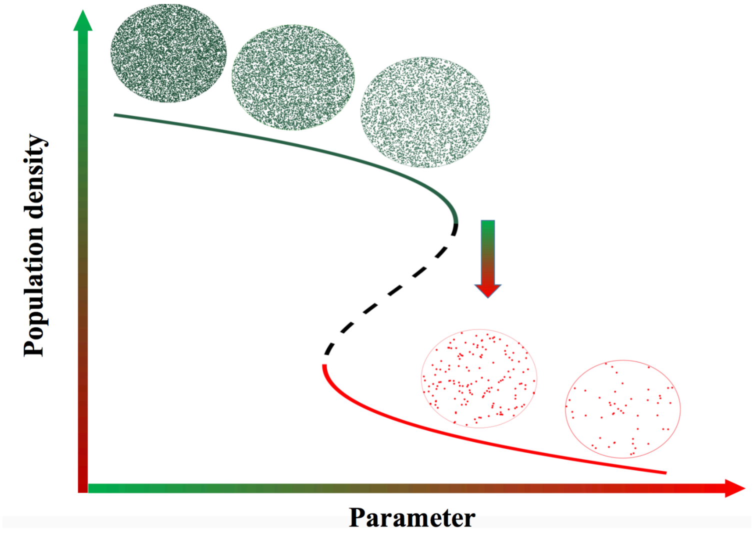

Figure 6.1. Schematic of a natural population subject to a critical transition. The state of the system changes abruptly from one equilibrium to another due to a slow change in the parameter.

In this work, we introduce a model-free approach, referred to as the bifurcation forecasting method [4,8], to address the aforementioned questions. Based on observations of the system response to perturbations only in the pre-transition regime, the method forecasts the bifurcation diagram which characterizes the stability and equilibria of the system in upcoming conditions (Fig. 6.2). The idea of the bifurcation forecasting method has been successfully evaluated using simulations and experiments in some engineered systems [4,8,101]. The aim of this work is to introduce and investigate the application of the bifurcation forecasting method in living systems. The forecasting approach described herein uses the phenomenon of critical slowing down, namely the slowing down of the dynamics around an equilibrium when the system approaches a tipping point [34].

Determining the conditions under which the forecasting method is reliable in ecological and biological systems requires experimental validation. To this end, we use a budding yeast population with cooperative growth, with sucrose as the carbon source which is known to exhibit a critical transition as the environment deteriorates [11]. The existence of the Allee effect [141] leads to bi-stability and a fold bifurcation at which the yeast population exhibits a catastrophic transition, accompanied by a critical slowing down phenomenon as the environment deteriorates, resembling an ecological collapse. The bifurcation parameter of the system is selected to be the mortality rate, which represents real environmental conditions, e.g. mortality because of predation. As the mortality rate increases, the system is pushed toward a critical transition resulting in population extinction.

The present study is the first experimental validation of bifurcation forecasting method for ecological systems which are inherently complex. The main focus of this study is to demonstrate and experimentally validate the suggested forecasting method, using a real living system. The forecasting method is also investigated theoretically, using the yeast population as a model system, as described below in more detail.

6.2 Forecasting method overview

The bifurcation forecasting method is a model-free approach and is based on time-series measurements of the system's response to perturbations (only) in the pre-transition regime. The method is based on the critical slowing down phenomenon, and is able to forecast the bifurcation diagrams of systems exhibiting this phenomenon, such as systems approaching to a fold, pitchfork, Hopf or transcritical bifurcation. Forecasting the bifurcation diagram enables us to identify the distance to upcoming transitions, the type of the transitions (catastrophic/non-catastrophic) and future equilibrium points of the system in study.

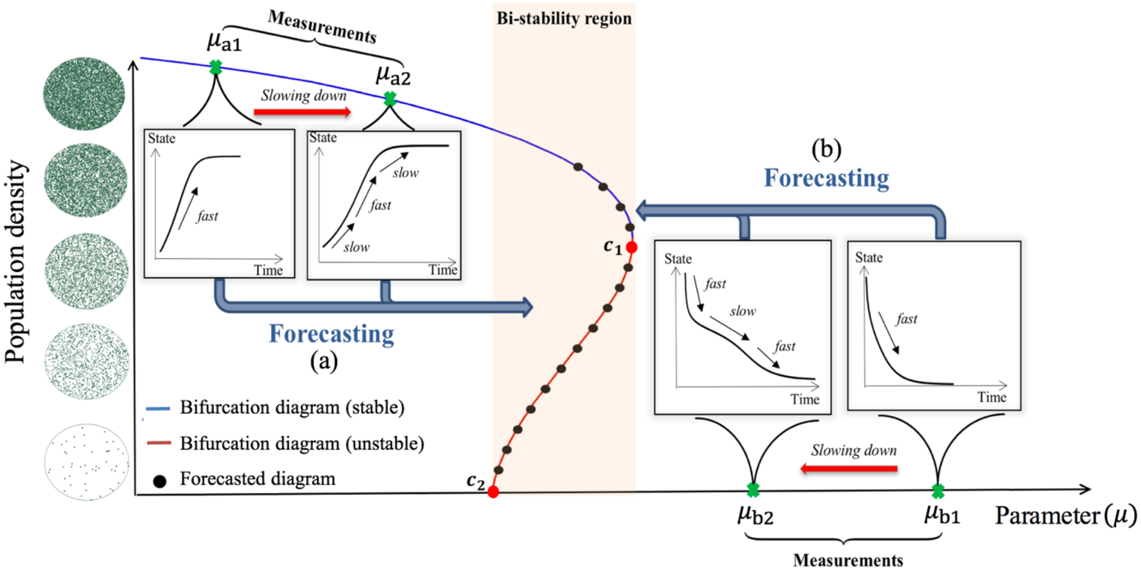

Figure 6.2. Schematic overview of the bifurcation forecasting method. Measurements from perturbations in pre-bifurcation conditions (a) are employed to forecast the upcoming transition (black dots). As the system approaches a bifurcation, the rate of system's recovery is decreased. At a fixed amplitude, the recovery rate decreases when the system approaches the bifurcation. At a fixed parameter, the smallest recovery rate corresponds to the amplitude which is closest to the actual bifurcation diagram. The future stability of the system is forecasted considering this change in the recovery rates. The system has two critical points (c_1 and c_2) which determine the boundaries of the bi-stability region. Cases (a) and (b) demonstrate the schematic of forecasting procedure for the system operating at either side of the critical points, and are addressed in the experimental study.

Close to the bifurcation point, external perturbations lead to a long transient before the system reaches its stable state, which means that the system's recovery rate decreases. Therefore, the system's recovery rate from perturbations can be used as an indicator, and is correlated to the distance to bifurcations. The total recovery time from perturbation is a good indicator of the distance to the tipping points [142]. However, it should be mentioned that the recovery rate is different at different amplitudes, and the rate of recovery at each amplitude cannot be compared with that in the other amplitudes. Taking this difference into account results in more accurate estimation of the future stability of the system. At a fixed amplitude, the recovery rate decreases when a system approaches bifurcation. Similarly, at a fixed parameter, the smallest recovery rate corresponds to the amplitude which is closer to the actual bifurcation diagram. This idea is employed in the bifurcation forecasting method and results in forecasting the bifurcation diagram of the system, which reveals the type of the transition and the future fixed points of the system.

We define the recovery rate as $\lambda = \dot{r}/r$, where r is the system amplitude and the over-dot represents the time derivative. The recovery rate is a function of both the system's parameter and of the amplitude. For example, in an ecological system, the amplitude can be the population density and the parameter is an environmental feature, such as temperature, mortality rate or any other index representing a specific environmental condition. We measure the system's recovery from perturbations at least at two system parameters, and recovery rates are approximated for the available amplitudes at each parameter. At each amplitude computed recovery rates are extrapolated to identify the parameter at which the system is expected to have a zero recovery rate. A zero recovery rate corresponds to a fixed point on the bifurcation diagram, regardless of its stability. Repeating this procedure for different measured amplitudes enables us to approximate the bifurcation diagram of the system. Hence, the system's future stability can be approximated using the forecasting method (Fig. 6.3).

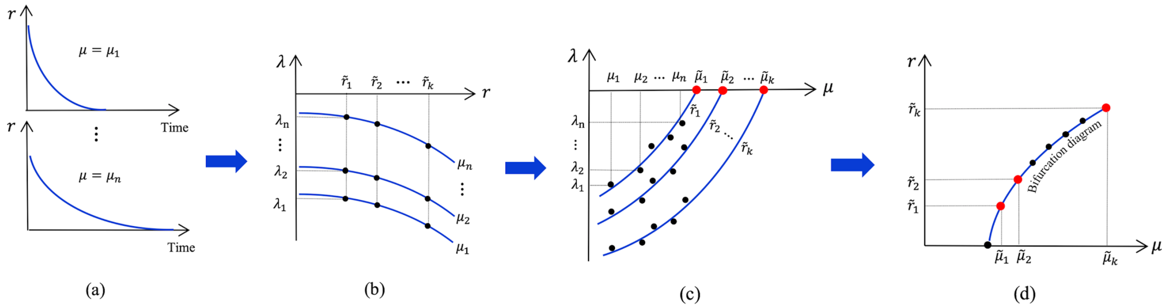

Figure 6.3. Steps followed to forecast the bifurcation diagram: (a) measure the system response to perturbations at several parameter values, (b) approximate the recovery rates from time series measurements, (c) identify the parameter $\tilde{\mu}$ at which the recovery rate for a specific amplitude $\tilde{r}$ is zero, (d) repeat steps (b) and (c) for several amplitudes $\tilde{r}$, and finally construct the bifurcation diagram using pairs of ($\tilde{\mu}$,$\tilde{r}$).

We forecast the bifurcation diagram of the yeast population using measurements from one side of the bifurcation diagram. We demonstrate the forecasting method separately for each side (see cases (a) and (b) in Fig. 6.2). Each case corresponds to a type of transition which is commonly reported for many systems. One is the extinction case, where the population is approaching a critical transition which results in the collapse of the population, as is observed in ecological systems [1,24,34] (case (a) in Fig. 6.2). The second is the emergence case, where a sudden increase in the population occurs, as is observed in outbreaks of infectious diseases [143–145] (case (b) in Fig. 6.2).

To forecast the bifurcation diagram, one needs measured recoveries at two or more parameter values in the pre-transition regime. In general, increasing the number of measured parameter values and the number of measured recoveries at each parameter value alleviates the effect of noise and enhances the forecasting accuracy. Both small and large perturbations can be used for the forecasting purpose. However, one should note that all forecasted amplitudes in the bifurcation diagram must be included in the measured system's response to perturbations. Since the approach is not restricted to small perturbations, one can forecast the critical points which have amplitude far away from the current equilibrium point of system. For instance, in a saddle node bifurcation, there is a tipping point which has large amplitude, also known as turning point. Both the amplitude and the parameter at which this critical point occurs can be forecasted, an achievement of great importance since this point marks the beginning of the bistability region (Fig. 6.2).

There are a number of requirements for the forecasting method to be accurate. First, it is required that the system is close enough to the bifurcation to exhibit a measurable slowing down in the recorded recovery. The interpretation of "close enough" may vary for different systems, and depends on the system dynamics. Second, the obtained measurements have to contain identifiable parts on the inertial manifold to ensure that changes in the recovery rates are due to the slowing down phenomenon. The inertial manifold is an invariant set where the dynamics is the slowest in time and contains key dynamic features of the system [146,147]. This manifold is the slowest, and if the system starts from a state in this set, it remains in that set at all times. This fact needs more attention for large dimensional systems, where the fast dynamics of the system needs to be filtered out [101]. A third requirement is that the dynamics and the inertial manifold should vary smoothly with the bifurcation parameter. If the change in dynamics between two measured parameters is significant, the forecasting is not accurate [8].

6.3 Experimental procedure

The core design of our experiments is based on the system introduced by Dai and colleagues [11], and used successfully in other experimental studies of catastrophic transitions and early warning signals [148–151]. The system is an ecological system designed by exploiting the cooperative growth of budding yeast in sucrose. The yeast system is used because it is easy to manipulate and displays key similarities with many natural populations.

We culture a selected yeast (*Saccharomyces cerevisiae*) strain under well-controlled conditions. The strain BY44741 is selected based on its auxotrophic properties and cooperative growth [152]. *Saccharomyces cerevisiae* displays cooperative growth, where individual cells use metabolites produced extracellularly by neighbor cells [149]. Hence, the system possesses a strong Allee effect [141], which can cause bi-stability and lead to catastrophic transition. The cell density is an important factor affecting population growth in this system. On one hand, at low densities it is difficult for cells to cooperate and produce enough resources to survive. On the other hand, the resources are not enough at high densities, and the growth rate is decreased due to competition among cells. Therefore, at intermediate densities, the per capita growth rate is maximal, while it is negative at low and high densities [11].

All experiments were performed on 96-well flat bottom sterile polystyrene microplates, Corning Falcon, USA, at 200uL volume, in IncuShaker orbital shaker, Denville Scientific, USA, at $30°C$, $300rpm$, in synthetic growth medium of BD Difco Dehydrated Culture Media Yeast Nitrogen Base (YNB) without amino acids, with the addition of Complete Supplement Mixture (CSM), Sunrise Science, USA, and 2% sucrose made from 20% sucrose stock solution in $1mM$ Tris buffer, pH 8.0, UV and filter sterilized, added fresh daily to the YNB/CSM mixture. All experiments in the same series were performed with the same solutions, to avoid variations in the experimental system. The bifurcation parameter of the system was selected to be the mortality rate introduced to the system by dilution. Namely, only a fraction of the population was transferred into fresh media every day. This corresponds to a population that is affected by an incident occurring periodically, such as predator invasion or the breakout of a disease, at which only a fraction of the initial population survives. Dilutions were performed every 23 hours, in predefined dilution factors, after the population density was monitored in a Cytation 1 Cell Imaging Multi-Mode Reader, BioTek, USA, by measuring the optical density at $620nm$. For each dilution factor, we performed 6 to 10 parallel experiments. Furthermore, each experiment had technical 7 replications using the same source of materials at the same experimental conditions. To this end, we prepared every day the initial sample and distributed it into 7 wells of a 96-well microplate, $200\mu L$ each. Perturbations were applied to the system using randomly selected initial population densities, and the recovery from perturbations was measured until the population returned to its equilibrium state.

Results show that at low mortality rates and after a perturbation, the population recovers to its non-zero equilibrium with a high recovery rate. Furthermore, the population can survive from large perturbations since the cooperative growth of cells dominates over the effect of mortality on the system. As the mortality rate increases, the system is pushed toward a critical transition resulting in population extinction. The reverse occurs as the mortality decreases, leading to emergence. The schematic of the experimental procedure is demonstrated in Fig. 6.4.

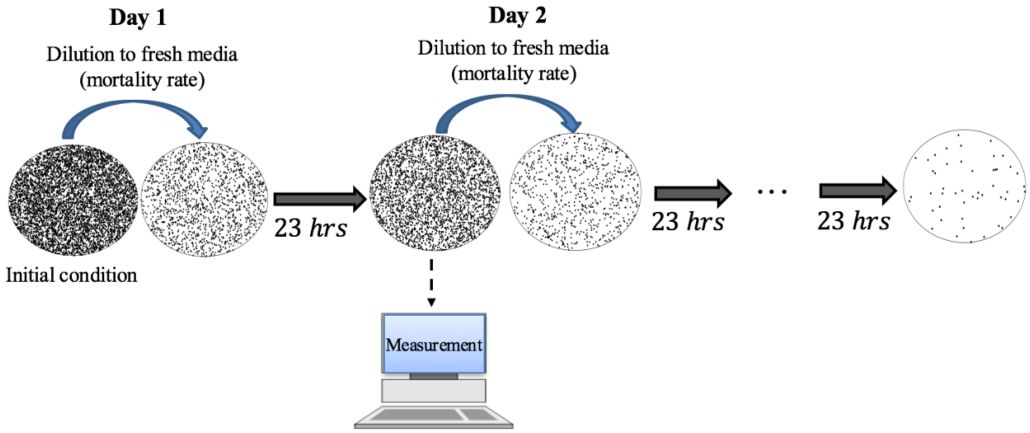

Figure 6.4. Overview of the experimental procedure. Starting from an initial population density, buddying yeast is cultured on 96-well microplates, in an orbital shaker at 30°C, 300rpm. After 23 hrs of growth, population density is measured using a photometer. Using a selected dilution factor, a fraction of population is then transferred to fresh media and is left to grow for another 23 hours. The procedure is repeated every day until the population is extinct, or it reaches its equilibrium state.

6.3.1 Calibration curve

Cell density was tracked by measuring the optical density of the yeast population at $620nm$. A calibration curve was constructed, showing the corresponding cell density for every measured optical density. To this aim, a series of yeast samples with different densities were prepared, at $200\mu L$ final volume. The optical density of each sample was measured using the

Cytation 1 Cell Imaging Multi-Mode Reader, BioTek, USA. Next, the actual cell density of each sample was measured using the Scepter 2.0 Handheld Automated Cell Counter, EMD Millipore, USA. Measured values are shown in Fig. 6.5 by square markers. A low order polynomial is fitted to the data and used as the calibration curve in the performed data analysis.

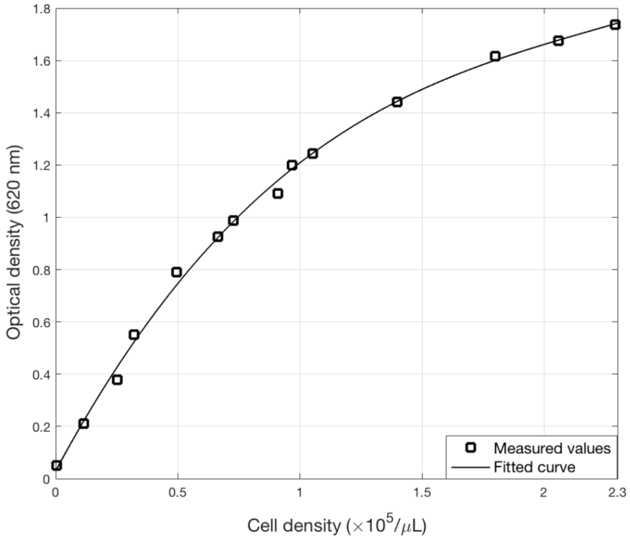

Figure 6.5. Calibration curve mapping the measured $620nm$ optical density to the actual cell density.

6.3.2 Verification of existence of saddle-node bifurcation in the system

In this part, we performed some experiments to verify that our experimental procedure results in a system exhibiting a bifurcation. Below are the experimental results at two selected dilution factors as the bifurcation parameters. It is observed that at the dilution factor of 1400, the population survives starting from large enough initial conditions, while in other cases the population undergoes extinction. Therefore, the system has bi-stability at this parameter which verifies the existence of Allee effect in the system. On the other hand, we observe that at the dilution factor of 1600, the only equilibrium point of the system is the extinction state, where no population exists (Fig. 6.6). Based on these observations, we conclude that the system exhibits a saddle-node (catastrophic) bifurcation, and the critical dilution factor which is the starting point of the bi-stability region (c_1 in Fig. 6.2) is between 1400 and 1600.

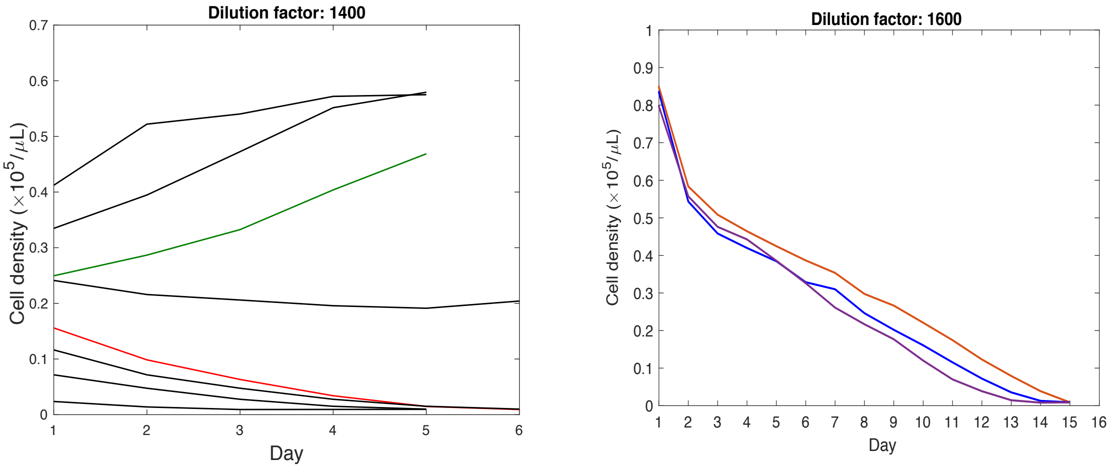

Figure 6.6. Results of the experiments performed to verify the existence of bifurcation and bi-stability in the system. Each line corresponds to a separate experiment. We observe bi-stability at the dilution factor of 1400 and extinction at the dilution factor of 1600, which verifies the existence of saddle-node bifurcation in the system.

6.3.3 Experimental points on the bifurcation diagram

A series of experiments were performed to identify several stable and unstable fixed points on the bifurcation diagram. We selected the dilution factors of 800, 1,000, 1,200, 1,300 and 1,400 to identify the non-zero stable values of population density at these parameter values. For this purpose, we started the experiments from selected initial population densities, and the system was monitored until the populations reached and stayed at their equilibrium state for several days. The stable values on the diagram were obtained by averaging the populations over the period during which they remained at their equilibrium state (Fig. 6.7).

Approximating unstable fixed points is more challenging since the system diverges from them. To approximate the values on the unstable branch, we considered dilution factors of 1,000, 1,200, 1,300 and 1,400. At each dilution factor, we monitored the population growth starting from several initial conditions. The region between two initial conditions resulting one in survival and one in extinction of the population was selected as the region containing the unstable fixed point (Fig. 6.8). Although the value of the unstable fixed points is not determined with high accuracy, this procedure provides an acceptable approximation of the unstable branch. This is required in order to evaluate the forecasting results, as well as to conduct the model calibration described in the next section.

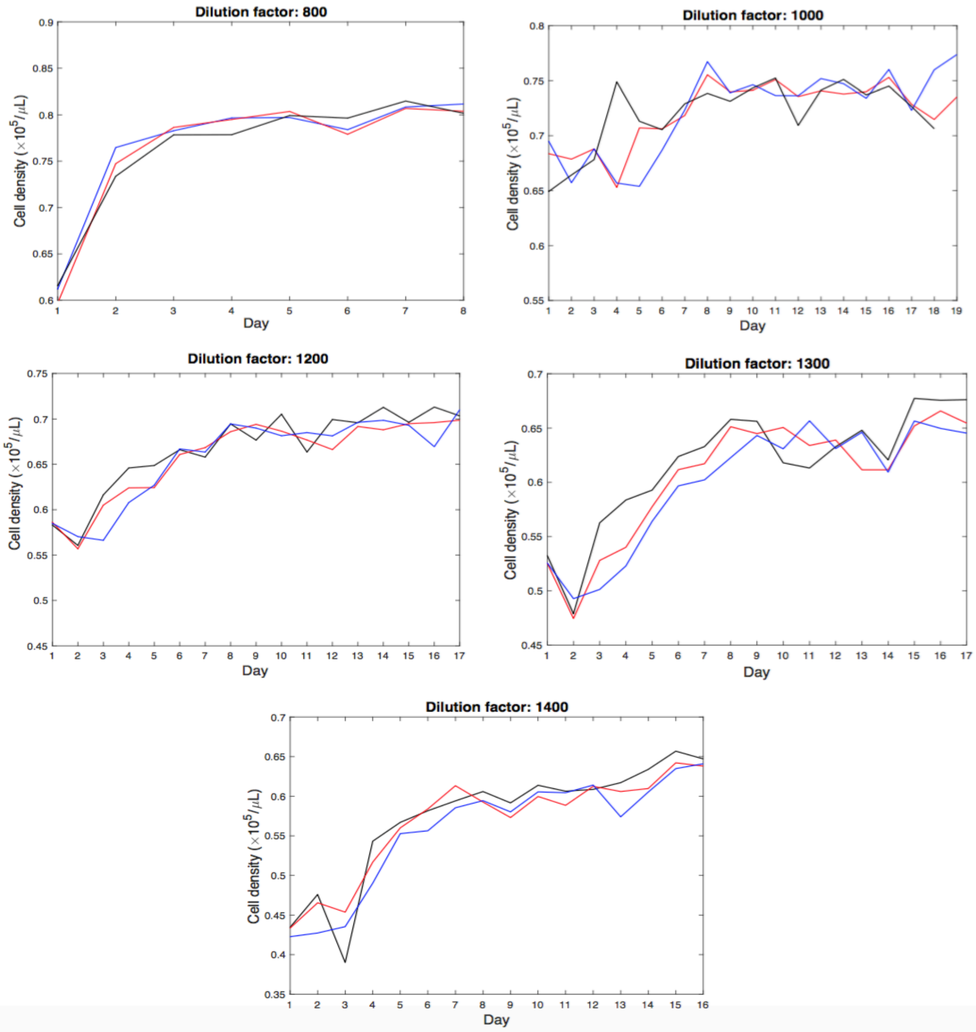

Figure 6.7. Results of the experiments performed to identify the stable fixed points of the bifurcation diagram. Three sets of experiments are run at each dilution factor. The stable values at each dilution factor are approximated by averaging the populations over the period during which they remain at the equilibrium state. Each line in the plots corresponds to a separate experiment.

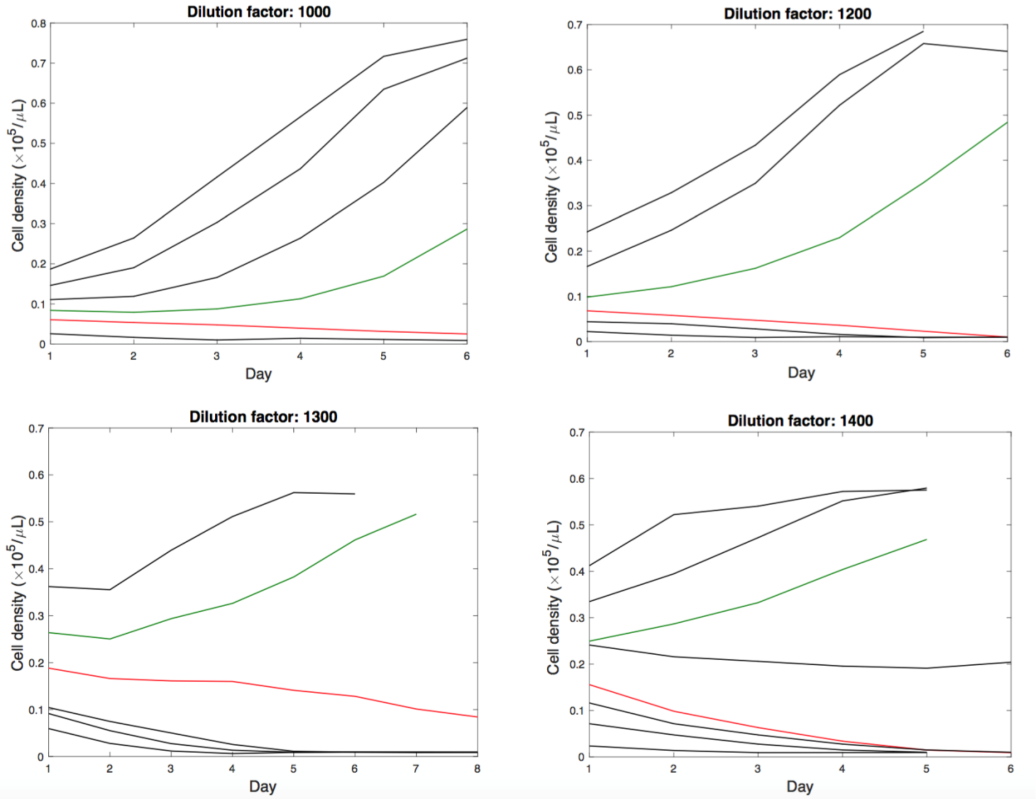

Figure 6.8. Results of the experiments performed to identify the unstable fixed points of the bifurcation diagram. At each dilution factor, the region between two initial conditions resulting in survival and extinction of the population is selected as the region containing the unstable fixed point.

6.3.4 Model calibration not used for forecasting

The forecasting method is a model-free approach, suitable for systems for which no mathematical model is available. However, based on the model suggested for the yeast growth by Dai et al. [11], we use the experimental data to find the best model parameters which match our experiments. This is done for two reasons. First, we build a model as close as possible to the experimental data to show that the proposed forecasting method can be successfully applied when no measurement or process noise is available in the system. Second, measuring stable and unstable fixed points close to the tipping point is practically not feasible in experiments due to noise and stochasticity in the dynamics. Since the focus of the proposed method is on the forecasting of tipping points and the parameter values close to these points, approximating the bifurcation diagram theoretically helps better interpret the results.

The two-phase mathematical model is in the following form [11]:

$$\frac{1}{N}\frac{dN}{dt} = \begin{cases} \gamma_{low} & 0 < N < N_c \\ \gamma_{high}\left(1 - \frac{N}{K}\right) & N_c < N < K \end{cases}, \tag{6.1}$$

where N is the population density, K is the carrying capacity, γ_{low} and γ_{high} are the per capita growth rates for population densities smaller and greater than a threshold N_c. Moreover, there is a lag before the cells start to grow after they are transferred to a new media. In the simulations, this time lag is included in the 23hrs time period which is considered for the cells' growth.

To approximate the five unknown parameters of this model, we fed the experimental measurements of the bifurcation diagram into a genetic algorithm, and the model parameters best matching the experiments were extracted as shown in Table 6.1.

Table 6.1: Calibrated model parameters using experimental data and a genetic algorithm

	$\boldsymbol{K}$ $Cells/\mu L$	$\boldsymbol{\gamma_{low}}$ (hr^{-1})	$\boldsymbol{\gamma_{high}}$ (hr^{-1})	$\boldsymbol{N_c}$ $(Cells/\mu L)$	$\boldsymbol{Time\ Lag}$ (hr)
Model fitting	0.923×10^5	0.255	0.419	174	1.38
Experiment	0.854×10^5	No measurements	0.503	No measurements	1.33

We have also computed the three parameters $\boldsymbol{K}$, γ_{high} and the time lag experimentally to evaluate the validity of the genetic algorithm results. To approximate the time lag before population growth, several experiments were initiated starting from different initial conditions. We started recording the population growth right after the initiation of the experiment using the plate reader. The plate was placed in the plate reader, with the temperature set to $30°C$ and the orbital shaking speed at $300rpm$. The optical density was measured every 10min for a total of 4.5hrs. The results depicted in Fig. 6.9 show that the population starts an exponential growth after approximately 80min, which represents the experimentally defined time lag.

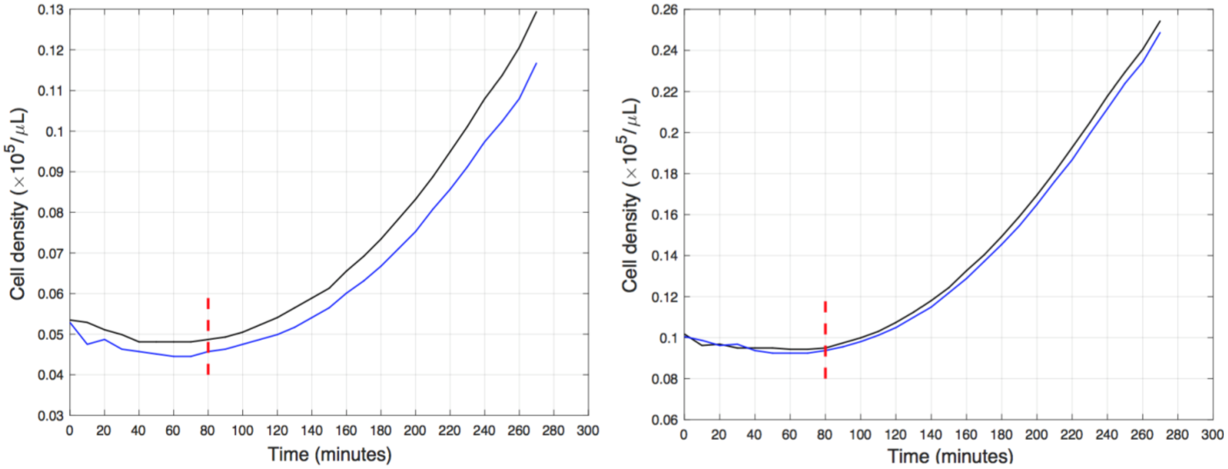

Figure 6.9. Estimating the time lag before population growth. Experiments are initiated from 2 sets of different initial conditions, and the population growth is monitored for 4.5hrs. Each solid line represents a separate experiment, and the estimated time lag is marked by a dashed line on each figure.

To approximate γ_{high} and K, we monitored the population growth starting from an initial density of $0.188 \times 10^5\ cells/\mu L$, which is expected to be greater than N_c. The experiment was initiated several hours in advance to make sure that the population was in the exponential growth phase (log phase). The population was then monitored for 17hrs until it reached and stayed at its saturated state (stationary phase) for about 5hrs (Fig. 6.10). We prepared the initial sample in a large volume and aliquoted the homogenous solution into 48 wells of a 96-well microplate, $200\mu L$ each. Results are shown in Fig. 6.10. Considering a logistic growth for the population, the parameters are found to be $\gamma_{high} \approx 0.503\ hr^{-1}$ and $K \approx 0.854 \times 10^5\ cells/\mu L$.

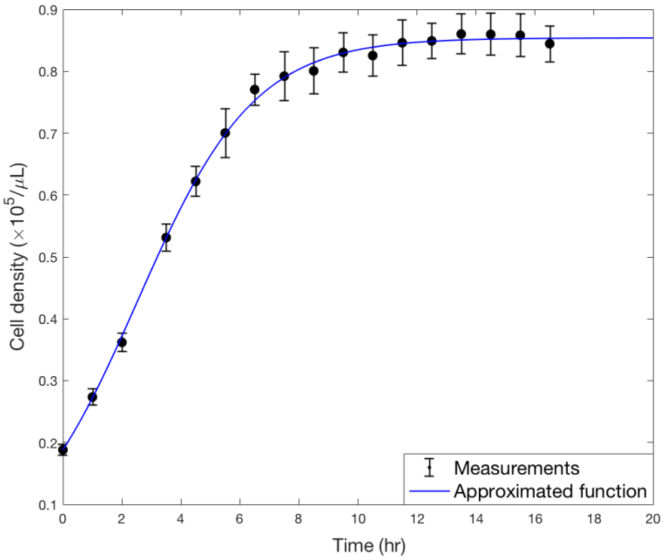

Figure 6.10. Experimental results of estimating γ_{high} and K. A population started from intermediate initial density was observed over 17hrs. Experimental results are demonstrated by mean and standard deviation error bars of 48 simultaneously performed replications.

Comparing the directly measured parameters to those obtained by using the genetic algorithm (in Table 6.1), it is observed that they are in the same range. The calibrated model is used to generate the bifurcation diagram of the system as a reference to be compared with the forecasting results.

6.4 Experimental forecasting results

We monitor the effects of different dilution factors (mortality rates) on the density of the yeast population and on its ability to recover from perturbations. Figure 6.11 shows the approximated bifurcation diagram of the system based on experimental measurements. Experimental results show that the population becomes extinct at a dilution factor of 1,600, and is stable at a high density at a dilution factor of 1,400. Hence, the tipping point is expected to be between dilution factors 1,400 and 1,600. In general, the effects of noise, stochasticity, and the slowing down make it particularly challenging to measure stable and unstable fixed points close to the tipping point. The closer the system is to the tipping point, the worse the signal to noise ratio becomes, and the longer the system has to be observed to determine its stability. To address this challenge, we feed the experimental data into a genetic optimization algorithm to calibrate a simple two-phase growth model suggested by Dai and Gore [11]. The bifurcation diagram of the calibrated model which matches best the experimental observations is constructed, as depicted in Fig. 6.11. Based on the calibrated model, the dilution factor at the tipping point is estimated to be approximately 1,505. Although this approximation provides an estimation of the system stability, it contains uncertainty and may not necessarily represent the true dynamics of the system. The approximated bifurcation diagram using the model does not quite agree with the location of the experimental fixed points. Therefore, any mismatch between the forecasting results in the following sections and the model-based estimation of the bifurcation diagram is not solely due to the forecasting accuracy. Note also that this model-based estimation of the bifurcation diagram is used only as a reference to validate the forecasting results presented in the following sections; forecasting does not require any model of the system and any bifurcation diagram *a priori.*

We forecast the bifurcation diagram of the yeast population using measurements from one side of the bifurcation diagram. We demonstrate the forecasting method separately for each side (see cases (a) and (b) in Fig. 6.2).

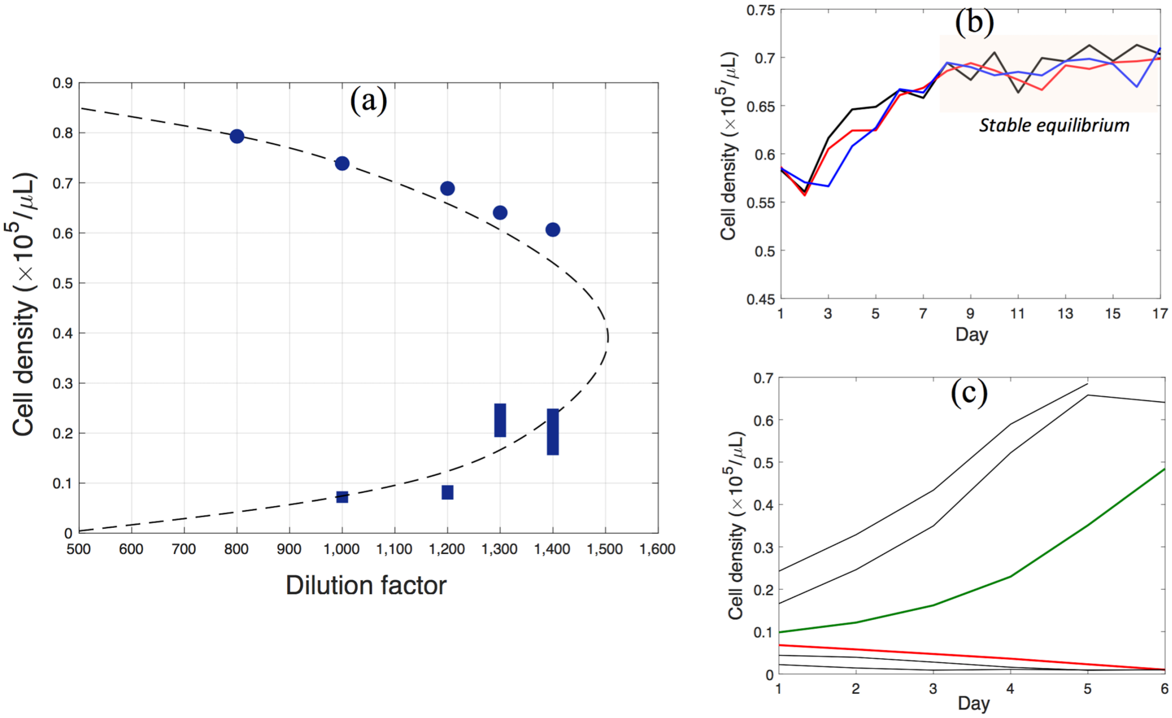

Figure 6.11. (a) Estimated bifurcation diagram of the buddying yeast system. Circles represent experimentally measured stable population densities at selected dilution factors obtained by averaging the populations which are at equilibrium over at least five days. Vertical bars represent experimentally approximated regions containing unstable fixed points at selected dilution factors obtained by monitoring the population growth starting from several initial densities and identifying the region between two initial conditions resulting in survival and extinction of the population. (b) and (c) depict the experiments performed at the dilution factor of 1,200 to identify the corresponding stable and unstable fixed points on the bifurcation diagram. The dashed line is the approximated bifurcation diagram using the calibrated model. The dilution factor at the tipping point is approximately 1,505. This bifurcation diagram is used as a reference to validate the forecasting results presented in the following sections.

As a first step we study extinction, which occurs as the dilution factor increases and has values closer and closer to the critical one (i.e. 1,505), as shown in case (a) in Fig. 6.2. The dilution factor is the bifurcation parameter, and the goal is to forecast both the type of upcoming transition and the dilution factor at which the extinction transition occurs. For forecasting we measure recoveries of the system from perturbations at two dilution factors (all prior to the transition). Specifically, we perturb the system using randomly selected initial population densities smaller than the stable values, at dilution factors of 1,200 and 1,300. Recoveries at other dilution factors can be used also. Figure 6.12 shows measured recoveries from perturbations.

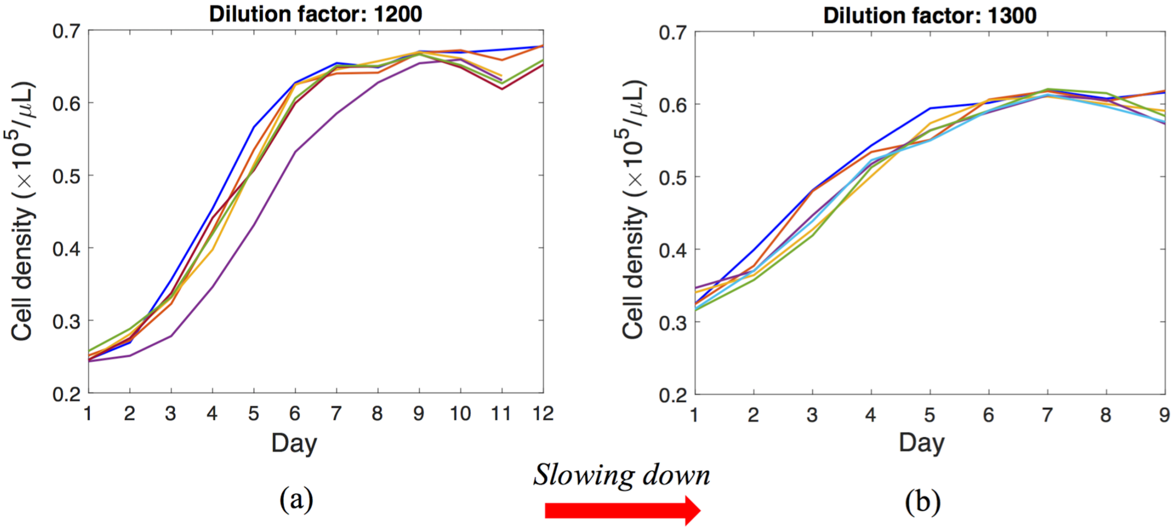

(a) (b)

Figure 6.12. Measured recoveries of the yeast population from perturbations at: (a) a dilution factor 1,200; (b) a dilution factor 1,300, while the system approaches to the tipping point from parameter values smaller than the critical parameter. Each line represents a separate experiment, and each experiment has 7 replications which are performed simultaneously using the same source of materials at exactly the same experimental conditions. The system slows down while approaching the critical transition, namely as the dilution factor increases from 1,200 to 1,300 (changing from (a) to (b)). These measurements are used to forecast the bifurcation diagram which corresponds to the schematic shown in case (a) of Fig. 2.

Figure 6.13(a) shows the recovery rates estimated from measurements. Note that the computed recovery rates in practical applications are noisy due to uncertainty in experiments (e.g., observe Figs. 6.13(a) and 6.14(b)). To alleviate the effect of noise and stochasticity, we exploit the idea that for amplitudes close to a bifurcation point, the change in the recovery rates with amplitude can be approximated by a second order polynomial. We smoothen the measured recovery rates using a second order polynomial in the *amplitude (r)-recovery rate* (λ) plane. This idea comes from the observation that recovery rates correlate with the distance to fixed points on the bifurcation diagram, with a peak value at the critical amplitude (see the schematic in Fig. 6.2, and the recovery rates computed in Figs 6.13(a) and 6.14(b) for further clarification). This approximation holds for both supercritical and subcritical bifurcations, although the accuracy may vary for different systems.

As expected, results show that the recovery rates decrease at all densities as the system approaches the tipping point. More importantly, the recovery rate at each population density is correlated to its distance from the bifurcation diagram. The system has its maximum recovery rate at a population density around $0.400 \times 10^5\ cells/\mu L$, meaning that this density is the farthest point on the bifurcation diagram from the current dilution factor. Using the approximated recovery rates, one can extrapolate data in the *dilution factor - recovery rate* plane to approximate the dilution factor ($\tilde{\mu}$) at which the recovery rate for a specific density ($\tilde{r}$) is zero (Fig. 6.13(b)). The point ($\tilde{\mu}, \tilde{r}$) is therefore a forecasted fixed point on the bifurcation diagram. This procedure is repeated for all available values of population densities, and the overall bifurcation diagram is forecasted (Fig. 6.13(c)). Based on the forecasting results, it is evident that the system is approaching a catastrophic fold bifurcation. Furthermore, the transition is forecasted to occur at a dilution factor of $1{,}582$ where the population density is $0.420 \times 10^5\ cells/\mu L$. The upcoming stable and unstable fixed points after the critical transition are forecasted also.

Using such results, one can approximate the maximum perturbations that the system can tolerate in the upcoming environmental conditions. For instance, it is forecasted that at the dilution factor of $1{,}400$, the population density would be stable at $0.575 \times 10^5\ cells/\mu L$, and if a perturbation pushes the population below the density of $0.248 \times 10^5\ cells/\mu L$, the population will not survive.

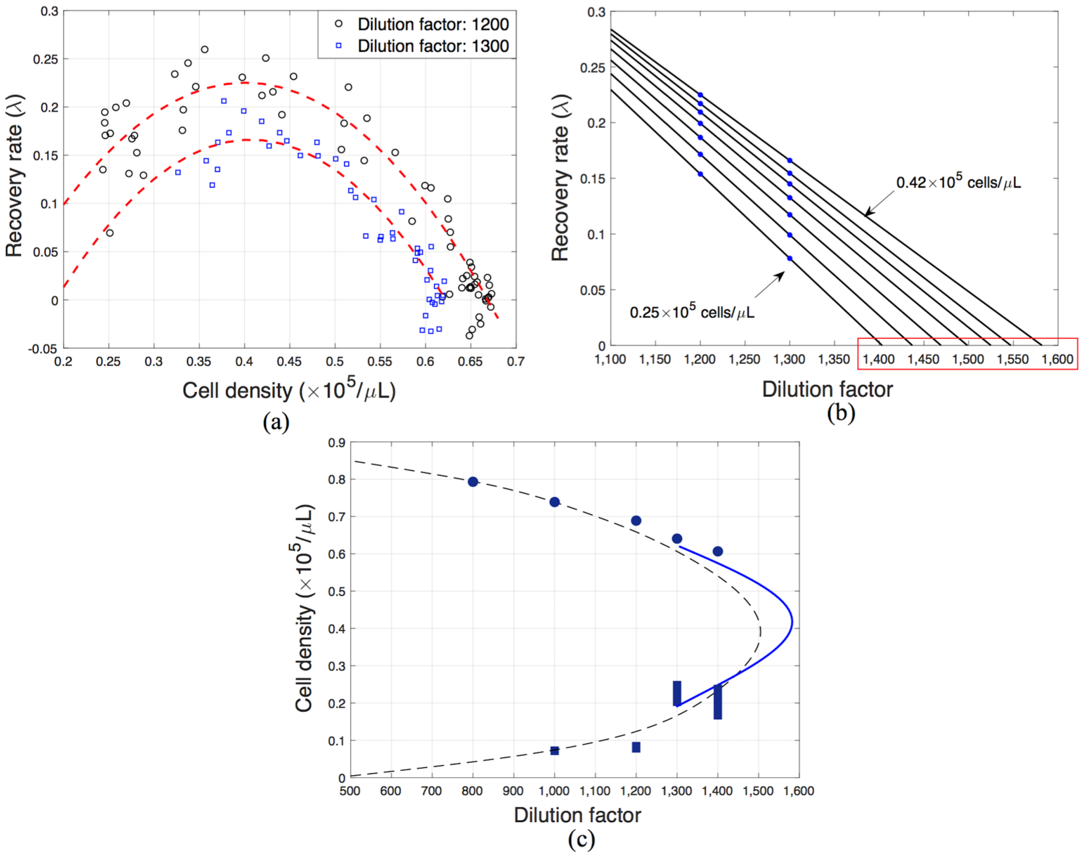

Figure 6.13. Forecasting using experimental measurements at dilution factors of 1,200 and 1,300 corresponding to case (a) shown in Fig. 6.2. (a) Recovery rates and quadratic polynomial fits at each amplitude estimated from the measurements shown in Fig. 6.12. (b) Example of extrapolated recovery rates at selected amplitudes to forecast the dilution factor at which the recovery rate is zero for each population density. (c) Forecasted bifurcation diagram (blue line). Circles and vertical bars represent experimentally approximated stable and unstable points on the bifurcation diagram, respectively. The dashed line is the approximated bifurcation diagram using the calibrated model.

As a next step we study emergence, which occurs as the dilution factor decreases and has values closer and closer to the critical one (i.e., 1,505), as shown in case (b) in Fig. 6.2. In this case, the system has only one equilibrium (at zero density), and perturbations in the density cannot lead to a transition. In this case, the system does not exhibit a bifurcation; however, if the parameter decreases below the critical value, the system enters a region of bi-stability where a perturbation may push the system to a large non-zero equilibrium. Using measurements of the system behavior before entering the bi-stability region, the goals are (a) to forecast the parameter value at which the bi-stability region begins and (b) in general, to forecast the bifurcation diagram which identifies the type of the upcoming transition and the system dynamics in at upcoming parameter values. This type of forecasting might be of interest in many cases, as in ecological systems [153,154], cancer dynamics [155,156] and outbreaks of a disease [143–145], where a system with a low density equilibrium may jump to a highly populated state.

In the experiments performed in this study, the critical dilution (and the beginning of the bi-stability region) is approximately 1,505 (Fig. 6.11). To forecast the upcoming bi-stability and possible transition, we monitor the population dynamics of buddying yeast in response to external perturbations at three larger dilution factors, namely $1{,}800$, $1{,}700$ and $1{,}600$.

The measured recoveries (Fig. 6.14(a)) show that the system undergoes slowing down as the dilution factor decreases from $1{,}800$ to $1{,}600$, namely it takes more days for the system to return to its equilibrium when the dilution factor decreases. Mathematically, this means that the recovery rate of the system (λ) decreases. The recovery rates are computed based on system responses and are shown in Fig. 6.14(b). The plots of recovery rates at all dilution factors exhibit a local maximum at the population density around $0.390 \times 10^5\ cells/\mu L$, which means that the system has the slowest recovery rate around this value.

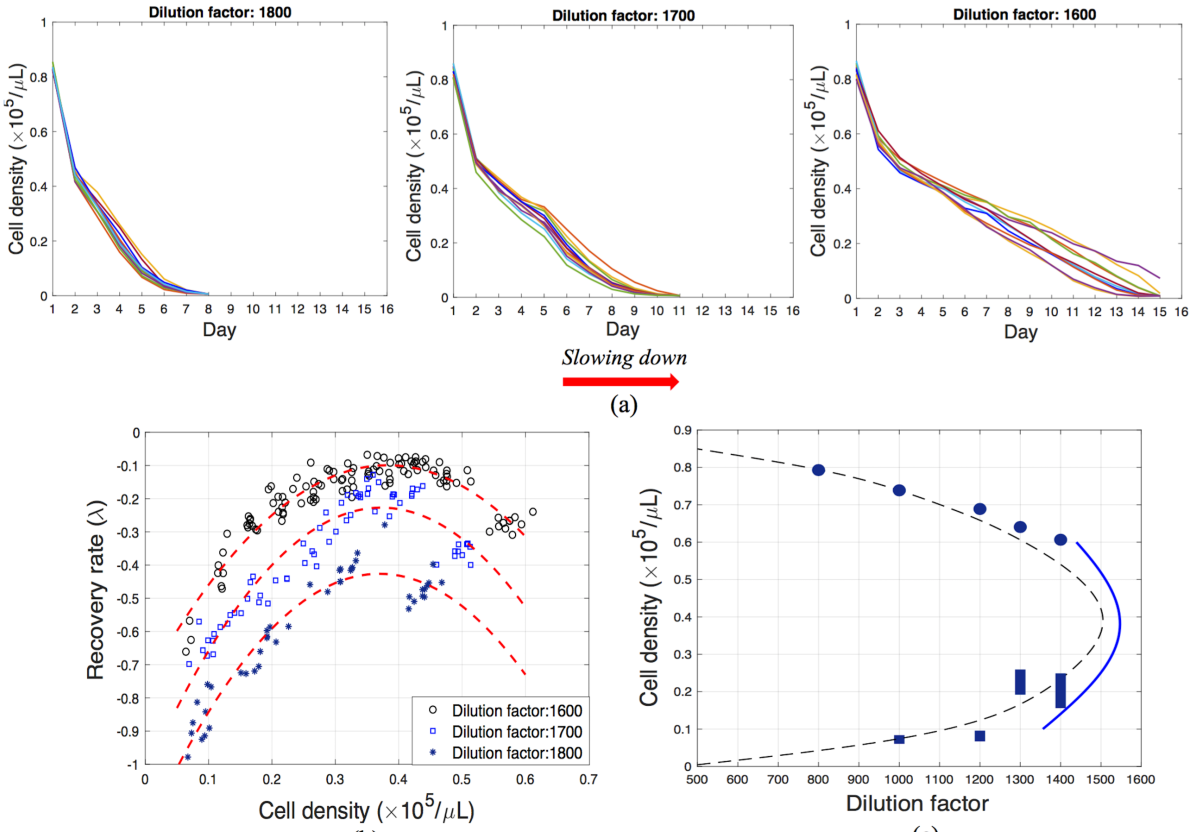

(a)

(b)

(c)

Figure 6.14. Forecasting using measurements at dilution factors of 1,600, 1,700 and 1,800 corresponding to case (b) shown in Fig. 6.2. (a) Measured recovery of the yeast population from perturbations at three selected dilution factors for the system approaching the tipping point from parameter values greater than the critical parameter. Each line represents a separate experiment, and each experiment has 7 replications which are performed simultaneously using the same source of materials at exactly the same experimental conditions. (b) Recovery rates at each amplitude computed from measurements shown in (a) and quadratic polynomial fits. (c) Forecasted bifurcation diagram (solid blue line). Circles and vertical solid bars represent experimentally approximated stable and unstable points on the bifurcation diagram. The dashed line is the approximated bifurcation diagram using the calibrated model.

The forecasting method therefore predicts that the closest non-zero equilibrium has a density of $0.390 \times 10^5\ cells/\mu L$. Hence, we expect a jump in the population density to this value (or greater values) when the dilution factor is further decreased. Using the approximated recovery rates, the bifurcation diagram is forecasted, as is depicted in Fig. 6.14(c). Results predict that the system is approaching a fold (catastrophic) bifurcation, at the critical dilution factor of 1,547 where the critical population density is $0.390 \times 10^5\ cells/\mu L$, which lies within the expected range based on direct observations of the system. Furthermore, the population densities on the stable and unstable branches of the diagram are also approximated for a small region around the tipping point. The forecasting results predict that if the dilution factor is decreased to values smaller than $1{,}547$, a large perturbation can change the system equilibrium from zero to a high population density.

6.5 Forecasting the bifurcation using the buddying yeast population model

To demonstrate the application of the proposed forecasting method when no measurement and no process noise is present, the method is evaluated theoretically using the simple population growth model (Eq. (6.1)). The model parameters are approximated using genetic algorithm to fit best the experimental system (Table 6.1). The simulations are performed similarly to the experimental procedure. We measure the simulated population every 23hrs, including the time lag. After each measurement, the selected dilution, which accounts for the mortality rate, is applied to the current population, and the new population density is simulated to grow for the next 23hrs. The model predicts that the population experiences a catastrophic transition at the dilution factor of $1{,}505$. We forecast the bifurcation diagram assuming that the system approaches the transition from dilution factors first all larger, and then separately all smaller than the critical value. Thus, we examine separately the forecasting approach in the extinction and the emergence cases.

Consider a population which is approaching an extinction tipping point as the environmental conditions change. At a fixed dilution factor, the population recovers to its equilibrium after a perturbation is applied. The rate of recovery from perturbation depends on the distance to the tipping point. Figure 6.15(a) shows the system response to perturbations at two parameter values. Following the forecasting procedure, the recovery rates are computed, as demonstrated in Fig. 6.15(b). It is observed that the recovery rates at all amplitudes decrease as the system approaches the tipping point. Furthermore, the slowest speed of recovery is observed for the population amplitudes which are closest to the bifurcation diagram. In this example, the maximum recovery rate corresponds to the tipping point, which is the point on the bifurcation diagram that lies the furthest from the current parameter value (dilution factor 1,300 in this case).

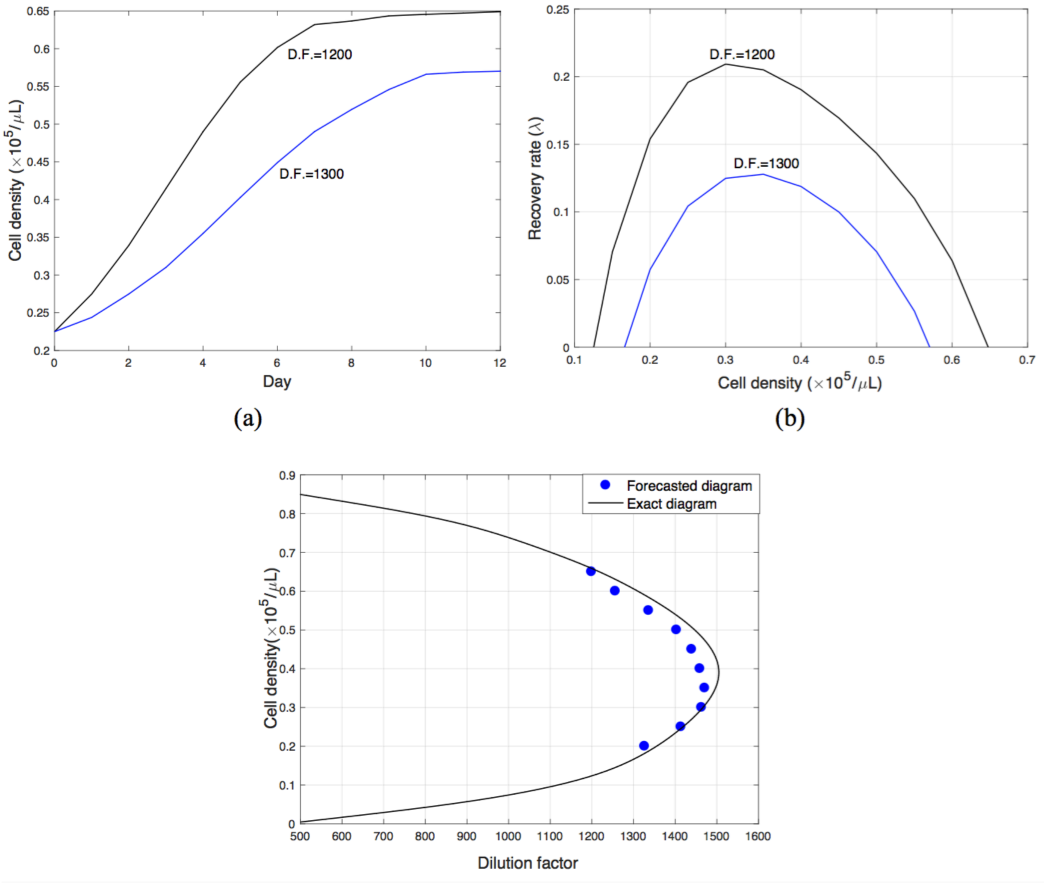

(a) (b)

(c)

Figure 6.15. Simulation results and forecasting of the bifurcation diagram using the budding yeast population model (Eq. 6.1) for the system approaching to the tipping point from dilution factors smaller than the critical value.

The forecasting results are presented in Fig. 6.15(c) which shows that the fixed points of the system are successfully forecasted. The tipping point is forecasted to occur at the dilution factor of $1{,}470$. Importantly, it is evident from the results that the upcoming transition is catastrophic. Furthermore, one can identify the basins of attraction of the stable equilibria in the upcoming parameter values. For example, at the dilution factor of $1{,}415$, it is forecasted that the minimum population density at which the system maintains its ability to recover to the non-extinct state is $0.250 \times 10^5 cells/\mu L$. A perturbation which would push the population below this boundary would lead to extinction.

The same procedure is applied for the emergence case, when the system is approaching the bifurcation from dilution factors greater than $1{,}505$. The system responses to large perturbations are demonstrated in Fig. 6.16(a), at three different dilution factors. One can observe from Fig. 6.16(b) that at each dilution factor the recovery rate is fast at first, then it slows down, and after passing a specific population density it speeds up again. It is also shown that the slowest recovery rate corresponds to population values around $0.400 \times 10^5 cells/\mu L$ (as shown in Fig. 6.16(b)). Hence, the closest fixed point to the current state of the system has a non-zero amplitude which is a feature of subcritical (catastrophic) bifurcations. The forecasting results are shown in Fig. 6.16(c). The closest tipping point is forecasted correctly at the dilution factor of $1{,}470$, where the system enters to a bistable region and a large perturbation can push the system from one equilibrium to another. The forecasted bifurcation diagram shows that the system is approaching a catastrophic transition where a jump may occur between equilibrium points. The forecasted bifurcation diagram is in agreement with the diagram computed directly from Eq. 6.1 (as shown in Fig. 6.16(c)).

It should be noted that the maximum forecasted amplitude in the bifurcation diagram cannot be greater than the maximum amplitude caused by perturbations. If, for example, the perturbations cause a change in cell density smaller than 0.400×10^5 $cells/\mu L$, the tipping point cannot be forecasted. However, it can still be identified from the forecasted portion of the diagram that the upcoming transition is catastrophic.

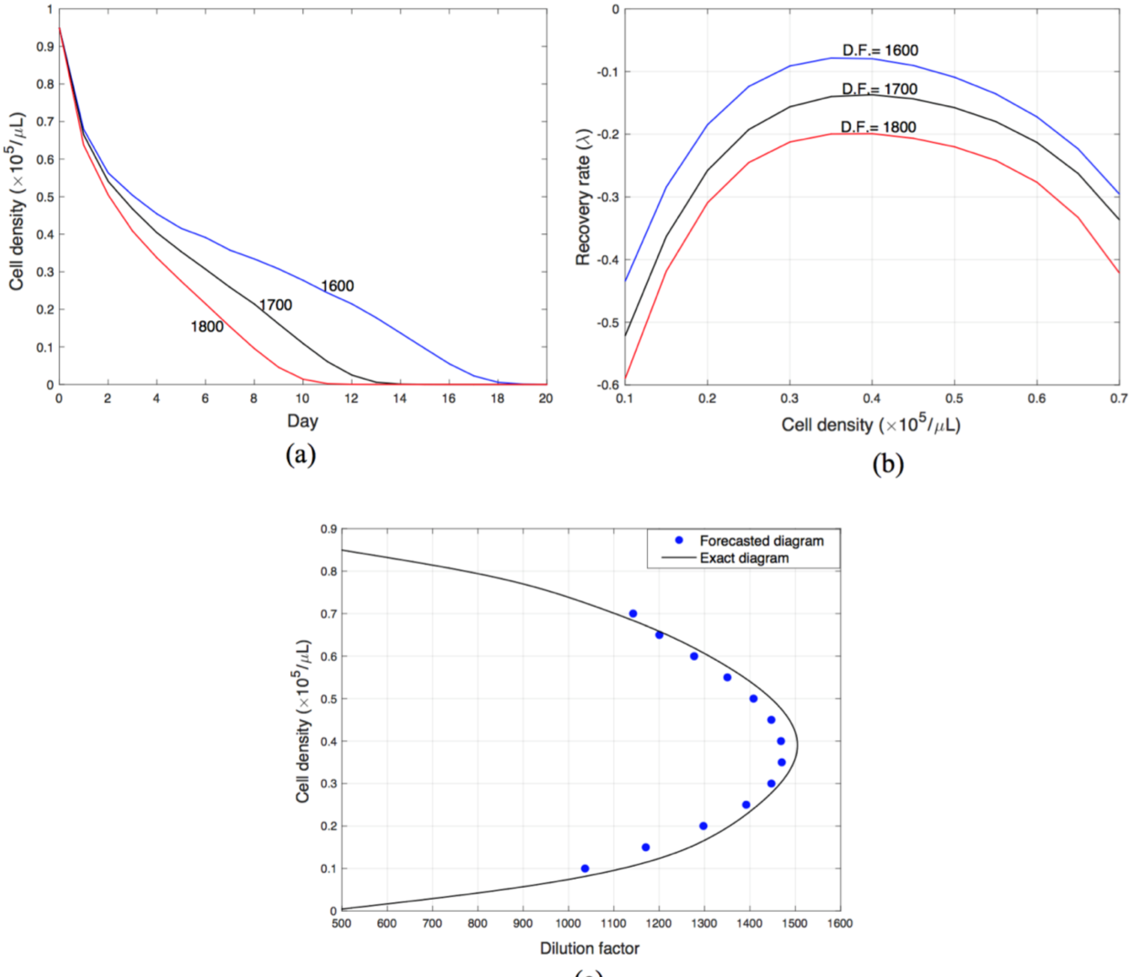

(a)

(b)

(c)

Figure 6.16. Simulation results and forecasting of the bifurcation diagram using the budding yeast population model (Eq. 6.1), for the system approaching to the tipping point from dilution factors greater than the critical value.

These results show the applicability of the forecasting approach theoretically when no source of noise and uncertainty exists. In experimental applications, one needs more measurements to increase the accuracy and alleviate the effect of noise. However, the method is still expected to successfully forecast future stability of system, as was shown in the previous section.

6.6 Discussion

Previous research has shown that several indicators based on changes in ecological time series can successfully ring the alarm when a system of interest approaches a critical transition. Our work highlights that by monitoring the system's response to perturbations it is possible to gain even more information about the future stability of the system. The proposed method requires larger perturbations compared to the small fluctuations around the equilibrium state which are required in early warning methods. However, we demonstrate that when such data can be obtained, the bifurcation diagram can be successfully extracted using the proposed forecasting method, leading to a deeper understanding of the system's future stability.

Close to the bifurcation point, external perturbations lead to long transients before the system reaches its stable state, which means that the system's recovery rate decreases. Therefore, the system's recovery rate from perturbations can be used as an indicator, and is correlated to the distance to bifurcations. The idea of relating the system recovery from perturbations to the upcoming ecological transitions has been also applied in some recent studies [142,157]. Those studies demonstrate that the increase in total recovery time from a perturbation is a good indicator of approaching a tipping point. In contrast, here we show that examining individual recovery rates at each amplitude instead of the total recovery time reveals more information about the system stability, such as the distance (in the parameter space) to the tipping point, the type of the transition and future stable and unstable equilibria.

The experimental data presented in this study are in agreement with the forecasting results, despite the fact that no mathematical model was used for forecasting, and all measurements were performed prior to the transition. Also, an important finding of the forecasting method is that the points of the bifurcation diagram which are closer to the current state of the system are forecasted with more accuracy compared to the rest of the diagram. For instance, in Fig. 6.14(c) the most accurately forecasted point is the tipping point, and the accuracy decreases for the points of the diagram that are farther. Similarly, it is expected that the forecasted points on the bifurcation diagram in the Fig. 6.13(c) have the best accuracy around the dilution factor of $1{,}300$, and the accuracy decreases toward the tipping point. Hence, one should account for this effect while interpreting forecasting results. Note that this variation in accuracy was expected from the theory of the proposed forecasting method (see Methods), since the points on the bifurcation diagram are forecasted by extrapolating the recovery rates. Therefore, the highest accuracy corresponds to amplitudes with the recovery rates closest to zero, i.e. the amplitudes closest to the bifurcation.

The use of parameters close to the tipping point generates more accurate forecasting results, since a more pronounced slowing down is observed close to transitions. For systems with low noise, a few measurements at each parameter value are sufficient for an accurate forecasting. However, in systems strongly affected by measurement and/or process noise, the more measurements are obtained, the higher the forecasting accuracy becomes. Also, the larger the perturbation is, the larger the noise intensity can be for a similar accuracy. For example, the method loses accuracy when the noise intensity is very high and the perturbations are very small. In such cases, one may choose to evaluate the system's stability using previously developed early warning signals [26–33,35].

The perturbations required for forecasting do not need to have the same intensity or the same source. They could be caused by various sources, either natural or anthropogenic. However, depending on the source of the perturbations, each perturbation might create different amplitudes for the resulting (perturbed) dynamics. The amplitudes in the forecasted bifurcation diagram cannot exceed the amplitudes experienced by the system in these perturbations. Moreover, if perturbations are applied by an external intervention, one should be cautious of applying excessively large perturbations. Such perturbations might result in jumping to another equilibrium state if the system is operating in the region of bi-stability. This is of higher importance for complex ecosystems, which contain several connected states. In that case, perturbing a single state might affect the dynamics of other states as well as the ecosystem as a whole. Smaller perturbations can still be used to forecast the bifurcation diagram; however, the larger the perturbation is, the larger the region of the diagram that can be forecasted is.

The forecasting approach is advantageous for complex systems which are at risk of catastrophic transitions, where there is a pressing need for information about upcoming thresholds. This work provides a tool to evaluate the stability of complex systems in more detail than early warning signals, and aids in the management of fragile ecosystems.

Chapter 7

Data driven Identification of the Most Reliable Sensor Species to Predict Ecological Regime Shifts

7.1 Introduction

Complex systems might undergo abrupt transitions from one stable state to another [24]. Rapid degradation of grazelands [158], sudden collapse of global financial markets [159], failures in large-scale electric power transmission systems [160], abrupt climate changes [12,13], and collapse of populations in ecosystems [11,126] are examples of such dramatic changes. Anticipating such abrupt transitions is challenging, especially when they are caused by slow, gradual changes in underlying conditions. Moreover, the complexity of such systems makes it difficult to develop detailed and accurate models to predict when critical transitions might occur.

To overcome this challenge, numerous studies have focused on developing model-free approaches to detect early-warning signals of impending critical transitions [2,33,88,161]. Most existing approaches are based on the phenomenon of "critical slowing down," which is defined as the slowing down of the dynamics around an equilibrium when a system approaches a tipping point [162,163]. Some manifestations of critical slowing down, i.e. increasing variance and autocorrelation, in the temporal dynamics of a system have been proposed as model-free early-warning signals to anticipate critical transitions [2,27,33,164]. The advantages of applying early-warning signals to successfully predict when a system is approaching a tipping point have been investigated in recent studies [26–33,35]. However, the application of such early-warning signals to large-dimensional systems (such as spatially-distributed systems with many components), remains a major challenge. The main challenging attributes of such systems are their complex dynamics involving large numbers of interacting components. Recent studies have shown that not all system components provide the same signal strength for predicting upcoming transitions [165–167]. However, owing to practical constraints, it is not feasible to measure the dynamics of all components of a system to detect these early-warning signals. The utility of the information gleaned from system components in regard to critical slowing down depends on both the topology and dynamics of the system in question. Measuring only a subset of system components may lead to critical transitions remaining undetected, because the measured components may not provide a strong enough signal to detect the upcoming transition. Thus, determining which system components to monitor and how to interpret the measurements to obtain accurate early-warning signals is an important consideration.

Critical slowing down is associated with the dominant eigenvalue of the locally linearized system, which suggests that the states most closely aligned with the corresponding dominant eigenvector are among the best candidates for measurements to extract early-warning signals (14). Mathematically, this is because the dynamics along the direction of the dominant eigenvector are at their slowest as the system approaches the critical transition. It is not feasible, however, to estimate the dominant eigenvector of a complex system in the absence of an accurate model. The dominant eigenvalue of a covariance matrix generated from system measurements has been proposed as an approximation [168] for cases where the system is close to the critical transition, and the system is subject to homogeneous noise (14). However, these requirements reduce the wide-spread efficacy of this approach.

Herein, we propose a data-driven approach to rank the species in an ecosystem (or the regions of a spatially distributed ecosystem) based on their reliability in providing a strong early-warning signals of critical transitions. For this purpose, a data-driven algorithm, known as the eigensystem realization algorithm, was employed to approximate the eigenvectors of systems, and as a result, to identify the best states to monitor to extract the most reliable early-warning signals of critical transitions. The system response to perturbations was used as input to the algorithm to approximate its dynamical properties. System recoveries from large perturbations contain richer information of the system dynamics than its response to continuous small perturbations [88,130,169]. Moreover, system dynamics at relatively large amplitudes are used to mitigate the effects of small continuous heterogeneous perturbation noise. Several numerical examples were studied and the species in the considered ecosystems were ranked based on their capability to provide adequate early-warning signals. The challenges associated with ranking the nodes in complex systems and several conditions resulting in false early-warning signals were analyzed as well.

7.2 Methods

Many large-dimensional natural and physical systems are constantly affected by random environmental perturbations. Thus, it is common to model this type of system using first-order differential equations with noise terms. Consider a p-dimensional nonlinear dynamical system with a vector $\mathrm{x}(t)$ of state variables described by first-order stochastic differential equations:

$$dx_i = f_i(\mathrm{x})dt + \sigma_i dW_i, \tag{7.1}$$

where $i = 1,2,\dots,p$. The force vector f(x) is a vector composed of all functions of f_i, which models the deterministic evolution of the system, and σ_i is the noise level at state variable x_i. Time series data can be obtained from model simulations. Next, the best indicator species to monitor (i.e., the species with the best early-warning signals) were identified using a data-driven algorithm to identify the slowest eigenvector of the system dynamics. To check that the species obtained do provide the best early-warning signals, the dynamics of all species was measured (i.e., by measuring all state variables x_i obtained from simulations). Then, all early-warning signals of critical transitions were calculated to determine the best one, which was then compared with the one obtained from the proposed approach based on the data-driven algorithm.

7.2.1 Early-warning signals

Early-warning signals are statistical indicators that reveal proximity to a tipping point. These signals are applicable to systems with small fluctuations around their equilibrium state resulting from stochastic perturbations. As a system approaches a bifurcation that exhibits critical slowing down, the rate at which the system recovers from perturbations decreases, and the time required for the system to return to its equilibrium state increases. Thus, the system becomes more correlated with its past, which leads to an increase in autocorrelation. Furthermore, perturbations can accumulate, which leads to an increase in the size of the fluctuations and as a result, an increase in variance [11]. Sometimes, the increase in the value of early-warning signals may be detected well before a tipping point ([11][16,36,128,129]).

Early-warning signals are estimated from time measurements of each state variable x_i obtained from simulations. The most important factor in using early-warning signals is the way the trend in these signals is interpreted and the way this trend is monitored as system parameters gradually change. In this study, trends in the early-warning signals prior to the critical transition were estimated based on the non-parametric trend statistic Kendall's τ, which is a measure of the correlation between the rank order of the observed values and their order in time [170,171]. Kendall's τ takes value from -1 to 1, where -1 represents a monotonic negative trend, and 1 represents a monotonic positive trend. A large positive Kendall's τ typically indicates that the system is approaching a transition. By comparing the Kendall's τ of an early-warning signal calculated from different state variables, we can verify the reliability ranking obtained from the data-driven algorithm analysis.

7.2.2 Data-driven algorithm to identify eigenvectors

In this study, we used data-driven techniques that are traditionally used for experimental modal analysis in engineering combined with the early-warning signals to identify the best indicator species in a connected system and to select early-warning signals with good reliability for predicting critical transitions. In particular, we used a data-driven algorithm known as the eigensystem realization algorithm, which is an effective method for identifying system dynamic characteristics using time domain measurements of the system dynamics [74]. This time domain multi-input multi-output algorithm provides estimates of modal parameters of the system (i.e., eigenvalues and eigenvectors of a system in the vicinity of its equilibrium) using measurements of system responses to external inputs and perturbations.

Consider a situation in which a stable system is exposed to an initial perturbation that results in a free response (i.e., decay) to its equilibrium state. Let y denote an n-dimensional vector of measured state variables as the system recovers from perturbation. The system may have more than n states. Then consider that the measured response is sampled with a Δt time increment, and

$y(k)$ denotes the measured state variables at $t = k\,\Delta t,\ k = 0,1,2,\ldots,$. If the measurements are available from m independent perturbations, one can define $\mathrm{Y}(k)$ as a sequence of experimentally measured state variables as $t = k\,\Delta t$, i.e. $\mathrm{Y}(k) = [\mathrm{y}_1(k)\ \mathrm{y}_2(k)\ \ldots\ \mathrm{y}_m(k)]$. The first step in the algorithm was to form generalized Hankel matrices from the discrete measurements as follows [74,75]:

$$\mathrm{H}(k) = \begin{bmatrix} \mathrm{Y}(k) & \mathrm{Y}(k+1) & \ldots & \mathrm{Y}(k+v-1) \\ \mathrm{Y}(k+1) & \mathrm{Y}(k+2) & \cdots & \mathrm{Y}(k+v) \\ \vdots & \vdots & \ddots & \vdots \\ \mathrm{Y}(k+r-1) & \mathrm{Y}(k+r) & \cdots & \mathrm{Y}(k+r+v-2) \end{bmatrix}_{nr\times mv}, \tag{7.2}$$

where parameters r and v are chosen depending on the particular application and can be tuned for optimal accuracy by convergence studies. The singular value decomposition of $\mathrm{H}(0)$ can be written as $\mathrm{H}(0) = \underline{\mathrm{P}}\,\underline{\mathrm{Z}}\,\underline{\mathrm{J}}^{\mathrm{T}}$, with the singular values in the diagonal matrix $\underline{\mathrm{Z}}$ ordered in decreasing order (largest on the first row). The rank of the Hankel matrix is determined by the number of nonzero singular values in $\underline{\mathrm{Z}}$. However, the presence of measurement noise and/or (weak) nonlinearities leads to additional nonzero singular values of small magnitude [75]. Selecting the first N largest singular values (i.e., the dominant ones), matrices $\underline{\mathrm{Z}}$, $\underline{\mathrm{J}}$, and $\underline{\mathrm{P}}$ are truncated and denoted by Z, J, and P, respectively. Next, the state transition matrix S can be defined as follows [75]:

$$\mathrm{S} = \mathrm{Z}^{-1/2}\,\mathrm{P}^{\mathrm{T}}\,\mathrm{H}(1)\,\mathrm{J}\,\mathrm{Z}^{-1/2}. \tag{7.3}$$

Note that matrices Z, J, and P are obtained from $\mathrm{H}(0)$, while S is obtained also using $\mathrm{H}(1)$. Next, denote by T, the matrix of eigenvectors of S. Matrix T can be used to transform S into the diagonal matrix $\tilde{\mathrm{S}}$ as follows:

$$\tilde{\mathrm{S}} = \mathrm{T}^{-1}\mathrm{ST}, \tag{7.4}$$

where the i^{th} diagonal element of matrix $\tilde{\mathrm{S}}$ is $\tilde{s}_i$. It can be shown that the system eigenvalues are:

$$\eta_i = \frac{1}{\Delta t}\ln(\tilde{s}_i) = \sigma_i \pm i\omega_d, \tag{7.5}$$

Furthermore, the matrix C contains the corresponding eigenvectors of systems as follows:

$$\mathrm{C} = \left(\mathrm{E}_n^{\mathrm{T}}\mathrm{PZ}^{1/2}\right)\mathrm{T}, \tag{7.6}$$

where $\mathrm{E}_n^T = [\mathrm{I}_n \quad 0_n \quad 0_n \quad \dots \quad 0_n]$; I_n and 0_n represent the identity and zero matrices of order n, respectively.

Based on this approach, our goal was to approximate the dominant eigenvector of dynamical ecosystems without *a priori* knowledge of the underlying system equations (i.e., without a mathematical model of the system, but using only time-series measurements of some of its states). The system is exposed to perturbations from various sources, either natural or anthropogenic. The response of each species in the ecosystem to such small/large perturbations were measured and used to generate the matrix $\mathrm{Y}(k)$. Next, the slowest eigenvalue η_s and its corresponding eigenvector c_s were obtained using Eqns. (7.5) and (7.6). Once c_s was determined, it was not necessary to monitor/measure all species. Thus, only a subset of the species was monitored. The subset of species that corresponded to the largest absolute values in c_s were the most reliable in providing early-warning signals of critical transitions because those species have the most participation in the eigenvector where the slowing down of the dynamics occurs. For example, consider that only one species was monitored. The species that corresponds to the entry with the largest absolute value in c_s would be the optimal species to monitor.

An important consequence of using data along c_s is that the analysis is more robust to the presence of heterogeneous noise in the system compared with other methods. One should note that, although the eigensystem realization algorithm and other similar data-driven methods provide estimated eigenvalues, these estimated eigenvalues are not certain and are sensitive to system and algorithm parameters such as noise and dataset length. In contrast, the estimated eigenvectors are more robust and reliable. Thus, we focused on the estimated eigenvectors in our analysis.

In the present study, we evaluated this approach by ranking the reliability of the components of several well-known ecological models and comparing the ranking results with the early-warning signals computed from the time-series measurements.

7.3 Results and discussion

Three ecological models with increasing complexity due to increasing dimensionality were studied to gain insights and to evaluate the proposed approach.

7.3.1 Two species competition model

The first model we considered was a two-species Lotka–Volterra competition model, which considered two interacting populations at time t. The dynamics of the system with random excitations from the environment can be studied using the following stochastic differential equations [172,173]:

$$\begin{aligned} dx_1 &= \left[x_1\left(1-\frac{x_1+\alpha_{12}x_2}{K_1}\right)+u_1\right]dt+\sigma_1 dW_1, \\ dx_2 &= \left[x_2\left(1-\frac{x_2+\alpha_{21}x_1}{K_2}\right)+u_2\right]dt+\sigma_2 dW_2, \end{aligned} \tag{7.7}$$

where x_i is the population density of each species, K_i is the carrying capacity of the i^{th} species, and α_{ij} is the competition coefficient representing the effect of species j on species i. We assumed a small immigration term u_i to prevent species from reaching extinction, following a previous study [174].

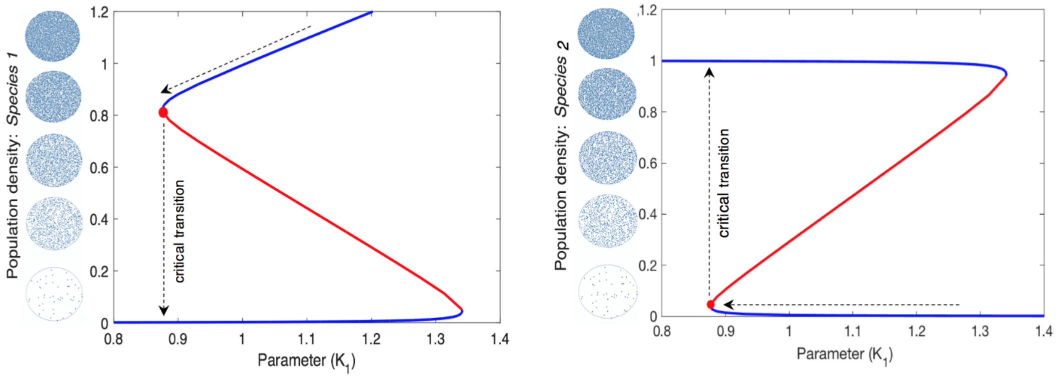

Figure 7.1. Bifurcation diagram for the two-species Lotka–Volterra competition model. Blue and red lines represent stable and unstable fixed points, respectively. Arrows show the critical transition considered.

We employed the data-driven algorithm discussed in Sec. 7.2 to identify the slowest eigenvector and determined the best indicator species. System recoveries from perturbations were the only input to the algorithm. The carrying capacity K_1 of the first species was chosen as a bifurcation parameter. As K_1 decreased, the system approached a catastrophic transition at $K_1 = 0.85$, as shown in Figure 7.1. We used small perturbations of the system in the pre-bifurcation regime as shown in Figure 7.2, for instance at $K_1 = 1.1$.

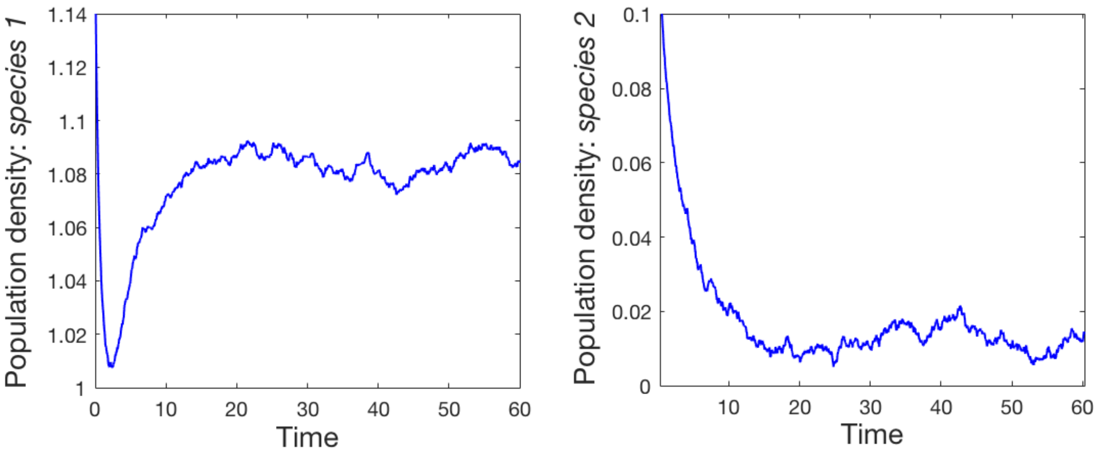

Figure 7.2. Noisy system recoveries from perturbations at $K_1 = 1.1$ used as an input to the data-driven algorithm to identify the eigenvectors of the two-species Lotka–Volterra model.

Figure 7.3(a) shows the exact eigenvectors of the system at the tipping point (i.e., the reference eigenvectors computed using the model in Eq. (7.7)) as well as the approximated eigenvectors of the system. The approximated eigenvectors match the reference eigenvectors, indicating that the data-driven algorithm works well in this case. Thus, a system model is not required to estimate the slowest eigenvector of the system, which simplifies the procedure for identifying which indicator species to monitor to extract reliable early-warning signals.

Figure 7.3(b) shows the variance of each species (taken separately) and the corresponding Kendall's τ obtained from noisy measurements collected for increasing values of the bifurcation parameter K_1. These results show that it is possible to extract reliable early-warning signals by measuring the population density of either species. Nevertheless, measuring the population density of the first species has a slight advantage. However, one should note that the dominant direction approximated at this system parameter is different from the one estimated at the critical parameter, i.e. at $K_1 = 0.85$. In general, the eigenvectors may vary with the parameter as the system approaches the transition. In which case, the approximation can be updated if the system is operating at parameters significantly far from the parameter corresponding to the initial approximation. This topic is discussed in more detail in Sec. 7.4.

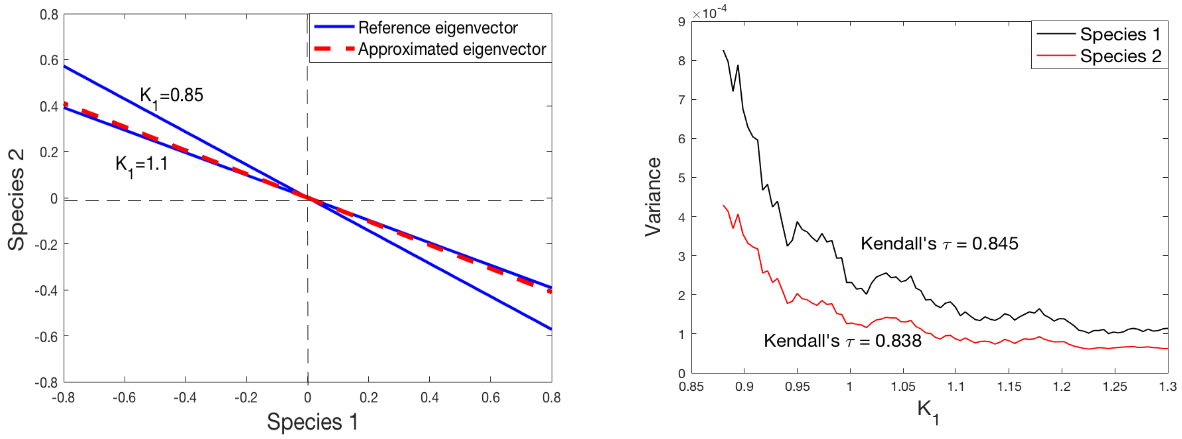

(a)

(b)

Figure 7.3. (a) Exact (reference) eigenvectors and approximated eigenvectors obtained using the data-driven algorithm. (b) Early-warning signals recorded using each one of the two species. Both species provide a good early-warning signal of critical transition.

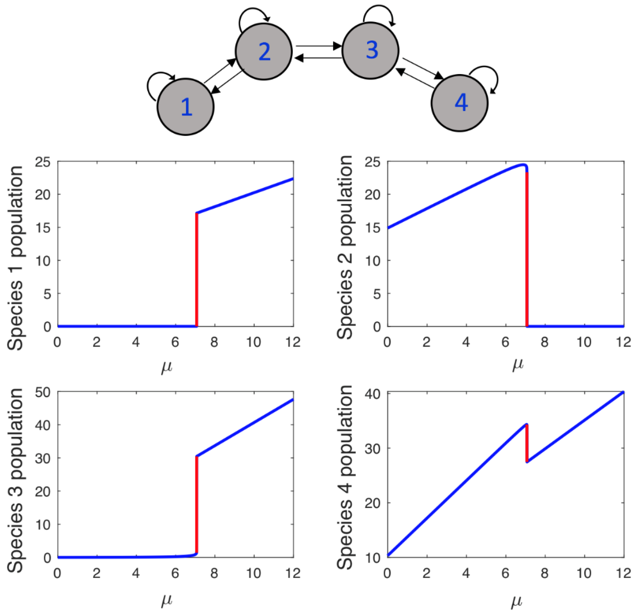

Figure 7.4. Bifurcation diagrams for each node in a network of four interacting species in a chain configuration. A critical transition occurs at $\mu = 6.8$.

7.3.2 Network of four interacting species

We considered a network of four connected species in a chain configuration (Fig. 7.4). The goal of the analysis was to rank the species of this system (i.e., a ranking of the nodes) based on their reliability in providing early-warning signals of the upcoming critical transition. The dynamics of each species are governed by the following stochastic differential equation:

$$dx_i = \left[x_i\left(1 - \frac{\sum_j \alpha_{ij} x_j}{K_i}\right) + u_i\right] dt + \sigma_i dW_i, \qquad i,j = 1,2,3,4, \tag{7.8}$$

where r_i is the maximum intrinsic growth rate, K_i the carrying capacity of species x_i, and competition between species is defined by coefficient α_{ij}. The values for r_i, K_i, and α_{ij} were randomly chosen from the intervals [0.6,1], [5,15], and [0,1.5], respectively. Moreover, a small immigration term u_i is assumed in the population of each species to mimic dispersal that prevents species from reaching extinction and negative values [174,175].

The parameter μ was introduced following a previous study [175] to reflect the effect of environmental change on the system by modifying the carrying capacity of each species as $K'_i = K_i\,(1 + \eta_i\,\mu)$. The parameter η_i was selected randomly from the interval [0,1] for each species, reflecting the fact that the change in the environment does not affect all species in the same way. By increasing the parameter μ, the system underwent a critical transition (Fig. 7.4).

Theoretical analysis of the equations showed that the exact dominant eigenvector of the system at the critical transition was $v_c = [-0.002, 0.734, -0.661, 0.158]^T$, reflecting that species 2 and 3 were the best ones to be monitored for identifying the upcoming transition. In contrast, species 1 and 4 participated the least in the dominant eigenvector. Thus, if the system stability was evaluated by monitoring species 1 and/or 4, then only a weak signal would be detected until the system is extremely close to the transition. To observe this phenomenon, the model in Eq. 7.8 was simulated using numerical methods to obtain surrogate measurements taken from each node and their performance assessed through comparison. Heterogeneous random excitations were modeled by a random walk process. The parameter μ was started at $\mu = 3.5$ and was gradually increased toward the critical value, i.e. $\mu = 6.8$.

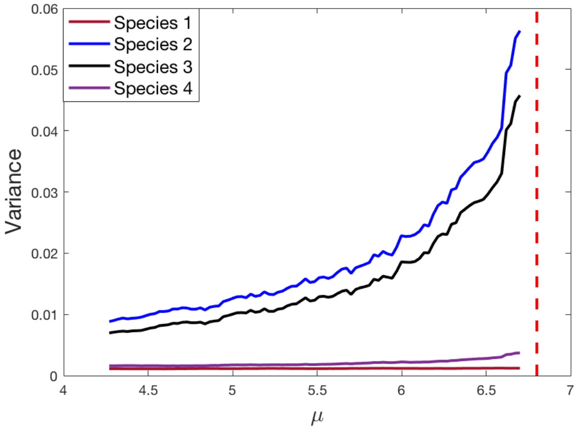

Figure 7.5. Early-warning signals recorded using each node in a network of four interacting species in a chain configuration. Species 2 and 3 provided the most significant early-warning signal of the critical transition. The vertical dashed line represents the critical transition.

Figure 7.5 shows the variance measured from the dynamics of each node. Species 2 and 3 showed the most significant signal of approaching a transition, while species 1 and 4 did not provide much useful information. This procedure was repeated 100 times using random heterogeneous measurements and process noise. The distribution of the measured Kendall's τ for the signal recorded at each node was computed. The results clearly show that species 2 and 3 provide the strongest Kendall's τ in most cases (Fig. 7.6), indicating that they are the best indicator species in this system, while species 1 and 4 did not provide reliable early-warning signals. This example demonstrates the importance of identifying the best indicator species in a system.

To identify the best indicator species for this system without a model of the system, we applied the data-driven algorithm to identify the slowest eigenvector of the system using only measured system recoveries to small perturbations. We considered the recoveries obtained at $\mu = 4.5$. A sample of the recovery data used in the algorithm is shown in Figure 7.7.

Figure 7.8 shows a comparison of the exact dominant eigenvector computed using theoretical formulations and the approximated eigenvector by the data-driven algorithm. The results suggest that the best indicator species can be identified using this model-free approach. The algorithm successfully ranked the species based on their importance regarding the extraction of reliable early-warning signals using some measurements of the system response to perturbations. The algorithm correctly ranked species 2 as the best indicator species and species 3 as the second-most reliable option, while it indicated that measuring species 1 would not provide a strong signal of approaching an upcoming critical transition.

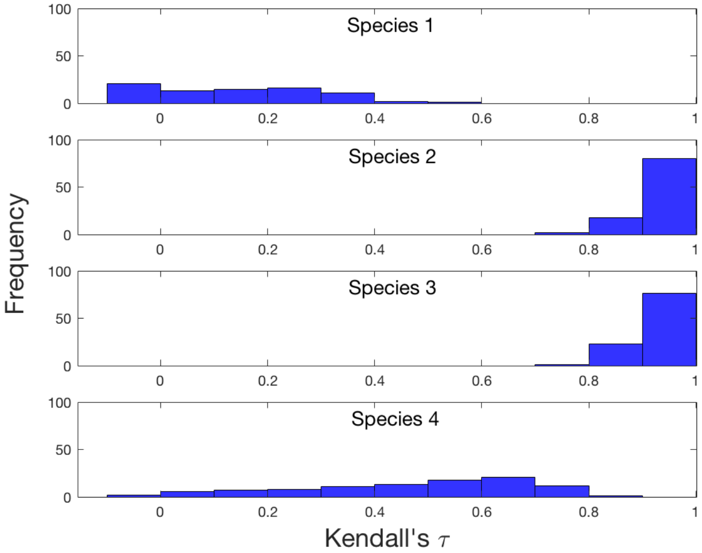

Figure 7.6. Distribution of computed Kendall's τ of early-warning signals recorded at each node for 100 independent simulations with random measurement and process noise. Species 2 and 3 were the best to monitor because they provided the most significant increasing trend in their early-warning signals.

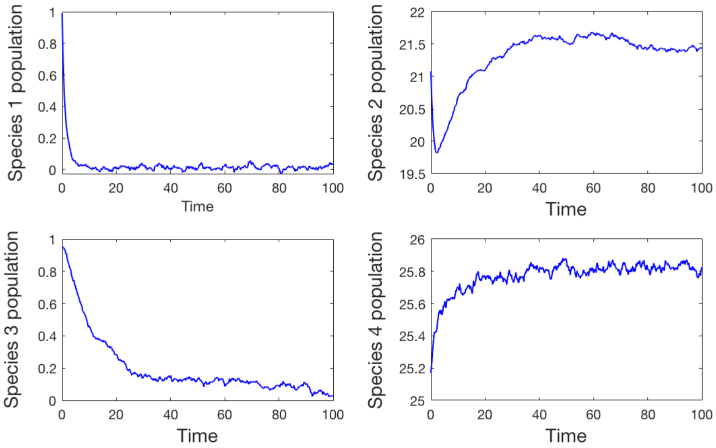

Figure 7.7. Examples of system recoveries from perturbations at $\mu = 4.5$ used as input to the data-driven algorithm to identify the slowest eigenvector of a network of four interacting species.

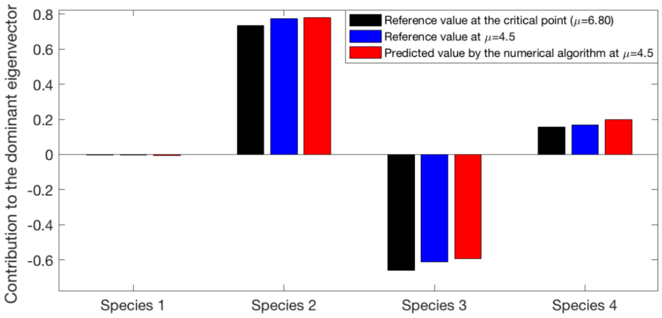

Figure 7.8. Slowest eigenvector of the system estimated using the proposed approach and the exact eigenvector (reference). The data-driven approach correctly identified nodes 2 and 3 as the ones with the most contribution and node 1 as the one with the least contribution to the dominant eigenvector.

7.3.2.1 Robustness of early warning signals to data analysis parameters

The decision regarding the stability of a system is taken looking at the trend of extracted early warning signals as the system parameter is gradually changing. Kendall's τ coefficient is the one which is often used to study the trend of statistics related to the critical slowing down phenomenon [170,171]. Because the sequence of the statistics are estimated from the time series, the value of Kendall's τ are affected by parameters such as window size, sample rate and etc. Therefore, the choice of data analysis parameters will affect the correlation in data, and thus affects the distribution of Kendall's τ. In this section, we study how sensitive are the extracted Kendall's τ from measuring the dynamics of each species to the choice of different set of data analysis parameters, and how robust are the identified Kendall's τ against measurement errors.

For the four interacting species studied in Sec. 7.3.2, we recorded system time series as it gradually approaches to the transition. We calculated the Kendall's τ of measured variance for a range of sampling resolutions and window sizes for each of the four species, and the results are shown in Fig. 7.9. It is observed that the Kendall's τ recorded from measuring species 2 and 3 are a smooth function of time resolution and the window size. However, looking at the plot of species 1, the recorded Kendall's τ shows a completely random behavior for different choice of parameters. For species 4, however, the plot is not significantly smooth or random, and lies between that of species 1 and species 2 and 3. Comparing the plots with the ranking results of Sec. 7.3.2., it is inferred that the uncertainty associated with the plots for each species is directly related to its contribution to the dominant eigenvector.

To analyze how robust are the reported Kendall's τ in Fig. 7.9 for each species, we added a small measurement uncertainty to the recorded time series and calculated the Kendall's τ for extracted early warning signals from measurements taken from each species. Comparing the results of this analysis (Fig. 7.10) with the previous results shown in Fig. 7.9, it is observed that the reported values of Kendall's τ for species 2 and 3 are robust to measurement uncertainties and the trend of the early warning signals recorded from these species remains almost the same as the case of clean measurements. The values of Kendall's τ recorded from species 4 has been significantly affected by the added measurement uncertainty, even in the regions where there are high resolution data available and a wide window is selected. Species 1, as of before, shows a completely random behavior and its reported early warning signals are not reliable.

Based on above analysis, it is observed that early warning signals recorded from the identified most reliable species, i.e. species 2 and 3, are more robust to data analysis parameters and measurement errors. Results of Figs. 9 and 10 show that for the same system observation, the reported Kendall's τ by species 1 can take values from large positive to large negative numbers depending on the choice of data analysis parameters, meaning that this species is completely uncertain about an upcoming regime shift. The uncertainty significantly decreases if we monitor the best indicator species, i.e. species 2 and 3, and they confirm existence of an increasing trend in the measured early warning signals in all set of studied parameters. This shows the significance of identifying the best sensor species to predict regime shifts since the predictions are more robust to the choice of data analysis parameters as well as uncertainties in measurements.

Note that this study does not provide the time resolution and window size which would be the best to extract early warning signals. To draw such a conclusion, a more detailed analysis of system statistics is required, as what is done in [40].

7.3.3 Spatial harvesting model

Identifying the best species to monitor in a system of higher dimensions, or the area to monitor in a spatially-distributed system, is of particular importance. When the system is spatially distributed and has a large dimension owing to a large number of interacting regions, it is costly and often infeasible to monitor the dynamics of the whole system. Therefore, it is desirable to identify a subset of indicator regions that can provide reliable early-warning signals of upcoming critical transitions. Such indicator regions are viewed similar to indicator species in the previous examples.

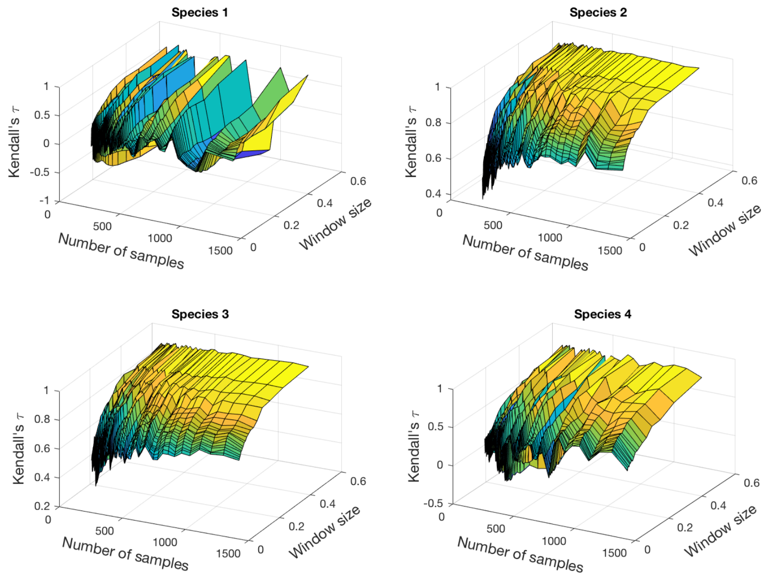

Figure 7.9. Measured Kendall's τ using the recorded signal of each of the four species of example 7.3.2. For a single observation of system dynamics as it approaches to the critical transition, Kendall's τ is approximated using measurements taken at each of the four species for different set of sampling resolutions and window sizes.

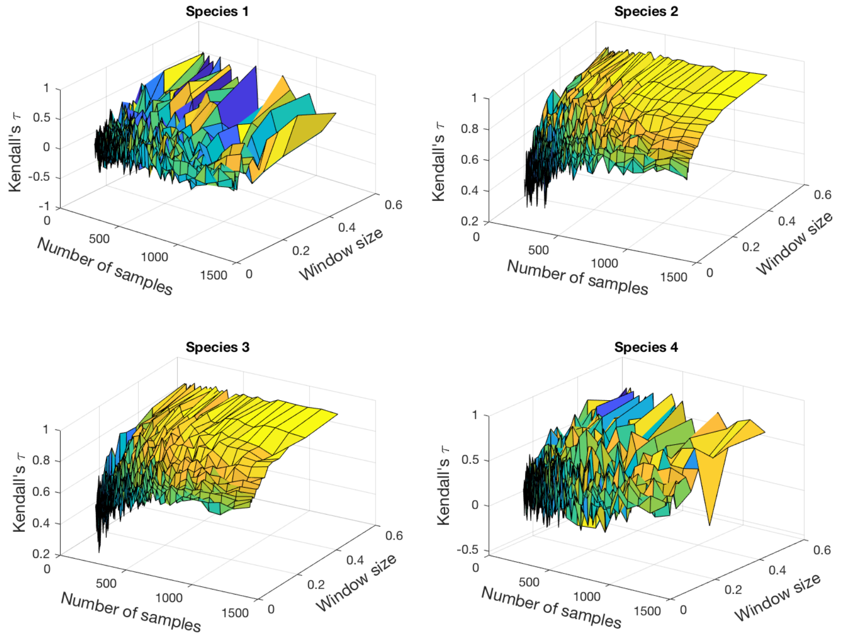

Figure 7.10. Measured Kendall's τ for the time series used to construct Fig. 7.9 with an added measurement uncertainty to each data point.

In this section, we considered a 2D spatially distributed ecosystem (a harvesting model), which was discretized in a grid of interconnected regions. The spatial harvesting model was as follows:

$$\frac{dx_{i,j}}{dt} = r_{i,j}x_{i,j}\left(1 - \frac{x_{i,j}}{K_{i,j}}\right) - c_{i,j}\frac{x_{i,j}^2}{x_{i,j}^2+1} + D\left(x_{i+1,j} + x_{i-1,j} + x_{i,j+1} + x_{i,j-1} - 4x_{i,j}\right) + \sigma_{i,j}dW_{i,j}, \tag{7.9}$$

where $K_{i,j}$ is the carrying capacity in region (i,j), $c_{i,j}$ is the harvesting rate in region (i,j), D is the dispersion rate, $x_{i,j}$ is the biomass in region (i,j) (i.e., a scalar state variable for each region), $r_{i,j}$ is the maximum growth rate in region (i,j), and $\sigma_{i,j}$ is the standard deviation of the noise excitation in region (i,j), for $i = 1, \ldots, P$, and $j = 1, \ldots, Q$, with P and Q being the number of nodes in the two dimensions of the spatially-distributed system. The dynamics in each region (i,j) are affected by a reaction process described by the nonlinear deterministic term $r_{i,j}x_{i,j}\left(1 - \frac{x_{i,j}}{K}\right) - c_{i,j}\frac{x_{i,j}^2}{x_{i,j}^2+1}$. Each region also interacts with its neighboring regions (with periodic boundary conditions) through a diffusion process with the dispersion rate D. We assumed that independent random excitations existed in each region, represented by the random walk process $dW_{i,j}$. We defined the harvesting rate in region (i,j) as $c_{i,j} = \mu_{i,j}c_{max}$, where $\mu_{i,j} \in [0.7,1]$, meaning that the harvesting is non-uniform among different patches. By increasing the harvesting rate c_{max}, the system exhibited a critical transition from an underexploited condition (a high-population equilibrium) to overexploitation (a low-population equilibrium).

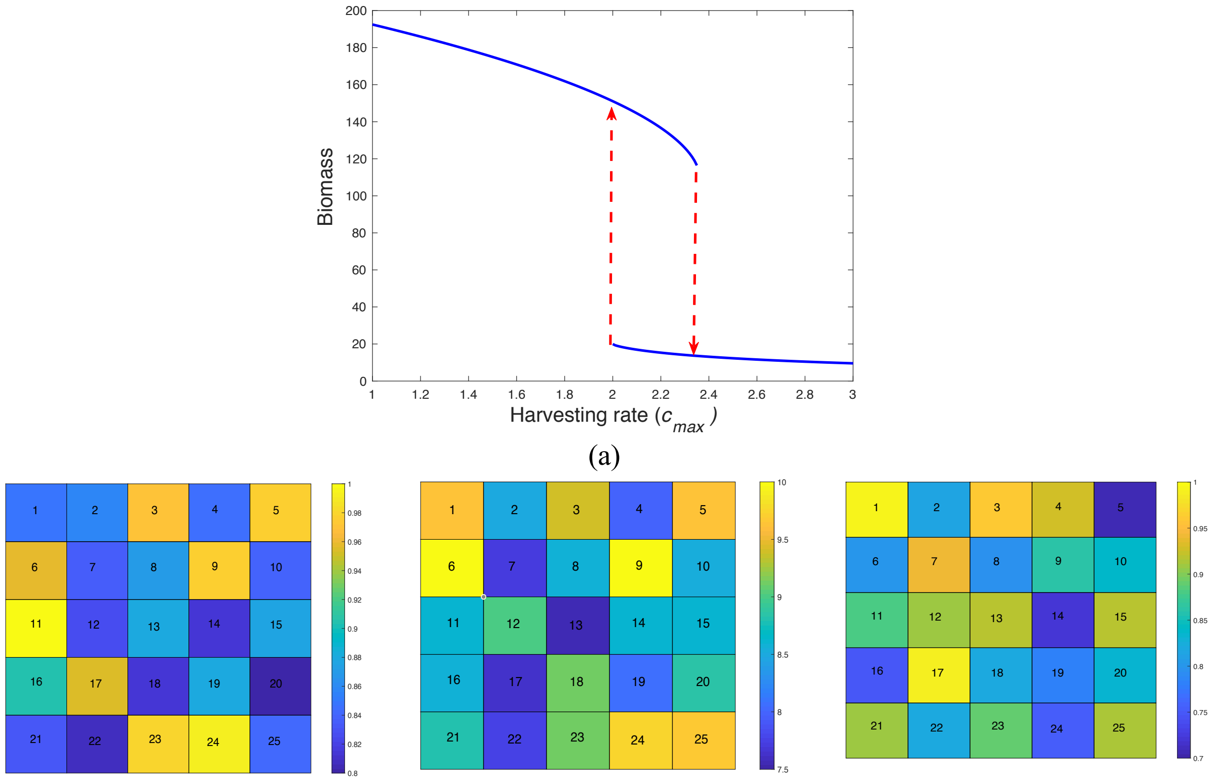

(a)

(b) (c) (d)

Figure 7.11. (a) Bifurcation diagram of the spatial harvesting model. Only the stable branches are shown in this figure. (b) The value of the growth rate $r_{i,j}$ in each region. (b) The value of the carrying capacity $K_{i,j}$ in each region. (d) The value of the harvesting rate $\mu_{i,j}$ in each region.

The proposed data-driven approach was applied to identify the best indicator regions in this large-dimensional ecosystem. Consider $P = Q = 5$, which results in a 25-dimensional system. The bifurcation diagram of the system is depicted in Figure 7.11(a). The dispersion rate was selected to be $D = 0.2$ for all patches. To introduce spatial heterogeneity to the system, the growth rates ($r_{i,j}$), carrying capacities ($K_{i,j}$) and harvesting rates ($\mu_{i,j}$) of each region were selected randomly from the intervals [0.8,1], [7.5,10] and [0.7,1], respectively (Fig. 7.11).

Identifying the best indicator regions in this system is important because monitoring all regions would require an excessive cost and effort. Thus, the proposed data-driven approach was employed with the measured system responses to small perturbations at a harvesting rate of

$c_{max} = 2$. In this example, instead of a single perturbation, system responses to 5 separate small perturbations were used to accurately identify the slowest eigenvector of the system. A larger number of perturbations was required because a single perturbation might not excite the whole dynamics of the system, i.e. it may not create dynamics along enough eigenvectors owing to the large-dimensionality of this system. A lack of sufficient dynamics can lead to less accurate estimations of the slowest eigenvector.

Theoretical analysis of the system showed that the slowest eigenvector of the system was that shown in Figure 7.12(a). Thus, the best indicator regions for this system were those around the bottom left corner of the field. The results of this model-free, data-driven approach are shown in Figure 7.12(b), and were consistent with the theoretical predictions. The results indicate that the most important regions in this spatially-distributed system can be accurately estimated without any knowledge of the underlying system equations. Region 21 was identified as the most-favorable region to be monitored, while the regions in the top right corner were correctly identified as the least-favorable regions to be monitored.

In spatially-distributed systems, it might be challenging to measure the entire system to approximate the dominant eigenvector. Furthermore, even if the best indicator region is known, it might not be accessible or feasible before long-term measurements to extract early-warning signals for critical transitions. Hence, it is important to identify the best indicator regions among those that are accessible for measurement. In the next example, we assumed that only some of the regions were accessible for measurements in the spatial harvesting model. For instance, we assume that the regions in the bottom and left edges of the system were the only measurable ones, and their response to small random perturbations was employed in the system identification algorithm. Figure 7.12(c) shows the ranking result for the measured patches. Results of this data-driven approach correctly identified that region 21 was the best indicator region compared with the other measured regions.

(a) (b) (c)

Figure 7.12. The slowest eigenvector obtained using (a) theoretical formulation, (b) data-driven algorithm by measuring all regions, and (c) data-driven algorithm measuring only the regions along the bottom and left edges of the 2D domain. Regions that were not measured are shown in white; no information is available for these regions. Results from all analyses suggest that region 1 was the best indicator region.

The model of Eq. (7.9) was simulated using numerical methods to compute early-warning signals using measurements taken from each region and their performance was compared. Random heterogeneous excitations with standard deviation $\sigma_{i,j}$ were considered. In addition, random measurement noise was added to the measured signals. The harvesting rate c_{max} started at $c_{max} = 1.5$ and gradually increased toward the critical value of $c_{max} = 2.35$. Figure 7.13 shows a comparison of the measured Kendall's τ for the early-warning signals extracted from selected regions. The results indicate that measuring region 21 provided the best indicator of the critical transition in this system, while regions 13 and 5, for instance, did not provide as much useful information for predicting the critical transition.

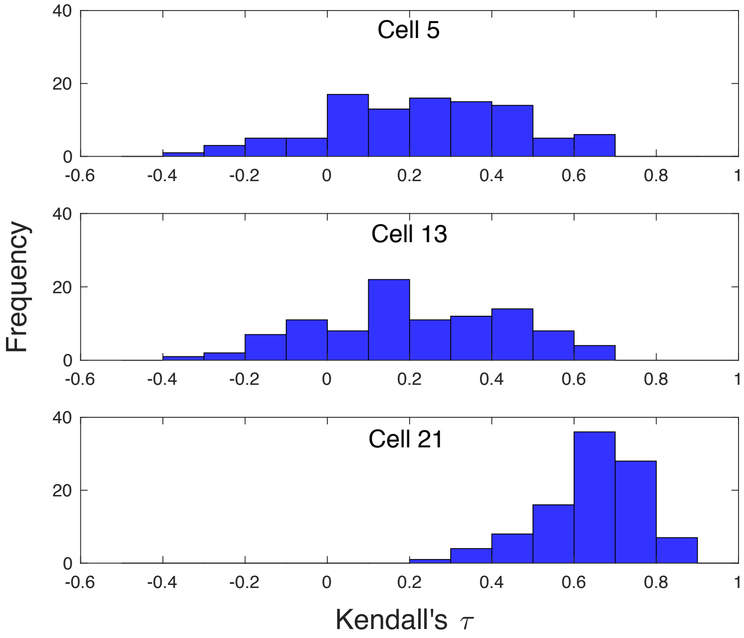

Figure 7.13. Distribution of computed Kendall's τ of early-warning signals for the spatial harvesting model discussed in Sec. 7.3.3. Signals were recorded at regions 5, 13, and 21 for 100 independent simulations in the presence of random heterogeneous measurements and process noise.

7.4 Complications arising from the best-indicator node ranking procedure

In the procedures discussed in previous sections, we focused on identifying the best indicator nodes in ecosystems using measured system dynamics at several nodes. The ranking procedure was mainly based on the direction of the dominant eigenvector, which is a valid assumption when the system is reasonably close to the transition. However, ranking the system components can be more complicated and requires a more detailed analysis of its underlying dynamics. Unfortunately, performing such a detailed analysis might not be feasible in practice. However, it is important to be aware of the factors affecting the reported early-warning signals to accurately interpret the results.

7.4.1 Challenges with large-dimensional systems

In large-dimensional systems, the system has a large set of eigenvalues. In such systems, several eigenvalues other than the dominant one might slow down and approach zero as the system approaches the transition. Hence, there may be several eigenvalues slowing down and affecting the early-warning signals, particularly those with a close value to the dominant eigenvalue. In such cases, the system state that contributes the most to the dominant eigenvector would still be among the best to be measured. However, small entries in the dominant eigenvector do not necessarily mean their corresponding states do not provide measurable early-warning signals.

As an example, the same harvesting model was considered, but with a different parameter distributions. Figure 7.14 shows the trend in eigenvalues of this system as it approaches the transition, which occurs at the harvesting rate of $c_{max} = 2.17$. The eigenvalues were closely spaced, and they were all slowing down as the harvesting rate increased and, as a result, more than a single eigenvalue was affecting the early-warning signals. In this case, the dominant eigenvector did not necessarily reflect the ranking of the nodes based on the reliability of their early-warning signals, unless the system was extremely close to the transition. To correctly rank the regions in this system, at least the first two dominant eigenvectors should be considered because their corresponding eigenvalues are close for a wide range of parameters before the transition occurs. Figure 7.15 shows the first two dominant eigenvectors of the system close to the transition. The dominant eigenvector shows that region 5 was the best to be measured. Moreover, based on the dominant eigenvector, region 21 would not provide measurable slowing down and should not be measured. However, Figure 7.15(b) shows that region 21 contributed the most to the second eigenvector of the system, which indicates that it may be a good candidate for monitoring.

We performed numerical methods to compute early-warning signals using measurements taken from each region and compared their performance. Figure 7.16 shows the results of a comparison of the measured Kendall's τ for the extracted early-warning signals among measurements from regions 5, 13, and 21. Results show that measuring region 5 provided a strong signal for the risk of critical transitions. Interestingly, one region 21 also provided comparably reliable early-warning signals and effectively captures the upcoming transition. However, considering only the dominant eigenvector does not confirm that. Moreover, although region 13 had almost the same value as region 21 in the dominant eigenvector, it was not a good candidate to be monitored because its contribution to the second dominant eigenvector was insignificant as well (Fig. 7.16). The results showed that, in large-dimensional systems, the effect of more than a single eigenvector should be considered to successfully rank the importance of species in the system for providing accurate early-warning signals.

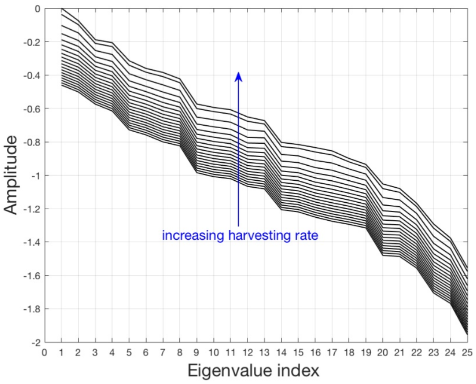

Figure 7.14. Eigenvalues corresponding to the 5 × 5 spatial harvesting model discussed in Sec. 4.1 and their variation with increasing harvesting rate.

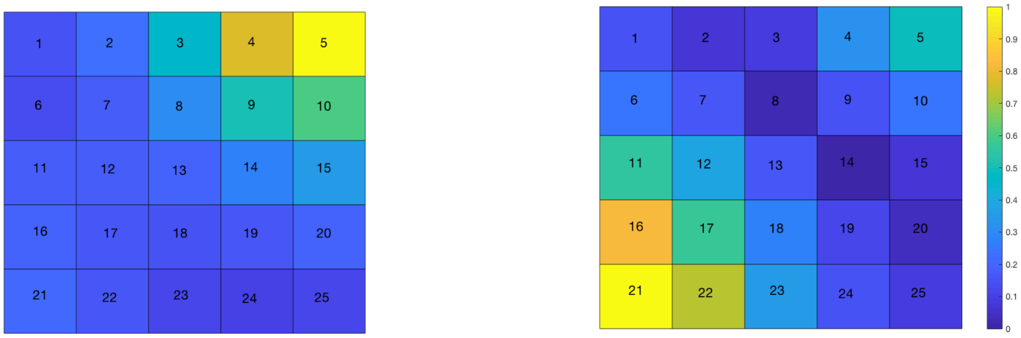

(a) (b)

Figure 7.15. Eigenvector corresponding to the 5 × 5 spatial harvesting model discussed in Sec. 4.1. (a) the first dominant eigenvector, (b) the second dominant eigenvector.

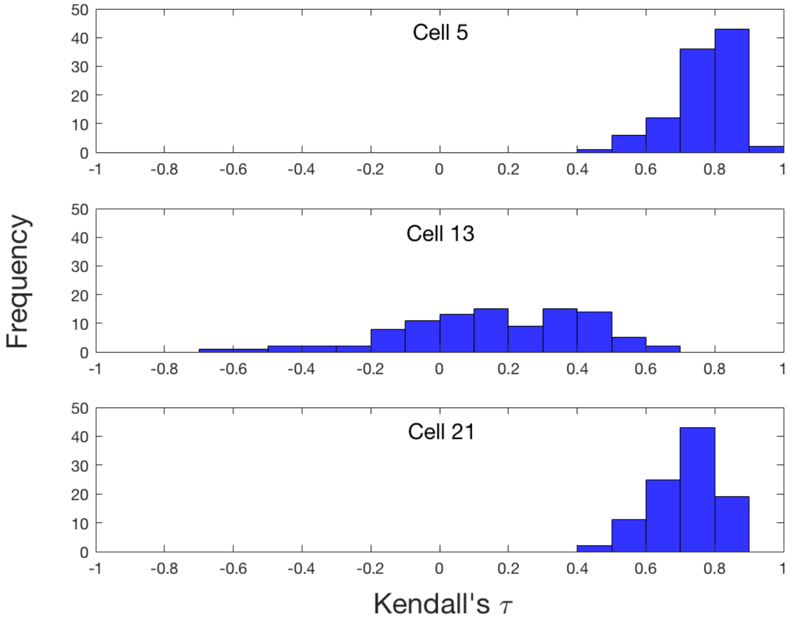

Figure 7.16. Distribution of computed Kendall's τ of early-warning signals for the spatial harvesting model discussed in Sec. 7.4.1. Signals were recorded at regions 5, 13, and 21 for 100 independent simulations in the presence of random heterogeneous measurements and process noise.

7.4.2 Variation of eigenvectors and a false alarm

Early-warning signals, including increases in variance and autocorrelation, can signal that a system is approaching a transition. However, for this statement to be completely valid, the system must be close enough to the critical point so that the effect of changing system dynamics on the results can be ruled out. The issue, however, is that it is not clear how far a system is from transition. Early-warning signals are a function of both eigenvalues and eigenvectors of a system. Consider a simple two-dimensional linear system with parameter μ, eigenvalues $\lambda_1(\mu)$ and $\lambda_2(\mu)$, and the right eigenvectors v_1 and v_2, respectively. The dynamics of the system would be as follows:

$$\frac{d\mathrm{x(t)}}{dt} = A(\mu)\mathrm{x(t)} + \mathrm{f}(t) \tag{7.10}$$

where x is the state vector, A is the system coefficients matrix, and f is the forcing term that is considered to be a stochastic excitation in this case, i.e. $\mathrm{f} = [\gamma_1 \mathrm{dW}_1, \gamma_2 \mathrm{dW}_2]^{\mathrm{T}}$. The transformation $\Phi = [\mathrm{v}_1\ \mathrm{v}_2]$, where v_1 and v_2 are the right eigenvectors of matrix A, can be defined as: $\mathrm{x(t)} = \Phi\mathrm{q(t)}$, where q is the vector of modal coordinates. If variance is considered to be the early-warning indicator, then in the steady state dynamics, the variance of the states x_1 and x_2, denoted by $\sigma_{\mathrm{x}_1}^2$ and $\sigma_{\mathrm{x}_2}^2$, can be defined as follows:

$$\begin{aligned} \sigma_{\mathrm{x}_1}^2 &= v_{1,1}^2\sigma_{q_1}^2 + v_{1,2}^2\sigma_{q_2}^2 + 2v_{1,1}v_{1,2}\sigma_{q_1q_2}^2, \\ \sigma_{\mathrm{x}_2}^2 &= v_{2,1}^2\sigma_{q_1}^2 + v_{2,2}^2\sigma_{q_2}^2 + 2v_{2,1}v_{2,2}\sigma_{q_1q_2}^2, \end{aligned} \tag{7.11}$$

where $\sigma_{q_1}^2$ is the modal variance containing the information regarding the variance of the dominant eigenvalue $\lambda_1(\mu)$, $\sigma_{q_2}^2$ contains information of the variance of the second eigenvalue $\lambda_2(\mu)$, and $\sigma_{q_1q_2}^2$ is the covariance of the modal coordinates. Moreover, $v_{i,j}$ represents the i^{th} element of the j^{th} eigenvector. Modal variances were calculated as follows:

$$\sigma_{q_1}^2 = \frac{h_1(\mathrm{z}_1,\gamma_1,\gamma_2)}{\lambda_1},$$

$$\sigma_{q_2}^2 = \frac{h_2(\mathrm{z}_2,\gamma_1,\gamma_2)}{\lambda_1}, \tag{7.12}$$

$$\sigma_{q_1 q_2}^2 = \frac{h_3(\mathrm{z}_1,\mathrm{z}_2,\gamma_1,\gamma_2)}{\lambda_1+\lambda_2},$$

where z_1 and z_2 are the left eigenvectors of the system matrix A, and h_is are scalar functions.

Considering the system has a dominant eigenvalue, the modal variance $\sigma_{q_1}^2$ contains important information regarding the upcoming transition because it is inversely proportional to the dominant eigenvalue of the system. Taking the variance of x_1 as an early-warning signal and assuming $\lambda_1(\mu) \gg \lambda_2(\mu)$ for simplicity, a rise in the early-warning signal can be observed from Eq. (7.11) due to two main reasons: 1) the dominant eigenvalue approaching zero, which increases the modal variance $\sigma_{q_1}^2$, and 2) change in the eigenvectors of the system. Note that $\sigma_{q_1}^2$ is the quantity that contains information of the upcoming transition (since it includes the dominant eigenvalue), and measuring/identifying the modal variance $\sigma_{q_1}^2$ would provide a value that is independent of the system states and should be used as the early-warning signal of the upcoming transition. Identifying this quantity, however, requires a detailed knowledge of the system, including measurements of all state variables. Equation (7.11) shows that a significant change in the dominant eigenvector by parameter (μ) can reduce the efficacy of measured early-warning signals by over- or underestimating its actual value. In some situations, change in the eigenvectors can result in raising a false critical-transition alarm. In dynamical systems, change in the eigenvectors with parameter is unavoidable, and the consequences for approximated early-warning signals must be examined to properly process and interpret the results.

As an example, we considered a simple two-dimensional system consisting of two interacting nodes with μ as the parameter. The linear instability occurs at $\mu = 0$. The system was designed to have a dominant eigenvalue approaching zero. For simplicity, the other eigenvalue selected was large enough ($|\lambda_2(\mu)| \geq 10|\lambda_1(\mu)|$) so the effect of the second eigenvalue and its corresponding eigenvector on the recorded early-warning signal was negligible. Figure 7.17(a) shows the change in the dominant eigenvector as the system approaches the instability. We observed that, although the component corresponding to node 1 (x_1) in the dominant eigenvector was always greater than that of node 2, it decreased toward its final value at the critical parameter. Conversely, the contribution of node 2 to the dominant eigenvector of the system was always less than that of node 1; however, its contribution was increasingly significant as the system approached the transition. If only the amplitudes of the dominant eigenvector at a fixed parameter were considered, then node 1 might be identified as the best indicator of the upcoming critical transition. Figure 7.17(b) shows the computed variance of each node as the system gradually approaches the transition. We observed that node 2 provided a more accurate prediction of the upcoming transition. For the parameter values up to $\mu = -0.5$, node 1 did not identify the upcoming transition, while the early-warning signal corresponding to node 2 exhibited a significant increasing trend. Notably, however, neither of the nodes provided correct early-warning signals because the signals provided by nodes 1 and 2 under- and overestimated the system distance to the transition, respectively. This was due to a significant change in the contribution of each node to the dominant eigenvector (Fig. 7.17(a)).

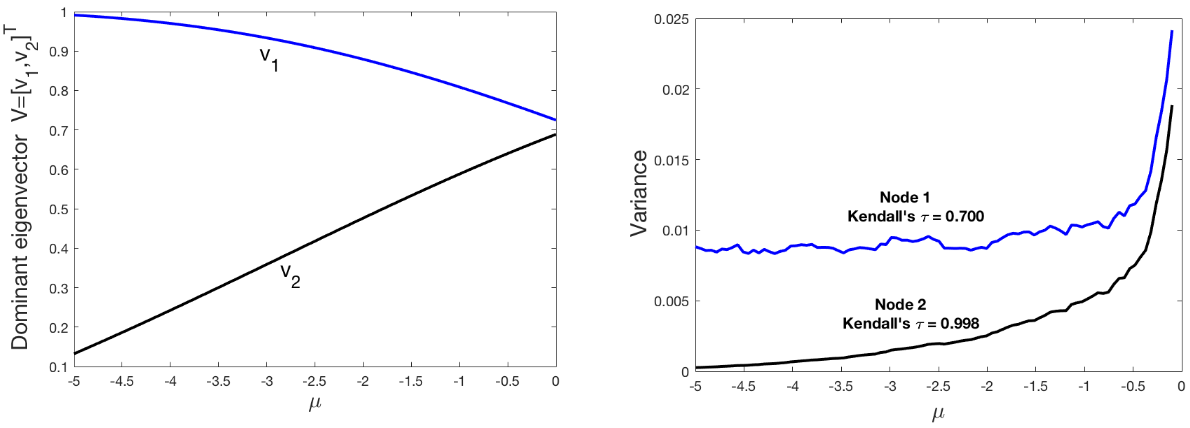

(a) (b)

Figure 7.17. (a) Change in the dominant eigenvector of the example system as the system approached the transition at $\mu = 0$, (b) early-warning signals measured from system components.

In the next example, we demonstrated a situation in which, change in the dominant eigenvector with parameter resulted in a completely false alarm. We considered a simple system of two interacting nodes, approaching a transition at $\mu = 0$, in which the dominant eigenvector changed with parameter as shown in Figure 7.18(a). Figure 7.18(b) shows the recorded variance of the nodes as the system approached the transition. We observed that a change in the eigenvector can lead to a false alarm as reported by node 2 at $\mu = -2.5$.

We have provided two simplified examples with a low-dimensional system and only a single dominant eigenvalue. The examples reveal the challenges that might be associated with interpreting early-warning signals. Further complications were found with large-dimensional systems with several close eigenvalues, and the well-known assumptions of early-warning signals are only maintained when the system is reasonably close to the transition. Theoretically, the solution to this issue would be to perform an eigenvalue decomposition and filter out the effect of all changes in the system except the change in the dominant eigenvalue. However, this would require continuous identification of left and right eigenvectors of the system. Although there are experimental procedures for identifying such properties [70,71], applying them to real systems, especially ecosystems, is costly and difficult. A data-driven algorithm such as the eigensystem realization algorithm could be used to approximate the dominant eigenvector of the system at several parameter values when possible and monitor its changes over time to get an idea of how the dominant modes vary with the parameter and how reliable the computed early-warning signals are.

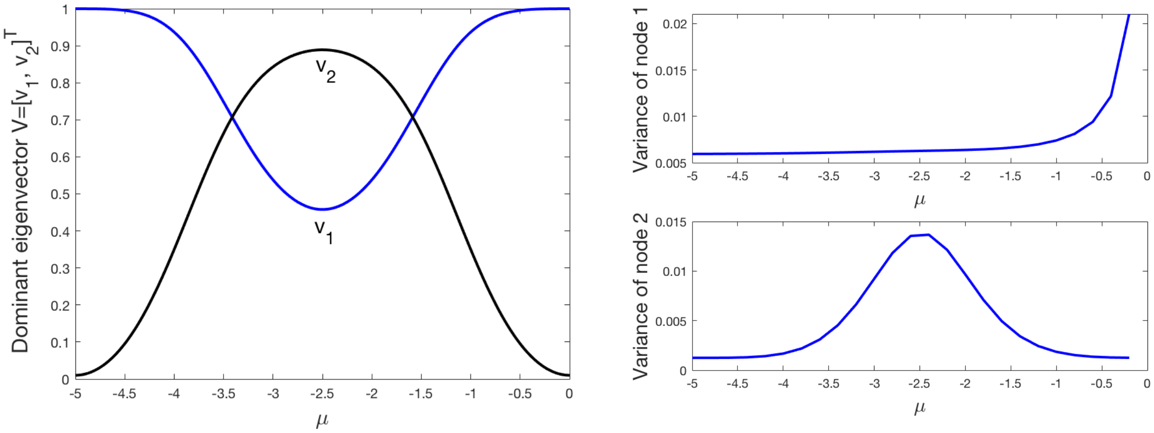

(a) (b)

Figure 7.18. (a) Change in the dominant eigenvector of the example system as the system approached the transition at $\mu = 0$, (b) early-warning signals measured from system components.

7.5 Conclusions

Detecting early-warning signals of critical transitions for large-dimensional complex ecosystems is a challenging task owing to the complex system dynamics involving many species. In such complex systems, to determine where to measure the system and how to interpret the measurements to achieve the most accurate early-warning signals of an upcoming transition is an important requirement. Herein, we propose a data-driven approach to rank the elements of a system based on their reliability in providing the best early-warning signals of critical transitions. We used experimental modal analysis techniques, which are widely used in engineering, combined with the early-warning signals to identify the best-indicator nodes in a connected system and extract the most reliable early-warning signals of critical transitions. The system response to perturbations was recorded and used as an input for the proposed technique, which is a common tool for identifying dynamical system features.

Numerical examples demonstrated that not all the species in an ecosystem provide reliable early-warning signals of a system approaching a transition, and the proposed technique was able to successfully rank the species/regions in the studied ecosystems based on the accuracy of their early-warning signals. In addition, results indicated that, to correctly rank species and interpret the recorded early-warning signals in an ecosystem, other dynamical features of the system should also be considered. For instance, we observed that gradual change in the system eigenvectors resulted in over- or underestimating trends in the recorded early-warning signals. Moreover, the results verified that, in large-dimensional systems, the effects of several eigenvectors other than the dominant one must be considered to successfully rank the importance of the species in the system.

Chapter 8

Conclusions and future work

8.1 Summary

It is becoming increasingly evident that many complex systems, ranging from ecological to engineered systems, are at risk of critical transitions at which the system shifts abruptly from one state to another. Such an unexpected change in the equilibrium state is usually undesirable, because it is often difficult to restore a system to its pre-transition state once the transition occurs. Hence, there is an acute need for reliable methods to predict such catastrophic events. It is notably difficult to predict critical transitions because the state of the system may show little change before the tipping point is reached. Moreover, models of complex systems are usually not accurate enough to predict reliably where critical thresholds may occur.

The focus of this research was on forecasting critical transitions in complex dynamical systems with application in several fields, from engineering to population dynamics. The main goal of this research was to create a novel method to quantitatively forecast critical transitions as well as the pre- and post-transition dynamics using some measurements of system before the transition occurs. Novel techniques were introduced to assess the existence of crucial thresholds in complex dynamical systems and to evaluate the future consequences of surpassing them. Based on observations of the system response to perturbations only in the pre-transition regime, the method forecasts the bifurcation diagram which discovers system’s stability and equilibria in upcoming conditions. The forecasting approach was based on the phenomenon of critical slowing down, referring to the slowing down of a system’s dynamics around its equilibrium when approaching a tipping point. This means that the rate of the system’s recovery from perturbations decreases when the system approaches the bifurcation. Therefore, rate of recovery from perturbations at each amplitude can be used as an indicator, and is correlated to the distance to the bifurcation. This finding was used to predict the bifurcation diagram which discovers system’s stability and equilibria in upcoming conditions.

The proposed bifurcation forecasting method is model-free, i.e. it is only required to measure a few system responses in the safe stable regime to forecast the bifurcation diagrams (without analyzing system equations). The method addresses some challenges which exist in complex systems where using classical methods is not possible (e.g., when a model of the system is not available, or is inaccurate) or is challenging (e.g., when the full model is very expensive computationally). Specifically, the forecasting method is developed and advantageous for two main cases. First, when a nonlinear system is studied experimentally, and there is no model of this system available to be analyzed using traditional methods. This is particularly important when there are a lot of unknowns and interactions in the system which makes developing and calibrating an accurate model of system difficult or impossible. The forecasting method makes it possible to forecast the bifurcation diagrams using measurements of the system response to perturbations in the pre-bifurcation regime without developing a model for the system. Second, the method is also advantageous when there exists a model for system, but the system is large dimensional and constructing the bifurcation diagram using theoretical methods is very expensive computationally. A common example of such a case is when a complex system is modeled using high-fidelity finite elements and the bifurcation point, bifurcation type and bifurcation diagram needs to be investigated. Such models often have millions of degrees of freedom. Identifying the post-bifurcation dynamics for such models using theoretical methods (e.g., center space reduction) is very difficult. More direct numerical methods such as time marching is very time consuming because the system has to be simulated many times, at many parameter values in order to construct the bifurcation diagram. In contrast, using the presented forecasting method the bifurcation diagrams can be constructed using only 2 or 3 simulations.

Supercritical and subcritical Flutters are observed in a variety of fluid-structural systems. Such phenomena lead to various types of stability issues and can cause dramatic changes in the dynamics. Therefore, forecasting such bifurcations, i.e. predicting bifurcations and the bifurcation diagram with measurements only from the pre-bifurcation regime is a significant challenge and an important need. This is especially important for complex large-dimensional systems when an accurate model of the system is not easily available or when the system properties/parameters are unknown. In this research, a unique forecasting approach was introduced to forecast bifurcation diagrams and post-bifurcation limit cycles in fluid-structural systems. The forecasting method was employed to forecast the flutter speed and bifurcation diagrams of nonlinear fluid-structural systems including two- and three-degree-of-freedom airfoils and large dimensional high aspect ratio wings using as few as three measured system recoveries from perturbations collected only in the pre-bifurcation regime. Numerical results shows that the method can accurately forecast the bifurcation diagram of the system although no mathematical model of the system is required for forecasting. Furthermore, the method identifies the type of bifurcation, i.e. supercritical or subcritical, and forecasts the complete dynamical behavior of the system in the post-bifurcation regime. This type of forecasting opens the door to a variety of applications where knowledge of nearby bifurcations is important for safety and maximum system performance.

Stop-and-go traffic jams can often be observed in real-life traffic situations. Although Study of traffic flow dynamics has a long tradition, predicting traffic jams before they occur is still a challenge due to the complex nature of the traffic phenomenon. Prediction of traffic congestions may allow implementation of effective dynamic control strategies. In this research, the onset of traffic jams on a circular road was forecasted using early warning indicators/signals and bifurcation forecasting methods. Forecasting approaches were applied to a microscopic model of cars on a circular road. Results show that forecasting approaches can successfully predict the critical parameter value at which traffic jams occur. Furthermore, the bifurcation forecasting method can be used for forecasting both the critical point (i.e., the onset of traffic jams) and the post-critical dynamics of the system (i.e. the bifurcation diagram). These results are particularly valuable when the state of the system after the bifurcation is of interest. Moreover, forecasting can be highly advantageous also for theoretical or computational analyses of traffic flow models where employing traditional methods for computation of bifurcation diagrams are computationally intense. The approaches and ideas presented can be used as a basis for more developments to address some of the challenges related to the complexity of traffic dynamics.

Regime shifts in complex ecological and living systems have received a growing attention since the cumulative human impact on the environment is increasing the risk of ecological regime shifts. Anticipating such critical transitions is an important need because it is often difficult to restore the system to its pre-transition state once the transition occurs. Hence, it is necessary to develop reliable methods capable of forecasting upcoming transitions, as part of a preventive plan against possible detrimental consequences. To address this important topic, we introduced and experimentally evaluated a unique forecasting method to forecast critical transitions in ecological systems and natural populations. The method forecasts critical points and post-critical dynamics of the system using measurements of the system response collected only in the pre-transition regime. The method was evaluated using as a model ecological system a population of budding yeast with cooperative growth in the lab which exhibits a catastrophic transition as the environment deteriorates, resembling an ecological collapse. The experimental results of this study are promising and address important challenges which exist in forecasting safety and stability of natural populations. Results highlight that by monitoring rate of recovery of the system's response to perturbations, it is possible to gain crucial information about the future system’s safety and stability, such as the quantitative distance to upcoming transition (collapse), the type of upcoming transition (i.e., catastrophic/non-catastrophic) and future equilibria of the system. We envision this approach to be used in stability and safety analysis of natural populations, which is exceedingly important in ecological management.

Detecting these early-warning signals of critical transitions for large dimensional complex ecosystems is a challenging task due to the complex dynamics of systems and the large number of species involved in the system. In such complex systems, to determine where to measure the system and how to interpret the measurements to achieve the most accurate early warning signals of an upcoming transition is an important need. We proposed a data driven approach to rank the elements of the system based on their reliability in providing the best early warning indicators of critical transitions. We employed experimental modal analysis techniques which are widely used in engineering in combination with the early warning indicators to identify the best-indicator nodes in a connected system and extract the most reliable indicators for critical transitions. The system response to perturbations are recorded and employed as an input to proposed technique which are common tools in identifying dynamical systems features. Numerical examples show that not all the species in an ecological system provide reliable early warning sign of approaching to a transition, and the proposed approached has successfully ranked the species/regions in the studied ecological systems based on the accuracy of their provided early warning signals. In addition, results show that to correctly rank the species and interpret the recorded early warning signals in an ecological system, one might consider other dynamical features of the system as well. For instance, it was observed that gradual change in the system eigenvectors would result in an overestimated/underestimated trend in the recorded early warning signals. Moreover, results verify that in large dimensional systems, one need to consider the effect of several eigenvectors other than the dominant one to successfully rank the importance of the species in the system.

8.2 Contributions

The major contributions of this dissertation are summarized as follows.

- A set of unique techniques, called bifurcation forecasting methods, are proposed to predict instabilities and bifurcation diagrams of nonlinear dynamical systems without analyzing system equations. Constructing such a diagram using conventional numerical or experimental methods needs accurate models, or massive computational effort.
- A novel forecasting method is introduced to predict the flutter speed and post-flutter dynamics of fluid-structural systems using a few system responses to gust perturbations in the pre-flutter regime.
- Techniques are introduced to increase forecasting accuracy in case of large dimensional systems by identifying and separating the effect of bifurcating mode in the measured recoveries from perturbations.
- Techniques are introduced to increase forecasting accuracy in case of noisy measurements and insufficient data.

- The phase difference between system states is included in an improved forecasting procedure to forecast three-dimensional bifurcation diagrams of fluid-structural systems, representing stable and unstable limit cycle amplitudes of system states at all phases.
- Rate of recovery from perturbations is shown to contain crucial information about future stability of natural populations which are at risk of catastrophic transitions.
- The bifurcation forecasting method is employed and experimentally validated to predict bifurcation diagrams and catastrophic transitions of an experimental ecological system monitoring system response to perturbations.
- Bifurcation forecasting methods and early warning indicators are proposed as effective tools to analyze the stability of vehicular traffic on roads, suggesting a strong potential for practical applicability of this approach in traffic engineering.
- The reliability early warning signals of critical transitions recorded from ecological networks is analyzed. It is shown that the reliability of early warning signals and robustness of early warning signals to data analysis parameters varies among different species in a network.
- Ranking of species/regions of ecological systems based on their reliability in providing the best early warning indicators of critical transitions is analyzed.

8.3 Challenges and limitations

The results of this research opens a door to a variety of numerical and experimental applications by introducing unique model-free tools for stability analysis of complex systems. However, there are several requirements for the proposed methods to be accurate. A first requirement is that the system exhibits slowing down as it approaches to transition. Many biological, ecological, engineering systems exhibit bifurcations such as Hopf, saddle node, pitchfork and transcritical bifurcations which satisfy the method assumptions. Examples are bifurcations in population dynamics, fluid-structural systems, periodically forced systems in engineering systems and disease dynamics, nonlinear circuits, to name a few. However, note also that critical slowing down does not exist in all types of bifurcations. For example, systems undergoing period doubling cannot be forecasted using the proposed approach. A second requirement is that the system dynamics and its inertial manifold vary smoothly with the bifurcation parameter. The critical point and the bifurcation diagram can be forecasted if the system is close enough to the transition to exhibit measurable slowing down in its recoveries. The challenge is that some systems do not exhibit any slowing down unless at parameters which are significantly close to the instability boundary. Hence, in order for the forecasting method to work, measurements need to be taken in a narrow parameter regime where slowing down is observed, which is a challenging task specially in experimental systems due to presence of noise and uncertainties in experiments.

In addition, noise can contaminate measurements, thus influencing the forecasting accuracy. Techniques were proposed to increase the forecasting accuracy when measurement noise exists in system. However, forecasting remains challenging if the noise level is high, if there are no enough measurements available and if stochasticity exists in both system parameters and measurements.

8.4 Future Research

The work presented in this dissertation can be extended in several directions.

1. Current research focused on forecasting bifurcation diagrams for deterministic systems and systems affected only by measurements noise and small stochasticity in their dynamics. However, the techniques might face a challenge if applied to systems which are highly stochastic. Therefore, it would be beneficial to study bifurcation diagrams and forecasting approaches in stochastic systems.
2. To study the stability and identify the post-flutter dynamics of large dimensional fluid structural systems using traditional methods is a great challenge, specifically if one needs to perform a parametric study to study the effect of change in the design parameters on the stability of systems. Up to date, there have been few studies on the impact of design parameters on post-flutter response, and only for highly simplified models. This is because post-flutter calculations are currently too demanding for design due to both nonlinear modeling challenges and the lack of analysis methods for computing bifurcation diagrams directly. The proposed forecasting method, however, provides an efficient tool to identify the bifurcation diagram of system with minimum number of simulations, which identifies necessary information required to analyze system stability. In the next step, the proposed forecasting method can be used to identify the bifurcation diagrams of large dimensional fluid-structural systems, e.g. flexible wings, for different set of design parameters. This approach provides a detailed understanding of the system dynamics around its stability boundary which is costly to be explored without the proposed forecasting approach.
3. Early warning signals and bifurcation forecasting methods were introduced to forecast the onset of traffic congestion and bifurcation diagram of traffic flow systems using microscopic traffic flow models. The forecasting method can be developed to forecast traffic congestions and bifurcation diagrams of macroscopic traffic flow models.

4. Current forecasting methods are developed in the context of autonomous systems. However, critical transitions and recorded system responses might be accompanied by periodic fluctuation of the environment/system parameters [176–178]. Critical transitions in disease dynamical systems are examples of these systems. Development of forecasting methods and early warning signals for such systems is beneficial for practical applications.

Appendix

Appendix A. Supplementary Information for Chapter 3

Consider the following damped single degree of freedom nonlinear system. For clarity, the nonlinearity is assumed to be cubic as

$$\ddot{x} + c\dot{x} + \omega^2 x = \gamma x^3. \tag{A.1}$$

Writing this equation in state space form gives

$$\begin{Bmatrix} \dot{x} \\ \ddot{x} \end{Bmatrix} = \begin{bmatrix} 0 & 1 \\ -c & -\omega^2 \end{bmatrix} \begin{Bmatrix} x \\ \dot{x} \end{Bmatrix} + \begin{Bmatrix} 0 \\ \gamma x^3 \end{Bmatrix}, \tag{A.2}$$

where the states are chosen to be position and velocity.

Next, define the following transformation

$$\mathrm{x} = \Phi \mathrm{y}, \tag{A.3}$$

where x is the state variables vector(x $= [x \ \dot{x}]^T$), y is vector containing the complex modal coordinates y $= [y_1 \ y_2]^T$, and Φ is the matrix of complex mode shapes of the system. Matrix Φ can be written as

$$\Phi = \begin{bmatrix} 1 & 1 \\ \lambda_1 & \bar{\lambda}_1 \end{bmatrix}, \tag{A.4}$$

where $\lambda_1 = (-c - ir)/2$, and $r = \sqrt{4\omega^2 - c^2}$.

Substituting (A.3) into (A.2), solving for y_1 and y_2, and defining $a = \lambda_1 + i\omega$, one obtains the following expressions which can be used in the normal form theory

$$\begin{aligned}\dot{y}_1 &= -i\omega y_1 + a y_1 + \frac{\gamma}{\lambda_1 - \lambda_2}(y_1 + y_2)^3,\\ \dot{y}_2 &= -i\omega y_2 + \bar{a} y_2 - \frac{\gamma}{\lambda_1 - \lambda_2}(y_1 + y_2)^3,\\ \dot{a} &= 0.\end{aligned} \tag{A.5}$$

Next, one may introduce the following nonlinear change of coordinates

$$\begin{aligned}y_1 &= u_1 + \left(-\frac{\gamma}{4\omega^2}u_1^3 + \frac{3\gamma}{4\omega^2}u_1 u_2^2 + \frac{\gamma}{8\omega^2}u_2^3\right),\\ y_2 &= u_2 + \left(-\frac{\gamma}{4\omega^2}u_2^3 + \frac{3\gamma}{4\omega^2}u_2 u_1^2 + \frac{\gamma}{8\omega^2}u_1^3\right).\end{aligned} \tag{A.6}$$

Using normal form theory, one can show that the system can be transformed using Eq. (A.6) into the following normal form up to 3rd order

$$\begin{aligned}\dot{u}_1 &= -i\omega u_1 + a u_1 + \frac{3i\gamma}{2\omega}u_1^2 u_2,\\ \dot{u}_2 &= -i\omega u_2 + \bar{a} u_2 + \frac{3i\gamma}{2\omega}u_2^2 u_1.\end{aligned} \tag{A.7}$$

The solution of above system of equations is in the following periodic form

$$u_1 = \bar{u}_2 = u_0 e^{-ct/2} e^{i\tilde{\omega} t}, \tag{A.8}$$

where u_0 is a complex number, and $\tilde{\omega}$ is real number in the following form

$$\tilde{\omega} = -\frac{r}{2} + \frac{3\gamma}{2\omega}u_0\bar{u}_0 \ . \tag{A.9}$$

Now, using Eq. (A.8) and Eq. (A.6), one may observe that y_1 and y_2 are complex conjugates. Substituting Eq. (A.8) into Eq. (A.6) and assuming small nonlinearities, one can obtain an approximation for the modal coordinates in the following form

$$y_1 = \bar{y}_2 \approx (w_1(t)\cos(\omega t) - w_2(t)\sin(\omega t)) + i(w_1(t)\sin(\omega t) + w_2(t)\cos(\omega t)), \qquad \text{(A.10)}$$

where $w_1(t)$ and $w_2(t)$ are functions of time containing exponentially decaying functions and the recovery rate of the system. Following the same procedure as in Eq. (A.10), one finds that both $w_1(t)$ and $w_2(t)$ have the same decay rate. The real and imaginary parts of the expression on the right hand side of Eq. (A.10) correspond to q_1 and q_2 used in the text as real valued modal coordinates, i.e.

$$\begin{aligned} q_1 &= w_1(t)\cos(\widetilde{\omega} t) - w_2(t)\sin(\widetilde{\omega} t), \\ q_2 &= w_1(t)\sin(\widetilde{\omega} t) + w_2(t)\cos(\widetilde{\omega} t). \end{aligned} \qquad \text{(A.11)}$$

Note that $q_1$and q_2 are in quadrature and form a regular spiral in the $q_1 - q_2$ plane; the same form as expressed in Eq. (11). Note also that this conclusion came from the fact that the modal bases were chosen to be position and velocity.

The above procedure can be extended to higher order systems and nonlinearities. More details can be found in refs. [56,179,180].

Bibliography

[1] M. Scheffer, Critical Transitions in Nature and Society, Princet. Stud. Complex. (2009) 384. doi:10.5860/CHOICE.47-1380.

[2] M. Scheffer, J. Bascompte, W.A. Brock, V. Brovkin, S.R. Carpenter, V. Dakos, H. Held, E.H. van Nes, M. Rietkerk, G. Sugihara, Early-warning signals for critical transitions, Nature. 461 (2009) 53–59. http://dx.doi.org/10.1038/nature08227.

[3] A. Ghadami, B.I. Epureanu, Bifurcation forecasting for large dimensional oscillatory systems: Forecasting flutter using gust responses, J. Comput. Nonlinear Dyn. 11 (2016). doi:10.1115/1.4033920.

[4] J. Lim, B.I. Epureanu, Forecasting bifurcation morphing: application to cantilever-based sensing, Nonlinear Dyn. 67 (2012) 2291–2298.

[5] J. Kramer, J. Ross, Stabilization of unstable states, relaxation, and critical slowing down in a bistable system, J. Chem. Phys. 83 (1985) 6234. doi:10.1063/1.449571.

[6] R.J. Olsen, I.R. Epstein, Bifurcation analysis of chemical reaction mechanisms. I. Steady state bifurcation structure, J. Chem. Phys. 94 (1991) 3083. doi:10.1063/1.459831.

[7] J.R. Tredicce, G.L. Lippi, P. Mandel, B. Charasse, A. Chevalier, B. Picqué, Critical slowing down at a bifurcation, Am. J. Phys. 72 (2004) 799. doi:10.1119/1.1688783.

[8] J. Lim, B.I. Epureanu, Forecasting a class of bifurcations: Theory and experiment, Phys. Rev. E - Stat. Nonlinear, Soft Matter Phys. 83 (2011). doi:10.1103/PhysRevE.83.016203.

[9] P. Chen, R. Liu, Y. Li, L. Chen, Detecting critical state before phase transition of complex biological systems by hidden Markov model, Bioinformatics. 32 (2016) 2143–2150.

doi:10.1093/bioinformatics/btw154.

[10] J.P. Scholz, J.A.S. Kelso, G. Schöner, Nonequilibrium phase transitions in coordinated biological motion: Critical slowing down and switching time, Phys. Lett. A. 123 (1987) 390–394. doi:10.1016/0375-9601(87)90038-7.

[11] L. Dai, D. Vorselen, K.S. Korolev, J. Gore, Generic Indicators for Loss of Resilience Before a Tipping Point Leading to Population Collapse, Science (80-.). 336 (2012) 1175–1177. doi:10.1126/science.1219805.

[12] V. Dakos, M. Scheffer, E.H. van Nes, V. Brovkin, V. Petoukhov, H. Held, Slowing down as an early warning signal for abrupt climate change., Proc. Natl. Acad. Sci. U. S. A. 105 (2008) 14308–12. doi:10.1073/pnas.0802430105.

[13] T.M. Lenton, Early warning of climate tipping points, Nat. Clim. Chang. 1 (2011) 201–209. doi:10.1038/nclimate1143.

[14] T.M. Lenton, H. Held, E. Kriegler, J.W. Hall, W. Lucht, S. Rahmstorf, H.J. Schellnhuber, Tipping elements in the Earth's climate system, Proc. Natl. Acad. Sci. 105 (2008) 1786–1793. doi:10.1073/pnas.0705414105.

[15] C. Trefois, P.M.A. Antony, J. Goncalves, A. Skupin, R. Balling, Critical transitions in chronic disease: Transferring concepts from ecology to systems medicine, Curr. Opin. Biotechnol. 34 (2015) 48–55. doi:10.1016/j.copbio.2014.11.020.

[16] M. a. Kramer, W. Truccolo, U.T. Eden, K.Q. Lepage, L.R. Hochberg, E.N. Eskandar, J.R. Madsen, J.W. Lee, A. Maheshwari, E. Halgren, C.J. Chu, S.S. Cash, Human seizures self-terminate across spatial scales via a critical transition, Proc. Natl. Acad. Sci. 109 (2012) 21116–21121. doi:10.1073/pnas.1210047110.

[17] A. Kianercy, R. Veltri, K.J. Pienta, Critical transitions in a game theoretic model of

tumour metabolism., Interface Focus. 4 (2014) 20140014. doi:10.1098/rsfs.2014.0014.

[18] P. Holme, M.E.J. Newman, Nonequilibrium phase transition in the coevolution of networks and opinions, Phys. Rev. E - Stat. Nonlinear, Soft Matter Phys. 74 (2006). doi:10.1103/PhysRevE.74.056108.

[19] J.C. González-Avella, M.G. Cosenza, K. Tucci, Nonequilibrium transition induced by mass media in a model for social influence, Phys. Rev. E - Stat. Nonlinear, Soft Matter Phys. 72 (2005). doi:10.1103/PhysRevE.72.065102.

[20] C.T. Bauch, R. Sigdel, J. Pharaon, M. Anand, Early warning signals of regime shifts in coupled human – environment systems, (2016). doi:10.1073/pnas.1604978113/-/DCSupplemental.www.pnas.org/cgi/doi/10.1073/pnas.1604978113.

[21] R. Biggs, S.R. Carpenter, W.A. Brock, Turning back from the brink: detecting an impending regime shift in time to avert it., Proc. Natl. Acad. Sci. U. S. A. 106 (2009) 826–31. doi:10.1073/pnas.0811729106.

[22] A.S. Gsell, U. Scharfenberger, D. Özkundakci, A. Walters, L.-A. Hansson, A.B.G. Janssen, P. Nõges, P.C. Reid, D.E. Schindler, E. Van Donk, V. Dakos, R. Adrian, Evaluating early-warning indicators of critical transitions in natural aquatic ecosystems, Proc. Natl. Acad. Sci. (2016) 201608242. doi:10.1073/pnas.1608242113.

[23] C.P. Doncaster, V.A. Chávez, C. Viguier, R. Wang, E. Zhang, X. Dong, J.A. Dearing, P.G. Langdon, J.G. Dyke, Early warning of critical transitions in biodiversity from compositional disorder, Ecology. 97 (2016) 3079–3090. doi:10.1002/ecy.1558.

[24] M. Scheffer, S. Carpenter, J.A. Foley, C. Folke, B. Walker, Catastrophic shifts in ecosystems, Nature. 413 (2001) 591.

[25] C. Folke, S. Carpenter, B. Walker, M. Scheffer, T. Elmqvist, L. Gunderson, C.S. Holling,

Regime shifts, resilience, and biodiversity in ecosystem management, Annu. Rev. Ecol. Evol. Syst. 35 (2004).

[26] S.J. Lade, T. Gross, Early warning signals for critical transitions: A generalized modeling approach, PLoS Comput. Biol. 8 (2012). doi:10.1371/journal.pcbi.1002360.

[27] V. Dakos, S.R. Carpenter, W.A. Brock, A.M. Ellison, V. Guttal, A.R. Ives, S. Kéfi, V. Livina, D.A. Seekell, E.H. van Nes, M. Scheffer, Methods for detecting early warnings of critical transitions in time series illustrated using simulated ecological data, PLoS One. 7 (2012). doi:10.1371/journal.pone.0041010.

[28] A.J. Veraart, E.J. Faassen, V. Dakos, E.H. van Nes, M. Lürling, M. Scheffer, Corrigendum: Recovery rates reflect distance to a tipping point in a living system, Nature. 484 (2012) 404–404. doi:10.1038/nature11029.

[29] V. Dakos, E.H. Van Nes, P. D'Odorico, M. Scheffer, Robustness of variance and autocorrelation as indicators of critical slowing down, Ecology. 93 (2012) 264–271. doi:10.1890/11-0889.1.

[30] V. Guttal, C. Jayaprakash, Changing skewness: An early warning signal of regime shifts in ecosystems, Ecol. Lett. 11 (2008) 450–460. doi:10.1111/j.1461-0248.2008.01160.x.

[31] W.A. Brock, S.R. Carpenter, Interacting regime shifts in ecosystems: Implication for early warnings, Ecol. Monogr. 80 (2010) 353–367. doi:10.1890/09-1824.1.

[32] S.R. Carpenter, W.A. Brock, Rising variance: A leading indicator of ecological transition, Ecol. Lett. 9 (2006) 308–315. doi:10.1111/j.1461-0248.2005.00877.x.

[33] J.M. Drake, B.D. Griffen, Early warning signals of extinction in deteriorating environments., Nature. 467 (2010) 456–459. doi:10.1038/nature09389.

[34] E.H. van Nes, M. Scheffer, Slow Recovery from Perturbations as a Generic Indicator of a

Nearby Catastrophic Shift, Am. Nat. 169 (2007) 738–747. doi:10.1086/516845.

[35] M. Scheffer, S.R. Carpenter, T.M. Lenton, J. Bascompte, W. Brock, V. Dakos, J. van de Koppel, I. a. van de Leemput, S. a. Levin, E.H. van Nes, M. Pascual, J. Vandermeer, Anticipating Critical Transitions, Science (80-.). 338 (2012) 344–348. doi:10.1126/science.1225244.

[36] S.R. Carpenter, J.J. Cole, M.L. Pace, R. Batt, W. a. Brock, T. Cline, J. Coloso, J.R. Hodgson, J.F. Kitchell, D. a. Seekell, L. Smith, B. Weidel, Early warnings of regime shifts: a whole-ecosystem experiment, Science (80-.). 332 (2011) 1079–1082. doi:10.1126/science.1203672.

[37] C. Jeffries, K. Wiesenfeld, Observation of noisy precursors of dynamical instabilities, Phys. Rev. A. 31 (1985) 1077.

[38] W. Horsthemke, R. Lefever, Noise induced transitions, Non-Equilibrium Dyn. Chem. Syst. Springer Berlin Heidelb. (1984) 150–160.

[39] P.M. Groffman, J.S. Baron, T. Blett, A.J. Gold, I. Goodman, L.H. Gunderson, B.M. Levinson, M.A. Palmer, H.W. Paerl, G.D. Peterson, Ecological thresholds: the key to successful environmental management or an important concept with no practical application?, Ecosystems. 9 (2006) 1–13.

[40] S. Chen, Anticipating Critical Transitions with Nonlinearity, Periodicity and Heterogeneity, (2018).

[41] P.M. Groffman, J.S. Baron, T. Blett, A.J. Gold, I. Goodman, L.H. Gunderson, B.M. Levinson, M.A. Palmer, H.W. Paerl, G.D. Peterson, N.L. Poff, D.W. Rejeski, J.F. Reynolds, M.G. Turner, K.C. Weathers, J. Wiens, Ecological thresholds: The key to successful environmental management or an important concept with no practical

application?, Ecosystems. 9 (2006) 1–13. doi:10.1007/s10021-003-0142-z.

[42] J.-Q. Sun, A.C.J. Luo, Bifurcation and chaos in complex systems, Elsevier, 2006.

[43] B.H.K. Lee, L.Y. Jiang, Y.S. Wong, Flutter of an airfoil with a cubic restoring force, J. Fluids Struct. 13 (1999) 75–101.

[44] B.H.K. Lee, S.J. Price, Y.S. Wong, Nonlinear aeroelastic analysis of airfoils: bifurcation and chaos, Prog. Aerosp. Sci. 35 (1999) 205–334.

[45] M. Amabili, F. Pellicano, M.P. Païdoussis, Non-linear dynamics and stability of circular cylindrical shells containing flowing fluid. Part I: stability, J. Sound Vib. 225 (1999) 655–699.

[46] K. Hayat, A.G.M. de Lecea, C.D. Moriones, S.K. Ha, Flutter performance of bend–twist coupled large-scale wind turbine blades, J. Sound Vib. 370 (2016) 149–162.

[47] Y. Weiliang, E. Dowell, Limit cycle oscillation of a fluttering cantilever plate, AIAA J. 29 (1991) 1929–1936.

[48] F.A. Jafri, A. Shukla, D.F. Thompson, A numerical bifurcation study of friction effects in a slip-controlled torque converter clutch, Nonlinear Dyn. 50 (2007) 627–638.

[49] T. Kalmár-Nagy, G. Stépán, F.C. Moon, Subcritical Hopf bifurcation in the delay equation model for machine tool vibrations, Nonlinear Dyn. 26 (2001) 121–142.

[50] B.P. Mann, P. V Bayly, M.A. Davies, J.E. Halley, Limit cycles, bifurcations, and accuracy of the milling process, J. Sound Vib. 277 (2004) 31–48.

[51] A. Mees, L. Chua, The Hopf bifurcation theorem and its applications to nonlinear oscillations in circuits and systems, IEEE Trans. Circuits Syst. 26 (1979) 235–254.

[52] L. Liu, E.H. Dowell, Harmonic balance approach for an airfoil with a freeplay control surface, AIAA J. 43 (2005) 802–815.

[53] A. Raghothama, S. Narayanan, Non-linear dynamics of a two-dimensional airfoil by incremental harmonic balance method, J. Sound Vib. 226 (1999) 493–517.

[54] M. Ghommem, A.H. Nayfeh, M.R. Hajj, Control of limit cycle oscillations of a two-dimensional aeroelastic system, Math. Probl. Eng. 2010 (2010).

[55] F. Lakrad, M. Belhaq, Periodic solutions of strongly non-linear oscillators by the multiple scales method, J. Sound Vib. 258 (2002) 677–700.

[56] A.H. Nayfeh, The method of normal forms, John Wiley & Sons, 2011.

[57] D. Jiang, C. Pierre, S.W. Shaw, Large-amplitude non-linear normal modes of piecewise linear systems, J. Sound Vib. 272 (2004) 869–891.

[58] W.J.F. Govaerts, Numerical methods for bifurcations of dynamical equilibria, SIAM, 2000.

[59] A. Spence, I.G. Graham, Numerical methods for bifurcation problems, Springer Ser. Comput. Math. 26 (1999) 177–216.

[60] E.J. Doedel, A.R. Champneys, T.F. Fairgrieve, Y.A. Kuznetsov, B. Sandstede, X. Wang, Auto97, continuation and bifurcation software for ordinary differential equations (with homcont). 1997, Available by Anon. Ftp from Ftp. Cs. Concordia. ca, Dir. Pub/Doedel/Auto. (n.d.).

[61] A. Dhooge, W. Govaerts, Y.A. Kuznetsov, W. Mestrom, A.M. Riet, B. Sautois, MATCONT and CL MATCONT: Continuation toolboxes in matlab, Univ. Gent, Belgium Utr. Univ. Netherlands. (2006).

[62] K. Engelborghs, T. Luzyanina, D. Roose, Numerical bifurcation analysis of delay differential equations using DDE-BIFTOOL, ACM Trans. Math. Softw. 28 (2002) 1–21.

[63] R. Szalai, PDDE-CONT: A continuation and bifurcation software for delay-differential

equations, Dep. Appl. Mech. Budapest Univ. Technol. Econ. (2005).

[64] E.H. Dowell, H.C. Curtiss, R.H. Scanlan, F. Sisto, A modern course in aeroelasticity, Springer, 1989.

[65] B.H.K. Lee, L. Gong, Y.S. Wong, Analysis and computation of nonlinear dynamic response of a two-degree-of-freedom system and its application in aeroelasticity, J. Fluids Struct. 11 (1997) 225–246.

[66] K. Kim, T.W. Strganac, Aeroelastic studies of a cantilever wing with structural and aerodynamic nonlinearities, AIAA Pap. 1412 (2002) 43.

[67] M. Amabili, Nonlinear vibrations and stability of shells and plates, Cambridge University Press, 2008.

[68] M. Amabili, F. Pellicano, Nonlinear supersonic flutter of circular cylindrical shells, AIAA J. 39 (2001) 564–573.

[69] M. Amabili, F. Pellicano, Multimode approach to nonlinear supersonic flutter of imperfect circular cylindrical shells, J. Appl. Mech. 69 (2002) 117–129.

[70] Z.-F. Fu, J. He, Modal analysis, Elsevier, 2001.

[71] W. Zhou, D. Chelidze, Generalized eigenvalue decomposition in time domain modal parameter identification, J. Vib. Acoust. 130 (2008) 11001.

[72] E.J. Hannan, B.G. Quinn, The determination of the order of an autoregression, J. R. Stat. Soc. Ser. B. (1979) 190–195.

[73] J.-N. Juang, Mathematical correlation of modal parameter identification methods via system realization theory, (1986).

[74] J.-N. Juang, R.S. Pappa, An eigensystem realization algorithm for modal parameter identification and model reduction, J. Guid. 8 (1985) 620–627.

[75] R.S. Pappa, Eigensystem realization algorithm user's guide for VAX/VMS computers, NASA TM. 109066 (1994) 1994.

[76] Y.C. Fung, An introduction to the theory of aeroelasticity, Courier Dover Publications, 2008.

[77] D. Dessi, F. Mastroddi, A nonlinear analysis of stability and gust response of aeroelastic systems, J. Fluids Struct. 24 (2008) 436–445.

[78] S. Irani, H. Sarrafzadeh, M.R. Amoozgar, Bifurcation in a 3-DOF airfoil with cubic structural nonlinearity, Chinese J. Aeronaut. 24 (2011) 265–278.

[79] R.L. Bisplinghoff, H. Ashley, R.L. Halfman, Aeroelasticity, Courier Corporation, 2013.

[80] G.F. Fussmann, S.P. Ellner, K.W. Shertzer, N.G. Hairston Jr, Crossing the Hopf bifurcation in a live predator-prey system, Science (80-.). 290 (2000) 1358–1360.

[81] C. Huang, L. Huang, J. Feng, M. Nai, Y. He, Hopf bifurcation analysis for a two-neuron network with four delays, Chaos, Solitons & Fractals. 34 (2007) 795–812.

[82] K. Wiesenfeld, Virtual Hopf phenomenon: A new precursor of period-doubling bifurcations, Phys. Rev. A. 32 (1985) 1744.

[83] R.A. Chisholm, E. Filotas, Critical slowing down as an indicator of transitions in two-species models, J. Theor. Biol. 257 (2009) 142–149.

[84] J. Lim, B.I. Epureanu, Forecasting bifurcation morphing: Application to cantilever-based sensing, Nonlinear Dyn. 67 (2012) 2291–2298. doi:10.1007/s11071-011-0146-8.

[85] J. Sieber, J.M.T. Thompson, Nonlinear softening as a predictive precursor to climate tipping, Phil. Trans. R. Soc. A. 370 (2012) 1205–1227.

[86] J.M.T. Thompson, J. Sieber, Climate tipping as a noisy bifurcation: a predictive technique, IMA J. Appl. Math. 76 (2011) 27–46.

[87] J.M.T. Thompson, J.A.N. Sieber, Predicting climate tipping as a noisy bifurcation: a review, Int. J. Bifurc. Chaos. 21 (2011) 399–423.

[88] K. D'Souza, B.I. Epureanu, M. Pascual, Forecasting bifurcations from large perturbation recoveries in feedback ecosystems, PLoS One. 10 (2015) e0137779.

[89] A. Ghadami, B.I. Epureanu, Forecasting subcritical and supercritical flutter using gust responses, in: ASME Int. Mech. Eng. Congr. Expo. Proc., 2015. doi:10.1115/IMECE2015-53105.

[90] S. Lenci, L. Consolini, F. Clementi, On the experimental determination of dynamical properties of laminated glass, Ann. Solid Struct. Mech. 7 (2015) 27–43.

[91] P. Marzocca, L. Librescu, G. Chiocchia, Aeroelastic response of 2-D lifting surfaces to gust and arbitrary explosive loading signatures, Int. J. Impact Eng. 25 (2001) 41–65.

[92] J.H. Chow, F.F. Wu, J.A. Momoh, Applied mathematics for restructured electric power systems, in: Appl. Math. Restructured Electr. Power Syst., Springer, 2005: pp. 1–9.

[93] I. Waugh, S. Illingworth, M. Juniper, Matrix-free continuation of limit cycles for bifurcation analysis of large thermoacoustic systems, J. Comput. Phys. 240 (2013) 225–247.

[94] M.J. Patil, D.H. Hodges, C.E.S. Cesnik, Limit-cycle oscillations in high-aspect-ratio wings, J. Fluids Struct. 15 (2001) 107–132.

[95] D.M. Tang, E.H. Dowell, Experimental and theoretical study for nonlinear aeroelastic behavior of a flexible rotor blade, AIAA J. 31 (1993) 1133–1142.

[96] A.F. Vakakis, Non-linear normal modes (NNMs) and their applications in vibration theory: an overview, Mech. Syst. Signal Process. 11 (1997) 3–22.

[97] A. Luongo, On the use of the multiple scale method in solving 'difficult'bifurcation

problems, Math. Mech. Solids. 22 (2017) 988–1004.

[98] R. Lind, K. Snyder, M. Brenner, Investigating transient and limit cycle behaviors of a nonlinear structure by wavelet transforms, in: Proc. 39th Struct. Struct. Dyn. Mater. Conf., 1998: pp. 942–952.

[99] S.L. Kukreja, M.J. Brenner, Nonlinear aeroelastic system identification with application to experimental data, J. Guid. Control. Dyn. 29 (2006) 374–381.

[100] R. Rico-Martınez, K. Krischer, G. Flätgen, J.S. Anderson, I.G. Kevrekidis, Adaptive detection of instabilities: an experimental feasibility study, Phys. D Nonlinear Phenom. 176 (2003) 1–18.

[101] A. Ghadami, B.I. Epureanu, Bifurcation Forecasting for Large Dimensional Oscillatory Systems: Forecasting Flutter Using Gust Responses, J. Comput. Nonlinear Dyn. 11 (2016) 61009.

[102] A. Ghadami, B.I. Epureanu, Forecasting the post-bifurcation dynamics of large-dimensional slow-oscillatory systems using critical slowing down and center space reduction, Nonlinear Dyn. 88 (2017). doi:10.1007/s11071-016-3250-y.

[103] A. Ghadami, B.I. Epureanu, Forecasting the post-bifurcation dynamics of large-dimensional slow-oscillatory systems using critical slowing down and center space reduction, Nonlinear Dyn. 88 (2017) 415–431. doi:10.1007/s11071-016-3250-y.

[104] C.M. Shearer, C.E.S. Cesnik, Nonlinear flight dynamics of very flexible aircraft, J. Aircr. 44 (2007) 1528–1545.

[105] W. Su, C.E.S. Cesnik, Dynamic response of highly flexible flying wings, AIAA J. 49 (2011) 324.

[106] W. Su, C.E.S. Cesnik, Strain-based geometrically nonlinear beam formulation for

modeling very flexible aircraft, Int. J. Solids Struct. 48 (2011) 2349–2360.

[107] D.A. Peters, M.J. Johnson, Finite-state airloads for deformable airfoils on fixed and rotating wings, Asme-Publications-AD. 44 (1994) 1.

[108] M. Bando, K. Hasebe, A. Nakayama, A. Shibata, Y. Sugiyama, Structure stability of congestion in traffic dynamics, Jpn. J. Ind. Appl. Math. 11 (1994) 203.

[109] A. Aw, A. Klar, M. Rascle, T. Materne, Derivation of continuum traffic flow models from microscopic follow-the-leader models, SIAM J. Appl. Math. 63 (2002) 259–278.

[110] R. Jiang, M.-B. Hu, H.M. Zhang, Z.-Y. Gao, B. Jia, Q.-S. Wu, B. Wang, M. Yang, Traffic experiment reveals the nature of car-following, PLoS One. 9 (2014) e94351.

[111] G. Orosz, R.E. Wilson, G. Stépán, Traffic jams: dynamics and control, (2010).

[112] Z.S. Qian, J. Li, X. Li, M. Zhang, H. Wang, Modeling heterogeneous traffic flow: A pragmatic approach, Transp. Res. Part B Methodol. 99 (2017) 183–204.

[113] J. Tian, G. Li, M. Treiber, R. Jiang, N. Jia, S. Ma, Cellular automaton model simulating spatiotemporal patterns, phase transitions and concave growth pattern of oscillations in traffic flow, Transp. Res. Part B Methodol. 93 (2016) 560–575.

[114] R. Jiang, Q.-S. Wu, Z.-J. Zhu, A new continuum model for traffic flow and numerical tests, Transp. Res. Part B Methodol. 36 (2002) 405–419.

[115] F.A. Carrillo, J. Delgado, P. Saavedra, R.M. Velasco, F. Verduzco, Traveling waves, catastrophes and bifurcations in a generic second order traffic flow model, Int. J. Bifurc. Chaos. 23 (2013) 1350191.

[116] P.G. Michalopoulos, P. Yi, A.S. Lyrintzis, Continuum modelling of traffic dynamics for congested freeways, Transp. Res. Part B Methodol. 27 (1993) 315–332.

[117] I. Gasser, G. Sirito, B. Werner, Bifurcation analysis of a class of 'car following'traffic

models, Phys. D Nonlinear Phenom. 197 (2004) 222–241.

[118] G.F. Newell, A simplified car-following theory: a lower order model, Transp. Res. Part B Methodol. 36 (2002) 195–205.

[119] Y. Li, D. Sun, W. Liu, M. Zhang, M. Zhao, X. Liao, L. Tang, Modeling and simulation for microscopic traffic flow based on multiple headway, velocity and acceleration difference, Nonlinear Dyn. 66 (2011) 15–28.

[120] G. Orosz, R.E. Wilson, R. Szalai, G. Stépán, Exciting traffic jams: nonlinear phenomena behind traffic jam formation on highways, Phys. Rev. E. 80 (2009) 46205.

[121] M. Yamamoto, Y. Nomura, Y. Sugiyama, Dissipative system with asymmetric interaction and Hopf bifurcation, Phys. Rev. E. 80 (2009) 26203.

[122] G. Orosz, G. Stépán, Subcritical Hopf bifurcations in a car-following model with reaction-time delay, in: Proc. R. Soc. London A Math. Phys. Eng. Sci., The Royal Society, 2006: pp. 2643–2670.

[123] W.-H. Ai, Z.-K. Shi, D.-W. Liu, Bifurcation analysis of a speed gradient continuum traffic flow model, Phys. A Stat. Mech. Its Appl. 437 (2015) 418–429.

[124] H.M. Zhang, Analyses of the stability and wave properties of a new continuum traffic theory, Transp. Res. Part B Methodol. 33 (1999) 399–415.

[125] A. Ghadami, B.I. Epureanu, Forecasting critical points and post-critical limit cycles in nonlinear oscillatory systems using pre-critical transient responses, Int. J. Non. Linear. Mech. 101 (2018). doi:10.1016/j.ijnonlinmec.2018.02.008.

[126] A. Ghadami, E. Gourgou, B.I. Epureanu, Rate of recovery from perturbations as a means to forecast future stability of living systems, Sci. Rep. 8 (2018) 9271. doi:10.1038/s41598-018-27573-0.

[127] H. Yamasaki, B.I. Epureanu, Forecasting supercritical and subcritical Hopf bifurcations in aeroelastic systems, Int. J. Non. Linear. Mech. (2016).

[128] T.M. Lenton, Early warning of climate tipping points, Nat. Clim. Chang. 1 (2011) 201.

[129] L. Rindi, M.D. Bello, L. Dai, J. Gore, L. Benedetti-Cecchi, Direct observation of increasing recovery length before collapse of a marine benthic ecosystem, Nat. Ecol. Evol. 1 (2017) 0153. doi:10.1038/s41559-017-0153.

[130] A. Ghadami, C.E.S. Cesnik, B.I. Epureanu, Model-less forecasting of hopf bifurcations in fluid-structural systems, J. Fluids Struct. 76 (2018). doi:10.1016/j.jfluidstructs.2017.09.005.

[131] M. Bando, K. Hasebe, A. Nakayama, A. Shibata, Y. Sugiyama, Dynamical model of traffic congestion and numerical simulation, Phys. Rev. E. 51 (1995) 1035.

[132] G. Orosz, R.E. Wilson, B. Krauskopf, Global bifurcation investigation of an optimal velocity traffic model with driver reaction time, Phys. Rev. E. 70 (2004) 26207.

[133] J.M. Del Castillo, F.G. Benitez, On the functional form of the speed-density relationship—I: General theory, Transp. Res. Part B Methodol. 29 (1995) 373–389.

[134] M. Batista, E. Twrdy, Optimal velocity functions for car-following models, J. Zhejiang Univ. A. 11 (2010) 520–529.

[135] C. Marschler, J. Sieber, R. Berkemer, A. Kawamoto, J. Starke, Implicit methods for equation-free analysis: convergence results and analysis of emergent waves in microscopic traffic models, SIAM J. Appl. Dyn. Syst. 13 (2014) 1202–1238.

[136] R. Wang, J. a. Dearing, P.G. Langdon, E. Zhang, X. Yang, V. Dakos, M. Scheffer, Flickering gives early warning signals of a critical transition to a eutrophic lake state, Nature. 492 (2012) 419–422. doi:10.1038/nature11655.

[137] M. Hirota, M. Holmgren, E.H. Van Nes, M. Scheffer, Global Resilience of Tropical Forest and Savanna to Critical Transitions, Science (80-.). 334 (2011) 232–235. doi:10.1126/science.1210657.

[138] M. Krkošek, J.M. Drake, On signals of phase transitions in salmon population dynamics, Proc. R. Soc. B Biol. Sci. 281 (2014) 20133221. doi:10.1098/rspb.2013.3221.

[139] S.R. Hare, N.J. Mantua, Empirical evidence for North Pacific regime shifts in 1977 and 1989, Prog. Oceanogr. 47 (2000) 103–145. doi:10.1016/S0079-6611(00)00033-1.

[140] J. van Belzen, J. van de Koppel, M.L. Kirwan, D. van der Wal, P.M.J. Herman, V. Dakos, S. K?fi, M. Scheffer, G.R. Guntenspergen, T.J. Bouma, Vegetation recovery in tidal marshes reveals critical slowing down under increased inundation, Nat. Commun. 8 (2017) 15811. doi:10.1038/ncomms15811.

[141] W.C. Allee, O. Park, A.E. Emerson, T. Park, K.P. Schmidt, Principles of animal ecology., WB Saundere Co. Ltd., 1949.

[142] L. Dai, K.S. Korolev, J. Gore, Slower recovery in space before collapse of connected populations, Nature. 496 (2013) 355–358. doi:10.1038/nature12071.

[143] T.C. Reluga, J. Medlock, A.S. Perelson, Backward bifurcations and multiple equilibria in epidemic models with structured immunity, J. Theor. Biol. 252 (2008) 155–165. doi:10.1016/j.jtbi.2008.01.014.

[144] M.J. Keeling, P. Rohani, Modeling Infectious Diseases in Humans and Animals, 2008. doi:10.1086/591197.

[145] F. Brauer, Backward bifurcations in simple vaccination models, J. Math. Anal. Appl. 298 (2004) 418–431. doi:10.1016/j.jmaa.2004.05.045.

[146] J. Guckenheimer, P.J. Holmes, Nonlinear oscillations, dynamical systems, and

bifurcations of vector fields, Springer Science & Business Media, 2013.

[147] K. D'Souza, B.I. Epureanu, M. Pascual, Forecasting bifurcations from large perturbation recoveries in feedback ecosystems, PLoS One. 10 (2015). doi:10.1371/journal.pone.0137779.

[148] L. Dai, K.S. Korolev, J. Gore, Relation between stability and resilience determines the performance of early warning signals under different environmental drivers, Proc. Natl. Acad. Sci. (2015) 201418415. doi:10.1073/pnas.1418415112.

[149] A. Sanchez, J. Gore, Feedback between Population and Evolutionary Dynamics Determines the Fate of Social Microbial Populations, PLoS Biol. 11 (2013). doi:10.1371/journal.pbio.1001547.

[150] M. Sen Datta, K.S. Korolev, I. Cvijovic, C. Dudley, J. Gore, Range expansion promotes cooperation in an experimental microbial metapopulation, Proc. Natl. Acad. Sci. 110 (2013) 7354–7359. doi:10.1073/pnas.1217517110.

[151] H. Celiker, J. Gore, Competition between species can stabilize public-goods cooperation within a species., Mol. Syst. Biol. 8 (2012) 621. doi:10.1038/msb.2012.54.

[152] R. Cohen, D. Engelberg, Commonly used Saccharomyces cerevisiae strains (e.g. BY4741, W303) are growth sensitive on synthetic complete medium due to poor leucine uptake, FEMS Microbiol. Lett. 273 (2007) 239–243. doi:10.1111/j.1574-6968.2007.00798.x.

[153] R.M. May, Thresholds and breakpoints in ecosystems with a multiplicity of stable states, Nature. 269 (1977) 471–477. doi:10.1038/269471a0.

[154] G.J. Van Geest, H. Coops, M. Scheffer, E.H. Van Nes, Long transients near the ghost of a stable state in eutrophic shallow lakes with fluctuating water levels, Ecosystems. 10 (2007) 36–46. doi:10.1007/s10021-006-9000-0.

[155] K.S. Korolev, J.B. Xavier, J. Gore, Turning ecology and evolution against cancer., Nat. Rev. Cancer. 14 (2014) 371–80. doi:10.1038/nrc3712.

[156] J. Sardanyés, R. Martínez, C. Simó, R. Solé, Abrupt transitions to tumor extinction: a phenotypic quasispecies model, J. Math. Biol. 74 (2017) 1589–1609. doi:10.1007/s00285-016-1062-9.

[157] I.A. van de Leemput, V. Dakos, M. Scheffer, E.H. van Nes, Slow Recovery from Local Disturbances as an Indicator for Loss of Ecosystem Resilience, Ecosystems. (2017) 1–12.

[158] M. Rietkerk, S.C. Dekker, P.C. De Ruiter, J. van de Koppel, Self-organized patchiness and catastrophic shifts in ecosystems, Science (80-.). 305 (2004) 1926–1929.

[159] R.M. May, S.A. Levin, G. Sugihara, Complex systems: Ecology for bankers, Nature. 451 (2008) 893.

[160] B.A. Carreras, V.E. Lynch, I. Dobson, D.E. Newman, Critical points and transitions in an electric power transmission model for cascading failure blackouts, Chaos An Interdiscip. J. Nonlinear Sci. 12 (2002) 985–994.

[161] V. Dakos, E.H. van Nes, R. Donangelo, H. Fort, M. Scheffer, Spatial correlation as leading indicator of catastrophic shifts, Theor. Ecol. 3 (2010) 163–174.

[162] C. Wissel, A universal law of the characteristic return time near thresholds, Oecologia. 65 (1984) 101–107.

[163] S.H. Strogatz, Nonlinear dynamics and chaos: with applications to physics, biology, chemistry, and engineering, CRC Press, 2018.

[164] V. Dakos, S. Kéfi, M. Rietkerk, E.H. Van Nes, M. Scheffer, Slowing down in spatially patterned ecosystems at the brink of collapse, Am. Nat. 177 (2011) E153–E166.

[165] V. Dakos, J. Bascompte, Critical slowing down as early warning for the onset of collapse

in mutualistic communities, Proc. Natl. Acad. Sci. 111 (2014) 17546–17551.

[166] S.R. Carpenter, W.A. Brock, J.J. Cole, J.F. Kitchell, M.L. Pace, Leading indicators of trophic cascades, Ecol. Lett. 11 (2008) 128–138.

[167] M.C. Boerlijst, T. Oudman, A.M. de Roos, Catastrophic collapse can occur without early warning: examples of silent catastrophes in structured ecological models, PLoS One. 8 (2013) e62033.

[168] V. Dakos, Identifying best-indicator species for abrupt transitions in multispecies communities, Ecol. Indic. (2017).

[169] S. Chen, B. Epureanu, Forecasting bifurcations in parametrically excited systems, Nonlinear Dyn. 91 (2018) 443–457.

[170] M.G. Kendall, Rank correlation methods, (1955).

[171] M.G. Kendall, A new measure of rank correlation, Biometrika. 30 (1938) 81–93.

[172] A.J. Lotka, Elements of mathematical biology, (1956).

[173] V. Volterra, Variations and fluctuations of the number of individuals in animal species living together, ICES J. Mar. Sci. 3 (1928) 3–51.

[174] V. Dakos, Identifying best-indicator species for abrupt transitions in multispecies communities, Ecol. Indic. 94 (2018) 494–502.

[175] E.H. van Nes, M. Scheffer, Large species shifts triggered by small forces, Am. Nat. 164 (2004) 255–266.

[176] S. Bathiany, M. Scheffer, E.H. Van Nes, M.S. Williamson, T.M. Lenton, Abrupt Climate Change in an Oscillating World, Sci. Rep. 8 (2018) 5040.

[177] D.J.D. Earn, P. Rohani, B.T. Grenfell, Persistence, chaos and synchrony in ecology and epidemiology, Proc. R. Soc. London B Biol. Sci. 265 (1998) 7–10.

[178] P.B. Miller, E.B. O'Dea, P. Rohani, J.M. Drake, Forecasting infectious disease emergence subject to seasonal forcing, Theor. Biol. Med. Model. 14 (2017) 17.

[179] L. Jezequel, C.-H. Lamarque, Analysis of non-linear dynamical systems by the normal form theory, J. Sound Vib. 149 (1991) 429–459.

[180] S.A. Neild, A.R. Champneys, D.J. Wagg, T.L. Hill, A. Cammarano, The use of normal forms for analysing nonlinear mechanical vibrations, Phil. Trans. R. Soc. A. 373 (2015) 20140404.